From the holdings of the Department of Special Collections , Princeton University Library, Princeton, NJ

These documents are either in the public domain, or can only be used for educational and research purposes (Fair use) as per U.S. Copyright law (text below). By accessing this file, all users agree that their use falls in the public domain or within fair use as defined by the copyrightlaw. We do not charge any permission or usage fees for the publication of images of material inour collections, including those provided by Princeton University Library, via our website, catalog, or directly from staff.For more information regarding copyright, credit, and citation please review the information onthe Copyright, Credit and Citation Guidelines page of our website.
https://library.princeton.edu/special-collections/policies/copyright-credit-and-citation-guidelines. If you have any questions, including how to order higher-quality images from the collection, contact Special Collections Public Services via our Ask Us! Form. https://library.princeton.edu/special-collections/ask-us

---

Doctoral Dissertations, 2011-2026 Astrophysical Sciences

2013

Dynamics of Thin Astrophysical Boundary Layers

Belyaev, Mikhail

Princeton, NJ : Princeton University

---

http://arks.princeton.edu/ark:/88435/dsp01qn59q405t

U.S. Copyright law: The copyright law of the United States (Title 17, §108, United States Code) governs the making of photocopies or other reproductions of copyrighted material. Under certain conditions specified in the law, libraries and archives are authorized to furnish a photocopy or other reproduction. One of these specified conditions is that the photocopy or reproduction is not to be used for any purpose other than private study, scholarship, or research. If a user makes a request for, or later uses, a photocopy or reproduction for purposes in excess of fair use that user may be liable for copyright infringement. This institution reserves the right to refuse to accept a copying order if, in its judgment, fulfillment of the order would involve a violation of copyright law. https://www.copyright.gov/title17/title17.pdf

Dynamics of Thin Astrophysical Boundary Layers

Mikhail Alexander Belyaev

A Dissertation

Presented to the Faculty

of Princeton University

in Candidacy for the Degree

of Doctor of Philosophy

Recommended for Acceptance

by the Department of

Astrophysical Sciences

Advisers: Roman R. Rafikov and James M. Stone

April 2013

© Copyright by Mikhail Alexander Belyaev, 2013.

All rights reserved.

Abstract

We study the modal structure and angular momentum transport mechanisms of astrophysical boundary layers. We focus on the case where the accretion disk extends all the way to surface of the star and the boundary layer is thin in comparison with the stellar radius. Such a scenario is applicable, for example, to weakly magnetized neutron stars and white dwarfs, for which the strength of the magnetic field outside the star is too small to disrupt the disk and funnel matter to the poles.

Within the boundary layer, material rotating at the Keplerian velocity within the disk slows down to the rotational velocity inside the star. This generates intense velocity gradients and makes the boundary layer susceptible to shear instabilities. By performing a linear stability analysis for the simplified case of a plane-parallel, compressible shear layer, we argue that astrophysical boundary layers are unstable to the sonic instability. This instability is part of a more general class of acoustic instabilities that includes the Papaloizou-Pringle instability.

We confirm the predictions of our linear stability analysis by running a suite of simulations in 2D and 3D, with and without stratification, and with and without magnetic field. In our numerical experiments, we find that acoustic modes excited by the sonic instability persist even in the nonlinear regime. We explain the morphological properties and derive analytic formulas for the pattern speed of these acoustic modes.

Our work has significant implications for semianalytic models describing the structure and spectral emission from boundary layers. Typically, these models adopt a local, effective viscosity prescription for the angular momentum transport. However, in our simulations we find that angular momentum transport in the boundary layer is facilitated by acoustic modes. In this scenario, accreting material inside the boundary layer loses angular momentum to sound waves that propagate into both the star and the disk. Since transport of angular momentum by waves is inherently nonlocal, our work invites the construction of new phenomenological models of the

boundary layer in which angular momentum is transported by waves rather than by an anomalous viscosity.

Acknowledgments

I would like to thank above all Roman Rafikov, whose physical insights helped me to forge through many an apparent impasse in my research, and without whose help this thesis would have far less depth. I would also like to thank Jim Stone for writing a tool as excellent as Athena. Even with the seemingly unlimited processing power available today, the resolution required for the simulations was on the brink of what is possible, and the code never disappointed in producing high quality results. I would also like to thank Jeremy Goodman and Anatoly Spitkovsky for lively discussions during the thesis committee meetings, Jill Knapp for her support, and Charlotte Zanidakis for easing the thesis submission process.

A big thanks goes out to the Princeton University computing facilities, and special thanks is given to Artemis for cooperating so well with her "divine" counterpart Athena. An equally big thanks goes out to the NASA HECC division for giving me access to the (nearly) omnipotent machines at their disposal.

Finally, I would like to thank my parents for their support, tangible and intangible, over the years, as well as the fine denizens of Peyton Hall.

Preface

The thesis is organized into six chapters and is based on four papers that have been accepted or submitted to *The Astrophysical Journal*. Chapter 1 is a short introduction and Chapter 2 is based on a published work with little modification. Chapters 3-5 are based entirely on two works, one published one submitted, but have been rearranged for clarity and to avoid repetition that would necessarily result if the published works were made into stand-alone chapters. Chapter 6 is entirely based on a single submitted work with little modification. Chapter 2 was completed under the guidance of Roman Rafikov and Chapters 3-6 under the guidance of Roman Rafikov and Jim Stone.

Some of the research from this thesis has been presented on a conference "X-ray sky: from stars and black holes to cosmology", held in Kazan, Russia in September 2012.

Chapter 2

In this chapter I discuss the linear stability of the compressible plane parallel vortex sheet and piecewise linear shear layer. The purpose of this chapter is to identify the types of shear instabilities that operate in astrophysical boundary layers. This chapter is based on the publication Belyaev & Rafikov (2012). I performed all derivations and wrote the manuscript.

Chapter 3

In this chapter, I discuss the model setup and numerical parameters used in the simulations discussed throughout chapters 4-6. This chapter is based entirely on sections that were taken verbatim from the publications Belyaev et al. (2012a), Belyaev et al. (2012b), Belyaev et al. (2012c), except for notational changes and connecting sentences required to glue together the different parts of each paper. All of the content in this chapter was written by me, and I performed all simulations. The supercomputers used to perform the simulations are *Artemis*, which belongs to Princeton University and *Pleiades*, which belongs to NASA.

Chapter 4

Here I discuss general morphological properties of an isothermal BL (without vertical stratification and magnetic field) and give an overview of the temporal evolution of a BL simulation. I show that sonic instabilities introduced in Chapter 2 do indeed occur in BL simulations and that these sonic instabilities excite acoustic modes with a well-defined pattern speed (the subject of Chapter 5). This chapter contains sections taken verbatim from the publications Belyaev et al. (2012a) and Belyaev et al. (2012b), except for notational changes and connecting sentences. I wrote the content and performed all derivations contained in this chapter. The introduction was co-written by Roman and me.

Chapter 5

In this chapter, I discuss in more detail the acoustic modes introduced in Chapter 4. In particular, I show that the isothermal BL supports three wave branches that are related to the wave branches of the isothermal vortex sheet (Chapter 2). I derive dispersion relations for each of these three wave branches and study angular momentum transport by acoustic modes within the BL. I find that waves rather than turbulence account for angular momentum transport in the isothermal boundary layer. This is incompatible with the view of a local effective viscosity, and I discuss the relevance of this result to semianalytic models of the boundary layer. I also discuss the effect that vertical stratification has on the acoustic modes. This chapter is based on content taken verbatim from the publications Belyaev et al. (2012a) and Belyaev et al. (2012b), except for notational changes and connecting sentences. All content and derivations in this chapter are my own work with the exception of the appendix about mass accretion by shocks, which was written by Roman and later modified by me to make it fit with the notation of the thesis. The introduction and discussion were co-written by Roman and me.

Chapter 6

In this chapter, I discuss how the presence of a magnetic field affects acoustic modes and angular momentum transport in the BL. The most important result is that for a weak field (gas pressure much greater than magnetic pressure), the acoustic modes discussed in chapters 4 & 5 become magnetosonic modes. However, their properties are only slightly modified compared to the hydrodynamical case, and our hydrodynamical results on acoustic modes remain valid. This

chapter is based on material being prepared for publication in the *Astrophysical Journal* and all content and derivations contained in it are my own work.

Bibliography

Belyaev, M. A. & Rafikov, R. R. 2012, ApJ, 752, 115

Belyaev, M. A., Rafikov, R. R., & Stone, J. M. 2012a, ApJ, 760, 22

Belyaev, M. A., Rafikov, R. R., & Stone, J. M. 2012b, ArXiv e-prints

Belyaev, M. A., Rafikov, R. R., & Stone, J. M. 2012c, (in preparation)

Contents

Abstract **iii**

Acknowledgments **v**

Preface **vi**

Bibliography viii

1 Introduction **1**

Bibliography 4

2 Supersonic Shear Instabilities in Astrophysical Boundary Layers **6**

1 Introduction 7

1.1 Initiation of Boundary Layers 8

1.2 Shear Instabilities in Compressible Fluids 10

2 Formalism 11

3 The Vortex Sheet without Gravity 15

3.1 Solutions for $M \gg 1$ 17

3.2 Dispersion Relation in the General Case 20

4 The Isothermal Vortex Sheet with Gravity 20

4.1 Highly Subsonic Vortex Sheet with Gravity 24

4.2 The Weak Gravity Limit at High Mach Number 24

5 Sonic Instabilities in a Finite Width Layer of Constant Shear 29

5.1 Dispersion Relation 30

5.2 Numerical Verification 31

5.3 Physical Intuition 33

6 Discussion and Conclusions . . . 38
Bibliography . . . 40
Appendix A Reduction of Equations . . . 42
Appendix B Generalized Rayleigh Equation and Boundary Conditions . . . 43
B.1 Derivation of the Generalized Rayleigh Equation . . . 43
B.2 Derivation of the Boundary Conditions at the Interface . . . 44
Appendix C Finite Width Shear Layer . . . 46
C.1 Setup of the Problem . . . 46
C.2 Dispersion Relation . . . 47
C.3 The Vortex Sheet Limit . . . 49

3 Numerical Model and Simulation Parameters 51

1 Overview . . . 51
2 Numerical Model . . . 52
2.1 Governing Equations . . . 52
2.2 Nondimensional Units . . . 52
2.3 Gravitational Potential . . . 53
2.4 Initial Rotation Profile . . . 54
2.5 Initial Density and Pressure Profiles . . . 55
2.6 Initial Magnetic Field Configuration (MHD Simulations) . . . 55
2.7 Boundary Conditions . . . 57
2.8 Initial Perturbations and Burn-In . . . 60
2.9 Simulation-Specific Parameters . . . 60
Bibliography . . . 62

4 General Overview of the Isothermal BL 64

1 Introduction and Astrophysical Motivation . . . 64
2 Sonic Instability . . . 66
3 Acoustic Modes . . . 69

4 Temporal Evolution of the BL . . . 72
5 Width of the BL as a Function of Mach Number . . . 75
5.1 Secondary KH Instabilities . . . 77
Bibliography . . . 79

5 Angular Momentum Transport: Hydro Simulations 81
1 Introduction . . . 82
2 Notation for Measured Quantities . . . 84
3 Boundary Layer Modes . . . 87
3.1 Plane Parallel Vortex Sheet . . . 87
3.2 Dispersion Relations for the Isothermal Boundary Layer . . . 88
3.3 Spatial Morphology of the Upper, Middle, and Lower Branches . . . 95
3.4 Modes with $k_z \neq 0$ . . . 99
4 Angular Momentum Transport . . . 101
4.1 Transport by Waves: General Formulas . . . 102
4.2 Upper Branch . . . 105
4.3 Lower Branch . . . 111
4.4 Relation of Angular Momentum Transport to Temporal Evolution . . . 113
4.5 Relation of Angular Momentum Transport to Mass Accretion Rate . . . 115
5 Effect of Stratification on Acoustic Modes . . . 117
6 The Incompatibility of α Models and Angular Momentum Transport by Waves . . . 121
7 Discussion . . . 122
7.1 Implications: Energy Transport in the BL . . . 124
7.2 Implications: stellar spinup . . . 126
7.3 Implications: mixing in the BL . . . 127
7.4 Implications: variability of emission . . . 127
7.5 Future prospects . . . 129
Bibliography . . . 130
Appendix A Dispersion Relation for Loosely Wound Modes Having $m \gg 1$ in the Disk 133

Appendix B Dispersion Relation for an Isothermal Stratified Atmosphere in Cylindrical Geometry . . . 135
Appendix C Parseval's Theorem . . . 137
Appendix D Mass Accretion Rate Due to Weak Shocks. . . . 138
Appendix E Dissipation Rate in the Isothermal Limit . . . 139

6 Angular Momentum Transport: MHD Simulations. 142

1 Introduction . . . 143
2 Angular Momentum Transport: Equations . . . 145
3 Angular Momentum Transport by MRI in the Disk . . . 147
3.1 Magnetic Pitch Angle . . . 148
3.2 Convergence Across Different Resolutions . . . 148
3.3 The Value of α due to MRI Turbulence in the Disk . . . 151
4 Magnetic Field Amplification in the BL . . . 152
5 Acoustic Modes in the MHD context . . . 154
5.1 Modification to the Hydrodynamical Dispersion Relation . . . 155
5.2 Simulation Results . . . 157
6 Angular Momentum Transport by Waves in the BL, Star, and Inner Disk . . . 160
6.1 Density Gap in the Inner Disk and Accretion onto the Star . . . 160
6.2 Angular Momentum Transport due to Waves and MRI . . . 164
6.3 Hydrodynamical Nature of Angular Momentum Transport in the Star and BL 166
6.4 Boundary Layer Width . . . 167
7 Discussion . . . 169
Bibliography . . . 172
Appendix A Dispersion Relation for the Compressible Vortex Sheet in the Presence of a Constant Magnetic Field that is Oriented Perpendicular to the Motion . . . 174

Chapter 1

Introduction

The boundary layer (BL) is one of the outstanding problems of accretion disk theory. However, there has been surprisingly little work on the dynamics of the physical processes that occur within it, although Kippenhahn & Thomas (1978), Alexakis et al. (2002), Armitage (2002), Steinacker & Papaloizou (2002), Balsara et al. (2009), Inogamov & Sunyaev (2010), Romanova et al. (2012), and Pessah & Chan (2012) have all tackled various aspects of this problem. Nevertheless, there does not even exist a mainstream view of what mechanism is responsible for angular momentum transport within the BL.

In fact, the BL is linearly stable to the magnetorotational instability (MRI), which leads to turbulence and is likely responsible for the anomalous viscosity within the disk proper. This is because the rotational profile rises within the BL ($d\Omega/d\varpi > 0$), smoothly transitioning between the Keplerian rotation profile of the disk and that of the more slowly rotating star. Indeed, Pessah & Chan (2012) have argued that shearing magnetic waves are inefficient at transporting angular momentum if $d\Omega/d\varpi > 0$. Extrapolating from their results, even if magnetic field could diffuse into the BL from the disk, this field would not provide a viable mechanism of angular momentum transport. Of course linear stability does not necessarily mean the flow must be laminar. Turbulence, once generated by some nonlinear mechanism, can persist without decaying in certain classes of rotating linearly stable hydrodynamical flows (Lesur & Longaretti, 2005).

Clearly, the study of angular momentum transport in the BL is a rich subject in its own right, but it also has important implications for semianalytic studies, such as those of Kippenhahn & Thomas (1978), Popham & Narayan (1995), Popham & Narayan (1992), Inogamov & Sunyaev (1999), Piro & Bildsten (2004), and Inogamov & Sunyaev (2010) that model spectral emission from or elemental mixing within the BL. These studies typically adopt a prescription for the

angular momentum transport based on either an effective viscosity model or assume a rotational profile that hovers around a stability criterion, such as the Richardson criterion for stratified shear flows. However, without knowing the mechanism of angular momentum transport, which in turn sets the rotational profile and the energy dissipation rate, it is difficult to construct an accurate phenomenological model to compare with observations of the BL.

The goal of this work is to shed light on the dynamical processes that facilitate angular momentum transport and produce temporal variability within the BL. In principle, one might imagine two disparate approaches to this problem. The first is to try to include as much physics as possible from the outset and perform a few sophisticated, but complex simulations of the BL. The second is to start with a simple physical setup that is analytically tractable, confirm analytical results with simulations, and make the simulations increasingly more sophisticated by adding new physics layer by layer. We adopt the second approach, since running a simulation that is too complicated from the outset can obscure the most important physical effects. Our philosophy is that it's better to start with the simple case, understand it completely, and see what changes as new physics is introduced. This way, when we reach the stage at which we are ready to run the most realistic simulations possible, we are armed with knowledge gained along the way and know what to look for.

Chapter 2 of the thesis (based on the publication Belyaev & Rafikov (2012)) is an analytic study of an extremely simplified version of a boundary layer: a compressible plane parallel shear layer with a piecewise linear velocity profile, an isothermal equation of state, and a density contrast between the fluid above and below the shear layer. This ignores potentially important effects, such as stratification of the fluid inside the star, Coriolis force, gravity modes, and magnetic field effects to name a few. However, even the stability properties of our simplified system are a subtle topic, when the Mach number, M, of the flow is high, which is the case for astrophysical boundary layers (e.g. $M \sim 100$ for white dwarfs). At high Mach numbers, the boundary layer behaves as a compressible fluid, and the primary mode of instability is due to interaction of sound waves with a critical layer, which is a location in the flow where the phase speed of the mode equals the flow velocity. Thus, a critical layer is analogous to a corotation

resonance in a rotating system. We speculate that sonic instability is the prevalent form of shear instability in astrophysical boundary layers. This makes it likely that acoustic modes excited by the sonic instability play an important role in angular momentum transport within the BL; an assertion we later test and confirm with simulations.

Chapter 3 of the thesis does not focus on new scientific results, but rather technical information about the BL simulations discussed in later chapters. This technical information includes the equations solved, the model setup of the simulations, and the parameters used. In this chapter, we include a table which contains all of the pertinent details of individual simulations. This table is a compendium of simulations discussed in the publications Belyaev et al. (2012a), Belyaev et al. (2012b), and Belyaev et al. (2012c) and in later chapters of the thesis.

Chapter 4 of the thesis is based on the publications Belyaev et al. (2012a) and Belyaev et al. (2012b) and discusses the general morphology and typical time evolution of the isothermal BL in our simulations that do not include vertical stratification or magnetic field. We find that sonic instabilities excite acoustic modes in the BL (studied in detail in Chapter 5) that facilitate angular momentum transport and drive mass accretion onto the star, creating a density gap in the inner disk. We also discuss general morphological properties of an isothermal BL, such as the scaling of the radial thickness with the Mach number.

Chapter 5 of the thesis is also based on the publications Belyaev et al. (2012a) and Belyaev et al. (2012b) and focuses on the dispersion relation of and angular momentum transport by the acoustic modes introduced in Chapter 4. We find that acoustic modes observed in our 2D and 3D unstratified (in the z direction) hydro simulations are direct analogs of the supersonic vortex sheet modes described in Chapter 2. However, the dispersion relation of these acoustic modes in BL simulations is modified by the presence of Coriolis force within the disk and gravity and radial stratification within the star. Additionally, differential rotation in the disk results in an evanescent region, which is not present in the setup described in Chapter 2. For certain wavebranches, this leads to reflection of sound waves emitted from the BL and creates a standing pattern of shocks between the BL and the evanescent region in the disk.

The acoustic modes transport angular momentum away from the BL in the form of sound waves that propagate into both the disk and the star. These sound waves can potentially travel long distances before dissipating and redepositing their angular momentum to the fluid. Thus, angular momentum transport in our simulations is fundamentally nonlocal and is not well-described by any simple effective viscosity model. This has important implications for semianalytic studies of the BL, which typically adopt a local model of angular momentum transport. Finally, we discuss the effect of stratification on acoustic modes.

Chapter 6 of the thesis discusses the effect of a magnetic field on the morphology of the BL and angular momentum transport within it. It is based entirely on the publication Belyaev et al. (2012c). We try a variety of field configurations and find that a magnetic field has only a small effect on the acoustic modes themselves. However, the MRI significantly modifies the angular momentum transport rate in the disk compared to the hydro case. Nevertheless, we find that acoustic modes continue to play an important role in angular momentum transport within the BL itself, even when a magnetic field is present.

Bibliography

Alexakis, A., Young, Y., & Rosner, R. 2002, Phys. Rev. E, 65, 026313

Armitage, P. J. 2002, MNRAS, 330, 895

Balsara, D. S., Fisker, J. L., Godon, P., & Sion, E. M. 2009, ApJ, 702, 1536

Belyaev, M. A. & Rafikov, R. R. 2012, ApJ, 752, 115

Belyaev, M. A., Rafikov, R. R., & Stone, J. M. 2012a, ApJ, 760, 22

Belyaev, M. A., Rafikov, R. R., & Stone, J. M. 2012b, ArXiv e-prints

Belyaev, M. A., Rafikov, R. R., & Stone, J. M. 2012c, (in preparation)

Inogamov, N. A. & Sunyaev, R. A. 1999, Astronomy Letters, 25, 269

Inogamov, N. A. & Sunyaev, R. A. 2010, Astronomy Letters, 36, 848

Kippenhahn, R. & Thomas, H.-C. 1978, A&A, 63, 265

Lesur, G. & Longaretti, P.-Y. 2005, A&A, 444, 25

Pessah, M. E. & Chan, C.-k. 2012, ApJ, 751, 48

Piro, A. L. & Bildsten, L. 2004, ApJ, 610, 977

Popham, R. & Narayan, R. 1992, ApJ, 394, 255

Popham, R. & Narayan, R. 1995, ApJ, 442, 337

Romanova, M. M., Ustyugova, G. V., Koldoba, A. V., & Lovelace, R. V. E. 2012, MNRAS, 421, 63

Steinacker, A. & Papaloizou, J. C. B. 2002, ApJ, 571, 413

Chapter 2

Supersonic Shear Instabilities in Astrophysical Boundary Layers

Abstract

Disk accretion onto weakly magnetized astrophysical objects often proceeds via a boundary layer that forms near the object's surface, in which the rotation speed of the accreted gas changes rapidly. Here we study the initial stages of formation for such a boundary layer around a white dwarf or a young star by examining the hydrodynamical shear instabilities that may initiate mixing and momentum transport between the two fluids of different densities moving supersonically with respect to each other. We find that an initially laminar boundary layer is unstable to two different kinds of instabilities. One is an instability of a supersonic vortex sheet (implying a discontinuous initial profile of the angular speed of the gas) in the presence of gravity, which we find to have a growth rate of order (but less than) the orbital frequency. The other is a sonic instability of a finite width, supersonic shear layer, which is similar to the Papaloizou-Pringle instability. It has a growth rate proportional to the shear inside the transition layer, which is of order the orbital frequency times the ratio of stellar radius to the boundary layer thickness. For a boundary layer that is thin compared to the radius of the star, the shear rate is much larger than the orbital frequency. Thus, we conclude that sonic instabilities play a dominant role in the initial stages of nonmagnetic boundary layer formation and give rise to very fast mixing between disk gas and stellar fluid in the supersonic regime.

1 Introduction

Accretion onto astrophysical objects possessing a material surface (as opposed to accretion onto black holes) always involves a non-trivial interaction of the incoming gas with the object's outer layers. Examples of such objects include white dwarfs in cataclysmic variables (CVs), young stars gaining material from a protoplanetary disk, and accreting neutron stars. In all these systems, one must understand how the incoming gas shares its angular momentum with the accreting object and how it mixes with the previously accreted material.

If the magnetic field of the central object is strong enough, it can disrupt the disk at some distance above the surface. Inside this region, accretion proceeds along field lines (Ghosh & Lamb, 1978; Koldoba et al., 2002). The critical value of the magnetic field at the surface of the central object for magnetic disruption is given by

$$B_{*,\mathrm{crit}} = 5 \times 10^4 \left(\frac{\beta}{.5}\right)^{-7/4} \left(\frac{M_*}{.6 M_\odot}\right)^{1/4} \left(\frac{\dot{M}}{10^{-8} M_\odot \ \mathrm{yr}^{-1}}\right)^{1/2} \left(\frac{R_*}{9 \times 10^3 \ \mathrm{km}}\right)^{-5/4} \mathrm{G}. \qquad (2.1)$$

Here, we have used parameters for the mass and radius that are typical for CVs in outburst (Bergeron et al., 1992; Hachisu, 1986; Patterson, 1984). The parameter β is a dimensionless factor of order unity that depends on the model adopted for the disruption of the disk by the stellar magnetic field (Ghosh & Lamb, 1978).

For $B_* < B_{*,\mathrm{crit}}$, the accretion disk will extend all the way to the surface of the star, for which there is good observational evidence in neutron star low mass X-ray binaries (Gilfanov et al., 2003) and in dwarf nova systems in outburst (Wheatley et al., 2003). Since the rotation rate of the star, Ω_*, is slower than the Keplerian rotation rate at the stellar surface, $\Omega_K(R_*)$, a boundary layer (BL) will exist inside of which $d\Omega/dR > 0$ and the rotation profile of the star attaches smoothly to that of the disk. If the accretion rate is high enough, it is also possible for material to spread meridionally to high latitudes forming a spreading layer (SL) (Inogamov & Sunyaev, 1999; Piro & Bildsten, 2004). For both a BL and a SL, the intense energy release in a localized region near the stellar surface leads to easily observable signatures such as hard spectral components, variability of emission, and so on.

A considerable amount of effort has been previously devoted to understanding the structure of well-developed, steady-state BLs, which have been evolving for long enough to establish a smooth rotation profile in their interior. An outstanding question in the study of steady-state BLs is identifying the mechanism of angular momentum transport in the layer. Several potential mechanisms have been explored over the years, among them shear instabilities (Kippenhahn & Thomas, 1978), baroclinic instabilities (Fujimoto, 1987; Hanawa, 1987), and the Tayler-Spruit dynamo (Spruit, 1999; Piro & Bildsten, 2007). Despite this effort, no clear answer exists at present regarding the nature of the angular momentum transport and mixing in well-developed BLs.

1.1 Initiation of Boundary Layers

An interesting aspect of the BL problem that has received less attention in the past is the issue of BL *initiation*, i.e. the initial stage of BL formation which must occur when the accreted material first touches the surface of the star. In this case the physical setup is going to be quite different from the steady-state BL primarily because of the much larger velocity shear, justifying the study of BL initiation in the limit of an essentially discontinuous rotation profile at the interface between the star and accreting material.

Even though the initiation stage is just a transient phase in the BL evolution, one still needs to understand it to get a full picture of the BL phenomenon. Also, one need not think that the BL initiation is a unique event for every accreting object — it may, in fact, be repetitive. The most common situation in which this BL initiation is recurrent involves the dramatic increase of the mass accretion rate (due to some sort of outburst triggered by an instability) through the disk which is magnetically disrupted outside the star under normal circumstances. According to Equation (2.1), a sudden increase of $\dot{M}$ by several orders of magnitude as typical for some accreting systems (e.g. dwarf novae, FU Ori outbursts, etc.) can rapidly compress the stellar magnetosphere to the point at which disk material starts touching the stellar surface and a BL starts to form.

There is good observational evidence for this kind of recurrent behavior. For instance, Livio & Pringle (1992) have argued that the observed lag in the rise time of the UV emission relative to

the optical in a CV system transitioning to outburst can be explained if the disk is magnetically disrupted in quiescence but not in outburst. Thus, the hottest, innermost part of the disk is evacuated in quiescence, and UV radiation is not emitted immediately in the transition to outburst, since the empty region requires time to become filled.

FU Ori stars are another type of system in which the disk can extend all the way to the stellar surface, due to the high accretion rate - $\dot{M} \sim 10^{-4} M_{\odot} \mathrm{yr}^{-1}$ (Kenyon et al., 1988). In these systems, the BL can puff up to become of order the stellar radius and the distinction between the boundary layer, the disk, and the star becomes blurred (Popham et al., 1993).

The goal of our present work is to make a first step towards understanding the *formation* of the BL. As in the case of a well-developed BL, the major issue for this initial stage lies in details of the angular momentum transport and mixing. However, because of the enormous shear present at the star-disk interface at this stage, it is highly likely that purely hydrodynamical shear instabilities would dominate the transport of mass and momentum rather than anything else.

For that reason, in this work we primarily focus on exploring the properties of various shear-driven instabilities under the conditions typical at the BL formation stage. First, we seek to identify a particular variety of the shear instability that most efficiently initiates mixing between the two fluids, i.e. has the fastest growth rate. Second, we examine the conditions needed for its operation, such as the density contrast between fluids, initial velocity profile, etc.

There are several physical ingredients which can potentially affect operation of shear instabilities: stratification, rotation, magnetic fields, turbulence, radiative transfer, and the supersonic nature of the flow. The latter aspect of the problem is very important and is inevitable during the BL initiation phase, when disk material rotating at the Keplerian speed comes into contact with the more slowly spinning stellar surface. The differential azimuthal velocity between the two interacting flows is then bound to be a significant fraction of the Keplerian velocity at R_* and should highly exceed the sound speed both in the disk and in the outer layers of the star.

1.2 Shear Instabilities in Compressible Fluids

The study of shear instabilities in compressible fluids is of fundamental physical significance and has received much attention in the past. Landau (1944), Hatanaka (1949), Pai (1954), Miles (1958), and Gerwin (1968) have all studied the problem in the vortex sheet approximation, where one half plane of compressible fluid moves at constant velocity over another. When the two fluids move at a low Mach number relative to each other, one finds that infinitesimal perturbations are governed by the classical Kelvin-Helmholtz (KH) dispersion relation for two incompressible fluids. However, Miles (1958) showed that above a critical Mach number, the vortex sheet becomes marginally stable to two-dimensional disturbances along the direction of the flow. This is a surprising result considering that one might have expected increasing the shear to lead to an increased growth rate for the instability rather than stabilization. Understanding the implications of this result for the momentum and mass transport in the astrophysical BLs is one of the goals of our study.

Later, Blumen et al. (1975), Ray (1982), Choudhury & Lovelace (1984) and Glatzel (1988) studied the stability of a fluid with a continuous and monotonically varying velocity profile. They found that unlike the vortex sheet, continuous velocity profiles with a supersonic velocity difference across them were unstable even at high Mach number. Glatzel (1988) showed that the instability was similar to the Papaloizou-Pringle instability which operates in hydrodynamical disks with radial boundaries (Papaloizou & Pringle, 1987). Thus, for high Mach number flow in a compressible fluid, a finite thickness velocity profile exhibits fundamentally different behavior from the vortex sheet, since it can support unstable modes. Moreover, the growth rate of the unstable modes scales as $\propto 1/L$, where L is the thickness of the shear layer. Thus, the thinner the shear layer, the faster the instability operates! This is exactly the opposite of what one might have expected from the vortex sheet stability criterion and we will provide an explanation for this in §5.

Previous studies of possible instabilities inside astrophysical BLs have been primarily concerned with the sub-sonic regime when the flow can be considered as almost incompressible (Kippenhahn & Thomas, 1978; Fujimoto, 1988). This regime may indeed apply in well-developed BLs with smooth shear profiles, even though at the present level of knowledge one can hardly

exclude the possibility of the existence of localized regions in steady-state BLs where compressibility is still important. Our primary goal here is to extend these studies into the regime of highly compressible, supersonic flows and to explore the implications for astrophysical objects. In the course of studying supersonic shear instabilities, we will sometimes also incorporate stratification in our calculations and explore the role of rotation.

The paper is organized as follows. In §2 we present our governing set of equations and describe the formalism we use to study the stability problem. Then in §3 we study the case of the compressible vortex sheet with no gravity and show that our formalism reproduces the dispersion relation obtained by previous authors (Landau, 1944; Hatanaka, 1949; Pai, 1954; Miles, 1958; Gerwin, 1968). In §4, we introduce gravity as a small parameter and perform a perturbation expansion to study what influence this has on the stability of the vortex sheet. Finally, in §5 we study the stability of a finite width shear layer with a linear velocity profile. We derive new dispersion relations for this case and test the growth rate of the fastest growing mode using the Godunov code Athena (Stone et al., 2008).

2 Formalism

Here we discuss the formalism that we use for analytic calculations throughout the paper. We adopt cylindrical coordinates (ϖ, θ, z) and for simplicity assume that all equilibrium quantities are independent of z. Thus, for our purposes gravity is given by $-g(\varpi)\hat{\boldsymbol{\varpi}}$ $(g(\varpi) > 0)$, and we ignore the vertical stratification of the disk. Such a setup does not allow for the baroclinic instability, which would require $d\Omega/dz \neq 0$, but it does contain the necessary ingredients for studying shear instabilities. Given our assumptions, the equation of hydrostatic equilibrium reads

$$\bar{g}(\varpi) \equiv g(\varpi) - \varpi\Omega^2(\varpi) = -\frac{1}{\rho}\frac{dP}{d\varpi}, \tag{2.2}$$

where $\bar{g}(\varpi)$ is the effective gravity. The equilibrium density, pressure, and sound speed are given by $\rho(\varpi)$, $P(\varpi)$, and $s(\varpi)$ respectively.

Denoting the (ϖ, θ, z) velocities by (u, v, w), using $v = \Omega\varpi$, and assuming adiabaticity, the Euler equations in cylindrical coordinates are

$$
\begin{aligned}
-\frac{\partial \rho}{\partial t} &= \frac{1}{\varpi}\frac{\partial}{\partial \varpi}(\rho \varpi u) + \frac{1}{\varpi}\frac{\partial}{\partial \theta}(\rho v) + \frac{\partial}{\partial z}(\rho w) && (2.3)\\
\frac{Du}{Dt} &= -\frac{1}{\rho}\frac{\partial P}{\partial \varpi} + \frac{v^2}{\varpi} - g && (2.4)\\
\frac{Dv}{Dt} &= -\frac{1}{\rho\varpi}\frac{\partial P}{\partial \theta} - \frac{uv}{\varpi} && (2.5)\\
\frac{Dw}{Dt} &= -\frac{1}{\rho}\frac{\partial P}{\partial z} && (2.6)\\
\frac{D\left(P\rho^{-\gamma}\right)}{Dt} &= 0 && (2.7)\\
\frac{D}{Dt} &\equiv \frac{\partial}{\partial t} + u\frac{\partial}{\partial \varpi} + \frac{v}{\varpi}\frac{\partial}{\partial \theta} + w\frac{\partial}{\partial z} && (2.8)
\end{aligned}
$$

On top of the zeroth order equilibrium state, we consider infinitesimal two-dimensional perturbations of the form $\delta f(\varpi)\exp[i(m\theta + k_z z - \omega t)]$, where the δ denotes an Eulerian perturbation. Starting from Equations (2.3)-(2.7), the linearized first order equations are given by

$$
\begin{aligned}
i\bar{\omega}\delta\rho &= \frac{1}{\varpi}(\varpi\rho\delta u)' + \frac{im\rho}{\varpi}\delta v + ik_z\rho\delta w && (2.9)\\
i\bar{\omega}\delta u &= \frac{1}{\rho}\delta P' + \frac{\bar{g}}{\rho}\delta\rho - 2\Omega\delta v && (2.10)\\
i\bar{\omega}\delta v &= \frac{im}{\varpi\rho}\delta P + 2B\delta u && (2.11)\\
i\bar{\omega}\delta w &= \frac{ik_z}{\rho}\delta P && (2.12)\\
i\bar{\omega}\delta\rho &= -C_L\rho\delta u + \frac{i\bar{\omega}}{s^2}\delta P, && (2.13)
\end{aligned}
$$

where $\bar{\omega} = \omega - m\Omega$ is the phase speed in the locally corotating frame, $B = (\Omega + d(\varpi\Omega)/d\varpi)/2$ is Oort's B constant, $C_L = \gamma^{-1} d\ln P/d\varpi - d\ln\rho/d\varpi$ is the Ledoux discriminant, and the primes denote differentiation with respect to ϖ. Note that in Equations (2.9)-(2.13), we have made Cowling's approximation by ignoring the first order perturbation to the gravitational potential (Cowling, 1941). This means that we are taking the self-gravity of the BL to be negligible.

We can reduce the above set of linear equations to a pair of equations in δP and δu:

$$i\left(\frac{\bar{\omega}^2}{s^2} - k_z^2 - \frac{m^2}{\varpi^2}\right)\delta P = \rho\left(C_L\bar{\omega} + \frac{2Bm}{\varpi}\right)\delta u + \frac{\bar{\omega}}{\varpi}(\varpi\rho\delta u)' \quad (2.14)$$

$$i\rho(\bar{\omega}^2 - \bar{g}C_L - \kappa^2)\delta u = \bar{\omega}\delta P' + \frac{\bar{\omega}\bar{g}}{s^2}\delta P - \frac{2\Omega m}{\varpi}\delta P. \quad (2.15)$$

Here we have introduced the epicyclic frequency $\kappa^2 = 4B\Omega$.

One generally expects the BL width δ_{BL} to be small compared to the stellar radius, $\delta_{BL} \ll R_*$. Under this assumption, we show in Appendix A that Equations (2.14)-(2.15) can be simplified to the following set of equations:

$$i\left(\frac{\bar{\omega}^2}{s^2} - k_z^2 - \frac{m^2}{R_*^2}\right)\delta P = \rho\left(C_L\bar{\omega} + \frac{m}{R_*}S\right)\delta u + \bar{\omega}(\rho\delta u)' \quad (2.16)$$

$$i\rho(\bar{\omega}^2 - \bar{g}C_L)\delta u = \bar{\omega}\delta P' + \frac{\bar{\omega}\bar{g}}{s^2}\delta P, \quad (2.17)$$

where $S \equiv \varpi d\Omega/d\varpi$ is the shear rate. The form of Equations (2.16) and (2.17) is the same as for a plane-parallel stratified shear flow (Alexakis et al., 2002). This suggests that the effects of Coriolis force and curvature are unimportant in a radially thin BL if shear instabilities provide the turbulence, and leads us to redefine the cylindrical (ϖ, θ, z) coordinate system into a Cartesian (x, y, z) system. The perturbed quantities now have the form $\delta f(x)\exp[i(k_y y + k_z z - \omega t)]$, where $k_y \equiv m/R_*$. From this it immediately follows that $\bar{\omega} = \omega - k_y V_y(x)$, where $V_y(x) = R_*\Omega(x)$ is the velocity profile. From here on, we will ignore the rotation terms, and treat the flow in the BL as a plane parallel shear flow.

From Squire's theorem for plane parallel compressible shear flows (Fejer & Miles, 1963), any three-dimensional perturbation is mathematically equivalent to a two-dimensional perturbation upon making the transformations $k_y \to k_y/\cos\theta$, $k_z \to 0$, and $V_y \to V_y\cos\theta$, where $\cos\theta = k_y/\sqrt{k_y^2 + k_z^2}$. Thus, it is sufficient to only consider two-dimensional perturbations ($k_z = 0$) in the stability problem, and for the rest of this paper we take perturbations in the form

$$\delta f(x)\exp[i(k_y y - \omega t)]. \quad (2.18)$$

Assuming two-dimensional perturbations, Equations (2.16) and (2.17) become

$$i\left(\frac{\bar{\omega}^2}{s^2}-k_y^2\right)\delta P = \rho\left(C_L\bar{\omega}+k_yV_y'\right)\delta u+\bar{\omega}(\rho\delta u)' \tag{2.19}$$

$$i\rho(\bar{\omega}^2-\bar{g}C_L)\delta u = \bar{\omega}\delta P'+\frac{\bar{\omega}\bar{g}}{s^2}\delta P, \tag{2.20}$$

where the primes now denote differentiation with respect to x. Equations (2.20) and (2.19) can be used to obtain the generalized Rayleigh equation (Appendix B.1), which using a notation similar to Alexakis et al. (2002) reads

$$\delta\phi''+\left(k_x^2-g\tilde{\rho}\frac{k_s+k_g}{\tilde{W}^2}-\frac{\tilde{W}''}{\tilde{W}}\right)\delta\phi = 0. \tag{2.21}$$

Here,

$$\delta\phi=-\delta u\sqrt{\rho}/k_x, \tag{2.22}$$

is a modified stream function, and for simplicity we have dropped the bar over $\bar{g}$, so now g denotes the effective gravity. We have also defined the quantities:

$$\tilde{W}=k_yW\sqrt{\tilde{\rho}}/ik_x \tag{2.23}$$

$$W=V_y-c \text{ where } c=\omega/k \text{ is the phase speed.} \tag{2.24}$$

$$k_x^2=k_y^2(W^2/s^2-1) \text{ is the square of the x-component of the wavevector} \tag{2.25}$$

$$\text{in the absence of shear or stratification.} \tag{2.26}$$

$$\tilde{\rho}=\rho f^2, \text{ where } \rho \text{ is the density.} \tag{2.27}$$

$$f=\exp\left(\int_0^x k_g(\zeta)d\zeta\right). \tag{2.28}$$

$$k_g=g/s^2 \text{ is a measure of the inverse of the local pressure scale height.} \tag{2.29}$$

$$k_s=\rho'/\rho \text{ is the inverse stratification length scale.} \tag{2.30}$$

Note that the Ledoux discriminant is given by $C_L=-(k_g+k_s)$.

The boundary conditions on $\delta\phi$ that must be satisfied at a discontinuity in the density or the velocity are that the upper and lower fluids stay in contact and that the pressure perturbation is continuous across the interface. We show explicitly in Appendix B.2 that these conditions can be formulated as

$$\frac{\delta\phi_+}{\tilde{W}_+} = \frac{\delta\phi_-}{\tilde{W}_-} \tag{2.31}$$

$$\tilde{W}_+\delta\phi'_+ - \tilde{W}'_+\delta\phi_+ - \frac{g_+\tilde{\rho}_+\delta\phi_+}{\tilde{W}_+} = \tilde{W}_-\delta\phi'_- - \tilde{W}'_-\delta\phi_- - \frac{g_-\tilde{\rho}_-\delta\phi_-}{\tilde{W}_-}. \tag{2.32}$$

The $+/-$ signs denote evaluation of a quantity in the upper/lower fluid at the location of the interface.

3 The Vortex Sheet without Gravity

Equations (2.21)-(2.32) are fully general and apply to an arbitrary velocity profile. In particular, we can assume that the velocity varies discontinuously at some radius $x = 0$:

$$V_y(x) = \begin{cases} \bar{V}_y, & x > 0 \\ -\bar{V}_y, & x < 0, \end{cases} \tag{2.33}$$

where $\bar{V}_y$ is a constant. This is known as a vortex sheet approximation. It represents the simplest possible description of the velocity variation between the two limiting values by essentially ignoring the details of the transition. Subsequently in §5, we explore a more realistic model of the velocity variation, in which the transition occurs in a region of finite radial width. We point out that the vortex sheet approximation is valid for $k_y\delta_{BL} \ll 1$. We show in Appendix C.3 that in this limit the dispersion relation for a finite width layer of constant shear reduces to the vortex sheet dispersion relation.

We assume in this section that $g = 0$, so there is no gravity, and that ρ and s are constant above and below the interface, but can be discontinuous across it. This case has already been considered by other authors in the past including Landau (1944), Hatanaka (1949), Pai (1954),

Miles (1958), and Gerwin (1968). However, the results for the case without gravity will often be referenced later in the paper and serve as a verification of the formalism we developed in §2.

Using the velocity profile (2.33), the generalized Rayleigh equation (2.21) becomes

$$\delta\phi_{\pm}'' + k_{x,\pm}^2 \delta\phi_{\pm} \quad = \quad 0, \tag{2.34}$$

$$\tag{2.35}$$

where just as in §2, the $+/-$ signs denote the upper/lower fluids respectively. Since $k_{x,\pm}$ is constant for $V_y(x)$ given by Equation (2.33), we have that

$$\delta\phi_{\pm} \quad \propto \quad e^{-ik_{x,\pm}x}. \tag{2.36}$$

In general, $k_{x,\pm}$ is complex, and the sign is determined by applying the appropriate boundary conditions. We discuss the boundary conditions shortly, which will also make clear the reason for the negative sign in the exponential of Equation (2.36). Plugging the expressions for $\delta\phi_{\pm}$ into Equation (2.32) gives

$$\tilde{W}_+ k_{x,+} \delta\phi_+ = \tilde{W}_- k_{x,-} \delta\phi_-, \tag{2.37}$$

where we have used $\delta\phi_{\pm}' = ik_{x,\pm}\delta\phi_{\pm}$, $\tilde{\rho}_{\pm} = \rho_{\pm}$, and $\tilde{W}_{\pm}' = 0$. Using Equation (2.31) to substitute for $\delta\phi_-$ in terms of $\delta\phi_+$, and substituting for $\tilde{W}$ in terms of W and ρ we have

$$\frac{k_y}{k_{x,+}} \rho_+ W_+^2 = \frac{k_y}{k_{x,-}} \rho_- W_-^2. \tag{2.38}$$

Introducing the density ratio $\epsilon = \rho_+/\rho_-$, the Mach number in the upper fluid $M = \bar{V}_y/s_+$, and the phase speed normalized by the sound speed in the upper fluid $\varphi = c/s_+$, we have

$$\epsilon(M-\varphi)^2 \sqrt{(M+\varphi)^2 \frac{s_+^2}{s_-^2} - 1} = (M+\varphi)^2 \sqrt{(M-\varphi)^2 - 1}. \tag{2.39}$$

By the definition of the sound speed, $s^2 = \gamma P/\rho$, the condition of pressure balance everywhere throughout the flow requires that $\gamma_+^{-1}\rho_+ s_+^2 = \gamma_-^{-1}\rho_- s_-^2$, where γ_+ and γ_- are the adiabatic indices above and below the interface. Assuming $\gamma_+ = \gamma_-$, we have from pressure balance that $(s_-/s_+)^2 = \rho_+/\rho_- = \epsilon$. Thus, the dispersion relation becomes:

$$\epsilon(M-\varphi)^2\sqrt{(M+\varphi)^2\epsilon^{-1}-1} = (M+\varphi)^2\sqrt{(M-\varphi)^2-1}. \tag{2.40}$$

Miles (1958) has studied Equation (2.40) and found that the stability criterion, i.e. that φ is purely real, is given by

$$M > M_{\rm crit} = \frac{1}{2}(1+\epsilon^{1/3})^{3/2}. \tag{2.41}$$

This shows the surprising result that infinitesimal disturbances are stabilized at high Mach number.

However, Fejer & Miles (1963) pointed out that due to Squire's theorem, it is always possible to choose an angle θ for the wavevector with respect to the flow velocity such that the projected Mach number $M\cos\theta$ is smaller than $M_{\rm crit}$. Thus, even at high Mach number, the vortex sheet without gravity is still unstable to three dimensional disturbances, which are almost perpendicular to the direction of the flow; these unstable oblique modes resemble classical KH modes. However, in the astrophysical context, a thin disk has a scale height $s/\Omega \ll R_*$, and the wavelength of the oblique modes will be small relative to the disk scale height only for very small wavelengths $\lambda \ll s/\Omega$. If the BL itself has a thickness $\delta_{BL} \gtrsim s/\Omega$, the vortex sheet approximation for the oblique modes is invalid, since either the modes don't fit into a disk scale height, or the condition $\lambda \gg \delta_{BL}$ is not satisfied.

3.1 Solutions for $M \gg 1$

Since we are interested in the high Mach number limit for the initiation of the BL, we now find analytical solutions to the dispersion relation (2.40) for $M \gg M_{\rm crit}$, where $M_{\rm crit}$ was defined in

Equation (2.41). Squaring Equation (2.40), one obtains a sixth order polynomial in φ:

$$(\epsilon^2 - (M+\varphi)^2\epsilon)(M-\varphi)^4 - (1-(M-\varphi)^2)(M+\varphi)^4 = 0. \tag{2.42}$$

This polynomial has two easy to find analytic factors (Miles, 1958)

$$\varphi = \left\{ -M\left(\frac{1-\epsilon^{1/2}}{1+\epsilon^{1/2}}\right), -M\left(\frac{1+\epsilon^{1/2}}{1-\epsilon^{1/2}}\right) \right\}. \tag{2.43}$$

We now take the limit $M \gg M_{\rm crit}$, in which case to terms of order $\mathcal{O}(M^{-4})$, the other four solutions to the polynomial in Equation (2.42) are

$$\varphi = \Bigg\{ M+1+\frac{\epsilon}{2(2M+1)^2},\ M-1-\frac{\epsilon}{2(2M-1)^2}, \\ -M+\epsilon^{1/2}+\frac{\epsilon^{1/2}}{2(2M-\epsilon^{1/2})^2},\ -M-\epsilon^{1/2}-\frac{\epsilon^{1/2}}{2(2M+\epsilon^{1/2})^2} \Bigg\}. \tag{2.44}$$

It is easy to see that the six roots of the polynomial (2.42) correspond to sound waves. Starting from Equation (2.25) and rearranging terms we obtain

$$W^2 k_y^2 = s^2(k_x^2 + k_y^2). \tag{2.45}$$

As long as k_x is real, this is the dispersion relation for a sound wave, since W^2 is the square of the phase velocity in the frame comoving with the fluid. Plugging in the six roots from Equations (2.43) and (2.44) into Equation (2.25), it is straightforward to verify that $k_{x,\pm}$ are indeed real for all of them. Each of the four roots in Equation (2.44) has a further simple interpretation. The first two correspond to sound waves that propagate almost parallel to the interface in the $+y$ and $-y$ directions in the upper fluid, whereas the second two correspond to sound waves that propagate almost parallel to the interface in the $+y$ and $-y$ directions in the lower fluid. The two roots in Equation (2.43) are more difficult to interpret, but the first of these corresponds to a standing sound wave when the two fluids have equal density (i.e. $\epsilon = 1$).

One may wonder how we arrived at a sixth order polynomial (equation [2.42]), starting from a fourth order polynomial (equations [2.16, 2.17]). The answer is that each root of the sixth order polynomial has a specific relationship for k_y in terms of k_x as given by equation (2.25), whereas in the general case, a wave having a given value of k_y can have *any* value of k_x. The reason we have a relationship between k_x and k_y for the vortex sheet is that we have assumed waves on either side of the vortex sheet are either incoming or outgoing, but not both. In general, a sound wave incident on a vortex sheet will yield both a transmitted and a reflected wave (Miles, 1957b). Only for certain angles of incidence is there no reflected wave, and these angles are what determine the relationship between k_x and k_y in our treatment.

Since each of the six roots for $M \gg M_{\rm crit}$ yields a real value for $k_{x,\pm}$, the solutions do not damp away from the interface, and we need to apply radiation boundary conditions at $x = \pm\infty$. The proper procedure is to demand that all waves are outgoing in each fluid in a frame which is subsonic with respect to the fluid (Miles, 1957b), and it is convenient to work in the comoving frame of each fluid. The dimensionless phase velocity in the frame comoving with the upper fluid is $\varphi_{+,CF} = \varphi - M$, and the analogous expression for the lower fluid is $\varphi_{-,CF} = \varphi + M$.

In order to satisfy Equation (2.38), $k_{x,+}$ and $k_{x,-}$ must have the same sign, so we must have either $\delta\phi_\pm \propto e^{i(|k_{x,\pm}|x-\omega t)}$ or $\delta\phi_\pm \propto e^{i(-|k_{x,\pm}|x-\omega t)}$. Moreover, since $k_{x,+}$ and $k_{x,-}$ have the same sign, it is clear that $\varphi_{+,CF}$ and $\varphi_{-,CF}$ must have the opposite sign to yield outgoing waves in the comoving frames of each of the two fluids. Only three of the six roots found above satisfy this condition:

$$\varphi_l = -M + \epsilon^{1/2} + \frac{\epsilon^{1/2}}{2(2M - \epsilon^{1/2})^2} \tag{2.46}$$

$$\varphi_m = -M\left(\frac{1 - \epsilon^{1/2}}{1 + \epsilon^{1/2}}\right) \tag{2.47}$$

$$\varphi_u = M - 1 - \frac{\epsilon}{2(2M-1)^2}. \tag{2.48}$$

We will refer to these three roots as the lower, middle, and upper branches, respectively. Furthermore, it is straightforward to check that the solutions which yield outgoing waves in both

the upper and lower fluids have $\delta\phi_\pm \propto e^{i(-|k_{x,\pm}|x-\omega t)}$, so $k_{x,\pm}$ are positive given our definition (2.36).

3.2 Dispersion Relation in the General Case

We now relax the assumption of $M \gg 1$ and numerically solve the dispersion relation (2.40) at arbitrary Mach number for $\epsilon = 1$ (Figure 2.1a) and $\epsilon = .01$ (Figure 2.1b). At the critical Mach number given by Equation (2.41), the upper and lower branches merge together in the real plane and bifurcate in the complex plate. These bifurcated solutions turn into the two incompressible KH modes for $M \ll M_{\rm crit}$.

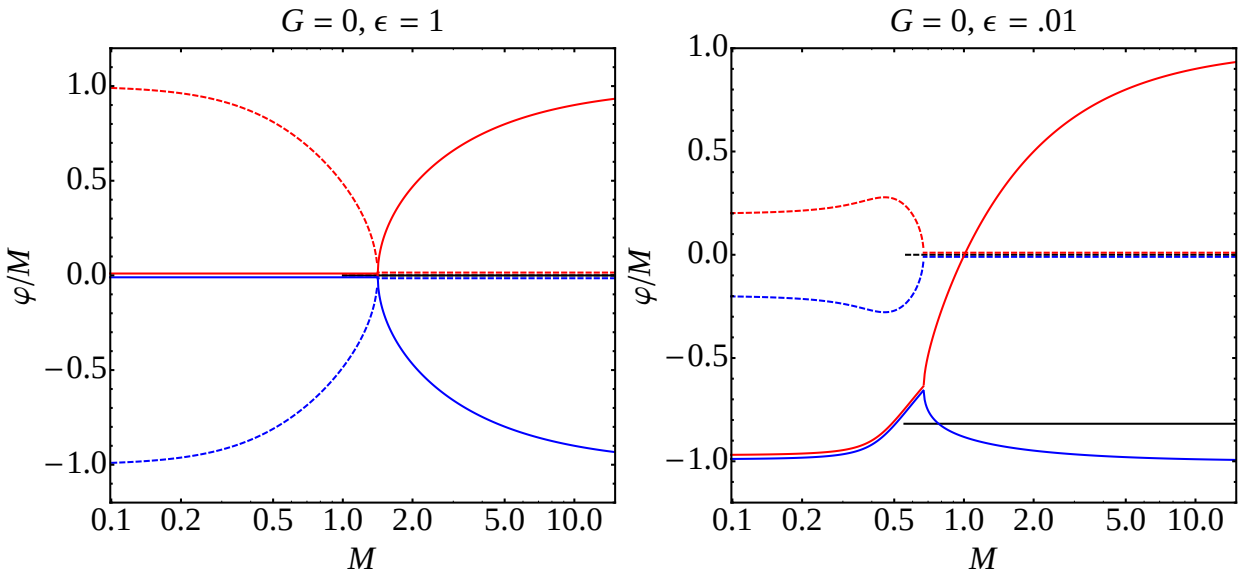
Unlike, the lower and upper branches, the middle branch has no incompressible analog and ceases to be a *physical solution* below a critical Mach number

$$2M_m = 1 + \epsilon^{\frac{1}{2}}, \tag{2.49}$$

although it remains a mathematical solution to equation (2.42). The reason for this is that for $M < M_m$, $k_{x,\pm}$ switches from real to imaginary. Thus, rather than having sinusoidal oscillations, we have exponential growth or decay as $x \to \pm\infty$. For a physically viable solution, we must have decay rather than growth, otherwise the solution blows up at infinity. However, inspection of equation (2.38) reveals that $\mathrm{sgn}(k_{x,+}) = \mathrm{sgn}(k_{x,-})$, since $W_\pm$ is real for the middle branch. For real $k_{x,\pm}$ (i.e. for $M < M_m$), the solution for the middle branch *always* blows up at either $x = \infty$ or $x = -\infty$ and is therefore unphysical.

4 The Isothermal Vortex Sheet with Gravity

We now go beyond the simplifying assumption of no gravity used in §3 and consider the case where g is non-zero and constant. We shall shortly assume an isothermal equation of state, but for now we consider the more general polytropic equation of state of the form $P = K_\pm \rho^n$ in each



(a) (b)

Figure 2.1: The dispersion relation φ/M as a function M for $\epsilon = 1$ and $\epsilon = .01$. The solid and dashed curves give the real and imaginary components respectively. The blue, black, and red curves correspond to the lower, middle, and upper branches respectively. The red and blue curves have been slightly offset vertically so they do not overlap.

of the two fluids. For any equation of state of this form, we have

$$k_g = \frac{g}{s^2} = -\frac{\frac{\partial P}{\partial \rho}\frac{d\rho}{dr}}{\gamma P} = -\frac{n}{\gamma}\frac{d\ln\rho}{dr} = -\frac{n}{\gamma}k_s, \tag{2.50}$$

which means $k_s + k_g = (1 - \gamma/n)k_g$. If $n = \gamma$, corresponding to the case of an adiabatic atmosphere, the second term in parentheses in Equation (2.21) drops out, but then the third term becomes difficult to treat analytically. However, for an isothermal atmosphere ($n = 1$) the sound speed is constant, and both the second and third terms in Equation (2.21) reduce to a tractable form. Since we are only interested in the gross, qualitative properties of the flow, we assume both fluids are isothermally stratified, since this assumption significantly simplifies the analytical treatment.

For $n = 1$, the second term in Equation (2.21) becomes

$$-g\tilde{\rho}\frac{k_s + k_g}{\tilde{W}^2} \quad = \quad gk_g(1-\gamma)\frac{k_x^2}{k_y^2 W^2} \tag{2.51}$$

We now again assume a vortex sheet velocity profile (Equation (2.33)), in which case for $n = 1$, the third term in Equation (2.21) is given by

$$\frac{\tilde{W}''}{\tilde{W}} = \frac{(\sqrt{\tilde{\rho}})''}{\sqrt{\tilde{\rho}}} = \left(\frac{2-\gamma}{2}k_g\right)^2 \tag{2.52}$$

Putting Equations (2.51) and (2.52) into Equation (2.21), we have

$$\begin{aligned} &\delta\phi'' + \tilde{k}_x^2\delta\phi = 0, \\ &\tilde{k}_x^2 \equiv \left[k_x^2\left(1-(\gamma-1)\left(\frac{k_g}{k_y}\right)^2\left(\frac{s}{W}\right)^2\right) - \left(\frac{2-\gamma}{2}k_g\right)^2\right]. \end{aligned} \tag{2.53}$$

The perturbation is then given as

$$\delta\phi_\pm \propto e^{-i\tilde{k}_{x,\pm}x}. \tag{2.54}$$

We now comment on the terms present in Equation (2.53). In the absence of gravity, $k_g = 0$, and we simply have $\tilde{k}_x = k_x$. If $k_g \neq 0$, then the second term on the right hand side of Equation (2.53) can be written in a more familiar form as

$$(\gamma-1)\left(\frac{k_g}{k_y}\right)^2\left(\frac{s}{W}\right)^2 = \left(\frac{N}{\omega - k_y V_y}\right)^2, \tag{2.55}$$

where

$$N^2 = \frac{(\gamma-1)g^2}{s^2} \tag{2.56}$$

is the Brunt-Väisälä frequency. Thus, the second term on the right hand side of Equation (2.53) provides a lower frequency cutoff for sound waves at the Brunt-Väisälä frequency. The last term in Equation (2.53) arises because we have *not* made the short wavelength approximation $k_x \gg k_g$.

Now, we use the boundary conditions (2.31) and (2.32) to determine the dispersion relation. Substituting $\delta\phi'_{\pm} = -i\tilde{k}_{x,\pm}\delta\phi_{\pm}$, and $\tilde{W}'_{\pm} = (2-\gamma)k_{g,\pm}\tilde{W}_{\pm}/2$ into the condition (2.32), we have

$$-\left[i\tilde{k}_{x,+} + \left(\frac{2-\gamma}{2}\frac{g}{s_+^2}\right)\right]\tilde{W}_+\delta\phi_+ - \frac{g\tilde{\rho}_+\delta\phi_+}{\tilde{W}_+} = \\ -\left[i\tilde{k}_{x,-} + \left(\frac{2-\gamma}{2}\frac{g}{s_-^2}\right)\right]\tilde{W}_-\delta\phi_- - \frac{g\tilde{\rho}_-\delta\phi_-}{\tilde{W}_-}. \quad (2.57)$$

Next, using the second boundary condition (2.31) to substitute for $\delta\phi_-$ in terms of $\delta\phi_+$, and using the fact that $\tilde{\rho}_{\pm} = \rho_{\pm}$ at the interface, we have

$$-\left[i\tilde{k}_{x,+} + \left(\frac{2-\gamma}{2}\frac{g}{s_+^2}\right)\right]\tilde{W}_+^2 - g\rho_+ = -\left[i\tilde{k}_{x,-} + \left(\frac{2-\gamma}{2}\frac{g}{s_-^2}\right)\right]\tilde{W}_-^2 - g\rho_-. \quad (2.58)$$

We now introduce the dimensionless gravity parameter

$$G = \frac{g}{k_y s_+^2}, \quad (2.59)$$

which is closely related to the ratio of the wavelength to the pressure scale height, h_s. Thus, $G \sim 1$ when $k_y h_{s,+} \sim 1$, and $G\epsilon^{-1} \sim 1$ when $k_y h_{s,-} \sim 1$. Using $\epsilon = \rho_+/\rho_- = s_-^2/s_+^2$, and performing some algebra, we have

$$\left[i\frac{\tilde{k}_{x,+}}{k_y} + \left(\frac{2-\gamma}{2}G\right)\right]\left(\frac{k_y}{k_{x,+}}\right)^2\left(\frac{W_+}{s_+}\right)^2\epsilon + G(1-\epsilon) = \\ \left[i\frac{\tilde{k}_{x,-}}{k_y} + \left(\frac{2-\gamma}{2}G\epsilon^{-1}\right)\right]\left(\frac{k_y}{k_{x,-}}\right)^2\left(\frac{W_-}{s_+}\right)^2. \quad (2.60)$$

Setting $G = 0$ it is clear that we recover the vortex sheet dispersion relation in the absence of gravity (Equation (2.38)).

We now check Equation (2.60) by showing that it reproduces the well-known incompressible KH dispersion relations in the limit $M \ll M_{\rm crit}$, before going on to treat the case of the supersonic vortex sheet with gravity.

4.1 Highly Subsonic Vortex Sheet with Gravity

We assume that $\bar{V}/s_{\pm} \ll 1$, which immediately implies $M \ll M_{\rm crit}$, and we also assume $G \ll 1$ and $G\epsilon^{-1} \ll 1$, which means that the wavelength of the perturbation is much smaller than the scale height in both the upper and lower fluids ($k_{g,\pm}/k_y \ll 1$). Next, we eliminate sound wave modes by assuming $\varphi \ll 1$ (phase velocity much lower than sound velocity in upper fluid) and $\varphi\epsilon^{-1/2} \ll 1$ (phase velocity much lower than sound velocity in lower fluid). According to Equation (2.53), this means $k_x = \pm ik_y$, and given our definition for $\delta\phi_{\pm}$ in Equation (2.54), we must chose the minus sign in the upper fluid and the plus sign in the lower fluid to give vanishing solutions at $x = \pm\infty$. Equation (2.60) then yields

$$-\epsilon\left(\frac{\omega}{k_y} - \bar{V}_y\right)^2\sqrt{1 - \frac{(\gamma-1)G^2}{(M-\varphi)^2}} + \frac{g}{k_y}(1-\epsilon) = \left(\frac{\omega}{k_y} + \bar{V}_y\right)^2\sqrt{1 - \frac{(\gamma-1)G^2\epsilon^{-1}}{(M+\varphi)^2}}. \qquad (2.61)$$

Next, we note that $(\gamma-1)G^2/(M-\varphi)^2 = N_+^2/(\omega - k_y\bar{V}_y)^2$ and that $(\gamma-1)G^2\epsilon^{-1}/(M+\varphi)^2 = N_-^2/(\omega + k_y\bar{V}_y)^2$, where N is the Brunt-Väisälä frequency for an isothermal atmosphere and was given in Equation (2.56). We expect $|\omega \pm k_y\bar{V}_y| \gtrsim \sqrt{gk}$, which is the characteristic frequency of surface gravity waves. Since $N\pm \sim \sqrt{gk_{g,\pm}}$, and we have already assumed $k_{g,\pm}/k_y \ll 1$, it follows that $N_{\pm} \ll |\omega \mp k_y\bar{V}_y|$. Consequently, Equation (2.61) reduces to

$$-\epsilon\left(\frac{\omega}{k_y} - \bar{V}_y\right)^2 + \frac{g}{k_y}(1-\epsilon) = \left(\frac{\omega}{k_y} + \bar{V}_y\right)^2, \qquad (2.62)$$

which is the well known KH dispersion relation for an incompressible fluid in the presence of gravity.

4.2 The Weak Gravity Limit at High Mach Number

As mentioned before in §3.1, Miles (1958) has demonstrated that in the absence of gravity, the vortex sheet is stable above a critical Mach number given by Equation (2.41). We now address the question of whether the system still remains stable when $G \neq 0$.

To answer this question, we will use our general dispersion relation (2.60) in which we will additionally assume $M \gg M_{\rm crit}$, since this assumption significantly simplifies the algebra. Since we have already obtained solutions for the case $G = 0$ and $M \gg M_{\rm crit}$ (§3.1), we proceed by considering gravity as a perturbation. We consider wavelengths that are much smaller than the pressure scale height and ask what happens in the limit $G \to 0$. In our analysis, we will assume that the density ratio $\epsilon \leq 1$, so that the system is stable to the Rayleigh-Taylor instability.

Because the introduction of gravity makes the upper and lower fluids stratified, some care should be taken when determining which solutions are physical and which are not. Miles (1957b) has shown that for $G = 0$, the three supersonic KH modes can be understood in terms of sound waves emitted from the interface between the two fluids. This interpretation is useful as well for the case with gravity and leads to a couple of insights. First, the amplitude of sound waves is not constant as they propagate through a stratified medium. Rather, to conserve energy, waves propagating upward (to lower densities) must increase in amplitude, and those propagating downward (to higher densities) must decrease in amplitude. Second, since the sound waves are emitted from the interface, if ω has an imaginary component, then the amplitude of the emitted waves changes with time. Thus, if $\Im[\omega] > 0$, and there is an instability, then the amplitude of the waves will decay with distance from the interface, since the waves emitted in the past had lower amplitude. Conversely if $\Im[\omega] < 0$ and the perturbation is damping in time, then the amplitude of the emitted waves will increase with distance from the interface, since the waves emitted in the past had a larger amplitude. Both of these effects mean that the amplitude of the waves can blow up as we move away from the interface. Thus, we take as physical those solutions which yield outgoing waves (away from the interface) in both the upper and lower fluids, even if these solutions diverge as $x \to \pm\infty$. For the limit $G \to 0$, this means that the physical solutions are still the lower, middle, and upper branches but now modified by the presence of a weak gravitational field.

We note here that although the dispersion relation (2.60) is valid for all values of G and not just for small G, the simple picture of outgoing sound waves in the upper and lower fluids is only valid for $G \to 0$. From a physical point of view, this can be attributed to the following fact.

Sound waves (p-modes) traveling in a stratified atmosphere have a frequency cutoff at $\omega^2 = N^2$ below which propagation is not possible. Given our definitions of k_y and $\tilde{k}_x$, the frequency of a sound wave in the frame comoving with the fluid is $\omega^2 \sim (k_y^2 + \tilde{k}_x^2)s^2$. Substituting $N^2 \sim \omega^2$ and using the definition of N^2 (Equation (2.56)) yields $G^2 < (\gamma - 1)^{-1}(1 + (|\tilde{k}_x|/k_y)^2)$ for sound waves to propagate. If this condition is not fulfilled, then the picture of outgoing sound waves is invalid, and the boundary conditions need to be formulated in a different way, which is beyond the scope of the present work.

The Lower Branch

We begin by considering how the lower wave is modified in the limit $G \to 0$ and $M \gg M_{\rm crit}$. If $G = 0$ exactly, then $\tilde{k}_x = k_x$, and in the limit $G \to 0$ we have $\tilde{k}_x = k_x \left(1 + \mathcal{O}(G^2)\right)$. Keeping terms only to first order in G, Equation (2.60) becomes

$$\left[i\frac{k_{x,+}}{k_y} + \left(\frac{2-\gamma}{2}G\right)\right]\left(\frac{k_y}{k_{x,+}}\right)^2\left(\frac{W_+}{s_+}\right)^2\epsilon + G(1-\epsilon) = \left[i\frac{k_{x,-}}{k_y} + \left(\frac{2-\gamma}{2}G\epsilon^{-1}\right)\right]\left(\frac{k_y}{k_{x,-}}\right)^2\left(\frac{W_-}{s_+}\right)^2. \quad (2.63)$$

Writing this out explicitly in terms of M and φ gives

$$\frac{i(M-\varphi)^2\epsilon}{\sqrt{(M-\varphi)^2-1}} - \frac{i(M+\varphi)^2}{\sqrt{(M+\varphi)^2\epsilon^{-1}-1}} + G(1-\epsilon) = \frac{2-\gamma}{2}G\left(\frac{(M+\varphi)^2\epsilon^{-1}}{(M+\varphi)^2\epsilon^{-1}-1} - \frac{(M-\varphi)^2\epsilon}{(M-\varphi)^2-1}\right). \quad (2.64)$$

Next, we assume that gravity only weakly affects the dispersion relation and make the perturbative expansion

$$\varphi = \varphi_0 + \varphi_1, \quad |\varphi_1|/|\varphi_0| \ll 1, \quad (2.65)$$

where φ_0 is the solution for $G = 0$ and $M \gg M_{\rm crit}$.

For the lower branch, we can use Equation (2.46) for φ_0, and in the limit $M \gg M_{\rm crit}$ we have

$$\begin{aligned} \varphi_0 &\approx -M + \epsilon^{1/2} && (2.66)\\ \frac{k_{x,+}}{k_y} &= \sqrt{(M-\varphi_0)^2 - 1} \approx 2M - \epsilon^{1/2} && (2.67)\\ \frac{k_{x,-}}{k_y} &= \sqrt{(M+\varphi_0)^2\epsilon^{-1} - 1} \approx \frac{1}{2M - \epsilon^{1/2}}. && (2.68) \end{aligned}$$

Defining

$$M_l \equiv 2M - \epsilon^{1/2}, \tag{2.69}$$

Equation (2.64) becomes

$$\frac{i(M_l-\varphi_1)^2\epsilon}{\sqrt{(M_l-\varphi_1)^2-1}} - \frac{i(\epsilon^{1/2}+\varphi_1)^2}{\sqrt{(\epsilon^{1/2}+\varphi_1)^2\epsilon^{-1}-1}} + G(1-\epsilon) = \frac{2-\gamma}{2} G\left(\frac{(\epsilon^{1/2}+\varphi_1)^2\epsilon^{-1}}{(\epsilon^{1/2}+\varphi_1)^2\epsilon^{-1}-1} - \frac{(M_l-\varphi_1)^2\epsilon}{(M_l-\varphi_1)^2-1}\right). \tag{2.70}$$

It will turn out (Equation (2.72)) that φ_1 is proportional to G, so working to first order in G is equivalent to working to first order in φ_1. Equation (2.70) then simplifies to

$$i(M_l-\varphi_1)\epsilon - \frac{iM_l\epsilon(1+2\epsilon^{-1/2}\varphi_1)}{1+M_l^2\epsilon^{-1/2}\varphi_1} + G(1-\epsilon) = \frac{2-\gamma}{2} G\left(M_l^2\frac{1+2\epsilon^{-1/2}\varphi_1}{1+2M_l^2\epsilon^{-1/2}\varphi_1} - \epsilon\right). \tag{2.71}$$

Assuming $|M_l^2\epsilon^{-1/2}\varphi_1| \ll 1$, and keeping terms to leading order in M_l, we can solve for φ_1 in terms of G.

$$\varphi_{1,l} \approx -\frac{2-\gamma}{2}\frac{G}{M_l\epsilon^{1/2}}i. \tag{2.72}$$

We immediately see two things from Equation (2.72). First, φ_1 is purely imaginary, and second, if $\gamma < 2$, φ_1 is negative and the perturbation damps, whereas if $\gamma > 2$, φ_1 is positive and the perturbation grows. For realistic equations of state, $\gamma \leq 5/3$, so the lower wave always damps.

The Middle and Upper Branches

We can find an approximate solution for φ_1 in the limit $G \to 0$ and $M \gg M_{\rm crit}$ for the middle and upper branches in much the same manner as for the lower branch. The first order correction for the middle branch is

$$\varphi_{1,m} = -\frac{\gamma}{2}\frac{G(1-\epsilon^{1/2})}{\epsilon^{1/2}}i, \tag{2.73}$$

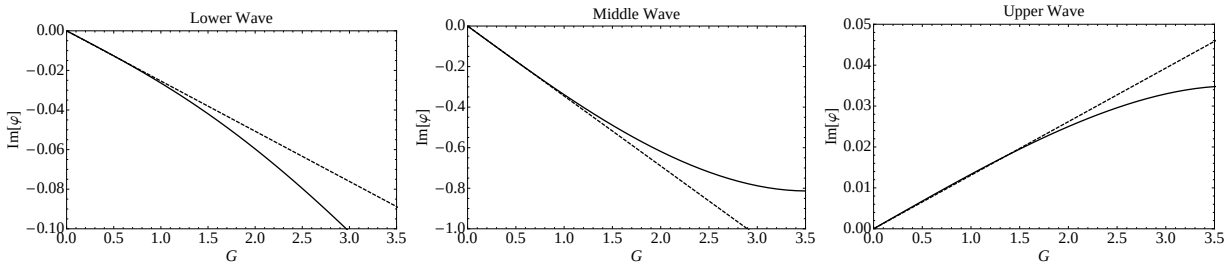
and for the upper branch is

$$\varphi_{1,u} \approx \frac{2-\gamma}{2}\frac{G\epsilon^{1/2}}{2M-1}i. \tag{2.74}$$

Just as in the case of the lower branch, φ_1 is purely imaginary for both the middle and upper branches. We see that φ_1 is negative for the middle branch if $\epsilon < 1$. However, for the upper branch if $\gamma < 2$, φ_1 is positive and if $\gamma > 2$, φ_1 is negative. This is opposite from the lower branch meaning that for any $\gamma \neq 2$ in the limit $M \gg 1$, one of the two branches is always unstable and the other one is damped. For a realistic equation of state, $\gamma \leq 5/3$ *so the upper branch is the unstable one*, and the lower branch damps.

Numerical Verification

We verify Equations (2.72), (2.73), and (2.74) numerically by solving the fully general dispersion relation (2.60) and comparing $\Im(\varphi)$ with our analytical estimate for the parameters $M = 5$, $\epsilon = .5$, and $\gamma = 5/3$. We plot $\Im(\varphi)$ vs. G in for both our analytical solutions (solid lines) and the ones obtained numerically (dashed lines) in Figure 2.2. The analytical solution converges to the numerical one in the limit $G \to 0$.



(a) (b) (c)

Figure 2.2: Plots of $\Im(\varphi)$ vs. G for the lower (a), middle (b), and upper (c) branches respectively, using $M = 5$, $\epsilon = .5$, $\gamma = 5/3$. The solid curves show the numerical solution obtained by solving Equation (2.60) and the dashed curves correspond to the approximate solutions from Equations (2.72), (2.73), and (2.74).

5 Sonic Instabilities in a Finite Width Layer of Constant Shear

The calculations presented in §3,4 were performed for the velocity profile (2.33) featuring a discontinuity at some radius. We now consider a more complicated (and more realistic at later stages of the BL evolution) initial setup in which the velocity between the two fluids varies *continuously* within a narrow shear layer. Unlike the vortex sheet, the finite width shear layer without gravity is known to be unstable at high Mach number (Glatzel, 1988; Choudhury & Lovelace, 1984; Ray, 1982), and in this case the growth rate of the instability scales inversely with the width of the shear layer and in proportion to the shear, $S \sim \Omega_K R_*/\delta_{BL}$.

In the following, we extend some of the findings of Glatzel (1988) to study sonic instabilities in a finite width shear layer without gravity and apply them to the problem of the BL initiation. The setup we consider has the velocity profile

$$V(x) = \begin{cases} \bar{V}, \ x > \delta_{BL}, \\ \bar{V}x/\delta_{BL}, \ -\delta_{BL} \leq x \leq \delta_{BL}, \\ -\bar{V}, \ x < -\delta_{BL} \end{cases} \tag{2.75}$$

and the density profile

$$\rho(x) = \begin{cases} \rho_+, \ x > -\delta_{BL} \\ \rho_-, \ x < -\delta_{BL} \end{cases} \tag{2.76}$$

Pressure equilibrium again requires that $\rho_+ s_+^2 = \rho_- s_-^2$, which sets the sound speed everywhere in the flow, and as before we have $\epsilon = \rho_+/\rho_-$ and $M = \bar{V}/s_+$.

Although we only consider a linearly varying velocity profile in the shear layer, Ray (1982) and Choudhury & Lovelace (1984) have found that different shear profiles are qualitatively similar. Thus, we consider a constant shear to be representative of more general shear profiles.

5.1 Dispersion Relation

We now study the dispersion relation of the finite width shear layer. In applying the dispersion relation to the initiation of the BL, we are most interested in the growth rate of the fastest growing mode for $M \gg 1$. Glatzel (1988) has already obtained the dispersion relation for the case $\epsilon = 1$, and using his techniques, we derive the dispersion relation for the case of arbitrary ϵ in Appendix C. We also show in Appendix C.3 that the dispersion relation for a finite width shear layer reduces to the dispersion relation for a vortex sheet in the limit $k_y \to 0$ at constant δ_{BL}.

In Figure 2.3, we plot the dispersion relation (2.120) as a function of wavenumber for the parameters $M = 5$ and $\epsilon = 1$, $\epsilon = .25$, $\epsilon = .1$, $\epsilon = .01$, and $\epsilon = 0$. The $\epsilon = 0$ case is equivalent to having a hard reflecting boundary at $x = -\delta_{BL}$. The modes depicted are the ones that converge to the upper and lower branches from §3 in the vortex sheet limit ($k_y \delta_{BL} \ll 1$). For $\epsilon < 1$, the upper branch always has a larger growth rate than the lower branch, and both the upper and lower branches have the same growth rate for $\epsilon = 1$. In the $\epsilon = 1$ case, we can identify the upper and lower branches as the $n_\pm = 0$ decoupled modes in §5.4 of Glatzel (1988). In addition to the upper and lower waves, Glatzel (1988) has shown that there is an infinite spectrum of damped modes, but we do not consider these here, since we are interested in determining the growth rate of the fastest growing mode.

We now revisit the seemingly paradoxical statement that the vortex sheet is stable to two dimensional disturbances along the flow direction above a critical Mach number; yet at the same time, the growth rate of the fastest growing mode scales with δ_{BL}^{-1}, which implies that the thinner the shear layer, the faster the instability proceeds. The key to resolving this apparent controversy is to consider a mode having $k_y \delta_{BL} \ll 1$. Its growth rate is diminished if we decrease δ_{BL} while

keeping k_y constant for $M > M_{\rm crit}$ and becomes vanishingly small if we take the limit $\delta_{BL} \to 0$. This can be seen from the dying left hand tail of the curve in Figure 2.3b, and keeping k_y constant, while decreasing δ_{BL} we move leftward along the tail. This means $\Im[\omega]$ becomes smaller, since $\varphi = \omega/k_y s_+$ is directly proportional to ω for constant k_y even as we decrease δ_{BL}. We next point out that the curve in Figure 2.3c remains unchanged in shape or amplitude as we decrease δ_{BL}, keeping $k_y\delta_{BL}$ constant. Consequently, the value of k_y for which the maximum in $\Im[\omega]$ occurs $k_{y,\max} \propto \delta_{BL}^{-1}$ and likewise $\max[\Im[\omega]] \propto \delta_{BL}^{-1}$. Thus, as δ_{BL} is decreased, the instability shifts to shorter wavelengths and becomes more rapid, while at the same time, modes having $k_y\delta_{BL} \ll 1$ are stabilized for a given value of k_y. Since any real shear layer is likely to have a nonzero width, one may therefore remark that taking the vortex sheet limit for $M \gg M_{\rm crit}$ masks the instability.

5.2 Numerical Verification

To independently verify our dispersion relation (2.120), we ran direct hydrodynamical simulations of shear layers using the Godunov code Athena (Stone et al., 2008) and compared the growth rate of the fastest growing mode predicted by our dispersion relation to that obtained in the simulations. We initialized a flow along the y-direction using the setup described by Equations (2.75), and for all of the simulations we used $\gamma = 5/3$, $\delta_{BL} = 1$ for the half width of the shear layer, and periodic boundary conditions in the y-direction; Table 2.1 summarizes the simulation specific parameters. To seed the instability, we initialized random perturbations to v_x of magnitude 10^{-6} in the region $x > -1$. We found that for the $M = 5$ runs, we needed a high resolution in the x-direction to get converged estimates for the growth rates. Figure 2.4 shows $\rho v_x^2/2$ averaged over box as a function of time. The solid lines show simulation results, and the dashed lines show the predictions from considering the fastest growing mode for the upper branch, using the dispersion relation (2.120). There is good agreement between the two, especially for the limiting cases of $\epsilon = 0$ and $\epsilon = 1$.

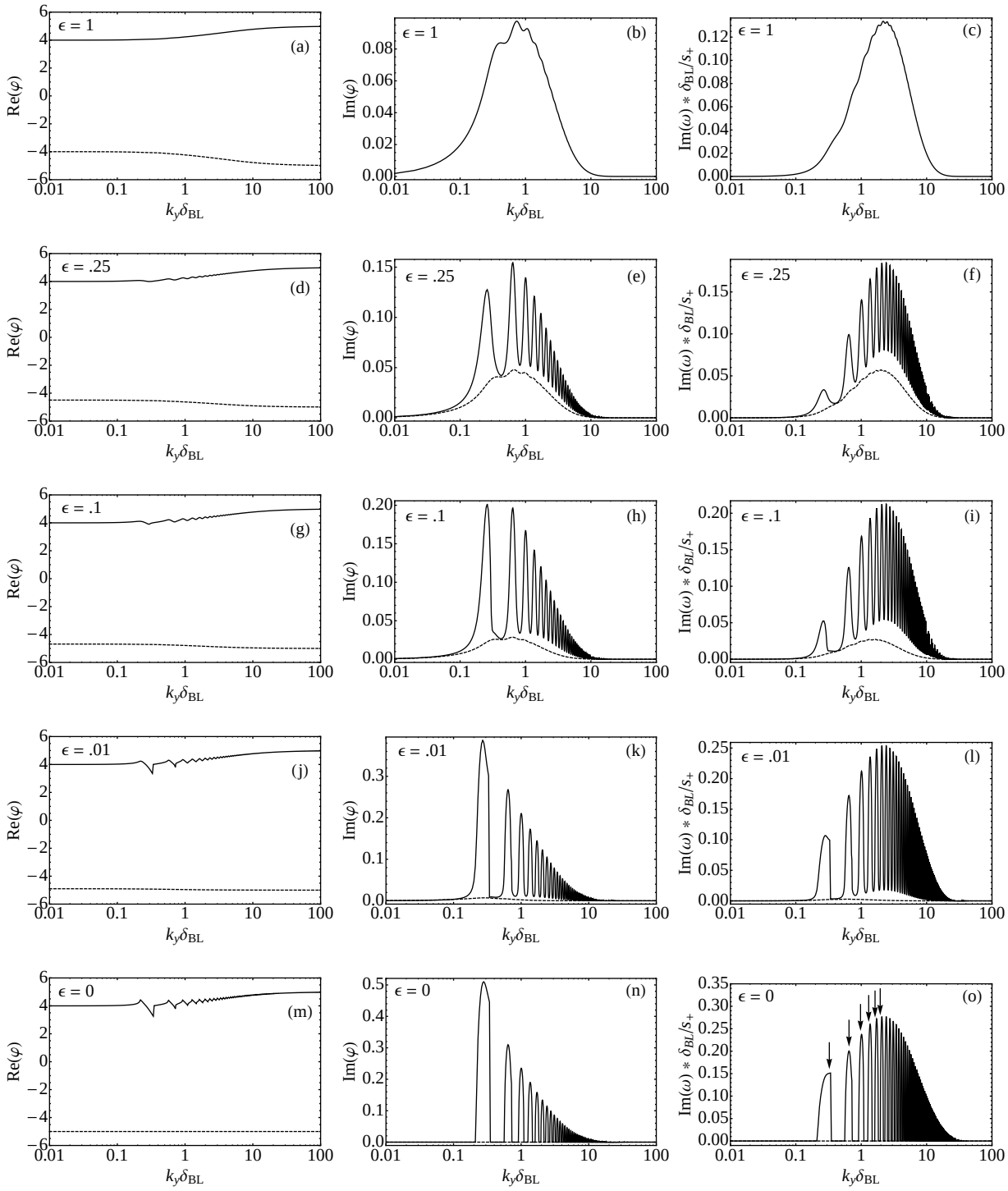
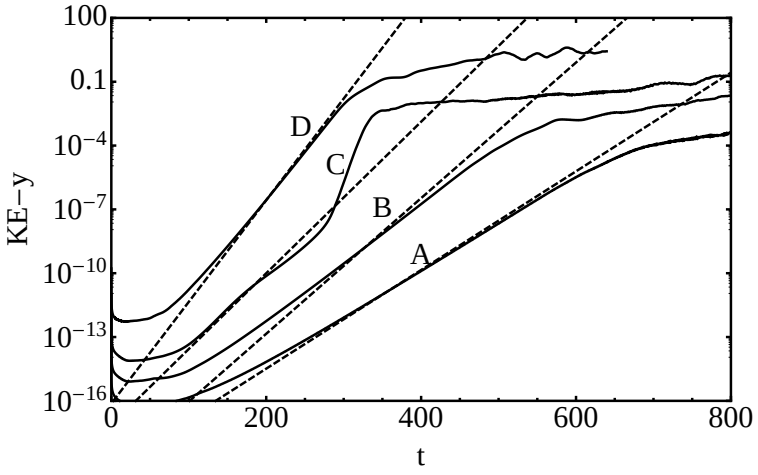


Figure 2.3: Dispersion relations for $M = 5$ and a finite width shear layer. The top row is for $\epsilon = 1$, the second row for $\epsilon = .25$, the third row for $\epsilon = .1$, the fourth row for $\epsilon = .01$, and the bottom row for $\epsilon = 0$. The first column shows the real part of φ, the second the imaginary part of φ and the third the imaginary part of ω. The solid line corresponds to the upper branch and the dashed line to the lower branch. In the top row, the upper and lower branches have the same growth rate. The arrows in panel (o) show the wavenumbers corresponding to trapped wavemodes (§5.3).

Label	M	ϵ	x-range	y-range	$N_x \times N_y$	(BC-x1, BC-x2)
A	5	1	(-4,4)	(-16,16)	8192×8192	(outflow, outflow)
B	5	.25	(-4,4)	(-16,16)	8192×8192	(outflow, outflow)
C	5	.1	(-4,4)	(-16,16)	8192×8192	(outflow, outflow)
D	5	0	(-1,4)	(-16,16)	2048×2048	(reflecting, outflow)
E	.05	1	(-4,4)	(-8,8)	512×512	(reflecting, reflecting)

Table 2.1: Parameters for the simulations with Athena. M – Mach number, ϵ – density ratio, x, y-range – box size in x, y-direction, $N_x \times N_y$ – number of cells in x, y-direction, (BC-x1, BC-x2) – lower and upper boundary conditions in x direction.



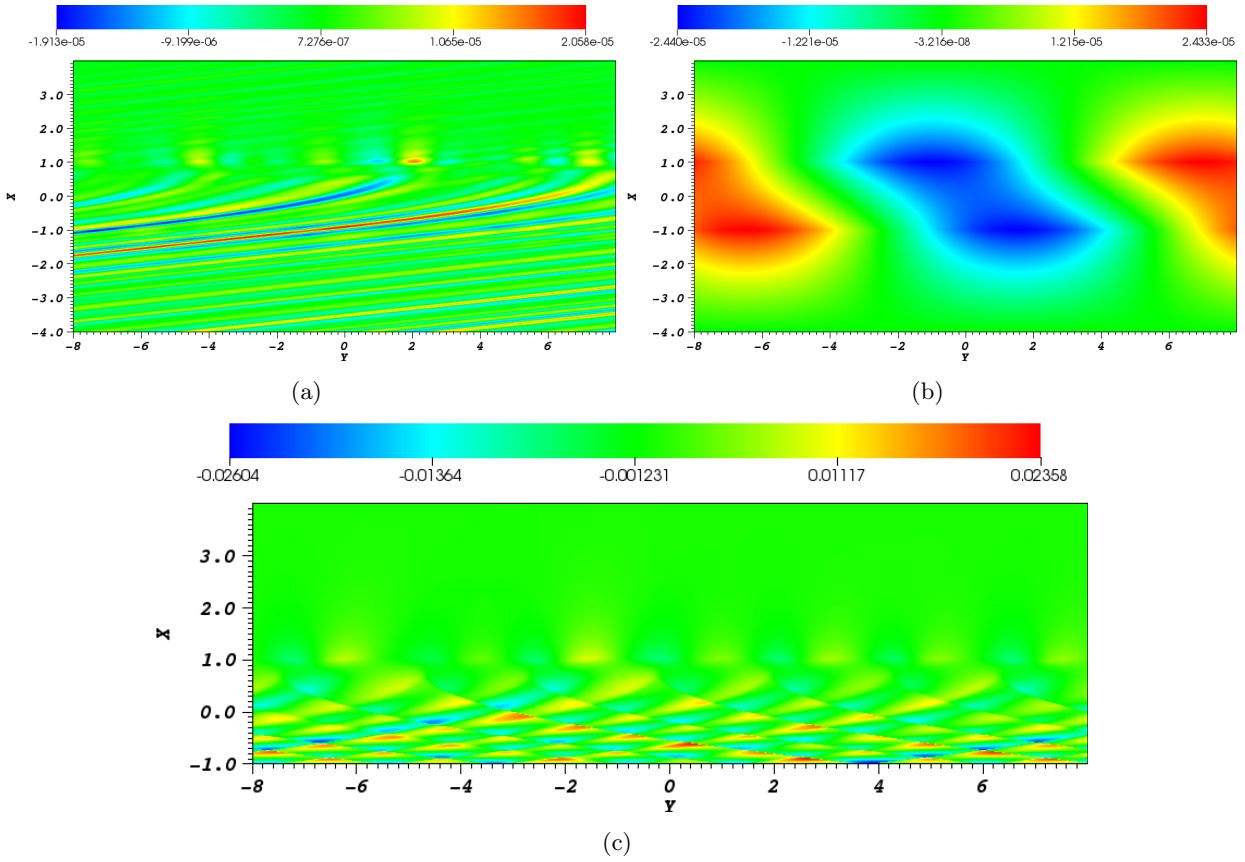
(a)

Figure 2.4: Comparison of the analytically derived growth rates (given by the slopes of the dashed lines) to the ones obtained using Athena (solid lines). The curves A, B, C, D correspond to $\epsilon = 1$, .25, .1, and 0, respectively (see text for further simulation details) and have been offset vertically for clarity.

5.3 Physical Intuition

Panels, (a), (b), and (c) of Figure 2.5 show the spatial structure of v_x for simulations A, E & D during the linear stage of the instability. The fastest growing modes in these three cases are very different, illustrating the different instability mechanisms which operate for the $M \gg M_{\rm crit}$ vs. $M \ll M_{\rm crit}$ cases and also for $\epsilon = 1$ vs. $\epsilon = 0$. The case $M \ll M_{\rm crit}$, in panel (b) has been extensively studied (e.g. (Vallis, 2006)), so we will not consider it here..

For the $M \gg M_{\rm crit}$ case with $\epsilon = 1$, the instability is caused by a *radiation mechanism*. This mechanism has already been discussed by Glatzel (1988), so we only mention it here briefly. Each



(a) (b)

(c)

Figure 2.5: Panels (a), (b), and (c) show v_x during the linear stage of the instability for simulations A, E, & D respectively and have been rotated by 90 degrees.

mode of the dispersion relation can be associated with a pseudo-energy that is conserved. If a mode has a negative pseudo-energy, then radiation of energy away from the boundary layer region will cause the pseudo-energy to become even more negative, amplifying the mode and leading to instability. The radiation mechanism is responsible for the smooth, broad hump in panels (b) and (c) of Figure 2.3.

For the case of $M \gg M_{\rm crit}$ and $\epsilon = 0$, the instability mechanism is quite different. Rather than a broad hump, panels (n) and (o) of Figure 2.3 exhibit sharp localized peaks. The physical cause of these peaks is due to over-reflection of waves that become trapped between the lower boundary and the critical layer. Thus, we shall call this the *over-reflection mechanism*. In the case of a single reflecting wall, the radiation mechanism occurs in conjunction with the over-reflection

mechanism since radiation from the trapped mode leaks through the critical layer and comes out the other side with the opposite value of pseudo-energy.

The over-reflection mechanism is discussed in Narayan et al. (1987), who considered a rotating shear layer adjacent to a reflecting wall. They explained the instability in the $\epsilon = 0$ case in terms of the leaking of action density past the corotation radius, which is the analog of the critical layer for a rotating system. Like the pseudo-energy of Glatzel (1988), the action density is a conserved quantity, and instability occurs because a wavemode that is trapped between the critical layer and the wall has a negative action density, whereas positive action leaks out past the critical layer. As a result, the amplitude of the trapped wavemode becomes even more negative and grows with time. Put in this way, it is clear that the over-reflection and radiation mechanisms are related. However, they lead to a very different structure for the dispersion relation, as evidenced by panels (n) and (o) vs. panels (b) and (c) of Figure 2.3. Thus, we prefer to regard them as separate mechanisms, but point out that in both cases, instability is ultimately caused by radiation emitted from the boundary layer region.

We now elucidate some of the properties of the modes that are trapped between the critical layer and the lower reflecting boundary using a simple model. Consider a sonic mode that is trapped between the lower boundary and the critical layer. If the mode has a well-defined phase velocity, then by performing a velocity boost one can transform into a frame in which the wavefronts are stationary. Let us work in this frame, since it makes the explanations more clear. In order for the wavefronts to be stationary, the equation for a wavefront is

$$\frac{dy}{dx} = \pm\sqrt{\mathcal{M}(x)^2 - 1}. \tag{2.77}$$

Here, $\mathcal{M}(x)$ is the Mach number as a function of x, and the positive sign is for waves propagating in the $-x$ direction, while the negative sign is for waves propagating in the $+x$ direction. Equation (2.77) is obtained from the fact that the wavefront propagates at the speed of sound, and in order for it to be stationary, the angle that the wavefront forms with the y-direction obeys $\sin(\theta) = 1/\mathcal{M}(x)$.

Consider now the upper branch from §3.1, for which the critical layer is at $x_c = \delta_{BL}(M-1)/M$. At the critical layer, we set $dy/dx = 0$, which is just to say that an upward traveling sound wave is reflected there. It immediately follows that inside the region of shear

$$\mathcal{M}(x) = -M\left(1 - \frac{x}{\delta_{BL}}\right),\ -\delta_{BL} \leq x \leq \delta_{BL}. \tag{2.78}$$

$$\tag{2.79}$$

Thus, the frame in which sound waves are stationary and reflect at the critical layer is boosted by $-M$ relative to the frame we defined in Equations (2.75).

We now consider the fate of a wavepacket that is trapped between the lower boundary and the critical layer. Figure 2.6 shows a set of wavefronts derived by integrating Equation (2.77) with red segments corresponding to propagation in the $+x$ direction and blue segments corresponding to propagation in the $-x$ direction. Consider a localized wavepacket at point A in Figure 2.6a. The wavevector of the wavepacket is oriented perpendicular to the wavefront, and as the wavepacket propagates towards point B, its wavevector is rotated by the shear. When the wavepacket reaches the critical layer at point C, it is reflected back towards point D, and the reflected wavepacket has a higher amplitude than the incident one (see Narayan et al. (1987) for the case of a rotating shear layer). After reflecting off the critical layer, the wavepacket propagates downward to point D, its wavevector continuing to be rotated in the same sense as before due to the shear. Finally the wavevector reaches the perfectly reflecting boundary at point E, whereupon the x-component of its wavevector is reflected and the cycle begins anew. It is thus clear that the repeating cycle A-E will lead to exponential amplification of the wavepacket, due to over-reflection at the critical layer.

The distance in y between points A and E is the wavelength of the longest wavelength mode, $\lambda_{\max,y}$, that can be trapped between the lower boundary and the critical layer. A trapped mode can have a wavelength shorter than $\lambda_{\max,y}$, as long as its wavelength satisfies the relation $\lambda_y = \lambda_{\max,y}/n$ where n is an integer. Thus, the relation for the wavenumber of the n-th trapped mode in the general case is

$$k_{n,y} = \frac{2\pi n}{\lambda_{\max,\mathrm{y}}}. \tag{2.80}$$

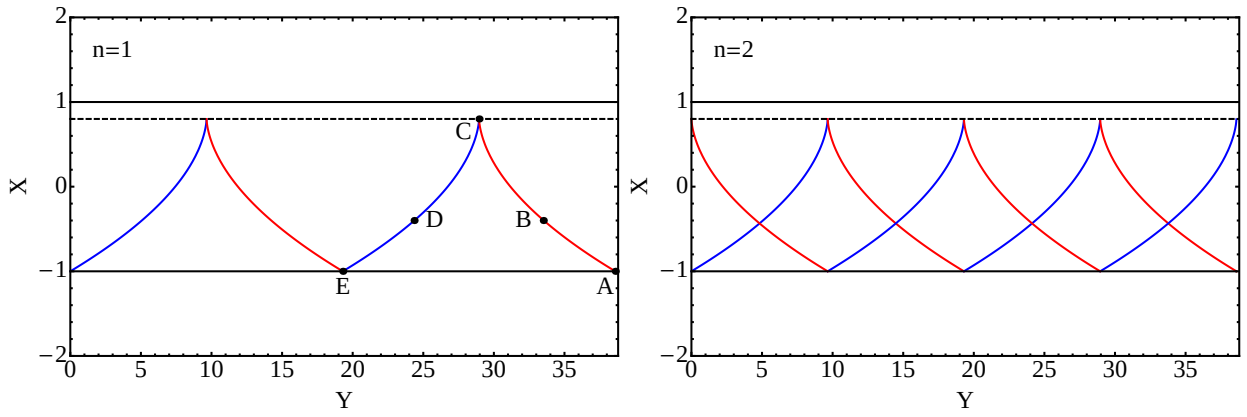


Figure 2.6: The $n = 1$ and $n = 2$ trapped modes for $M = 5$ and $\delta_{BL} = 1$. The lower black line denotes the solid lower boundary, the upper black line denotes the top of the shear layer, and the dashed black line denotes the critical layer. The red segments correspond to propagation in the $+x$ direction and the blue segments correspond to propagation in the $-x$ direction.

We indicate using arrows the values of $k_{n,y}$ for the first six trapped modes in panel (o) of Figure 2.3, and it is clear that they agree well with the locations of the peaks in the dispersion relation, which lends support for the over-reflection argument. We also plot the $n = 2$ case in Figure 2.6b and point out the similarity between the analytical curves in Figure 2.6 and the shape of the wavefronts from simulation D in Figure 2.5c.

We have discussed the radiation mechanism for $\epsilon = 1$ and the over-reflection mechanism for $\epsilon = 0$. We now discuss what happens in the more general case of $0 < \epsilon < 1$. As we can see from Figure 2.3, *both* mechanisms operate simultaneously for $0 < \epsilon < 1$. In this case, there is partial reflection at the lower boundary, and as ϵ goes from one to zero, less and less of the radiation can escape from the boundary layer region, so the radiation mechanism becomes weaker and weaker. This is evidenced by the decreasing size of the bump in the second and third columns of Figure 2.3 as ϵ goes to zero. For $\epsilon = 0$, the bump disappears entirely, and the radiation mechanism no longer operates. On the other hand, as ϵ goes from one to zero the reflection mechanism becomes stronger and stronger, since more and more of the energy is reflected at the lower boundary with total reflection at $\epsilon = 0$. Interestingly, there are still some small-scale wiggles in the dispersion relation, even for $\epsilon = 1$. This is because even if the density is everywhere uniform, radiation can still partially reflect off the discontinuity in the velocity derivative at $x = -1$ (Glatzel, 1988).

However, reflections off a discontinuity in the velocity derivative are quite weak, so the wiggles are small, and the radiation mechanism is dominant.

6 Discussion and Conclusions

We have studied supersonic shear instabilities that could drive the turbulence in the BLs of stars for which the disk is undisrupted by a magnetic field. Our study is aimed mainly at identifying the instabilities that lead to the formation of the BL when the disk just touches the surface of the star. The main result of our work is the identification of two types of instabilities that could operate in the BLs of such systems and had not been previously discussed in this context.

The first is an instability of a vortex sheet at high Mach number caused by gravity. Although the vortex sheet is stable above a critical Mach number, the addition of a small amount of gravity destabilizes it. We have found that the eigenfrequencies of the dispersion relation in the limit $G \to 0$ acquire a purely imaginary term, which is proportional to the small parameter G. This has the effect of making the upper branch unstable. We now consider whether the instability of the upper branch in the limit $G \to 0$ is likely to be relevant during the initiation of the BL, when one may expect the vortex sheet approximation to be valid. Redimensionalizing Equation (2.74), we obtain

$$\omega_1 \sim \Omega_K \epsilon^{1/2} i, \tag{2.81}$$

where Ω_K is the Keplerian velocity at the surface of the star. During the initiation of the BL, we expect disk material to be less dense than stellar material, which means that $\epsilon \lesssim 1$. It then follows from Equation (2.81) that the characteristic growth rate of the instability is $\lesssim \Omega_K$ and is independent of the wavenumber.

If the BL is radially thin, as would be expected during the initiation phase, then the growth rate given by Equation (2.81) is small compared to the shear rate $S \sim \Omega_K R_* / \delta_{BL} \gg \Omega_K$. Considering that S is the characteristic growth rate for shear instabilities, if there are other

mechanisms for instability with growth rates proportional to S, they will quickly become dominant.

In particular, we have demonstrated that the growth rate of the sonic instability of a finite width shear layer at high Mach number is proportional to S. The sonic instability is similar in nature to the Papaloizou-Pringle instability in that both are global instabilities and cannot be derived from a local analysis. There are two destabilizing mechanisms for the sonic instability. The first corresponds to emission of radiation and gives instability over a broad range of wavenumbers. The second corresponds to over-reflection of trapped modes and results in sharply peaked, disconnected regions of instability in k-space. Because sonic instabilities operate on a much faster timescale than the gravity mechanism for a vortex sheet, this makes them an appealing candidate for the initial stages of boundary layer formation, when one might expect large shears to be present.

We mention that Alexakis et al. (2004) have considered the Miles instability (Miles, 1957a) in the context of boundary layer formation. Specifically, they invoked the Miles instability to generate mixing of WD and stellar material and explain the enrichment in heavy elements observed in nova explosions. The Miles instability was proposed as a mechanism for generating waves over water at low wind speeds and operates through a resonant interaction between the wind and the water wave. Due to this interaction, a component of the pressure perturbation is created that is in phase with the velocity of the air-water interface, and much like pumping a swing, swings up the interface to large amplitudes. However, the Miles instability was initially introduced as a way of explaining the formation of waves on water at weak wind speeds, for which the air-water interface is stable to the KH instability. During boundary layer formation, however, large shears are generated, so we are not in the weak wind regime, and the Miles instability is likely to be swamped by sonic instabilities.

There are two main astrophysical implications of our findings. First, we demonstrate that the initiation of the BL is likely to take only very short amount time after the first material from the disk arrives to the stellar surface. This is because the sonic instabilities that we explored in this paper have an extremely short growth rate, which is very weakly dependent on the density

contrast between the disk and stellar material.[1] Thus, mixing of the two fluids starts almost immediately after they come into contact.

Second, given the efficiency with which the sonic instability operates, it is likely that it may play important role also in more developed phases of the BL evolution. As long as the BL possesses some effective "boundaries" (e.g. sharp changes in the velocity of density behavior) and the gas flow within it is supersonic the purely hydrodynamic sonic instabilities are going to operate in it potentially providing means for continuing mixing and angular momentum transport inside the layer. Future numerical calculations capable of following the nonlinear development of sonic instabilities should be able to address this issue.

We are grateful to Jim Stone for useful discussions. The financial support for this work is provided by the Sloan Foundation and NASA grant NNX08AH87G.

Bibliography

Abramowitz, M. & Stegun, I. A. 1972, Handbook of Mathematical Functions

Alexakis, A., Calder, A. C., Heger, A., Brown, E. F., Dursi, L. J., Truran, J. W., Rosner, R., Lamb, D. Q., Timmes, F. X., Fryxell, B., Zingale, M., Ricker, P. M., & Olson, K. 2004, ApJ, 602, 931

Alexakis, A., Young, Y., & Rosner, R. 2002, Phys. Rev. E, 65, 026313

Bergeron, P., Saffer, R. A., & Liebert, J. 1992, ApJ, 394, 228

Blumen, W., Drazin, P. G., & Billings, D. F. 1975, Journal of Fluid Mechanics, 71, 305

Chimonas, G. 1970, Journal of Fluid Mechanics, 43, 833

Choudhury, S. R. & Lovelace, R. V. E. 1984, ApJ, 283, 331

Cowling, T. G. 1941, MNRAS, 101, 367

[1]This statement is not true for the supersonic KH instability with gravity investigated in §4, see Equation (2.74).

Fejer, J. A. & Miles, J. W. 1963, Journal of Fluid Mechanics, 15, 335

Fujimoto, M. Y. 1987, A&A, 176, 53

Fujimoto, M. Y. 1988, A&A, 198, 163

Gerwin, R. A. 1968, Reviews of Modern Physics, 40, 652

Ghosh, P. & Lamb, F. K. 1978, ApJ, 223, L83

Gilfanov, M., Revnivtsev, M., & Molkov, S. 2003, A&A, 410, 217

Glatzel, W. 1988, MNRAS, 231, 795

Hachisu, I. 1986, ApJS, 62, 461

Hanawa, T. 1987, A&A, 179, 383

Hatanaka, H. 1949, J. Soc. Sci. Culture, 2, 3

Inogamov, N. A. & Sunyaev, R. A. 1999, Astronomy Letters, 25, 269

Kenyon, S. J., Hartmann, L., & Hewett, R. 1988, ApJ, 325, 231

Kippenhahn, R. & Thomas, H.-C. 1978, A&A, 63, 265

Koldoba, A. V., Romanova, M. M., Ustyugova, G. V., & Lovelace, R. V. E. 2002, ApJ, 576, L53

Landau, L. 1944, C.R. Acad. Sci. U.S.S.R., 44, 139

Livio, M. & Pringle, J. E. 1992, MNRAS, 259, 23P

Miles, J. W. 1957a, Journal of Fluid Mechanics, 3, 185

Miles, J. W. 1957b, Acoustical Society of America Journal, 29, 226

Miles, J. W. 1958, Journal of Fluid Mechanics, 4, 538

Narayan, R., Goldreich, P., & Goodman, J. 1987, MNRAS, 228, 1

Pai, S. I. 1954, J. Aero. Sci., 21, 325

Papaloizou, J. C. B. & Pringle, J. E. 1987, MNRAS, 225, 267

Patterson, J. 1984, ApJS, 54, 443

Piro, A. L. & Bildsten, L. 2004, ApJ, 610, 977

Piro, A. L. & Bildsten, L. 2007, ApJ, 663, 1252

Popham, R., Narayan, R., Hartmann, L., & Kenyon, S. 1993, ApJ, 415, L127

Ray, T. P. 1982, MNRAS, 198, 617

Spruit, H. C. 1999, A&A, 349, 189

Stone, J. M., Gardiner, T. A., Teuben, P., Hawley, J. F., & Simon, J. B. 2008, ApJS, 178, 137

Vallis, G. K. 2006, Atmospheric and Oceanic Fluid Dynamics

Wheatley, P. J., Mauche, C. W., & Mattei, J. A. 2003, MNRAS, 345, 49

A Reduction of Equations

Defining $S \equiv \varpi d\Omega/d\varpi$ to be the shear rate, and assuming $\delta_{BL} \ll R_*$ and $\Omega_* \ll \Omega_K$ we have that $2B \approx S \sim \Omega_K R_*/\delta_{BL} \gg \Omega_K$. We next note that $|\bar{\omega}|^2 \geq (\Im[\bar{\omega}])^2$ with exact equality at the location of a critical layer, where $\Re[\bar{\omega}] = 0$. According to Chimonas (1970), the growth rate of the fastest growing mode in a plane parallel stratified shear flow is of the order

$$\Im[\omega] \sim \frac{1}{4}S^2 - N^2, \tag{2.82}$$

where N is the Brunt-Väisälä frequency (Equation (2.56)). If we assume that shear instabilities provide the turbulence in the BL, then we can estimate that $|\bar{\omega}|^2 \gtrsim S^2$. Using this estimate on the left hand side of Equation (2.15), we find that the first term, $\bar{\omega}^2$, dominates the third term, $\kappa^2 \approx 2\Omega S$ by a factor of $R_*/\delta_{BL} \gg 1$, so we can ignore the third term. Next, we compare the second to last term $\bar{\omega}\bar{g}/s^2$ to the last term $2\Omega m/\varpi$ on the right hand side of Equation (2.15).

Defining $h_s \equiv s^2/\bar{g}$, dividing the second to last term by the last term, and ignoring constants of order unity we have $\bar{\omega}R_*/h_s m\Omega \gtrsim SR_*/h_s m\Omega \sim R_*^2/h_s\delta_{BL}m$. Next, we make the additional reasonable assumption that the fastest growing mode has $m/R_* \sim h_s^{-1}$, since h_s is of order the scale height and sets the natural length scale in the problem. Continuing our line of reasoning, we then have $R_*^2/h_s\delta_{BL}m \sim R_*/\delta_{BL} \gg 1$. This means that the last term in equation (2.15) is negligible compared to the second to last term and can be ignored. Finally, we compare the first term, $C_L\bar{\omega}$, and the second term, $2Bm/\varpi$, on the right hand side of Equation (2.14). Dividing the first term by the second term, using $2B \approx S$, $|\bar{\omega}|^2 \gtrsim S^2$ and $m/R_* \sim h_s^{-1}$, and noting that $C_L \sim h_s^{-1}$, we have $C_L\bar{\omega}R_*/mS \gtrsim h_sS/h_sS \sim 1$. Thus, both terms can potentially be of comparable magnitude and both must be retained.

Keeping only the dominant terms for $\delta_{BL} \ll R_*$, using $\varpi \approx R_*$, and assuming that $\rho'/\rho \gg R_*^{-1}$ and $\delta u'/\delta u \gg R_*^{-1}$, Equations (2.14) and (2.15) finally reduce to Equations (2.16) and (2.17).

B Generalized Rayleigh Equation and Boundary Conditions

B.1 Derivation of the Generalized Rayleigh Equation

We start with Equations (2.19) and (2.20). Using the definitions from §2, Equation (2.19) can be written as

$$\begin{aligned} \delta u' + C_1(x)\delta u &= C_2(x) && (2.83)\\ C_1(x) &= -(k_g + W'/W) && (2.84)\\ C_2(x) &= i(1 - W^2/s^2)k_y\delta P/\rho W, && (2.85) \end{aligned}$$

and similarly Equation (2.20) can be written as

$$\begin{aligned} \delta P' + C_3(x)\delta P &= C_4(x) && (2.86)\\ C_3(x) &= k_g && (2.87)\\ C_4(x) &= -i\rho(k_y^2W^2 + g(k_g + k_s))\delta u/k_yW. && (2.88) \end{aligned}$$

We can use the integrating factor method of solving first order differential equations to make a change of variables and get rid of the δu term in Equation (2.83) and the δP term in Equation (2.86). Making these changes of variable, we have

$$\delta q' = \frac{(1 - W^2/s^2)k_y \delta P}{\rho W^2 f}, \ \delta q \equiv (iWf)^{-1}\delta u \tag{2.89}$$

$$\delta \tilde{P}' = -\frac{if\rho(k_y^2 W^2 + g(k_g + k_s))\delta u}{k_y W}, \ \delta \tilde{P} \equiv f\delta P. \tag{2.90}$$

We can combine Equations (2.89) and (2.90) into a single equation for δq:

$$\left(\frac{\tilde{\rho}W^2\delta q'}{1 - W^2/s^2}\right)' = \tilde{\rho}(k_y^2 W^2 + g(k_g + k_s))\delta q. \tag{2.91}$$

This is the same basic form as Chimonas (1970). Since Equation (2.91) is a second order differential equation for δq, we can convert it to standard form (get rid of the first order term) with the change of variable

$$\delta\phi = \tilde{W}\delta q/k_y. \tag{2.92}$$

Making this change of variable yields Equation (2.21) which is the generalized Rayleigh equation (Alexakis et al., 2002).

B.2 Derivation of the Boundary Conditions at the Interface

We present here a physically motivated derivation of the interfacial boundary conditions, Equations (2.31) and (2.32). The two classical boundary conditions for the vortex sheet that should be satisfied at the interface are (1) that the two fluids should stay in contact at the interface, and (2) that the force exerted on the lower fluid by the upper fluid is equal and opposite to the force exerted on the upper fluid by the lower fluid. These can be expressed as

$$\delta\xi_+ = \delta\xi_- \tag{2.93}$$

$$\Delta P_+ = \Delta P_-, \tag{2.94}$$

where $\delta\xi$ is the displacement of the interface in the x-direction, and Δ denotes the Lagrangian differential. However, we must formulate both of these boundary conditions in terms of the generalized streamfunction perturbation $\delta\phi$.

We begin with the condition $\delta\xi_+ = \delta\xi_-$. We start with the relation

$$\frac{D\delta\xi}{Dt} = -i(\omega - k_y V_y)\delta\xi = \delta u, \tag{2.95}$$

where D/Dt, denotes the Lagrangian derivative. From Equations (2.93) and (2.95) we have

$$\frac{\delta u_+}{\omega - k_y V_y} = \frac{\delta u_-}{\omega + k_y V_y}. \tag{2.96}$$

Using the definitions of $\delta\phi$, $\tilde{W}$, and $\tilde{\rho}$ given in §2, and noting that $\tilde{\rho} = \rho$ at the interface ($x = 0$), we immediately get Equation (2.31):

$$\frac{\delta\phi_+}{\tilde{W}_+} = \frac{\delta\phi_-}{\tilde{W}_-}. \tag{2.97}$$

For the second boundary condition, we begin by writing

$$\Delta P = \delta P - g\rho\delta\xi. \tag{2.98}$$

Using Equation (2.89) we can substitute for δP in terms of δq, which gives at the interface

$$\frac{\tilde{W}_+^2}{k_y}\delta q'_+ - g_+\rho_+\delta\xi_+ = \frac{\tilde{W}_-^2}{k_y}\delta q'_- - g_-\rho_-\delta\xi_-. \tag{2.99}$$

Using Equations (2.95), (2.89), and (2.92) to substitute for $\delta\xi$, δq, and δu in terms of $\delta\phi$, we arrive at Equation (2.32):

$$\tilde{W}_+\delta\phi'_+ - \tilde{W}'_+\delta\phi_+ - \frac{g_+\tilde{\rho}_+\delta\phi_+}{\tilde{W}_+} = \tilde{W}_-\delta\phi'_- - \tilde{W}'_-\delta\phi_- - \frac{g_-\tilde{\rho}_-\delta\phi_-}{\tilde{W}_-}. \tag{2.100}$$

C Finite Width Shear Layer

We derive here the dispersion relation for a finite width shear layer in the absence of gravity and for a constant shear. Our analysis extends the work of Glatzel (1988) to arbitrary density ratios above and below the shear layer. We will use his notation in this section and consider the pressure perturbation δP rather than the generalized stream function $\delta\phi$. Where appropriate, we describe how to transform the results back into the notation used in the body of the text.

C.1 Setup of the Problem

Consider the velocity profile

$$V(x) = \begin{cases} -1, \ x < -1 \\ x, \ -1 \leq x \leq 1 \\ 1, \ x > 1, \end{cases} \tag{2.101}$$

and the density profile

$$\rho(x) = \begin{cases} \rho_-, \ x < -1 \\ \rho_0, \ -1 \leq x \leq 1 \\ \rho_+, \ x > 1. \end{cases} \tag{2.102}$$

The adiabatic index and equilibrium pressure are everywhere constant so we have $\rho_- s_-^2 = \rho_+ s_+^2 = \rho_0 s_0^2$. The perturbations are assumed to be of the form $\delta P = \delta f(x) \exp[i(k_y y - \omega t)]$. We define $M = 1/s_0$ to be the Mach number at $x = 1$ inside the shear layer. We also define

$$\epsilon_- = \rho_0/\rho_- \tag{2.103}$$

$$\epsilon_+ = \rho_0/\rho_+ \tag{2.104}$$

and adopt the following quantities from Glatzel (1988)

$$\bar{\sigma} \equiv W = -\frac{\bar{\omega}}{k_y} \tag{2.105}$$

$$Q \equiv \bar{\sigma}^{-1/2}\delta P \tag{2.106}$$

$$\zeta = ik_y M\bar{\sigma}^2 \tag{2.107}$$

$$\chi = \frac{i}{4}\frac{k_y}{M} \tag{2.108}$$

$$\mu = \frac{3}{4}. \tag{2.109}$$

Glatzel (1988) has shown that Q satisfies Whittaker's equation

$$\frac{d^2Q}{d\zeta^2} + \left(-\frac{1}{4} + \frac{\chi}{\zeta} + \frac{1/4-\mu^2}{\zeta^2}\right)Q = 0 \tag{2.110}$$

and inside the shear layer has the solution

$$Q = c_1 M_{\chi,\mu}(\zeta) + c_2 M_{\chi,-\mu}(\zeta), \tag{2.111}$$

where c_1 and c_2 are constants and $M_{\chi,\mu}(\zeta)$ is a Whittaker function. Outside the shear layer the velocity is constant, and the perturbation can be written as

$$Q \propto \begin{cases} \exp\left[\pm k_y(1-\epsilon_-^{-1}M^2\bar{\sigma}^2)^{1/2}x\right], & x<-1 \\ \exp\left[\pm k_y(1-\epsilon_+^{-1}M^2\bar{\sigma}^2)^{1/2}x\right], & x>1 \end{cases} \tag{2.112}$$

The signs in the exponentials should be chosen based on the condition of outgoing waves (§3.1).

C.2 Dispersion Relation

To derive the dispersion relation, we must apply the contact and pressure continuity boundary conditions at $x = \pm 1$ (Appendix B.2). Since the velocity and hence $\bar{\sigma}$ are everywhere continuous,

the pressure continuity boundary conditions at $x = \pm 1$ are simply

$$Q_{\rm in} = Q_{\rm out} \tag{2.113}$$

where the subscripts "in" and "out" denote evaluation of a quantity inside or outside the shear layer, respectively. Using the expression (Glatzel, 1988)

$$\delta u = \frac{i}{k\rho\bar{\sigma}}\delta P', \tag{2.114}$$

the contact boundary conditions at $x = \pm 1$ can be written as

$$\delta u_{\rm in} = \delta u_{\rm out} \tag{2.115}$$

$$\rho_{\rm out}\delta P'_{\rm in} = \rho_{\rm in}\delta P'_{\rm out} \tag{2.116}$$

$$\frac{1}{4\zeta} + \frac{1}{Q_{\rm in}}\frac{dQ_{\rm in}}{d\zeta} = \pm\frac{\rho_{\rm in}/\rho_{\rm out}}{2}\left(\frac{\rho_{\rm out}}{\rho_{\rm in}} - 4\frac{\chi}{\zeta}\right)^{1/2}. \tag{2.117}$$

In deriving the expression (2.117), we have made use of relations (2.105-2.108), and also the results (2.112) and (2.113). The sign in Equation (2.117) should be chosen on the basis of outgoing waves, and the lower sign should be chosen at $x = 1$ and the upper sign at $x = -1$. We also point out that $\rho_{\rm in}/\rho_{\rm out} = \epsilon_\pm$ at $x = \pm 1$.

Next, we substitute Equation (2.111) into Equation (2.117) at $x = \pm 1$, and set $c_1 = 1$, which sets the normalization. Using the property of the Whittaker function (Abramowitz & Stegun, 1972) that

$$\zeta\frac{dM_{\chi,\mu}}{d\zeta} = \left(\frac{\zeta}{2} - \chi\right)M_{\chi,\mu} + \left(\frac{1}{2} + \chi + \mu\right)M_{\chi+1,\mu}, \tag{2.118}$$

we can derive the dispersion relation

$$\frac{\left[1-4\chi+2\zeta_+ +2\epsilon_+\zeta_+\left(\epsilon_+^{-1}-4\frac{\chi}{\zeta_+}\right)^{1/2}\right]M_{\chi,\frac{3}{4}}(\zeta_+)+(4\chi+5)M_{\chi+1,\frac{3}{4}}(\zeta_+)}{\left[1-4\chi+2\zeta_+ +2\epsilon_+\zeta_+\left(\epsilon_+^{-1}-4\frac{\chi}{\zeta_+}\right)^{1/2}\right]M_{\chi,-\frac{3}{4}}(\zeta_+)+(4\chi-1)M_{\chi+1,-\frac{3}{4}}(\zeta_+)} =$$
$$\frac{\left[1-4\chi+2\zeta_- -2\epsilon_-\zeta_-\left(\epsilon_-^{-1}-4\frac{\chi}{\zeta_-}\right)^{1/2}\right]M_{\chi,\frac{3}{4}}(\zeta_-)+(4\chi+5)M_{\chi+1,\frac{3}{4}}(\zeta_-)}{\left[1-4\chi+2\zeta_- -2\epsilon_-\zeta_-\left(\epsilon_-^{-1}-4\frac{\chi}{\zeta_-}\right)^{1/2}\right]M_{\chi,-\frac{3}{4}}(\zeta_-)+(4\chi-1)M_{\chi+1,-\frac{3}{4}}(\zeta_-)}. \quad (2.119)$$

Using the relation between the confluent hypergeometric function and the Whittaker function (Glatzel, 1988), Equation (2.119) can be written in terms of the confluent hypergeometric function as

$$\bar{\sigma}_+^3\frac{\left[1-4\chi+2\zeta_+ +2\epsilon_+\zeta_+\left(\epsilon_+^{-1}-4\frac{\chi}{\zeta_+}\right)^{1/2}\right]{}_1F_1(\frac{5}{4}-\chi,\frac{5}{2},\zeta_+)+(4\chi+5){}_1F_1(\frac{1}{4}-\chi,\frac{5}{2},\zeta_+)}{\left[1-4\chi+2\zeta_+ +2\epsilon_+\zeta_+\left(\epsilon_+^{-1}-4\frac{\chi}{\zeta_+}\right)^{1/2}\right]{}_1F_1(-\frac{1}{4}-\chi,-\frac{1}{2},\zeta_+)+(4\chi-1){}_1F_1(-\frac{5}{4}-\chi,-\frac{1}{2},\zeta_+)} =$$
$$\bar{\sigma}_-^3\frac{\left[1-4\chi+2\zeta_- -2\epsilon_-\zeta_-\left(\epsilon_-^{-1}-4\frac{\chi}{\zeta_-}\right)^{1/2}\right]{}_1F_1(\frac{5}{4}-\chi,\frac{5}{2},\zeta_-)+(4\chi+5){}_1F_1(\frac{1}{4}-\chi,\frac{5}{2},\zeta_-)}{\left[1-4\chi+2\zeta_- -2\epsilon_-\zeta_-\left(\epsilon_-^{-1}-4\frac{\chi}{\zeta_-}\right)^{1/2}\right]{}_1F_1(-\frac{1}{4}-\chi,-\frac{1}{2},\zeta_-)+(4\chi-1){}_1F_1(-\frac{5}{4}-\chi,-\frac{1}{2},\zeta_-)}. \quad (2.120)$$

Equation (2.120) is a generalization of the dispersion relations considered by Glatzel (1988). For instance, taking $\epsilon_\pm \to 0$ we recover his dispersion relation (5.23) for the reflecting boundary condition $\delta u(x=\pm 1)=0$, taking $\epsilon_\pm \to \infty$ we recover his dispersion relation (5.24) for a vacuum boundary condition $\delta P(x=\pm 1)=0$, and taking $\epsilon_\pm = 1$ we recover his dispersion relation (5.38) for an infinite fluid with uniform density everywhere.

C.3 The Vortex Sheet Limit

We can show that Equation (2.120) reduces to the dispersion relation for the vortex sheet, (Equation (2.40)), by taking the limit $k_y \to 0$. In this limit, $\zeta \to 0$ and $\chi \to 0$, but $\bar{\sigma}$, the phase

speed in the comoving frame, is finite, and

$$4\frac{\chi}{\zeta} = (M^2\bar{\sigma}^2)^{-1} \tag{2.121}$$

is also finite. We also note the property of the hypergeometric function that in the limit $\zeta \to 0$

$${}_1F_1(l, m, \zeta) = 1 + \frac{l}{m}\zeta + \mathcal{O}(\zeta^2). \tag{2.122}$$

Using these relations, Equation (2.120) can be reduced to the form

$$\bar{\sigma}_+^2\epsilon_-(M^2\bar{\sigma}_-^2\epsilon_-^{-1} - 1)^{1/2} = \bar{\sigma}_-^2\epsilon_+(M^2\bar{\sigma}_+^2\epsilon_+^{-1} - 1)^{1/2} \tag{2.123}$$

Equation (2.40) can then be obtained by setting $\epsilon_+ = 1$, $\epsilon_- = \epsilon$, and using the relation $M = 1/s_+$.

Chapter 3

Numerical Model and Simulation Parameters

Abstract

In this chapter, we focus on the numerical model used to simulate the boundary layer. We perform a variety of simulations in cylindrical geometry including 2D hydro ($r-\phi$ plane), 3D unstratified (in the z-direction) hydro, 3D stratified hydro, and 3D unstratified MHD. We use a significantly higher resolution than previous authors, which lets us properly resolve the radial scale height of the star, as well as the vertical scale height in stratified simulations. This is important for studying modes excited in the BL, since the scale height represents a natural length scale in the problem. We provide a table that lists simulations along with their relevant parameters, which will be referenced in later chapters.

1 Overview

We perform global hydro and MHD simulations of the BL in cylindrical geometry in both 2D ($r-\phi$ plane) and 3D (MHD simulations are exclusively in 3D). In the case of 3D hydro, we perform simulations with and without vertical stratification, while in the case of MHD, we only perform simulations that are vertically unstratified. We use a simulation domain that extends for many (~ 15) radial pressure scale heights into the star and to several stellar radii into the disk. However, we do not include self-gravity and use a fixed $1/\varpi$ potential for vertically unstratified runs, where ϖ is the cylindrical radius, and a $1/r$ potential for vertically stratified runs. In all of our simulations, we adopt an isothermal equation of state, which can be physically interpreted as instantaneous cooling to a set temperature. Although this is not a realistic approximation of the

thermodynamics, it allows us to study the BL on long timescales (~ 100 orbits at the surface of the star) and to achieve quasi-steady state behavior in the simplest possible manner.

For the numerical evolution of equations, we use the Godunov code Athena (Stone et al., 2008) in cylindrical coordinates (Skinner & Ostriker, 2010). Athena is highly-parallelized and exhibits very low levels of numerical viscosity making it well-suited for studying the long-term evolution of the boundary layer.

2 Numerical Model

2.1 Governing Equations

For our simulations, we use Athena to solve the MHD equations with an isothermal equation of state in cylindrical geometry. These equations are

$$\frac{\partial \rho}{\partial t} + \boldsymbol{\nabla} \cdot (\rho \boldsymbol{v}) = 0, \tag{3.1}$$

$$\frac{\partial (\rho \boldsymbol{v})}{\partial t} + \boldsymbol{\nabla} \cdot (\rho \boldsymbol{v}\boldsymbol{v}) = -\boldsymbol{\nabla}\left(P + \frac{B^2}{2\mu}\right) + \frac{1}{\mu}(\boldsymbol{B} \cdot \boldsymbol{\nabla})\boldsymbol{B} - \rho \boldsymbol{\nabla}\Phi, \tag{3.2}$$

$$P = \rho s^2, \tag{3.3}$$

$$\frac{\partial \boldsymbol{B}}{\partial t} = \boldsymbol{\nabla} \times (\boldsymbol{v} \times \boldsymbol{B}) \tag{3.4}$$

Here, $\boldsymbol{v}$ is the velocity, ρ is either the density (3D) or the surface density (2D), P is the pressure, Φ is the gravitational potential, s is the sound speed, and $\boldsymbol{B}$ is the magnetic field (only in MHD simulations). We also use ϖ throughout the thesis to denote the cylindrical radius.

2.2 Nondimensional Units

Our initial setup, described in more detail below, consists of a star which attaches to a constant density disk via a thin interfacial region. Following the convention of Belyaev et al. (2012a), we nondimensionalize quantities by setting the radius of the star to $\varpi_\star = 1$, which defines a unit of length, the Keplerian angular velocity to $\Omega_K(\varpi_\star) = 1$, which defines a unit of time, and $\rho = 1$ at

the midplane of the disk, which defines a characteristic density. Expressed in these units, the orbital timescale at the surface of the star is $P_K = 2\pi$. In MHD simulations, the magnetic permeability is set to $\mu = 1$.

We also define a characteristic Mach number as $M \equiv 1/s$, which is the true Mach number of the flow in the disk at the surface of the star, since $V_K(\varpi_\star) = 1$. For a given simulation, the Mach number, and in the case of MHD, the initial magnetic field geometry, are the most important *physical* parameters in the simulation. The initial magnetic field strength can also be important, since it sets the scale for the wavelength of the fastest growing mode in simulations with a z-directed magnetic field (§2.6).

In practice there are also *numerical* parameters, e.g. the size of the simulation domain, resolution, etc. that influence the outcome of a simulation.

2.3 Gravitational Potential

We take the gravitational potential to be fixed throughout the course of a simulation. This amounts to ignoring the self-gravity of the outer layers of the star (Cowling's approximation, Cowling (1941)), which was discussed in the context of the BL in Belyaev & Rafikov (2012).

We run both vertically stratified and unstratified simulations. For vertically unstratified runs, we use the cylindrically symmetric potential

$$\Phi = -\frac{1}{\varpi}, \tag{3.5}$$

whereas for vertically stratified runs, we use the point mass potential

$$\Phi = -\frac{1}{\sqrt{\varpi^2 + z^2}}, \tag{3.6}$$

where z is the height above the midplane.

2.4 Initial Rotation Profile

Initially, the star attaches to the disk via a thin interface, inside of which the rotational velocity, v_ϕ, rises very nearly linearly from zero (the velocity in the star) to the Keplerian orbital velocity (the velocity in the disk). The initial rotation profile is given by

$$\Omega(\varpi) = \begin{cases} 0 & \varpi < 1 - \frac{\delta_{BL,0}}{2} \quad \text{“star”} \\ \varpi^{-3/2}\left(\frac{\varpi - 1}{\delta_{BL,0}} + \frac{1}{2}\right) & 1 - \frac{\delta_{BL,0}}{2} \le \varpi \le 1 + \frac{\delta_{BL,0}}{2} \quad \text{“interface”} \\ \varpi^{-3/2} & \varpi > 1 + \frac{\delta_{BL,0}}{2} \quad \text{“disk”} \end{cases} , \tag{3.7}$$

and is shown in Fig. 3.1. For all our runs, we use $\delta_{BL,0} = .01$, so the interface is as narrow as possible, while still being resolved with ~ 10 cells. Our results are independent of $\delta_{BL,0}$, since over the course of a simulation, the interface thickens into a self-consistent BL due to angular momentum transport by acoustic modes.

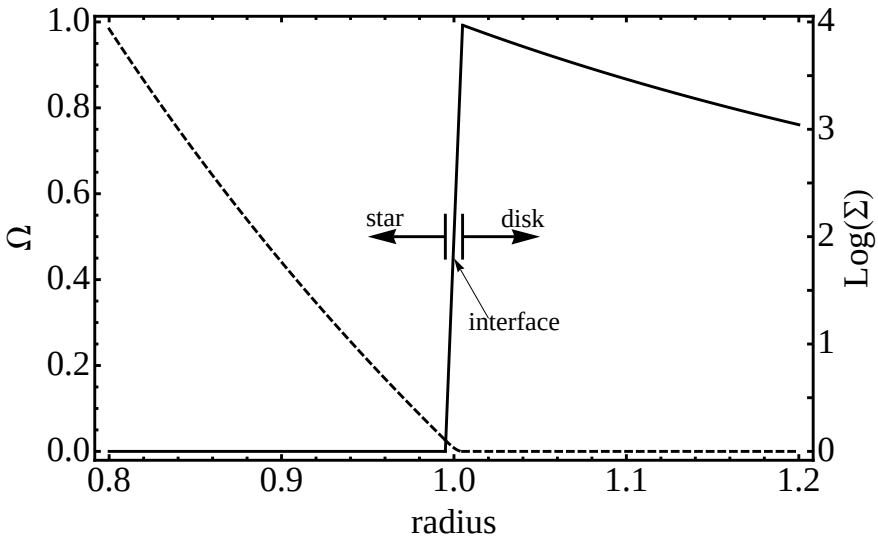


Figure 3.1: Initial rotation profile $\Omega(\varpi)$ (*solid line*) and the logarithm of the initial density (*dashed line*) for a simulation with $M = 6$. Note that the jump in Ω at $\varpi = 1$ is not discontinuous and is resolved in the simulations. Various regions of the simulation domain are indicated.

2.5 Initial Density and Pressure Profiles

The initial pressure profile is specified everywhere throughout the domain through the equation of hydrostatic equilibrium

$$\frac{1}{\rho}\frac{\partial P}{\partial \varpi} = -\frac{\partial \Phi}{\partial \varpi} + \Omega^2 \varpi, \tag{3.8}$$

$$\frac{1}{\rho}\frac{\partial P}{\partial z} = -\frac{\partial \Phi}{\partial z}. \tag{3.9}$$

The density is directly proportional to the pressure and is related to it through the equation of state (3.3).

For the 2D and 3D unstratified simulations, the initial density is $\rho(\varpi, t=0) = 1$ within the disk, and $\rho(\varpi, t=0) = \exp[-\Phi(\varpi)/s^2]$ within the star, where $\Omega = 0$. For the stratified simulations, these expressions are also accurate for the midplane density, $\rho_0(\varpi, t=0) \equiv \rho(\varpi, z=0, t=0)$, as long as we use the midplane potential $\Phi_0(\varpi) \equiv \Phi(\varpi, z=0)$. The initial density throughout the simulation domain for a stratified simulation can be expressed in terms of the initial midplane density as $\rho(\varpi, z, t=0) = \rho_0(\varpi, t=0)\exp[-(\Phi(\varpi, z) - \Phi_0(\varpi))/s^2]$. This formula is valid everywhere, including the interfacial region, since we have rotation on cylinders throughout the simulation domain, i.e. Ω is a function only of ϖ (equation [3.7]).

2.6 Initial Magnetic Field Configuration (MHD Simulations)

We now discuss the initial magnetic field strengths and geometries we use in our simulations. For all our simulations, we set $\boldsymbol{B} = 0$ for $\varpi < \varpi_\star$ (an unmagnetized star), and initialize one of three possible magnetic field geometries for $\varpi \geq \varpi_\star$:

$$\boldsymbol{B}(\varpi \geq \varpi_\star, z) = \begin{cases} \frac{B_0}{\varpi}\hat{\boldsymbol{z}}, & \text{NVF} \\ B_0\hat{\boldsymbol{\phi}}, & \text{NAF} \\ \frac{B_0}{\varpi}\sin\left[\frac{2\pi}{\lambda_\varpi}(\varpi - \varpi_\star)\right]\hat{\boldsymbol{z}}, & \text{ZNF} \end{cases}. \tag{3.10}$$

NVF simulation have a constant vertical magnetic flux through any radius, NAF simulations have a constant azimuthal magnetic flux, and ZNF simulations have on average zero net flux. For the ZNF simulation, we set $\lambda_\varpi = \Delta z/2$, where Δz is the extent of the simulation domain in the vertical direction. Thus, we have a rapid variation of the field in the radial direction, which allows comparison with shearing box ZNF simulations.

In all of our runs, we use an initial value of $B_0 = .002$ in units for which the magnetic permeability is $\mu = 1$. Defining the plasma parameter β as

$$\beta \equiv \frac{\rho s^2}{B^2/2\mu} \tag{3.11}$$

the initial value of β using B_0 for a baseline is $\beta_0 \approx 6200$. Note that in the NVF and ZNF simulations, β varies as a function of position and β_0 specifies the minimum initial value of β in the disk.

The particular value of $B_0 = .002$ is motivated by two considerations. The first is the need to resolve the wavelength of the fastest growing mode of the MRI in the case of a pure vertical field (NVF simulations), and the second is the need to fit several wavelengths of the fastest growing mode within the simulation domain.

For a global disk simulation in which the domain has constant width and resolution in the z direction, these two criteria are generally at odds with one another. This is because the z-wavelength of the fastest growing axisymmetric mode for constant vertical field in a Keplerian disk is given by Balbus & Hawley (1991)

$$\lambda_{z,\mathrm{MRI}} = \sqrt{\frac{16}{15}}\frac{2\pi B}{\Omega\sqrt{\rho}}. \tag{3.12}$$

For a Keplerian disk with constant B_z field and constant ρ, $\lambda_{z,\mathrm{MRI}} \propto \varpi^{3/2}$. For our NVF field geometry, the magnetic field strength falls off as $1/\varpi$ so $\lambda_{z,\mathrm{MRI}} \propto \varpi^{1/2}$. This is a weaker dependence than for a constant field and is the main reason we use a constant flux criterion in the NVF case, rather than simply using a constant field.

For the ZNF case, we no longer have to worry about fitting the vertical wavelength of the fastest growing mode within the simulation domain, since the field strength varies as a function of radius and the MRI grows on all scales. The same goes for NAF simulations, because instability manifests itself differently if the initial field is azimuthal rather than vertical. In the former case, the most unstable modes are non-axisymmetric ones that undergo transient exponential growth in the shearing sheet approximation (Balbus & Hawley, 1992; Tagger et al., 1992) or pure exponential growth in a global disk analysis (Matsumoto & Tajima, 1995; Coleman et al., 1995; Ogilvie & Pringle, 1996; Terquem & Papaloizou, 1996). In a shearing sheet analysis, the modes which undergo the most vigorous growth are the ones that have the largest values of k_z for a given value of k_x and k_y (Balbus & Hawley, 1992; Hawley et al., 1995). Thus, resolution of these modes in a simulation is limited by the grid resolution, but their vertical wavelength is always able to fit within the vertical extent of the simulation domain.

2.7 Boundary Conditions

Hydro

In our hydro simulations, we use periodic boundary conditions (BCs) in the ϕ direction, "do-nothing" BCs in the ϖ direction, and periodic BCs in the z direction.

The "do-nothing" BC simply means that all fluid quantities retain their initial, equilibrium values at the boundary. A "do-nothing" BC in ϖ is advantageous to an outflow BC, especially at the inner edge of the domain inside the star, since it prevents a systematic change in the density profile over the course of the simulation due to small deviations from equilibrium. A "do-nothing" BC is also advantageous to a reflecting BC, since it allows sound waves to leave the domain. However, a "do-nothing" BC does not absorb radiation perfectly (neither does an outflow BC), and there is some partial reflection of waves from the radial boundaries, although the reflection coefficient is significantly less than unity.

The reason for using periodic BCs in the z-direction, even in stratified hydro simulations, is that it is hard to achieve a good numerical equilibrium with outflow BCs. The application of

outflow BCs (in the θ-direction) is potentially more straightforward in spherical geometry, since in that case the gravity vector is parallel to the θ-boundary.

MHD

The boundary conditions we use in MHD simulations are periodic in the z and ϕ directions, and do-nothing at the inner radial boundary. At the outer radial boundary, we implement two different types of boundary conditions. The first type, which we call OBC0, is simply an open (outflow) boundary condition. The second type, OBC1, is a do-nothing boundary condition, just like at the inner radial boundary. In simulations implementing an outer do-nothing boundary condition, we initialize a nonmagnetic "buffer zone" between a fiducial radius in the disk $\varpi_{\rm B,max}$ and the outer boundary. The magnetic field is initialized to be zero in the region $\varpi_{\rm B,max} \leq \varpi \leq \varpi_{\rm out}$, where $\varpi_{\rm out}$ denotes the radius of the outer boundary. In all of our simulations implementing OBC1, $\varpi_{\rm B,max} = 4$.

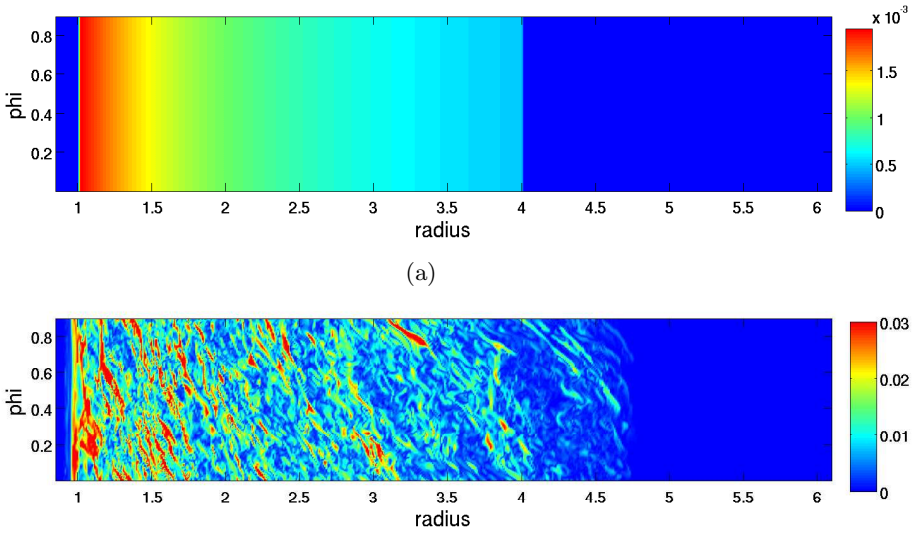


Figure 3.2: Panels a,b show the magnitude of the magnetic field in simulation M9d at times $t = 0$ and $t = 500$, respectively.

To demonstrate the buffer zone more clearly, we plot the magnetic field magnitude from simulation M9d at $t = 0$ and $t = 500$ in panels a and b of Fig. 3.2. In panel a, the field decays

$\propto 1/\varpi$ between the star at $\varpi = 1$ and the buffer zone at $\varpi = \varpi_{\rm B,max} = 4$. In the region $\varpi_{\rm B,max} < \varpi < \varpi_{\rm out}$, the field is initially set to zero. In panel b, magnetic field has penetrated into the buffer zone, as a result of the natural evolution of the MHD equations, but has not yet reached the outer boundary. In general, simulations implementing OBC1 are stopped before the magnetic field can diffuse through the buffer zone and reach the outer boundary. This allows us to run simulations for a long time, without having to worry about the effect of magnetic field at the outer boundary on the rest of the simulation domain.

label	dimension	M	stratified	ϖ-range	ϕ-range	z-range	$N_\varpi \times N_\phi \times N_z$
3D6a	3D	6	no	(.7, 2.5)	(0, 2π)	(-1/12, 1/12)	$2048 \times 2048 \times 32$
3D6b	3D	6	no	(.7, 2.5)	(0, 2π)	(-1/6, 1/6)	$2048 \times 2048 \times 64$
3D6c	3D	6	yes	(.7, 2.5)	(0, 2π)	(-1/3, 1/3)	$1536 \times 1536 \times 128$
3D6d	3D	6	no	(.7, 2.5)	(0, $\pi/3$)	(-1/12, 1/12)	$2048 \times 384 \times 32$
3D9a	3D	9	no	(.85, 2.5)	(0, 2π)	(-1/18, 1/18)	$2048 \times 2048 \times 32$
3D9b	3D	9	no	(.85, 2.5)	(0, 2π)	(-1/9, 1/9)	$2048 \times 2048 \times 64$
3D9c	3D	9	yes	(.85, 2.5)	(0, 2π)	(-2/9, 2/9)	$1536 \times 1536 \times 128$
3D9d	3D	9	no	(.85, 2.5)	(0, $\pi/3$)	(-1/18, 1/18)	$2048 \times 384 \times 32$
3D9e	3D	9	no	(.85, 2.5)	(0, $2\pi/7$)	(-1/18, 1/18)	$2048 \times 384 \times 32$
3D9f	3D	9	no	(.85, 2.5)	(0, $2\pi/7$)	(-1/18, 1/18)	$2048 \times 384 \times 64$
2D6a	2D	6	–	(.7, 2.5)	(0, 2π)	–	$2048 \times 2048 \times 1$
2D6b	2D	6	–	(.7, 2.5)	(0, $\pi/2$)	–	$2048 \times 512 \times 1$
2D6c	2D	6	–	(.7, 2.5)	(0, $\pi/4$)	–	$2048 \times 256 \times 1$
2D6d	2D	6	–	(.7, 2.5)	(-.4, .4)	–	$2048 \times 512 \times 1$
2D6e	2D	6	–	(.7, 2.5)	(-.4, .4)	–	$1024 \times 256 \times 1$
2D6f	2D	6	–	(.7, 2.5)	(-.4, .4)	–	$8192 \times 1024 \times 1$
2D6g	2D	6	–	(.7, 4.3)	(-.4, .4)	–	$4096 \times 512 \times 1$
2D9a	2D	9	–	(.85, 2.5)	(0, 2π)	–	$4096 \times 4096 \times 1$
2D9b	2D	9	–	(.85, 2.5)	(0, $\pi/2$)	–	$4096 \times 1024 \times 1$
2D9c	2D	9	–	(.85, 2.5)	(0, $\pi/4$)	–	$4096 \times 512 \times 1$
2D9d	2D	9	–	(.85, 2.5)	(-.4, .4)	–	$2048 \times 512 \times 1$
2D12a	2D	12	–	(.9, 2.5)	(0, 2π)	–	$6144 \times 6144 \times 1$
2D12b	2D	12	–	(.9, 2.5)	(-.4, .4)	–	$6144 \times 1024 \times 1$
2D15a	2D	15	–	(.94, 2.5)	(0, 2π)	–	$6144 \times 6144 \times 1$
2D15b	2D	15	–	(.94, 2.5)	(-.4, .4)	–	$6144 \times 1024 \times 1$

Table 3.1: Summary of simulation parameters for hydro simulations. The columns from left to right are: simulation label, dimensionality (2D or 3D), Mach number, stratification (yes = stratified, no = unstratified), radial extent of the simulation domain, azimuthal extent, vertical extent (only in 3D), number of grid points in the radial $\times$ azimuthal $\times$ vertical directions.

2.8 Initial Perturbations and Burn-In

Although we initialize our density and pressure profiles to satisfy the equations of hydrostatic equilibrium (equations [3.8] and [3.9]), we find that we need to burn-in our simulations for $t \sim 100$ to let any initial transients damp out and achieve a good numerical hydrostatic equilibrium. This burn-in procedure was previously used by Armitage (2002) in studying the BL, and we find it easier than setting up an exact numerical equilibrium (Zingale et al., 2002).

After the burn-in period, we introduce random perturbations to v_ϖ of amplitude $\delta v_\varpi \sim .001$ in the region $\varpi > 1$. These random perturbations to the radial velocity seed the sonic instability and facilitate the growth of acoustic modes. The reason for only introducing perturbations in the region $\varpi > 1$ is that waves traveling from high density to low density regions amplify by a factor of $\rho^{-1/2}$ to conserve energy. Since the density in the star is up to 10^6 times higher than that in the disk, we want to avoid any transient waves that amplify as they travel out of the star and into the disk.

2.9 Simulation-Specific Parameters

Hydro

Table 3.1 lists the simulation specific-parameters for the hydro runs. Typically, our simulations are run until a time of $t \approx 400 - 600$ ($70 - 100$ orbits at the inner edge of the disk), where $t = 0$ corresponds to the time when the random perturbations to the radial velocity are introduced.

The most important parameters that vary from simulation to simulation are dimensionality (2D or 3D), Mach number, stratification in the z-direction (unstratified or stratified), the ϕ extent of the simulation domain (full 2π or a wedge), and magnetic field geometry (for MHD runs). Comparing the effects of dimensionality and stratification across simulations with all other parameters held constant allow us to probe how the thickness of the disk affects the dynamics of the system. Varying the Mach number gives us a handle on how the phenomena we discuss translate over to astrophysical systems which tend to have higher Mach numbers (e.g. $M \sim 100$ for white dwarfs (Balsara et al., 2009)). We cannot simulate such high Mach numbers directly at

the moment due to a reduction in timestep with increasing Mach number, which is a consequence of the Courant condition. Changing the ϕ extent of the simulation domain gives us a measure of control over the wavelength of the dominant modes present in the box, allowing us to probe the dispersion relation for our model. Finally, varying the initial magnetic field geometry allows us to study the response of the boundary layer to a variety of magnetic field configurations in the disk.

MHD

label	**B** type	outer BC	ϖ-range	N_ϖ	N_z	$t_{\rm run}$
M9a	NVF	OBC0	(.85, 6.1)	4096	128	450
M9b	NAF	OBC0	(.85, 7.85)	6144	64	450
M9c	ZNF	OBC0	(.85, 6.1)	4096	128	450
M9d	NVF	OBC1	(.85, 6.1)	4096	64	800
M9e	NAF	OBC1	(.85, 6.1)	4096	48	1000
M9f	ZNF	OBC1	(.85, 6.1)	4096	64	1800

Table 3.2: Summary of simulation parameters for MHD simulations. The columns from left to right are: simulation label, initial field geometry (net vertical flux, net azimuthal flux, or zero net flux), outer boundary condition, radial extent of the simulation domain, number of grid points in the radial direction, number of grid points in the vertical direction, and the total time for which the simulation was run.

The only physical parameter varied across MHD simulations in this study is the initial field geometry. In principle, other parameters such as the Mach number, the vertical extent of the simulation domain, the presence of vertical stratification, etc., would also have an important effect on the dynamics of the BL. However, it is computationally expensive to undertake an exhaustive parameter study, so we limit ourselves to varying only the initial field geometry in this exploratory work. This allows us to explore the major effects a magnetic field has on BL dynamics with no added frills. We mention that we have explored how varying the dimensionality (2D/3D), stratification (stratified/unstratified), and Mach number affects the outcome of our *hydrodynamical* BL simulations.

Some important parameters that are fixed across different MHD runs are the Mach number, set to $M = 9$; the vertical extent of the simulation domain, set to $\Delta z = s/\Omega_K(\varpi_\star) = 1/9$; the ϕ

extent of the simulation domain, set to $\Delta\phi = 2\pi/7$; and the ϕ resolution set to $N_\phi = 384$ cells. Table 3.2 lists important numerical parameters that vary from simulation to simulation.

The specific choice of $\Delta\phi = 2\pi/7$, represents a compromise between computational resources and simulating a wedge that spans a wide enough azimuthal angle. Also, setting $\Delta\phi = 2\pi/7$, we resolve all modes having m a multiple of seven. The $m = 14$ mode happens to be close to a geometric resonance (equations (44,45) of Belyaev et al. (2012b)) for $M = 9$, which means its amplitude is enhanced relative to modes with a similar m number. Therefore, the $m = 14$ mode typically peaks in our simulations, simplifying the analysis, since we can study a single dominant mode rather than a superposition of modes having similar amplitudes.

Bibliography

Armitage, P. J. 2002, MNRAS, 330, 895

Balbus, S. A. & Hawley, J. F. 1991, ApJ, 376, 214

Balbus, S. A. & Hawley, J. F. 1992, ApJ, 400, 610

Balsara, D. S., Fisker, J. L., Godon, P., & Sion, E. M. 2009, ApJ, 702, 1536

Belyaev, M. A. & Rafikov, R. R. 2012, ApJ, 752, 115

Belyaev, M. A., Rafikov, R. R., & Stone, J. M. 2012a, ApJ, 760, 22

Belyaev, M. A., Rafikov, R. R., & Stone, J. M. 2012b, ArXiv e-prints

Coleman, C. S., Kley, W., & Kumar, S. 1995, MNRAS, 274, 171

Cowling, T. G. 1941, MNRAS, 101, 367

Hawley, J. F., Gammie, C. F., & Balbus, S. A. 1995, ApJ, 440, 742

Matsumoto, R. & Tajima, T. 1995, ApJ, 445, 767

Ogilvie, G. I. & Pringle, J. E. 1996, MNRAS, 279, 152

Skinner, M. A. & Ostriker, E. C. 2010, ApJS, 188, 290

Stone, J. M., Gardiner, T. A., Teuben, P., Hawley, J. F., & Simon, J. B. 2008, ApJS, 178, 137

Tagger, M., Pellat, R., & Coroniti, F. V. 1992, ApJ, 393, 708

Terquem, C. & Papaloizou, J. C. B. 1996, MNRAS, 279, 767

Zingale, M., Dursi, L. J., ZuHone, J., Calder, A. C., Fryxell, B., Plewa, T., Truran, J. W., Caceres, A., Olson, K., Ricker, P. M., Riley, K., Rosner, R., Siegel, A., Timmes, F. X., & Vladimirova, N. 2002, ApJS, 143, 539

Chapter 4

General Overview of the Isothermal BL

Abstract

We present a general overview of hydro simulation results (both 2D and 3D) and discuss the properties of an isothermal BL. We find that the BL setup described in Chapter 3 is unstable to sonic instabilities as predicted in Chapter 2. These sonic instabilities drive mass accretion from the inner part of the disk onto the star, widening the BL and creating a gap in the density profile of the inner disk. After the sonic instabilities have saturated, an acoustic mode with a well-defined pattern speed is set up within both the star and the disk. This acoustic mode facilitates angular momentum transport (the subject of Chapter 5) and provides a periodic source of variability within the BL. Finally we show that the width of the isothermal BL scales in the same way with the Mach number as the scale height, i.e. $\propto M^{-2}$. Since the pressure scale height, $h_s = \varpi_\star M^{-2}$, where $\varpi_\star$ is the radius of the star, this means that the BL spans the same number of scale heights independent of the Mach number (6-7 in our simulations).

1 Introduction and Astrophysical Motivation

In this chapter, our focus is on the gross morphology and time-dependent features of an isothermal BL without a magnetic field (the magnetic case is discussed in Chapter 6). The morphology of the BL in any simulated or astrophysical system is closely connected with the dynamical mechanism of angular momentum transport within the BL (the subject of Chapter 5). Since the rotational velocity of the gas passing through the BL changes with radius, some mechanism of angular momentum transport must operate there, ultimately leading to radial mass transport.

The nature of this mechanism is not understood at the moment. The magnetorotational instability (MRI; Velikhov (1959); Chandrasekhar (1960); Balbus & Hawley (1991); Hawley & Balbus (1991)) usually invoked to explain mass transport in accretion disks does not operate in the BL because $d\Omega^2/d\varpi > 0$ there (ϖ is the cylindrical radius). Magnetic field carried into the BL by accreting gas is sheared by differential rotation (Armitage, 2002; Steinacker & Papaloizou, 2002), but whether this can lead to sustained mass accretion has not been conclusively demonstrated. Indeed, Pessah & Chan (2012) have shown that if $d\Omega/d\varpi > 0$, then the stresses due to a sheared magnetic field are inefficient at transporting angular momentum and oscillate about zero. Of course, linear stability does not imply the flow is laminar. For instance, turbulence can persist without decay in certain classes of linearly stable rotating flows (Lesur & Longaretti, 2005), once it is generated nonlinearly.

Other transport mechanisms — Kelvin-Helmholtz instability (Kippenhahn & Thomas, 1978), baroclinic instability (Fujimoto, 1987), Tayler-Spruit dynamo (Tayler, 1973; Spruit, 1999; Piro & Bildsten, 2004) have also been proposed, but whether they can operate in the BL and give rise to efficient momentum transport there is far from clear. In the absence of a good understanding of the momentum and mass transport, even the morphology of the BL has been a matter of debate, with the proposed geometries ranging from a BL contained inside the star(Kippenhahn & Thomas, 1978) to a spreading layer extending to significant latitudes over the stellar surface (Inogamov & Sunyaev, 1999, 2010).

One of the major goals of this thesis is to shed light upon the mechanism of angular momentum transport in the BL. We devote Chapter 5 to a detailed study of angular momentum transport in an unmagnetized BL and Chapter 6 discusses the magnetized case. However, this topic is so important that we begin to touch upon it in this chapter when we discuss mass accretion in the BL and the formation of a density gap in the inner part of the disk.

In addition to angular momentum transport, a second major focus of this thesis is periodic behavior associated with the BL. The BL has also been associated with variability in accreting systems that occurs on timescales comparable to the dynamical timescale at the surface of the star. One example of such variability are dwarf nova oscillations (DNOs) in accreting white dwarf

systems (Warner, 2004), which do not have a definitive explanation. DNOs are characterized by an oscillation period of $P_{DNO} \gtrsim P_K(R_\star)$, where P_{DNO} is the DNO period and $P_K(R_\star)$ is the Keplerian rotational period at the surface of the star (Patterson, 1984). Since the DNO period is comparable to the Keplerian rotational period at the surface of the star, it is natural to associate DNOs with the boundary layer or with the region of the disk directly adjacent to it. We don't try to link our simulations directly to DNOs, but the periodic and quasi-periodic variability observed in our runs is food for thought when considering variability in accreting systems that occurs on timescales that are of order the orbital timescale at the surface of the star or faster.

We now give a detailed account of how this chapter is organized. We find that the boundary layer is unstable to sonic instabilities (§2), which tend to excite an acoustic mode inside the disk and star (§3). This acoustic mode is discussed in detail in Chapter 5, where it is shown that it can transport angular momentum and drive mass accretion onto the star. In (§4) we present figures from our 3D unstratified hydro simulations that clearly show mass accretion onto the star, depletion of the inner disk adjacent to the star, and modification of the initial rotation profile, all of which are indicators of angular momentum transport in the disk-star system. In §5 we discuss how BL thickness scales with Mach number for an isothermal BL.

2 Sonic Instability

Although hydrodynamical disks with a Keplerian rotation profile are stable to axisymmetric perturbations by the Rayleigh criterion, the large shear initially present in the interface (equation [3.7]) makes that region unstable to non-axisymmetric shear instabilities. Since the initial flow has a supersonic drop in the velocity across the interface, the instability that sets in is not the classical KH instability for an incompressible fluid, but rather the sonic instability (Glatzel, 1988; Belyaev & Rafikov, 2012). This is a global instability that cannot be derived from a local analysis and is similar to the Papaloizou-Pringle instability (Papaloizou & Pringle, 1984; Narayan et al., 1987; Glatzel, 1988).

The sonic instability operates in one of two ways, either by *overreflection* of sound waves from a critical layer (where the radial wavenumber becomes equal to zero or equivalently the phase

velocity of the mode equals the velocity of the flow) or by *radiation* of energy away from a critical layer, see Narayan et al. (1987); Glatzel (1988); Belyaev & Rafikov (2012). Both mechanisms can be loosely thought of as an exchange of energy between modes on either side of the critical layer. One mode has positive energy density, the other negative, and instability occurs due to exchange of energy across the critical layer which allows *both* modes to grow while conserving the total energy.

For a rotating flow, the critical layer of a mode is equivalent to the corotation resonance, which is located at the radius ϖ_{CR} where $\Omega(\varpi_{CR})$ equals the pattern frequency, Ω_P. Modes, which have a corotation resonance (critical layer) inside the fluid domain are susceptible to instability.

The origin of the sonic instability in the case of the overreflection mechanism is closely related to the existence of a conserved action (or pseudo-energy) associated with the mode, which is quadratic in perturbed fluid variables and changes sign at corotation (Narayan et al., 1987). A wave incident upon one side of the corotation region with a positive sign of the action is predominantly reflected. However, there is partial tunneling through the evanescent region around corotation, and the wave emerging on the other side of ϖ_{CR} has the opposite sign of the action (i.e. negative). Global conservation of action then requires the reflected wave to have greater positive action than that of the incident wave implying amplification of the wave on that side of corotation upon reflection. If a wave is trapped between two corotation resonances or a corotation resonance and solid wall, this amplification mechanism, known as a corotation amplifier (Mark, 1976; Goldreich & Tremaine, 1978), ultimately results in instability.

An important property of the sonic instability is that it operates regardless of the density contrast between the star and the disk. Belyaev & Rafikov (2012) have investigated the sonic instability in the presence of a density discontinuity for a piecewise linear shear profile. They found that the growth rate for the sonic instability was almost independent of the density contrast across the discontinuity. Indeed, even in the case when the shear flow occured over a plane reflecting wall, which can be thought of as the limit of infinite density contrast, the growth rate was comparable to the case of no density contrast at all. Although Belyaev & Rafikov (2012) did not extensively treat gravity in their analytic analysis, we do include it in our simulations.

The signature of the sonic instability during the linear stage of growth is the presence of sound waves that are emitted from the shear layer. In our initial setup, the region that has the greatest shear is the interface, and Fig. 4.1 shows the radial velocity, v_{ϖ}, at $t = 6$ for simulation 2D12b. One can compare this with Fig. 5a of Belyaev & Rafikov (2012) (Chapter2), which shows the linear stage of the sonic instability in a uniform density medium for a shear layer with a piecewise linear velocity profile[1]. The similarities between the two figures confirm that our initial setup is unstable to the sonic instability. In particular, a critical layer where the pattern speed of the mode matches the azimuthal speed of the flow and the perturbation undergoes a phase shift in the azimuthal direction can be seen in Figure 4.1 close to the top of the interface region, at $\varpi \approx 1.005$. Such a critical layer is a clear signature of sonic instability and is necessary for them to operate. We note that the sound waves emitted from the interface appear to vanish in Fig. 4.1 as they propagate inwards. This is due to the exponentially rising density towards the interior of the star, which causes their amplitude to decay as $\Sigma^{-1/2}$. On the contrary, there is no stratification in Fig. 5a of Belyaev & Rafikov (2012) (Chapter 2) so sound waves propagating away from the shear layer do not diminish as quickly. However there is still some reduction in amplitude due to the fact that sound waves emitted at later times have a larger amplitude than sound waves emitted at earlier times, due to the presence of an instability (see §4.2 of Belyaev & Rafikov (2012)).

Belyaev & Rafikov (2012) have also shown that a high numerical resolution, of order several hundred cells across the shear layer for $M = 10$, is necessary during the initial stages of evolution to correctly capture the linear growth rate of the sonic instability. Because it would be prohibitive to use such a high resolution in our simulations (we use ~ 30 cells across the interface), we do not attempt to accurately resolve the growth rate of the sonic instabilities during the linear regime. Despite this, we show in §5 that simulations with different numerical resolutions converge at late times, so the resolution does not affect the long term evolution of the BL. Moreover, using a lower resolution underestimates the growth rate, so going to higher resolution would simply make the initial instabilities proceed faster, rather than stabilizing the instability.

[1]Fig. 5a of Belyaev & Rafikov (2012) (Chapter 2) is rotated by 90 degrees relative to Figure 4.1.

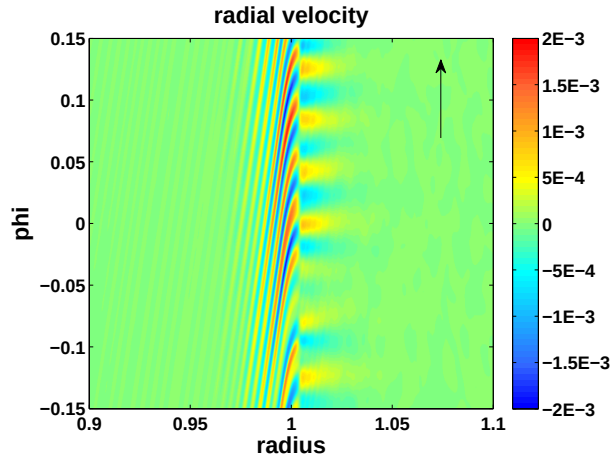


Figure 4.1: a) $\varpi - \phi$ plot of the radial velocity at $t = 6$ for simulation 2D12b ($M = 12$) in the vicinity of the interface, showing the development of sonic instability. Sound waves propagating in the flow both into the star (for $\varpi < 1$) and into the disk (for $\varpi > 1$) are clearly visible. The black arrow shows the direction of the unperturbed flow.

3 Acoustic Modes

After the sonic instabilities saturate, a quasi-steady state is estabilished. In this quasi-steady state, the boundary layer is deformed as shown by the curved streamlines in Fig. 4.2, which is an image of the radial velocity v_ϖ for simulation 2D6d. Since the flow is supersonic over the surface of the star, oblique shocks are launched into the disk. Additionally, sound waves are launched into the star away from the BL and diminish in amplitude according to $\delta\Sigma/\Sigma \propto \Sigma^{-1/2}$ to conserve energy and angular momentum.

The whole pattern of shocks (in the disk) and sound waves (in the star) rotates in a prograde fashion with a pattern speed $0 < \Omega_P < 1$. This pattern is what we refer to as an "acoustic mode", and we now describe some gross morphological properties of acoustic modes.

As we show in Chapter 5, there are actually three distinct wave branches of acoustic mode for the isothermal BL. Each of these wavebranches contains a corotation resonance in the BL, by virtue of the fact that $0 < \Omega_P < 1$. Moreover, each of these wavebranches also contains an evanescent region in the disk, inside of which there exists another corotation radius (in addition to the one within the BL). If the evanescent region in the disk is sufficiently well-separated from the BL, then outgoing shocks undergo reflection within the disk.

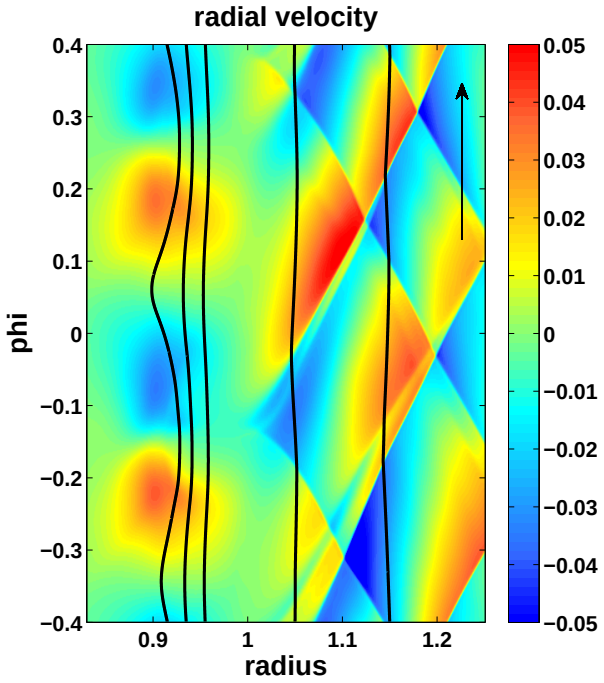


Figure 4.2: $r-\phi$ plot of the radial velocity v_ϖ in the vicinity of the BL at $t = 298$ for simulation 2D6d ($M = 6$). The general sense of the flow is from bottom to top, and the black lines are streamlines which trace the deformation of the interface. The phase shift at the critical layer around $\varpi \approx 1$ is clearly visible as are the weak shocks in the disk.

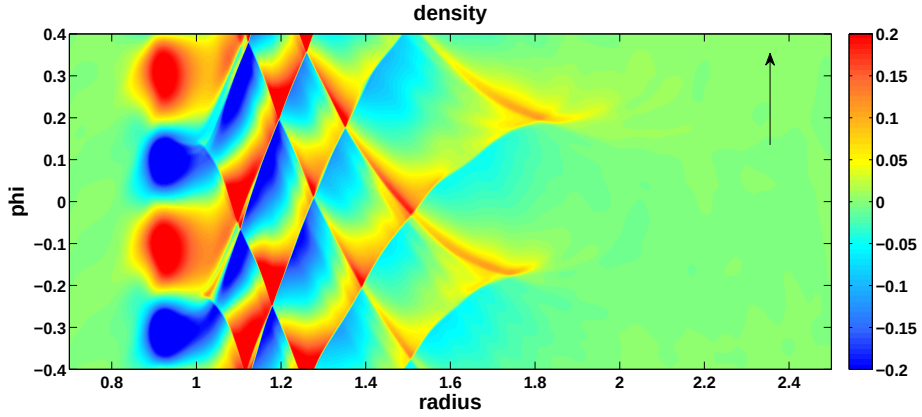
Fig. 4.3 shows images of $\delta\Sigma/\Sigma_0$, where Σ_0 is the azimuthally-averaged density, and v_ϖ within the disk for one particular type of acoustic mode (lower branch). The acoustic mode depicted in Fig. 4.3 has a pattern speed of $\Omega_P = .335$. The solid vertical line in the figure depicts the location of the corotation radius

$$\varpi_{CR} = \Omega_P^{-2/3}, \tag{4.1}$$

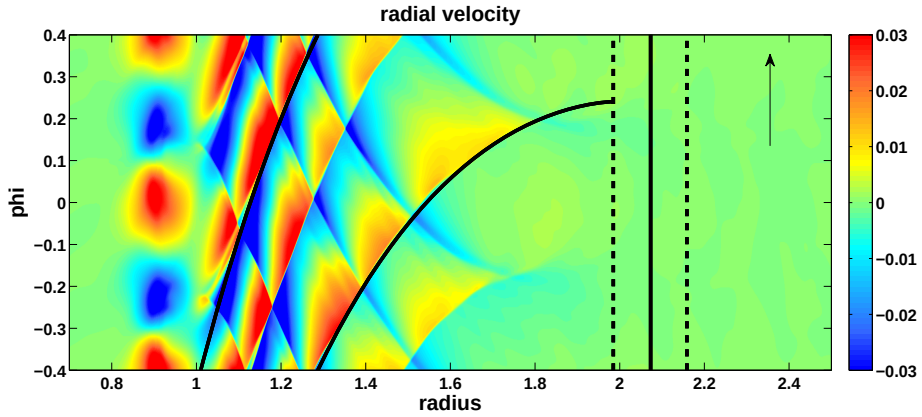
and the dashed lines depict the locations of the Lindblad radii

$$\varpi_{LR} = \left(\frac{m}{m \pm 1}\Omega_P\right)^{-2/3}. \tag{4.2}$$

These formulas assume a Keplerian rotation profile, which is a good approximation away from the BL. The evanescent region for the mode in Fig. 4.3 is contained between the two Lindblad radii, under the WKB approximation (Goldreich & Tremaine, 1978).



(a)



(b)

Figure 4.3: (a) Plot of the relative density perturbation $\delta\Sigma/\Sigma_0$ at $t = 284$ for simulation 2D6d. The density is enhanced at shock crossings, but otherwise $\delta\Sigma/\Sigma_0 \sim 0.1 - 0.2$. (b) Plot of radial velocity v_ϖ at $t = 284$ for simulation 2D6d ($M = 6$). The black curve shows the analytic WKB solution for the shock front (see Chapter 5). The dashed vertical lines show the locations of the inner and outer Lindblad resonances ($\varpi = 1.99$ and 2.16, respectively), and the solid vertical line shows the corotation radius ($\varpi = 2.07$). The black arrows show the direction of the unperturbed flow.

The explanation for the pattern of intersecting shocks in Fig. 4.3 is reflection of outward traveling shocks from the the evanescent region. The inner Lindblad radius gives a good description of the radius at which the shocks are reflected, because the shocks are relatively weak

($\delta\Sigma/\Sigma_0 \sim .2$ in Fig. 4.3a) and so their properties are well-described by linear theory (Goldreich & Tremaine, 1978). Futher proof of the applicability of linear theory is given by the agreement between the black curve in Fig. 4.3b, which shows the analytical result for the shape of the shockfront from WKB theory and the actual shape of the shock front in the simulation.

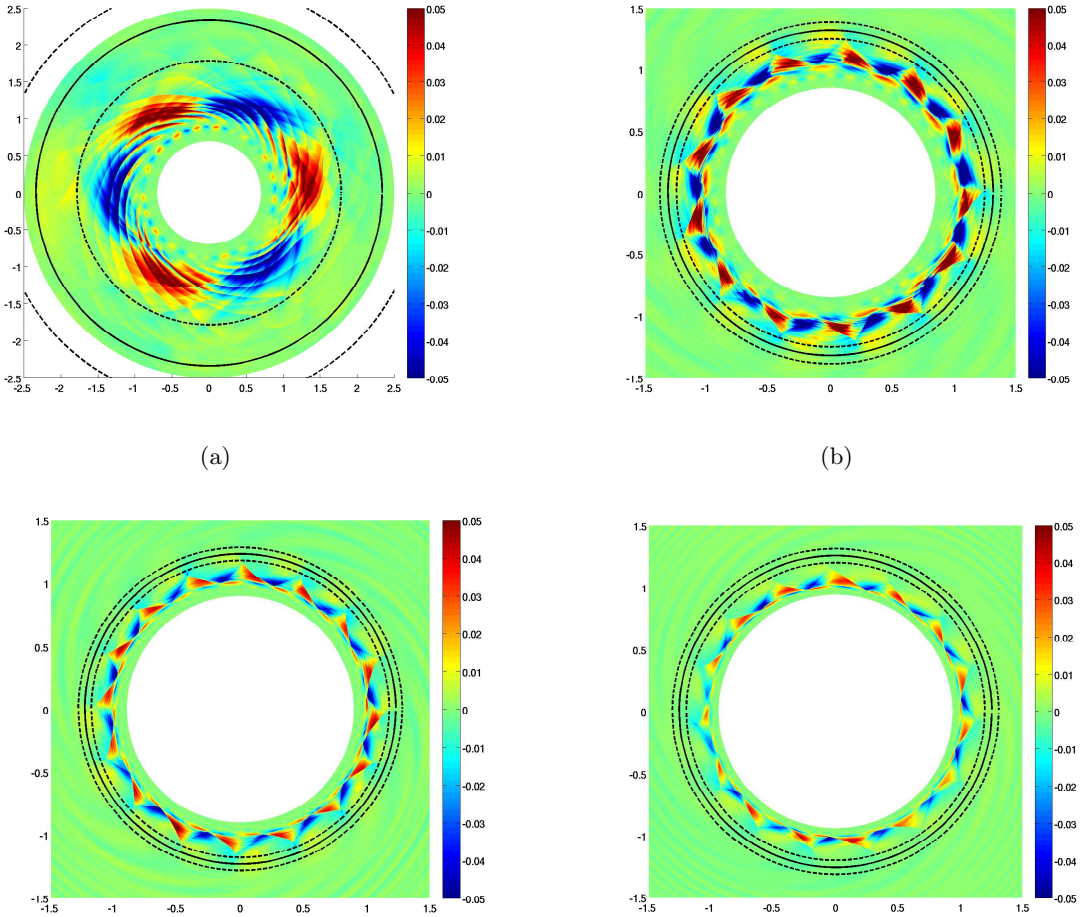
Figure 4.4 shows images of v_ϖ (for the lower branch) for a variety of different Mach numbers. As before, the solid lines represent corotation radii, and the dashed lines represent Lindblad radii. The presence of acoustic modes across a range of Mach numbers shows that they are a robust phenomenon for the isothermal BL. We will have more to say about them in Chapter 5.

4 Temporal Evolution of the BL

We now paint a picture of the typical evolution of one of our hydro simulations. Due to the large shear in the interfacial region (§2.4), our initial rotation profile is unstable to the sonic instability (Glatzel, 1988; Belyaev & Rafikov, 2012; Belyaev et al., 2012). Consequently, acoustic modes are excited starting from the initial seed perturbations to the radial velocity (§2.8). The amplitude of these acoustic modes increases with time until $t \sim 60$ when the sonic instability saturates.

Around $t \sim 60$, there is typically a single mode present with a well-defined azimuthal pattern number, m, and pattern speed, Ω_P. This mode (upper mode, see Chapter 5) has $\Omega_P \sim 1 - s$ and radiates angular momentum in the form of sound waves away from the vicinity of the interfacial region into both the disk and the star. This radiation of angular momentum causes the interfacial region to widen and drives accretion of material from the innermost portion of the disk onto the star.

Fig. 4.5a shows a radius-time image of Σ_0 for simulation 3D9a. From the image, it is clear that a gap in the density is opened up in the innermost portion of the disk starting at around $t \sim 60$, which is around the same time when the sonic instability saturates. This modifies the rotational profile and Figs. 4.6a & b show plots of Σ_0 and $\varpi\Omega$, respectively, at various times for simulation 3D9a. It is evident that as the inner region of the disk is depleted of mass, the shear in the BL diminishes, and the maximum rotation velocity in the simulation domain drops. However, the rotation profile is actually slightly super-Keplerian in the region of the disk where the density

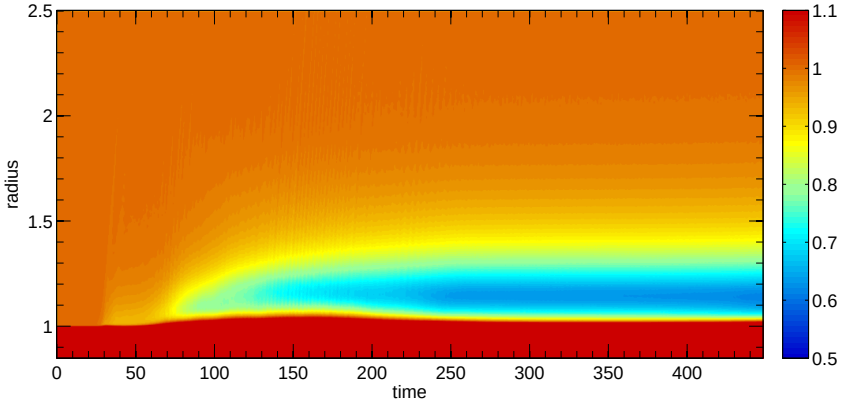


(a) (b)

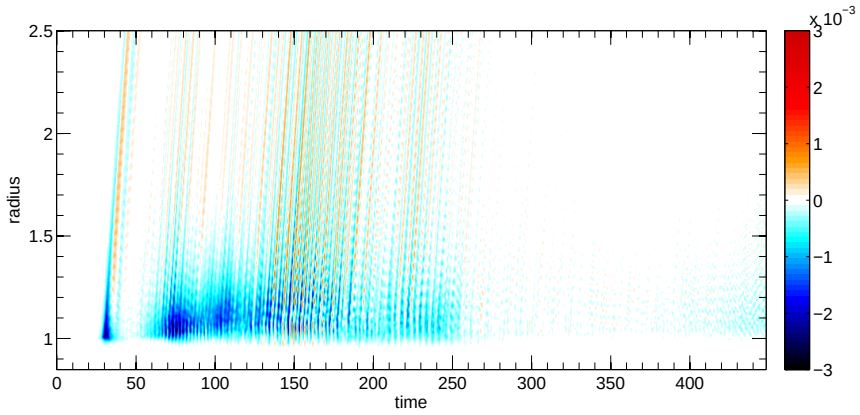
(c) (d)

Figure 4.4: Images of the radial velocity for simulations 2D6a (panel a), 2D9a (panel b), 2D12a (panel c), and 2D15a (panel d), which have $M = 6, 9, 12$, and 15 respectively. The view has been zoomed in, in panels (b), (c), and (d) to give a better view of the modal structure in the vicinity of the BL. The m-numbers of the dominant acoustic modes for panels (a)-(d) are $m = 21$, 13, 16, and 15 respectively, although there is also an $m = 3$ periodicity in panel a, which suggests a superposition of dominant modes. Solid and dashed circles show the locations of the corotation and the inner and outer Lindblad resonances in the disk, which are calculated using the pattern speed of the mode measured in simulations.

rises from its value in the gap to its value in the outer disk ($\rho \approx 1$). In this region, $d\rho/d\varpi > 0$, implying an inwardly directed force from the pressure gradient, which is balanced by a rotational velocity that is faster than Keplerian.



(a)



(b)

Figure 4.5: Panels a & b show radius-time plots of Σ_0 and $\langle v_\varpi \rangle$, respectively for simulation 3D9a. The angle brackets denote a density-weighted azimuthal average (see Chapter 5).

Fig. 4.5b shows a radius-time image of the radial velocity, and it is clear that there is radial infall in the inner region of the disk, which occurs during the same time as depletion of the inner disk in Fig. 4.5a. The striations in Fig. 4.5b correspond to density waves that emanate away from the boundary layer, and their "slant" indicates that by causality they are indeed emitted from the vicinity of the BL.

It is evident from Fig. 4.5b that after a period of vigorous infall, the radial velocity and hence the accretion rate in the inner disk drops off around $t \sim 250$. This can be attributed to a reduction in the amplitude of waves emitted from the BL, so the rate of angular momentum transport is diminished. Moreover, the pattern speed drops significantly during this period, and it

is possible for trapped shocks to develop between the BL and an evanescent region in the disk (§3). The reason for this shift in behavior seems to be related to the angular momentum budget of the inner disk, and we postpone a more detailed discussion until Chapter 5, in which we discuss angular momentum transport in depth.

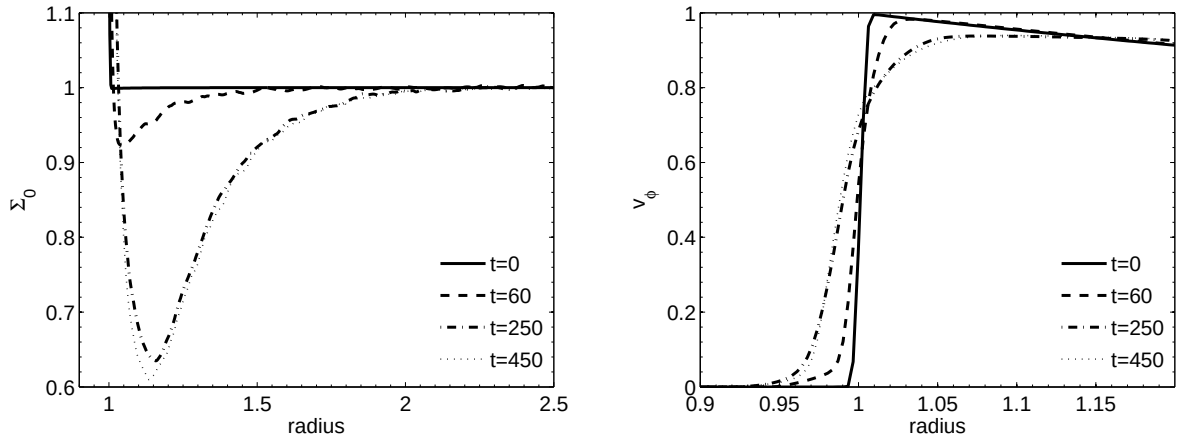


Figure 4.6: Panels a & b show Σ_0 (density averaged both azimuthally and vertically) and $\varpi\Omega$ vs. time respectively for simulation 3D9a.

5 Width of the BL as a Function of Mach Number

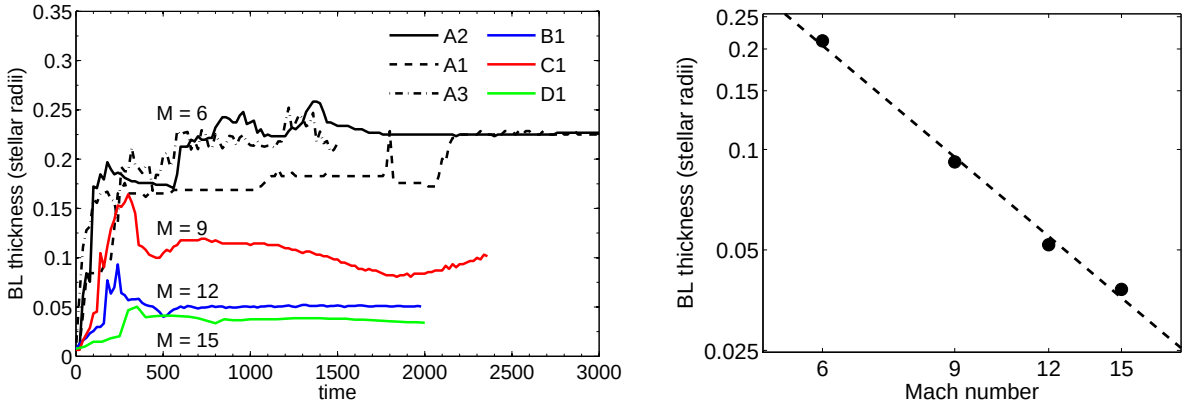
We now present a study of the width of the BL as a function of Mach number for our 2D hydro simulations. The reader will recall from Chapter 3 that the Mach number is the sole dimensionless physical parameter in the case of an unmagnetized isothermal BL.

For simplicity, we define the BL to be the region in which

$$0.1 < \langle v_\phi(\varpi)\rangle / v_K(\varpi) < 0.9, \tag{4.3}$$

where $v_K(R_\star) = 1$ is the Keplerian velocity at the surface of the star and $\langle v_\phi(\varpi)\rangle$ is the density-weighted average of the azimuthal velocity.

We plot the thickness of the BL defined by equation (4.3) as a function of time in Figure 4.7a for runs 2D6e, 2D6d, 2D6f, 2D9d, 2D12b, and 2D15b. The thickness of the BL greatly increases in the beginning of the simulation due to the sonic instabilities. It then stays approximately constant with sharp jumps in some simulations such as 2D6e, 2D6d, and 2D6f. The fact that runs 2D6e, 2D6d, and 2D6f yield almost the same BL width at late times suggests that the simulations are converged, since these three runs differ only in their resolution.



(a) (b)

Figure 4.7: a) Width of the BL as defined in equation (4.7) as a function of time. Runs 2D6e, 2D6d, and 2D6f all have $M = 6$, run 2D9d has $M = 9$, run 2D12b has $M = 12$, and run 2D15b has $M = 15$. This panel is taken from Belyaev et al. (2012), which uses a different numbering for simulations. The conversion from the numbering used in the legend of the panel to the numbering used in the thesis is A1 $\rightarrow$ 2D6e, A2 $\rightarrow$ 2D6d, A3 $\rightarrow$ 2D6f, B1 $\rightarrow$ 2D9d, C1 $\rightarrow$ 2D12b, D1 $\rightarrow$ 2D15b b) Boundary layer width at $t = 1500$ as a function of the Mach number in our simulations. The dashed line indicates the best fit line through the points and has a slope of -1.9. This is close -2, which is the expected value of the power law index for the scaling of the boundary layer width with the Mach number.

It is clear from Figure 4.7a that the boundary layer becomes thinner with increasing Mach number. In Figure 4.7b, we plot the width of the boundary layer at $t = 1500$ as a function of the Mach number for 2D simulations on a log-log plot. The data point for $M = 6$ is a simple average of simulations 2D6e, 2D6d, 2D6f and the points for $M = 9$, $M = 12$, and $M = 15$ are from simulations 2D9d, 2D12b, and 2D15b respectively. The dashed line shows the best least squares fit to the data, and from its slope we deduce that $h_{BL} \propto M^{-1.9}$, where h_{BL} is the width of the BL at $t = 1500$. Since the scale height goes as $h_s = M^{-2}$ ($h_s = g/s^2$ in the isothermal case), this

indicates that the deceleration of the flow in the BL occurs over an approximately fixed number of scale heights in the isothermal case ($\sim 6-7$), regardless of the Mach number.

Our 3D simulations are consistent with a BL that is $\sim 6-7$ scale heights in width, but there is more scatter among the 3D simulations. Fig. 4.8 shows the width of the BL (in scale heights) as a function of time for both our 3D unstratified simulations that span the full 2π in azimuthal angle (solid lines) and the 3D stratified simulations (dashed lines). The color denotes Mach number with black corresponding to $M = 9$ and red corresponding to $M = 6$.

One possible reason for the larger amount of scatter in the 3D case is that the 2D simulations were run for a longer time, and the measurement of BL width was performed at a later time in the runs. Thus, the BL in our 3D simulations may still be settling down to its steady state width.

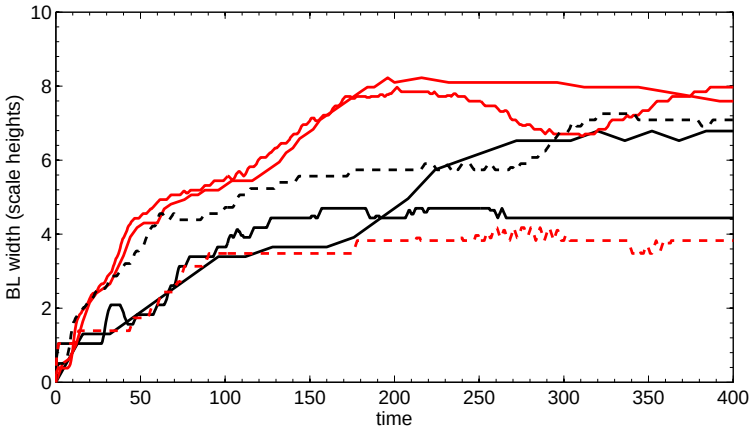
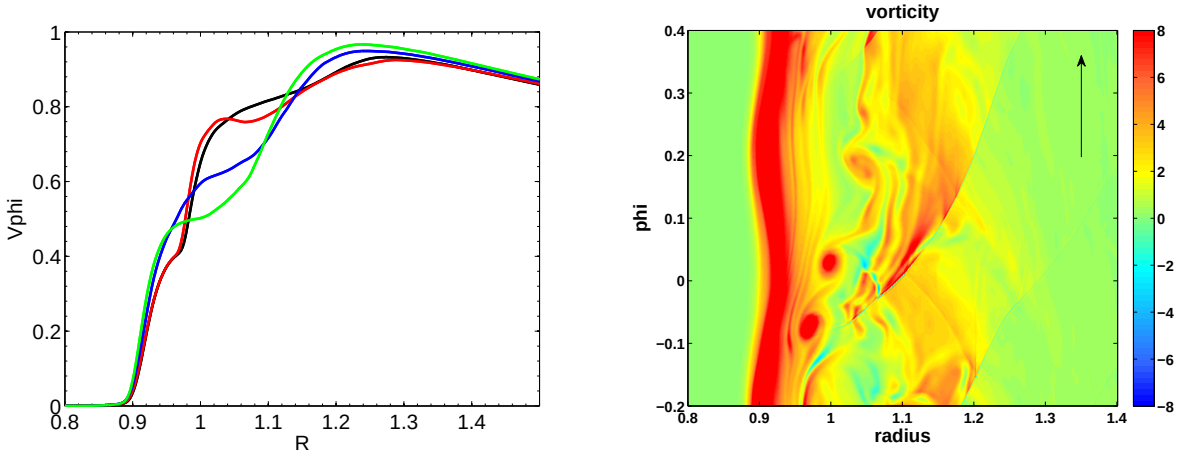


Figure 4.8: Width of the BL in scale heights as a function of time. The dashed curves correspond to 3D stratified simulations and the solid lines to 3D unstratified simulations spanning the full 2π in azimuthal angle. The color differentiates Mach number with $M = 9$ in black and $M = 6$ in red.

5.1 Secondary KH Instabilities

From Figure 4.7a it is clear that some of our simulations (2D6e,2D6d,2D6f) are characterized by sharp jumps in the width of the BL. For simulation 2D6d, these jumps are centered on $t = 150$, $t = 600$, $t = 1000$, and $t = 1400$ and coincide with large values of the mass accretion rate in the BL.

We can understand the reason for these bouts of high accretion that correspond to these sharp jumps in BL width by looking $\langle v_\phi \rangle$ as a function of time near one of the jumps. Fig. 4.9a shows $\langle v_\phi \rangle$ at $t = 800$, 900, 1000, and 1100 for simulation 2D6d. These times span the duration of one of the jumps in BL width for simulation 2D6d in Fig. 4.7b. We see that between $t = 800$ and $t = 900$, a bump develops in the azimuthal velocity profile. This leads to a rapid rearrangement of the velocity profile between $t = 800$ and $t = 900$, which erases the bump, and by $t = 1100$ the rearrangement of the velocity profile is complete.



(a) (b)

Figure 4.9: a) Profiles of mean azimuthal velocity $\langle v_\phi \rangle$ at $t = 800$ (black), $t = 900$ (red), $t = 1000$ (blue), and $t = 1100$ (green) for run 2D6d. b) Image of the vorticity, $\boldsymbol{\nabla} \times \boldsymbol{v}$, in high accretion state at $t = 1000$ for simulation 2D6d ($M = 6$). The cat's eyes are the red oval structures with wispy arms around $\varpi = 1$ and are indicative of KH instability.

The mechanism for generating the bump is not known, but once the bump has been created, the mechanism for erasing it is the KH instability. KH instabilities can operate near inflection points in the velocity profile. At an inflection point, the radial derivative of the vorticity is constant, making it permissible to mix neighboring fluid elements and extract energy from the shear in the flow. In the vicinity of the bump, the vorticity profile is very flat, which allows the KH instability to operate there. Fig. 4.9b shows a snapshot of the vorticity ($\boldsymbol{\nabla} \times \boldsymbol{v}$) in the vicinity of the BL at $t = 1000$ for simulation 2D6d. One can see that around $\varpi \sim 1$, the vorticity is concentrated into structures that resemble the cats eye pattern associated with KH instabilities.

We mention that this phenomenon of secondary KH instability is only observed in 2D simulations, and we find that the velocity profile does not develop bumps in 3D simulations.

Bibliography

Armitage, P. J. 2002, MNRAS, 330, 895

Balbus, S. A. & Hawley, J. F. 1991, ApJ, 376, 214

Belyaev, M. A. & Rafikov, R. R. 2012, ApJ, 752, 115

Belyaev, M. A., Rafikov, R. R., & Stone, J. M. 2012, ApJ, 760, 22

Chandrasekhar, S. 1960, Proceedings of the National Academy of Science, 46, 253

Fujimoto, M. Y. 1987, A&A, 176, 53

Glatzel, W. 1988, MNRAS, 231, 795

Goldreich, P. & Tremaine, S. 1978, ApJ, 222, 850

Hawley, J. F. & Balbus, S. A. 1991, ApJ, 376, 223

Inogamov, N. A. & Sunyaev, R. A. 1999, Astronomy Letters, 25, 269

Inogamov, N. A. & Sunyaev, R. A. 2010, Astronomy Letters, 36, 848

Kippenhahn, R. & Thomas, H.-C. 1978, A&A, 63, 265

Lesur, G. & Longaretti, P.-Y. 2005, A&A, 444, 25

Mark, J. W. K. 1976, ApJ, 205, 363

Narayan, R., Goldreich, P., & Goodman, J. 1987, MNRAS, 228, 1

Papaloizou, J. C. B. & Pringle, J. E. 1984, MNRAS, 208, 721

Patterson, J. 1984, ApJS, 54, 443

Pessah, M. E. & Chan, C.-k. 2012, ApJ, 751, 48

Piro, A. L. & Bildsten, L. 2004, ApJ, 610, 977

Spruit, H. C. 1999, A&A, 349, 189

Steinacker, A. & Papaloizou, J. C. B. 2002, ApJ, 571, 413

Tayler, R. J. 1973, MNRAS, 161, 365

Velikhov, E. P. 1959, J. Exptl. Theoret. Phys., 36, 1398

Warner, B. 2004, PASP, 116, 115

Chapter 5

Angular Momentum Transport: Hydro Simulations

Abstract

The nature of angular momentum transport in the boundary layers of accretion disks has been one of the central and long-standing issues of accretion disk theory. In this work we demonstrate that acoustic waves excited by supersonic shear in the boundary layer serve as an efficient mechanism of mass, momentum and energy transport at the interface between the disk and the accreting object. We develop the theory of angular momentum transport by acoustic modes in the boundary layer, and support our findings with 3D hydrodynamical simulations, using an isothermal equation of state. Our first major result is the identification of three types of global modes in the boundary layer. We derive dispersion relations for each of these modes that accurately capture the pattern speeds observed in simulations to within a few percent. Second, we show that angular momentum transport in the boundary layer is intrinsically nonlocal, and is driven by radiation of angular momentum away from the boundary layer into both the star and the disk. The picture of angular momentum transport in the boundary layer by waves that can travel large distances before dissipating and redistributing angular momentum and energy to the disk and star is incompatible with the conventional notion of local transport by turbulent stresses. Our results have important implications for semianalytical models that describe the spectral emission from boundary layers.

1 Introduction

Understanding the structure and dynamics of the boundary layer (BL) is one of the outstanding theoretical problems in accretion disk theory. We define the BL as the thin transitional region where the disk attaches to the star, gas slows down from the orbital to the stellar rotation velocity, and $d\Omega/d\varpi > 0$ (Ω is the angular velocity of the fluid and ϖ is the cylindrical radius). In this chapter we do not differentiate between the different types of accreting objects (a neutron star, a white dwarf, or a young star), as long as they have a surface. This assumes that the compact object has a weak enough magnetic field that the disk extends all the way down to the surface of the star without being disrupted and channeled to the magnetic poles. The criteria for this to occur is that the magnetic pressure should be less than the ram pressure of the gas at the surface of the star (Ghosh & Lamb, 1978). The critical value of the magnetic field at the surface of the central object for magnetic disruption is given by

$$B_{*,\mathrm{crit}} = 5 \times 10^4 \left(\frac{\beta}{.5}\right)^{-7/4} \left(\frac{M_*}{.6M_\odot}\right)^{1/4} \left(\frac{\dot{M}}{10^{-8}M_\odot \text{ yr}^{-1}}\right)^{1/2} \left(\frac{R_*}{9 \times 10^3 \text{ km}}\right)^{-5/4} \text{G}. \qquad (5.1)$$

Here, we have used parameters for the mass and radius that are typical for CVs in outburst (Bergeron et al., 1992; Hachisu, 1986; Patterson, 1984). The parameter β is a dimensionless factor of order unity that depends on the model adopted for the disruption of the disk by the stellar magnetic field (Ghosh & Lamb, 1978).

Within the BL, material slows down from the Keplerian rotational velocity to the rotational velocity inside the star. Since the radial width of the BL is significantly less than that of the star this implies that the BL is a region of intense shear. In fact, the rate of energy dissipation inside the BL can be as high as for the rest of the disk combined (Kluźniak, 1987), resulting in intense heating of the gas.

An open question in BL theory is the mechanism of angular momentum transport. Due to a rising rotation profile, the BL is linearly stable to the magnetorotational instability (MRI) which is responsible for accretion in the disk (Balbus & Hawley, 1991; Hawley & Balbus, 1991). Indeed, Pessah & Chan (2012) has shown that if $d\Omega/d\varpi > 0$, then the stresses due to a sheared magnetic

field are inefficient at transporting angular momentum and oscillate about zero. Thus, some other mechanism must be responsible for angular momentum transport within the BL.

Of course linear stability does not imply a laminar flow. Turbulence, once generated by some nonlinear mechanism, can persist without decaying in certain classes of rotating, linearly stable hydrodynamical flows (Lesur & Longaretti, 2005). Such turbulence provides one possible mechanism of angular momentum transport in the BL. However, no mechanism of turbulent anomalous viscosity has never been shown to operate in the BL, and we show in this chapter that the dominant angular momentum transport mechanism in the BL is radiation of acoustic waves away from the BL into the disk and star. These acoustic waves arise due to sonic instabilities in the BL, which are a type of shear instability akin to the Papaloizou-Pringle instability (Papaloizou & Pringle, 1987; Narayan et al., 1987) that operate in supersonic flows (Glatzel, 1988; Belyaev & Rafikov, 2012).

The focus of the present chapter will be the detailed description of acoustic modes in the BL and their relation to angular momentum transport and mass. We will study these modes both theoretically by solving for their dispersion relation and computationally with 2D, 3D unstratified, and 3D stratified hydro simulations of the BL with an isothermal equation of state.

Understanding the physics of acoustic modes is an important step towards understanding the temporal variability in the BL and constructing semianalytic models of BL spectra. Currently, virtually all semianalytic models of the BL assume that angular momentum transport is mediated by local turbulent stresses and adopt an effective α-prescription based on Navier-Stokes viscosity (Popham & Narayan, 1995; Inogamov & Sunyaev, 1999; Piro & Bildsten, 2004b). We argue, however, that angular momentum transport in the BL is driven by density waves, not turbulence. These waves can potentially travel long distances before dissipating, meaning that angular momentum and energy transport is inherently nonlocal and cannot be well-described by any model based on a local anomalous viscosity.

The chapter is organized into four parts. In the first part (§3), we derive the dispersion relation for the acoustic modes introduced in Chapter 4. We show that the acoustic modes observed in simulations of the isothermal BL have a dispersion relation that is well-described by a

few simple modifications to the dispersion relation of the supersonic vortex sheet (Miles, 1958; Gerwin, 1968; Belyaev & Rafikov, 2012). In second part (§4), we show that acoustic radiation from $k_z = 0$ acoustic modes entirely accounts for the angular momentum transport in our simulations and discuss the implications of this result for semi-analytic models of the BL. In the third part (§5), we discuss the effects of disk stratification in the z-direction on acoustic modes and angular momentum transport, and we find that stratification makes no fundamental difference to our results. Finally, in the fourth part we comment on the incompatibility of nonlocal transport of angular momentum by waves with an anomalous viscosity model, such as an α-prescription. This has important implications for semianalytic models, which tie theory to observable quantities.

2 Notation for Measured Quantities

We begin by introducing some notation regarding how simulation quantities are measured. For 3D simulations, we define a z-averaged density as

$$\Sigma(\varpi, \phi) \equiv \frac{1}{\Delta z} \int dz \rho, \tag{5.2}$$

where the integral is performed over the entire z-extent of the domain, and Δz is the thickness of the simulation domain in the z direction. The ϕ-averaged density and perturbations to the density are then defined as

$$\Sigma_0(\varpi) \equiv \frac{1}{\Delta\phi} \int d\phi \Sigma \tag{5.3}$$

$$\delta\Sigma(\varpi, \phi) \equiv \Sigma - \Sigma_0 \tag{5.4}$$

$$\delta\rho(\varpi, \phi, z) \equiv \rho - \Sigma_0. \tag{5.5}$$

Next, we define the density-weighted averaging operator represented by a set of triangle brackets as

$$\langle f \rangle \equiv \frac{1}{\Delta z \Delta \phi \Sigma_0} \int dz d\phi \rho f. \tag{5.6}$$

In 2D, the density-weighted average is the same, except that there is no integral over the z-dimension. Sometimes, we perform density-weighted averages in only the z-direction so we also define the operation

$$\langle f \rangle_z \equiv \frac{1}{\Delta z \Sigma} \int dz \rho f. \tag{5.7}$$

Density-weighted averages are the proper way of measuring simulation quantities, since mathematically exact analogs to the fluid equations can be formulated in terms of them (Balbus & Papaloizou, 1999). For instance, one-dimensional forms for the continuity and angular momentum transport equations are

$$\frac{\partial \Sigma_0}{\partial t} + \frac{1}{\varpi} \frac{\partial}{\partial \varpi} \left(\varpi \Sigma_0 \langle v_\varpi \rangle \right) = 0 \tag{5.8}$$

$$\frac{\partial}{\partial t} \left(\varpi^2 \Sigma_0 \Omega \right) + \frac{1}{\varpi} \frac{\partial}{\partial \varpi} \left(\varpi^2 \Sigma_0 \langle v_\phi v_\varpi \rangle \right) = 0, \tag{5.9}$$

where we have assumed molecular viscosity is negligible in equation (5.9), and we have defined the angular velocity as

$$\Omega \equiv \frac{\langle v_\phi \rangle}{\varpi} \tag{5.10}$$

Equation (5.9) expresses angular momentum conservation and the second term is the divergence of the angular momentum flux,

$$F_L \equiv \varpi \Sigma_0 \langle v_\phi v_\varpi \rangle. \tag{5.11}$$

Throughout the paper we shall also refer to the angular momentum current, which is defined as

$$C_L \equiv 2\pi\varpi F_L. \tag{5.12}$$

The angular momentum current has the intuitive interpretation that the rate of change of angular momentum in an annular region is the difference in angular momentum current between the two edges of the annulus.

The angular momentum flux, F_L, can be decomposed into two parts (Balbus & Papaloizou, 1999), which are the advective and stress terms

$$\begin{aligned} F_L &= F_A + F_S & (5.13)\\ F_A &\equiv \varpi^2\Sigma_0\Omega\langle v_\varpi\rangle & (5.14)\\ F_S &\equiv \varpi\Sigma_0\langle\delta v_\phi v_\varpi\rangle & (5.15)\\ \delta v_\phi &\equiv v_\phi - \varpi\Omega. & (5.16) \end{aligned}$$

These definitions are trivially generalized to 3D case by replacing Σ_0 with ρ_0.

The advective term corresponds to angular momentum transport by the bulk motion of the fluid and can be written in terms of the mass accretion rate, $\dot{M}$, as

$$\begin{aligned} F_A &= -\frac{\dot{M}}{2\pi\varpi}\varpi^2\Omega & (5.17)\\ \dot{M} &\equiv -2\pi\varpi\Sigma_0\langle v_\varpi\rangle & (5.18) \end{aligned}$$

The stress term, on the other hand, corresponds to angular momentum transport by turbulence and/or waves. In the standard α-viscosity treatment, the stress term is alternately written as

(Shakura & Sunyaev, 1973; Popham & Narayan, 1995; Balbus & Papaloizou, 1999)

$$F_S = \varpi\alpha\Sigma_0 s^2 \tag{5.19}$$

$$F_S = \varpi\alpha_\nu\Sigma_0 s^2\left(-\frac{d\ln\Omega}{d\ln\varpi}\right) \tag{5.20}$$

$$F_S = \varpi\alpha_{\rm PN}\Sigma_0 s^2\left(-\frac{d\ln\Omega}{d\ln\varpi}\right)\left[1+\left(\frac{s}{\Omega}\frac{d\ln P}{d\varpi}\right)^2\right]^{-1/2}. \tag{5.21}$$

For any of these (or any other) α viscosity model to provide a good description of the BL, α should be approximately independent of ϖ. However, all conventional α viscosity models are based on the notion of local turbulent stresses. As we discuss in §4, angular momentum transport is facilitated by waves not turbulence in our BL simulations, and so is not well described by any local model.

3 Boundary Layer Modes

We find in our simulations that the shear in the boundary layer can generate three distinct types of $k_z = 0$ acoustic modes. These three types of modes are directly related to the upper, lower, and middle branches discussed in Belyaev & Rafikov (2012) for a 2D plane parallel vortex sheet in the supersonic regime. However, the dispersion relation for these modes is modified in a simple way by the radial stratification in the star and the Coriolis force in the disk. To begin our discussion, we first review the dispersion relation of the 2D plane parallel vortex sheet.

3.1 Plane Parallel Vortex Sheet

In the absence of stratification or Coriolis force, the dispersion relation for a 2D vortex sheet with velocity profile

$$V_y(x) = \begin{cases} V, & x > 0 \\ 0, & x < 0, \end{cases} \tag{5.22}$$

sound speed s_+ for $x > 0$, and sound speed s_- for $x < 0$ in the limit $V \gg s$ is given by (Belyaev & Rafikov, 2012)

$$\omega/|k_y| \approx \begin{cases} V - s_+, & \text{Upper branch} \\ V\left(\frac{s_+}{s_+ + s_-}\right), & \text{Middle branch} \\ s_-, & \text{Lower branch.} \end{cases} \tag{5.23}$$

Note that by pressure balance $\rho_+/\rho_- = (s_-/s_+)^2$, assuming γ is everywhere constant. All three branches in equation (5.23) are sonic in nature, with outgoing sound waves emitted from the vortex sheet at $x = 0$.

The upper and lower branches have the property that the sound waves emitted from the vortex sheet in the half-planes $x > 0$ and $x < 0$, respectively, propagate nearly parallel to the vortex sheet. In other words, $|k_y/k_x| \gg 1$ for the upper and lower branches in the half-planes $x > 0$ and $x < 0$ respectively. The middle branch has the property that $|k_y/k_x|$ is a constant on both sides of the vortex sheet. Thus, the wavefronts form the same angle with the vortex sheet in both the $x > 0$ and $x < 0$ half-planes. This is true even if the densities are different in the two half-planes. These sets of properties for the isothermal vortex sheet are instrumental in determining how the dispersion relations for each of the three wave branches are modified in going to the disk-star system.

Panels a-c of Fig. 5.1 are schematics, which depict the geometry of the wavefronts for δv_x, the perturbed velocity perpendicular to the vortex sheet, for each of the three branches. The arrows show the direction of the flow, and the solid vertical line is the vortex sheet at $x = 0$. At the vortex sheet, δv_x undergoes both a change in amplitude and a change in sign (see equation (36) of Belyaev & Rafikov (2012)). Thus, the wavefronts of δv_x appear shifted in phase by π across the vortex sheet.

3.2 Dispersion Relations for the Isothermal Boundary Layer

We now discuss how the dispersion relations for each of the wave branches in the isothermal vortex sheet given by equation (5.23) are modified in going to the disk-star system. As a result,

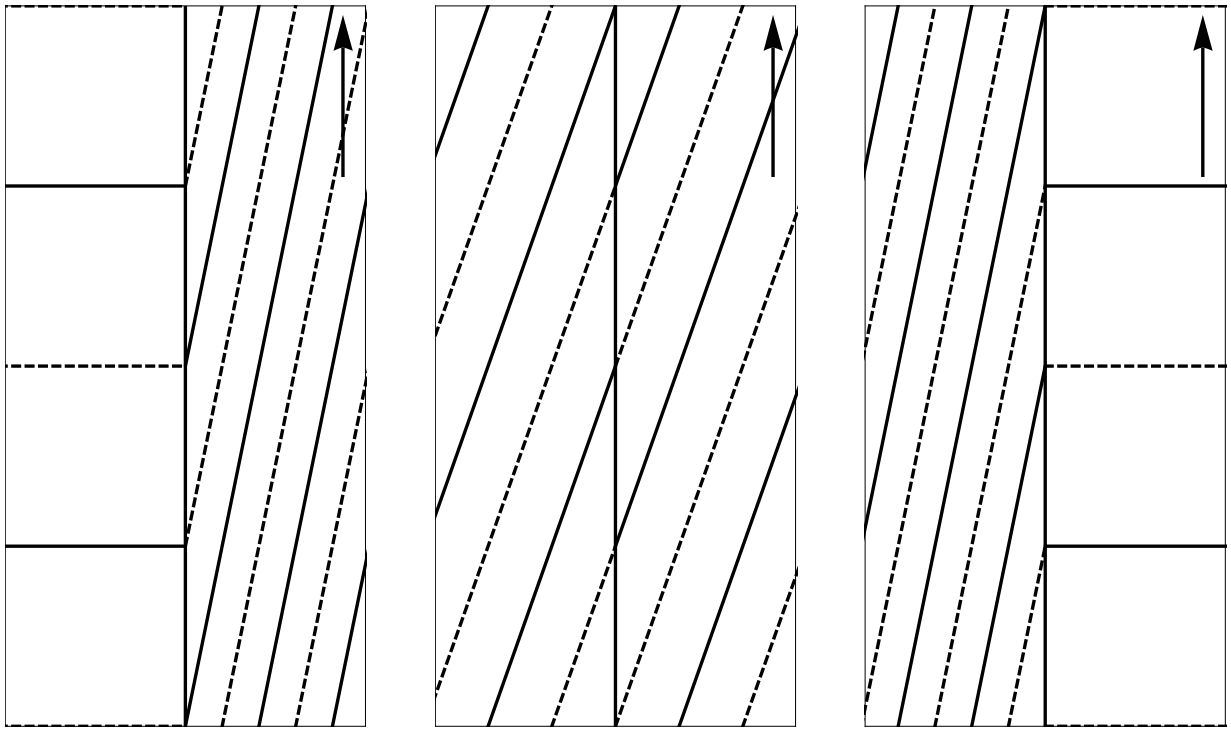


Figure 5.1: a) Wavefronts of δv_x for the lower wave for $M = 6$. The arrow depicts the direction of the flow in the $x > 0$ half-plane. The vortex sheet itself is depicted by the solid vertical line and is located at $x = 0$. The solid lines depict wave crests, and the dashed lines depict troughs. Notice that the perturbation to δv_x undergoes a change in sign (phase shift by π) at the vortex sheet. Panels b) and c) are the same as a), but for the middle and upper waves respectively.

we find accurate, though, heuristic dispersion relations for the generalization of these modes to the isothermal boundary layer studied in our simulations.

Upper Branch

As discussed in §3.1, the upper branch for the vortex sheet is characterized by a sound wave with phase speed $V - s_+$ in the half-plane $x > 0$, which propagates nearly parallel to the vortex sheet, i.e. $|k_y/k_x| \gg 1$.

In order to generalize this to the disk-star system, we postulate that in the disk-star system there is a branch characterized by a density wave in the disk that has $|k_\phi/k_\varpi| \gg 1$ at $\varpi = \varpi_\star$.

Here, and throughout the paper, we shall define $k_\phi \equiv m/\varpi$, where m is the azimuthal pattern number.

Since, $|k_\phi/k_\varpi| \gg 1$ in the disk near the BL, the wave fronts are very loosely wound, and we cannot apply the classical dispersion relation for a fluid disk in the tight-winding limit (Goldreich & Tremaine, 1978). However, it is straightforward to derive an approximate dispersion relation for a loosely wound density wave, if we additionally assume $m \gg 1$ (Appendix A). The result is

$$(\Omega - \Omega_P)^2 = \left(\frac{s}{\varpi}\right)^2 + \left(\frac{\kappa}{m}\right)^2. \tag{5.24}$$

Equation (5.24) generally has two solutions with one having $\Omega_P > \Omega$ and the other $\Omega_P < \Omega$. For the isothermal vortex sheet, it turned out that the physical solutions, which corresponded to outgoing waves had a phase velocity $\omega/k < V$ (Belyaev & Rafikov, 2012). By analogy, we take the solution to equation (5.24) having $\Omega_P < \Omega$ to be the physical one. In that case, taking $\varpi = \varpi_\star$, $V = \varpi_\star\Omega(\varpi_\star)$, and making the associations $\omega = m\Omega_P$, and $k_y = m/\varpi_\star$, we see that equation (5.24) is analogous to equation (5.23) for the upper branch of the vortex sheet, except for the additional term containing the epicyclic frequency, which is due to the Coriolis force.

We can generalize equation (5.24) to arbitrary values of k_ϖ by writing

$$m^2(\Omega - \Omega_P)^2 = s^2\left(k_\phi^2 + k_\varpi^2\right) + \kappa^2. \tag{5.25}$$

This approximate dispersion relation reduces to the one for tightly-wound waves in the limit $|k_\varpi/k_\phi| \gg 1$ (Goldreich & Tremaine, 1978) and to equation (5.24) in the limit $|k_\phi/k_\varpi| \gg 1$. Thus, it is accurate in both the tight-winding and loose-winding limits. The essential modification to the tightly-wound dispersion relation is the replacement of the radial wavenumber with the total wavenumber inside the braces in equation (5.25) i.e. $k_\varpi^2 \to k_\varpi^2 + k_\phi^2$.

An important feature of equation (5.25) is that it predicts an evanescent region in the disk directly adjacent to the BL. This can be deduced by noting that the left hand side of equation (5.25) vanishes when $\Omega = \Omega_P$, implying that k_ϖ is imaginary at the corotation radius.

Table 5.1 compares the value of Ω_P observed in simulations when the upper wave is present to that predicted by the dispersion relation (5.24). For simplicity, we set $\varpi = \varpi_\star$ and use the Keplerian values of Ω and κ when calculating the predicted values from equation (5.24) (i.e. all variables are evaluated just outside the BL). Nevertheless, the agreement between the analytical predictions and the simulations is good to the level of several percent for both 2D and 3D simulations and irrespective of stratification. However, some of our theoretical estimates tend to be slightly high, especially at late times ($t \gtrsim 60$ orbits) when the boundary layer has thickened substantially. One possible cause for the slight deviation between the measured and analytically predicted pattern speeds is that the boundary layer is not infinitesimally thin, but we have assumed so in evaluating the dispersion relation at $\varpi = \varpi_\star$.

label	time	m	Ω_P measured	Ω_P predicted
2D6a	20	≈ 40	.84	.831
2D6b	20	≈ 40	.835	.831
2D6c	20	≈ 40	.835	.831
3D6c	120	9	.77	.80
3D9a	100	10	.83	.850
3D9d	60	12	.85	.861
2D9a	30	≈ 29	.87	.884
2D9a	280	11	.815	.856
2D9b	30	≈ 24	.87	.881
2D9c	30	≈ 32	.88	.885

Table 5.1: Comparison between the analytical value of Ω_P and the value measured in simulations for the upper branch. The columns are from left to right: simulation label, time since the start of the simulation, m, pattern speed measured from the simulation, pattern speed predicted from equation (5.24).

Table 5.1 shows that the behavior of the phase speed pf the upper mode is in reasonable agreement with the simple vortex sheet prediction (5.23). Indeed, the latter would result in $\Omega_P = \omega/(k_y \varpi_\star) \approx 0.83$ and 0.89 for $M = 6$ and 9, respectively. This agrees with the trend seen in our simulations, where higher values of M results in somewhat larger values of Ω_P. Also, the magnitude of Ω_P is close to $\Omega_K(\varpi_\star)$, in accord with equation (5.23).

Lower Branch

For the case of the isothermal vortex sheet (§3.1), the lower branch is characterized by a sound wave which propagates nearly parallel to the vortex sheet in the half-plane $x < 0$ with phase velocity s_-. We now discuss the modifications that need to be made to this dispersion relation in order to apply it to the disk-star system.

We begin by postulating that the lower branch in the disk-star system is characterized by a sound wave which propagates azimuthally in the star. One immediate difference as compared to the isothermal vortex sheet case is that the star is stratified, so the phase velocity of the lower branch is not simply s, but is modified by the effects of gravity and stratification.

In a non-moving, plane-parallel atmosphere stratified in the x-direction with constant sound speed, s, and gravity, g, the dispersion relation for gravito-sonic waves (p and g modes) is given by e.g. Vallis (2006) as

$$\omega^2 = \frac{s^2 l^2}{2}\left[1 \pm \left(1 - \frac{4(\gamma-1)k_y^2}{\gamma^2 h_s^2 l^4}\right)\right] \tag{5.26}$$

$$l^2 \equiv k_x^2 + k_y^2 + 1/4h_s^2 \tag{5.27}$$

$$h_s \equiv s^2/\gamma g, \tag{5.28}$$

where h_s is the pressure scale height. Note that the dispersion relation (5.26) applies to *all wavelengths*, not just to those that are short compared to the scale height of the atmosphere.

The upper sign inside the braces on the right hand side of equation (5.26) corresponds to p-modes and the lower sign to g-modes. An isothermal equation of state ($\gamma = 1$) is neutrally buoyant, so g-modes have $\omega = 0$, and we will not consider them further. On the other hand, the dispersion relation for p-modes with $\gamma = 1$ reduces to

$$\omega^2 = s^2\left(k_x^2 + k_y^2 + \frac{1}{4h_s^2}\right). \tag{5.29}$$

Note that the effect of gravity and stratification enters into the dispersion relation through the $1/4h_s^2$ term, and in the limit $h_s \to \infty$ we recover the dispersion relation for a sound wave in an

unstratified medium. However, since $\lambda \gtrsim h_s$ in our simulations for the dominant modes, the stratification term in equation (5.29) is very important for comparing with simulations.

We can use equation (5.29) to derive a dispersion relation for the generalization of the lower branch to the disk-star system. We start by setting $k_y = m/\varpi$, and by analogy with the vortex sheet, we assume that $|k_y/k_x| \gg 1$ inside the star. Making again the association, $\omega = m\Omega_P$, we have

$$\Omega_P = s\sqrt{\left(\frac{1}{\varpi_0}\right)^2 + \left(\frac{1}{2mh_s(\varpi_0)}\right)^2} \tag{5.30}$$

$$= \Omega(\varpi_\star)\frac{\varpi_\star}{\varpi_0}\sqrt{M^{-2} + \left(\frac{M}{2m}\frac{\varpi_\star}{\varpi_0}\right)^2}. \tag{5.31}$$

Since Ω_P must be independent of radius, we have chosen an "effective radius", $\varpi_0 \lesssim \varpi_\star$, to use in the expression on the right-hand side of equation (5.30). Although the choice of an effective radius may seem like an "ad-hoc" prescription, we provide theoretical justification for it in Appendix B. It is further justified by the agreement between the value of $\Omega_P(m, M)$ measured in simulations and that given by equation (5.30).

Figure 5.2 shows a plot of Ω_P vs. m from our simulations when the lower wave is observed. It is evident that the agreement between equation (5.30) and the data is quite good over a wide range of values for m and Ω_P. Moreover, the 2D simulations (circles), 3D unstratified simulations (squares), and 3D stratified simulations (triangles) lie on the same curve for both $M = 6$ and $M = 9$, implying that the behavior is fundamentally the same in both 2D and 3D and with or without stratification.

It is of note that the lower mode in the BL has phase speed considerably higher than $\Omega_P = M^{-1}\Omega(\varpi_\star)$ predicted by the simple vortex sheet model, see equation (5.23). This is because the results presented in §3.1 were obtained assuming an *unstratified* star, in which case $h_s \to \infty$ and our BL dispersion relation (5.30) would reduce to its vortex sheet analog. However, the density gradient in an isothermally stratified star strongly modifies the dispersion relation, as evidenced by the second term in equation (5.31) and makes Ω_P a function not only of M but also of azimuthal wavenumber m.

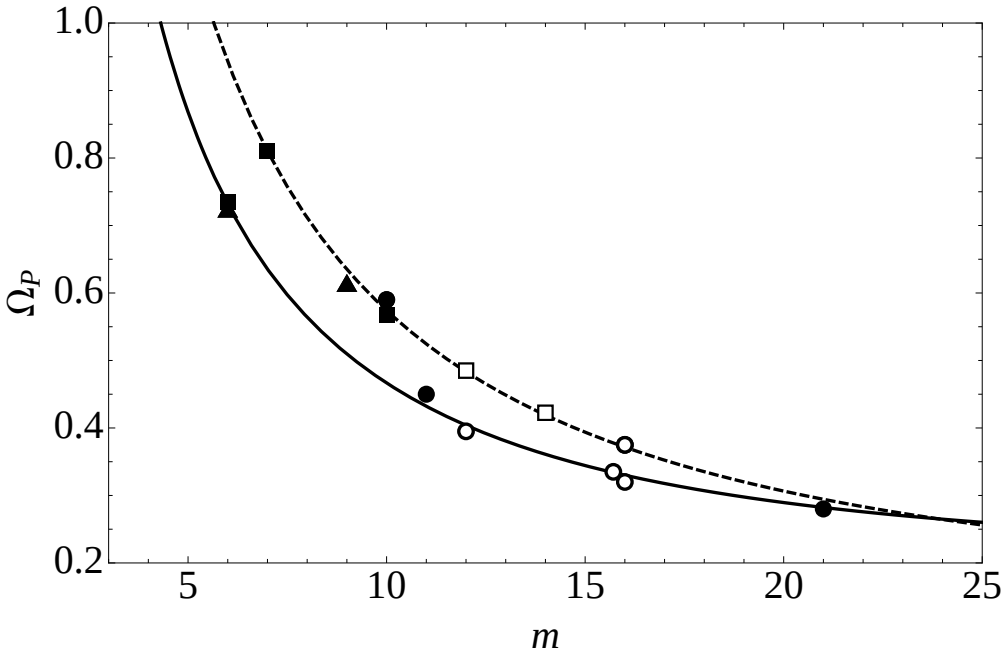


Figure 5.2: Comparison between the analytical dispersion relation, $\Omega_P(m, M)$, and simulation results for the lower branch. The solid line is the analytical prediction from equation (5.30) for $M = 6$ using an effective radius of $\varpi_0 = .84$, and the dashed line is for $M = 9$ using $\varpi_0 = .90$. The points show values of Ω_P and m measured from simulations when the lower branch is dominant. The circles represent 2D simulations, the squares 3D unstratified simulations, and the triangles 3D stratified simulations. Filled points represent simulations spanning the full 2π in azimuthal angle, and open points represent simulations for a wedge which spans an azimuthal angle $< 2\pi$. There is a solid triangle and a solid square that have merged near the solid curve at $M = 6$.

Middle Branch

For the isothermal vortex sheet with a constant sound speed everywhere throughout the domain ($s_+ = s_-$), the phase velocity of the middle branch is simply $V/2$ (§3.1). Moreover, the wavefronts make the same angle with respect to the vortex sheet both above and below it, which is true even for the case of non-equal densities above and below the vortex sheet (Belyaev & Rafikov, 2012). This last fact can be expressed mathematically as $k_{x,+}/k_y = k_{x,-}/k_y$, where the plus and minus signs denote the value of k_x in the $x > 0$ and $x < 0$ half-planes, respectively.

We now postulate that for the disk-star system the wavefronts in the star and in the disk form the same angle with respect to the azimuth across the boundary layer. Using equations (5.25) and

(5.29), we can write

$$\left(\frac{k_{\varpi,\mathrm{disk}}}{k_\phi}\right)^2 = \frac{(\omega - m\Omega)^2 + \kappa^2}{(sk_\phi)^2} - 1 \tag{5.32}$$

$$\left(\frac{k_{\varpi,\mathrm{star}}}{k_\phi}\right)^2 = \frac{\omega^2}{(sk_\phi)^2} - \frac{1}{(2h_s k_\phi)^2} - 1 \tag{5.33}$$

Setting equations (5.32) and (5.33) equal to each other at $\varpi = \varpi_\star$ (the condition that the wavefronts in the disk and star form the same angle with respect to the azimuth across the BL), the dispersion relation for the middle branch is

$$\Omega_P = \frac{\Omega(\varpi_\star)}{2}\left[1 + \frac{1}{m^2\Omega^2(\varpi_\star)}\left(\kappa^2(\varpi_\star) + \frac{s^2}{4h_{s,\star}^2}\right)\right]. \tag{5.34}$$

Table 5.2 lists the pattern speeds and m-numbers measured in simulations when the middle branch is clearly dominant and compares the pattern speed to that predicted by equation (5.34). For simplicity, we again assume a Keplerian profile for κ and Ω when computing the predicted pattern speed. The agreement between the predicted and measured values is at the several percent level. Also, Ω_P is very close to $\Omega(\varpi_\star)/2$, in agreement with the vortex sheet model, see equation (5.23).The discrepancy between the measured and analytically-predicted pattern speeds could arise because the condition $k_{\varpi,+}/k_\phi = k_{\varpi,-}/k_\phi$ is not exactly satisfied for the disk-star system as it is for the isothermal vortex sheet. Nevertheless, we find that equation (5.34) provides a good approximation to the pattern speed observed in our simulations when the middle branch is dominant. We also note that we have fewer measurements for the middle branch as compared to the upper and lower branches, because the middle branch is a transient phenomenon observed only during the linear growth regime of the sonic instabilities, if at all.

3.3 Spatial Morphology of the Upper, Middle, and Lower Branches

We have identified three branches in our simulations that are the generalizations of the upper, middle, and lower branches of the 2D isothermal vortex sheet. We now discuss the structural morphology of each of these branches.

label	time	m	Ω_P measured	Ω_P predicted
3D6a	10	≈ 42	.52	.502
3D6d	10	≈ 36	.515	.503
3D6c	10	≈ 44	.52	.502
3D9e	20	≈ 28	.57	.515

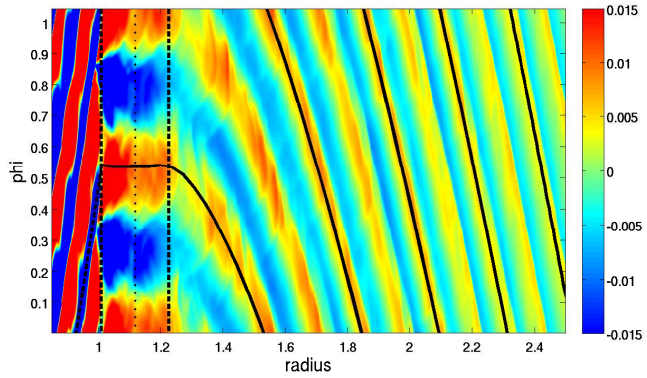
Table 5.2: Comparison of the analytically predicted value of Ω_P, and the value measured from simulations for the middle branch. The columns of the table are from left to right: simulation label, time since the start of the simulation, m, pattern speed measured from the simulation, pattern speed predicted by equation (5.34).

Fig. 5.3 shows snapshots of $\varpi\sqrt{\Sigma}\langle v_\varpi\rangle_z$ vertically-averaged in the z-direction for each of the three wave-branches from 3D unstratified simulations. The quantity $\varpi\sqrt{\Sigma}\langle v_\varpi\rangle_z$ is approximately constant throughout the star and disk, so it is especially useful for visualizing the radiation pattern. This is because waves conserve energy and angular momentum current, which are both of order $\varpi^2\Sigma\delta v^2$, where δv is the magnitude of the velocity perturbation. The dashed and dotted vertical lines in Fig. 5.3 depict the edges of evanescent regions and corotation radii respectively. Notice that there are always two corotation radii: one inside the boundary layer at $\varpi \approx 1$, and one inside the evanescent region within the disk. In principle, there is also an evanescent region around the corotation radius inside the BL, but this region is narrow, due to the steep radial gradient of angular velocity within the BL.

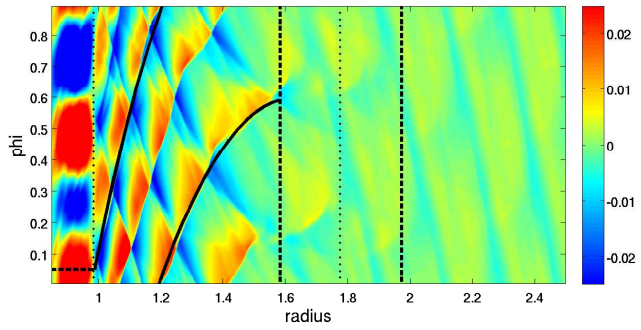
The sharp features seen in this Figure (especially in panel b) are the shocks into which the propagating acoustic modes evolve as a result of their nonlinearity. Even though the nonlinearity is relatively mild, with $v_\varpi \sim 0.1s$, implying a density jump of $\sim 10\%$ across the shock fronts in this particular simulation (see also Fig. 5.7), the waves propagating into the disk break and become weak shocks. In our simulations we typically find this to occur not too far from the BL, at separations of $(0.2-1)\varpi_\star$ away from their launching point.

The solid and dashed curves in Figure 5.3 trace the shape of shock fronts or wave fronts if the wave has not shocked. The formula for the shape of a front is simply

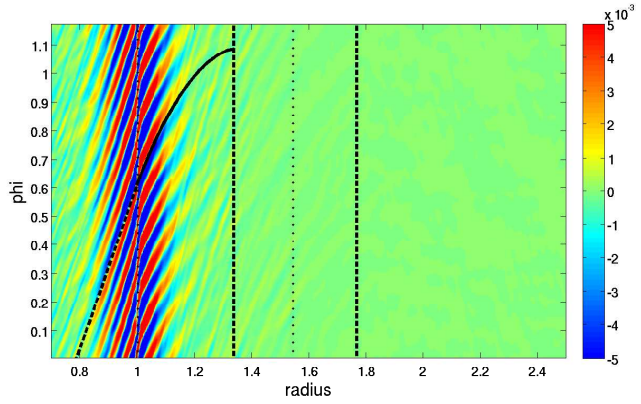
$$\frac{d\phi}{d\varpi} = \pm\frac{k_\varpi}{k_\phi}, \tag{5.35}$$



(a)



(b)



(c)

Figure 5.3: Panels a, b, c show snapshots of $\varpi\sqrt{\Sigma}\langle v_{\varpi}\rangle_z$, when the upper, lower, and middle branches are dominant. Panel a corresponds to simulation 3D9d at $t = 65$, b to simulation 3D9e at $t = 320$, panel c to simulation 3D6a at $t = 10$. Dashed vertical lines depict the boundaries of evanescent regions and dotted vertical lines depict corotation radii. There are exactly two corotation radii. One in the BL and one in the disk.

where k_ϖ is given by formula (5.25) inside the disk or (5.29) inside the star. The sign on the right hand side of equation (5.35) determines whether the wave front is angled up or down, assuming we take k_ϖ and k_ϕ to be positive. We see from Figure 5.3 that the analytic curves for the shock fronts are in excellent agreement with snapshots from the simulations, which is due to the fact that the waves are only weakly nonlinear.

For the upper branch, which has high Ω_P close to unity, the evanescent region extends all the way down to the boundary layer, so density waves emitted from the BL that propagate into the disk have a pattern speed that is faster than the angular speed of the disk material and wind up with increasing radius. For the lower and middle branches, however, the evanescent region in the disk is well-separated from the boundary layer, so density waves emitted from the BL have a slower pattern speed than the angular speed of the disk material. These density waves unwind as they travel towards the forbidden region, partially reflecting off it, with very little transmission (see §4.3 for a lower bound on the reflection coefficient measured from simulations).

As a result of this reflection, a standing shock pattern can be set up in the disk between the BL and the forbidden region (Fig. 5.3b) if a resonance criterion is satisfied. This criterion states that in order to achieve standing shocks, the total azimuthal angle subtended by a shock in traveling from the BL to the forbidden region and back must be an integer multiple of the angle subtended by one wavelength of the mode. Mathematically, this criterion is

$$\frac{2\pi p}{m} = 2\Delta\phi_{\rm shock} \tag{5.36}$$

$$\Delta\phi_{\rm shock} = \int_{\varpi_{\rm BL}}^{\varpi_0} d\varpi \frac{d\phi}{d\varpi}. \tag{5.37}$$

Here, ϖ_0 is the inner edge of the forbidden region in the disk, $\varpi_{BL} \approx 1$, and $d\phi/d\varpi$ is given by equation (5.35). The integer p gives the number of shock crossings for a shock traveling from the BL to the forbidden region or vice versa, counting the reflection point at the edge of the evanescent region as a shock crossing. For instance, solving equation (5.36) for the $m = 14$ mode depicted in Fig. 5.3b we find $p = 6.03$. Thus, p is very close to an integer, which allows the standing shock pattern to form, and it is evident that each outgoing and incoming shock undergoes six shock crossings (counting the point of reflection).

Although p does not necessarily need to be an integer, it is likely that modes with an azimuthal wavenumber, m, that is close to an integer value of p are reinforced relative to modes with a similar value of m, but for which p is not close to an integer by the resonance condition.

3.4 Modes with $k_z \neq 0$

The upper, lower, and middle branch modes are all two-dimensional in the $\varpi - \phi$ plane in the sense that they do not require the z-dimension to operate. In principle, there are also Kelvin-Helmholtz (KH) modes for vertical wavenumbers $k_z/k_\phi \gtrsim M$ (Belyaev & Rafikov, 2012).

To determine the relative importance of the $k_z \neq 0$ vs. the $k_z = 0$ modes, we compute the power spectrum from the simulations along the z-dimension. We work in the variable $\delta\rho/\sqrt{\Sigma_0}$, which by the definition of $\delta\rho$ (equation [5.5]) sums to zero when integrated over the entire simulation domain. This is a natural variable to use, since one expects the time-averaged value of $|\delta\rho/\sqrt{\Sigma_0}|$ to be roughly constant for a wave across the entire simulation domain up to factors related to the geometry and rotation profile.

To obtain the power spectrum, we first perform a discrete Fourier transform in the z-direction. In order to carry out summations, we let $\delta\rho/\sqrt{\Sigma_0}$ be a function of the grid points (l, m, n) in the (ϖ, ϕ, z), directions respectively. The Fourier transform in the z-direction then becomes

$$\mathcal{F}_n(l,m) \equiv \frac{1}{\sqrt{N_z}} \sum_{n=0}^{N_z-1} e^{-i2\pi nz/N_z} \frac{\delta\rho(l,m,n)}{\sqrt{\Sigma_0(l)}}, \tag{5.38}$$

where N_z is the number of cells in the z-dimension. The power spectrum is then defined as

$$P_n \equiv \frac{1}{N_\varpi N_\phi N_z} \sum_{l=0}^{N_\varpi-1} \sum_{m=0}^{N_\phi-1} (\mathcal{F}_n(l,m))^2. \tag{5.39}$$

We note that by Parseval's theorem,

$$\sum_{n=0}^{N_z-1} P_n = \frac{1}{N_\varpi N_\phi N_z} \sum_{n=0}^{N_z-1} \sum_{m=0}^{N_\phi-1} \sum_{l=0}^{N_\varpi-1} \left(\frac{\delta\rho(l,m,n)}{\sqrt{\Sigma_0(l)}} \right)^2. \tag{5.40}$$

Fig. 5.4 shows power spectra computed from the simulations. Plotted is $\log_{10}(P_n/\sum_n P_n)$ vs. k_z, where $k_z \equiv 2\pi n/\Delta z$, and Δz is the width of the simulation domain in the z-direction. The black lines are from simulation 3D9e, and the red lines are from simulation 3D9f which has the same parameters but twice the z-resolution. The solid lines correspond to a time when the upper mode is dominant, and the dashed lines to a time when the lower mode is dominant. From the figure, it is clear that the $n = 0$ mode has at least several orders of magnitude more power than all of the $n > 0$ modes combined. Note that we only plot the modes from $n = 0$ to $n = N_z/2$, where $N_z/2 = 16$ for simulation 3D9e. This is because modes having $n = N_z/2 + 1$ to $N_z - 1$ (if N_z is divisible by 2) are just the complex conjugates of modes having $n = N_z/2 - 1$ to $n = 1$, for a real signal with no imaginary component, such as ours. Simulation 3D9f has $N_z/2 = 32$, but we only show the modes up to $n = 16$, since there are no interesting features past $n > 16$, and the power spectrum simply continues to decay with increasing n.

It is clear from Fig. 5.4 that there is more power in the $k_z \neq 0$ modes relative to the $k_z = 0$ mode for the higher resolution simulation as compared to the lower resolution simulation. Thus, it is possible that our simulations are not fully converged in the z-direction. Nevertheless, the fact that the power in the $k_z \neq 0$ modes is still several orders of magnitude less than the power in the $k_z = 0$ mode even for the higher resolution simulation suggests that the $k_z = 0$ mode is indeed dominant irrespective of the resolution in z.

Fig. 5.5 shows a k_z-time plot of $\log_{10}(P_n)$ for simulations 3D9e and 3D9f. One can see interesting temporal features, such as rapid excitation of both $k_z \neq 0$ modes and $k_z = 0$ modes and their gradual subsequent decay. One possible source for these periodic outbursts are secondary KH instabilities Belyaev et al. (2012). However, in the 3D case, unlike the 2D case, a kink-like inflection point in the azimuthal velocity profile does not form, so this mechanism is not certain. It is also evident in Fig. 5.5 that the higher resolution simulation (3D9f) has a greater proportion of power in the $k_z \neq 0$ modes, but again the $k_z = 0$ mode is clearly dominant for the duration of the simulation even in the higher resolution case. Thus, one would expect the $k_z = 0$ modes to dominate the angular momentum transport in the system, which we show explicitly in the next section.

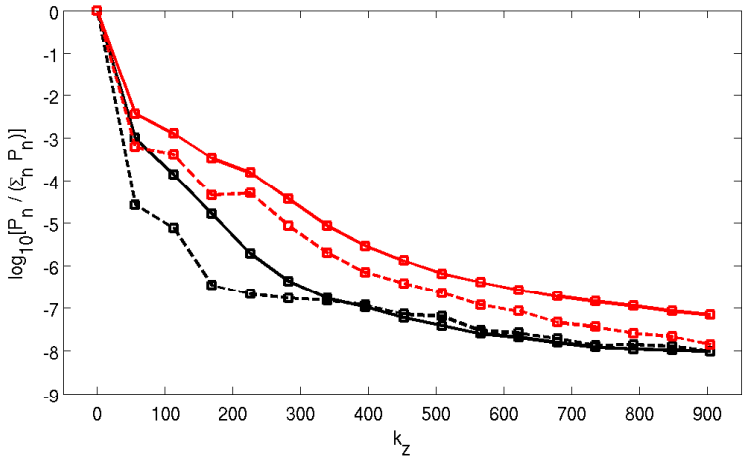
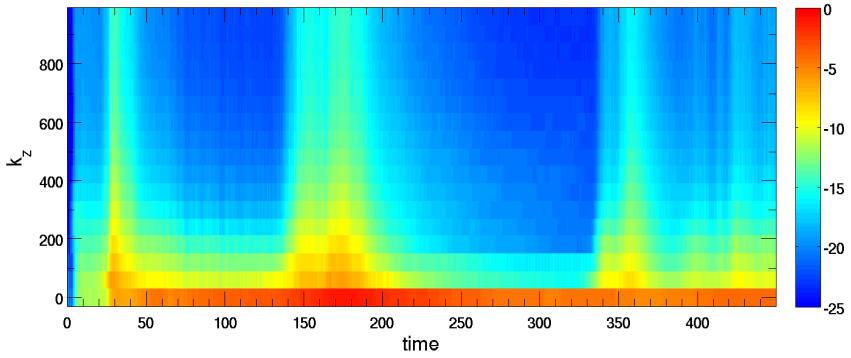


Figure 5.4: The power spectrum, $\log_{10}(P_n/\sum_n P_n)$ as a function of k_z. The solid lines are for the upper mode and the dashed lines for the lower mode. Simulation 3D9e is shown in black and 3D9f in red. Note that simulations 3D9e and 3D9f have the same vertical extent, Δ_z, but a different resolution in the z-direction. When comparing across simulations with different resolutions, one should compare k_z rather than n, since modes with the same value of k_z correspond to the same vertical wavelength, which is not true for modes with the same n if the simulations have different resolutions.

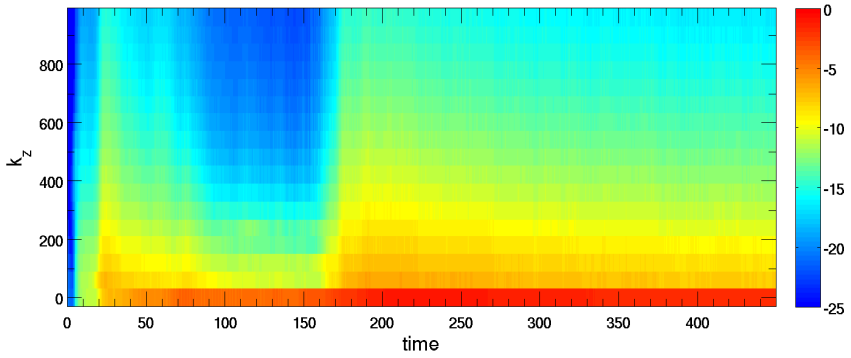
4 Angular Momentum Transport

Here we discuss angular momentum transport due to the upper and lower wave branches. We find good agreement between theory and simulation and conclude that the upper branch is more efficient at transporting angular momentum. We do not consider the middle branch here, since it is dominant only for short periods of time while the instabilities are still growing.

As we shall soon demonstrate, angular momentum transport in our simulations is dominated not by turbulent stresses, but rather by acoustic radiation of angular momentum away from the boundary layer both into the star and into the disk. Moreover, the $k_z = 0$ modes dominate the angular momentum transport, as hinted at in §3.4, which allows us to use the theory of density waves in thin disks to calculate the rate of angular momentum transport (e.g. Appendix J of Binney & Tremaine (2008)).



(a)



(b)

Figure 5.5: a) k_z-time plot of $\log_{10}(P_n)$ for simulation 3D9e. b) k_z-time plot of $\log_{10}(P_n)$ for simulation 3D9f, which has all the same parameters as simulation 3D9e, except that the z-resolution has been doubled. We again point out that comparing across simulations with different resolutions, one should compare k_z rather than n, since modes with the same value of k_z correspond to the same vertical wavelength.

4.1 Transport by Waves: General Formulas

The angular momentum current through radius ϖ is given by equation (5.12). By analogy with equation (5.13), it can be decomposed into a stress term and an advective term.

$$C_S(\varpi) \equiv 2\pi\varpi F_S \tag{5.41}$$

$$C_A(\varpi) \equiv 2\pi\varpi F_A. \tag{5.42}$$

Waves transport angular momentum exclusively through stresses, and we can use equations (5.41) and (5.15) to calculate C_S. Inside the star, C_S for a given mode with azimuthal wavelength

m is given in terms of the amplitude of the density perturbation $\delta\Sigma_m(\varpi)$, as

$$C_{S,m}(\varpi) = \pm\left(\frac{k_\varpi \varpi}{m}\right)\frac{\pi s^4 \Sigma_0}{\Omega_P^2}\left(\frac{\delta\Sigma_m}{\Sigma_0}\right)^2. \tag{5.43}$$

Here we have used the relations in Appendix B to express $\delta v_{\phi,m}$ and $\delta v_{\varpi,m}$ in terms of $\delta\Sigma_m$. The total angular momentum current due to waves is the sum over all modes for both incoming and outgoing waves and is given by

$$C_S(\varpi) = \sum_m C_{S,m}(\varpi). \tag{5.44}$$

We next assume that all waves propagate outwards from the BL, and that $k_\varpi \varpi/m$ is relatively insensitive to m near the dominant m value, which we denote as $\overline{m}$. This pair of assumptions will be verified later by comparison with simulation results. However, it fixes the sign in equation (5.43) and allows us to use Parseval's theorem (Appendix C) to write the total stress due to waves in the star as

$$C_S(\varpi) = -\left(\frac{k_\varpi(\overline{m})\varpi}{\overline{m}}\right)\frac{s^4\Sigma_0}{\Omega_P^2}\int_0^{2\pi} d\phi\left(\frac{\delta\Sigma}{\Sigma_0}\right)^2. \tag{5.45}$$

The analog to equation (5.45) for the angular momentum current due to density waves in the disk is (Binney & Tremaine, 2008)

$$C_S(\varpi) = \left(\frac{k_\varpi(\overline{m})\varpi}{\overline{m}}\right)\frac{s^4\Sigma_0}{(\kappa/m)^2 - (\Omega-\Omega_P)^2}\int_0^{2\pi} d\phi\left(\frac{\delta\Sigma}{\Sigma_0}\right)^2, \tag{5.46}$$

where we have again used Parseval's theorem and assumed that all waves propagate away from the BL.

Waves propagating into the disk shock, resulting in $\partial C_S/\partial\varpi \neq 0$ due to dissipation of the wave with increasing distance away from the BL. The change in angular momentum current carried by the pattern of shocks outside the evanescent region in the disk (for the upper mode) is

$$\frac{\partial C_S}{\partial \varpi} = -m\varpi\Sigma_0\frac{dE}{dm}. \tag{5.47}$$

Here, dE/dm is the energy converted into heat per unit mass of fluid crossing the shock, which comes at the expense of the energy contained in the shock and causes it to damp. The analysis is more complicated if there is reflection within the disk (e.g lower mode), and we provide further discussion of equation (5.47) as well as its relation to mass accretion by shocks in Appendix D.

For the isothermal case, the expression of Larson (1990) for dE/dm is

$$\frac{dE}{dm} = \frac{s^2}{6}\frac{\epsilon^3}{(1+\epsilon)^2}. \tag{5.48}$$

in the limit $\epsilon \ll 1$, where $\epsilon \equiv \Delta\Sigma/\Sigma$ is the jump in density across the shock divided by the preshock density.

It is also possible to derive an expression for dE/dm which is valid for arbitrary values of ϵ in the isothermal limit $\gamma \to 1$ (Appendix E)

$$\frac{dE}{dm} = s^2\frac{\epsilon(2+\epsilon) - 2(1+\epsilon)\ln(1+\epsilon)}{2(1+\epsilon)}. \tag{5.49}$$

This converges to Larson's result (equation [5.48]) to leading (third) order in ϵ.

In contrast to waves propagating into the disk, waves propagating away from the BL and into the star do not shock, because their amplitude is proportional to $\rho^{-1/2}$ by conservation of energy and angular momentum. Thus, as waves propagate into the star in our simulations, their amplitude is reduced, nonlinear effects are mitigated, and $\partial C_S/\partial\varpi = 0$. Inside a real star, the waves would either be absorbed, depositing their energy and angular momentum to the stellar fluid or reflected back towards the BL due to an increase in sound speed with decreasing radius into the star. If waves were absorbed deep inside the star, the BL would appear cooler than if the energy were dissipated locally. If waves were reflected, a standing wave would be set up between the corotation radius in the BL and the point of reflection in the star. This standing wave would resemble in appearance the pattern of intersecting shocks set up between the corotation radius in the disk and the BL for the lower branch (Fig. 5.3b).

We now apply these results to understand angular momentum transport by the upper and lower acoustic modes, which appear in our simulations most often.

4.2 Upper Branch

Disk

We now compare the analytical formulas given in the last section with results from simulations focusing on the upper branch. Fig. 5.6 shows C_S inside the disk at $t \sim 75$ for simulation 3D9d. This corresponds to approximately the same time as Fig. 5.3a, when the upper mode is clearly dominant. The solid black curve shows the measured value of C_S, using equations (5.15) and (5.41), and the red curves are the analytically-expected values of C_S, calculated using equation (5.46) together with the value of $\delta\Sigma$ measured from simulations. The solid red curve uses the standard WKB expression for k_ϖ (Goldreich & Tremaine, 1978), and the dashed red curve uses k_ϖ from equation (5.25). The standard WKB expression can be obtained from equation (5.25) by eliminating the k_ϕ term in the brackets. For simplicity, we use the Keplerian values of κ and Ω in equation (5.46) when calculating the analytically-expected value of C_S (red curves). This is a good approximation, since the rotation profile is very nearly Keplerian in the disk, away from the direct vicinity of the BL.

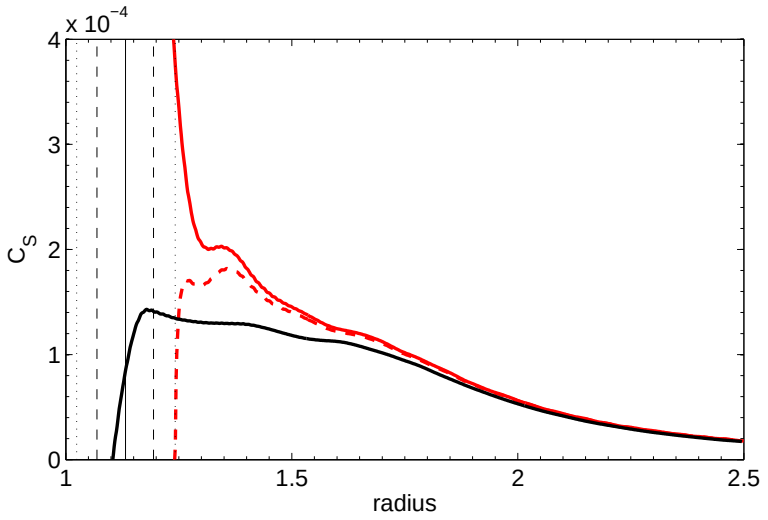


Figure 5.6: Plot of C_S for simulation 3D9d at time $t = 75$ within the disk.

Regardless of which form for k_ϖ is employed, equation (5.46) itself is only valid in the tight-winding approximation. Thus, the red curves converge to the black at large ϖ, but deviate

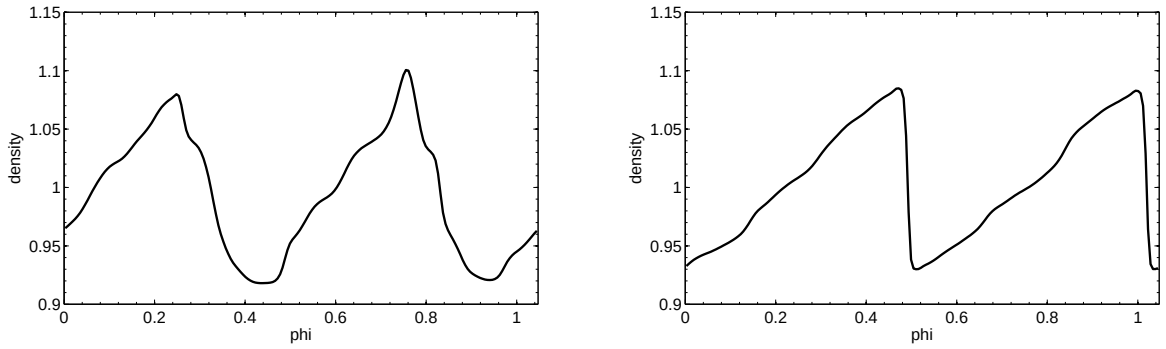
significantly as we approach the evanescent region around corotation, where the upper mode is loosely wound. For the solid red curve, the evanescent region is located between the vertical dashed lines, which correspond to the two Lindblad radii, and for the dashed red curve, the evanescent region is located between the dotted vertical lines. The corotation radius is marked by a solid vertical line. The fact that the red curves converge to the black far away from the evanescent region around corotation is decisive evidence that angular momentum is radiated away from the BL in the form of density waves.

Something else to note is that the black curve in Fig. 5.6 switches sign close to corotation. This is exactly what would be expected if angular momentum were carried by waves, since the angular momentum density of a wave undergoes a change in sign at the corotation radius (Binney & Tremaine, 2008).

We also point out that in Fig. 5.6 the flux is approximately constant between the edge of the evanescent region and $\varpi \approx 1.7$, but then starts to decrease more rapidly with radius. This reduction in flux is caused by shocking of the wave, which is illustrated in Fig. 5.7. In this Figure, we show the profile of the density perturbation $\Delta\Sigma/\Sigma$ in the azimuthal direction, i.e. at fixed ϖ, before (a, at $\varpi = 1.5$) and after (b, at $\varpi = 1.9$) breaking for simulation 3D9d at $t = 75$. It is obvious that in the latter case the wave has shocked, with clear discontinuity in the wave profile, which converges towards the "N-wave" shape (Landau & Lifshitz, 1959). Note that the analytically-expected value of C_S (equation [5.46]), automatically takes into account the dissipation of the wave due to shocking, through the factor of $\delta\Sigma^2$.

We now turn to the reduction of the wave flux with radius after the wave has shocked. Fig. 5.8 shows $-\partial C_S/\partial\varpi$ as a function of radius for simulation 3D9d at $t = 75$. The black curve shows the value of $-\partial C_S/\partial\varpi$ computed from the simulation data, where C_S is calculated using equation (5.41). The red curves are the analytical expectations for $-\partial C_S/\partial\varpi$ due to wave dissipation by shocks calculated using equation (5.47). The dashed red curve uses the value of dE/dm from equation (5.48), and the solid red curve uses the value of dE/dm from equation (5.49).

In measuring $\Delta\Sigma/\Sigma$ in order to calculate dE/dm, we find it necessary to correct for the finite width of the shock in the simulation. This is because the shock in our simulations extends over



(a) (b)

Figure 5.7: Azimuthal profiles of the wave before shocking (panel a) at $\varpi = 1.5$ and after shocking (panel b) at $\varpi = 1.9$.

several cells and is not a true discontinuity. Thus, we extrapolate the shock density profile from a simulation and estimate what the value of $\Delta\Sigma/\Sigma$ would be for a true discontinuity. For our resolution, this correction increases $\Delta\Sigma/\Sigma$ by $\approx 8\%$. Given the stiff dependence of dE/dm on $\Delta\Sigma/\Sigma$ (leading order dependence is $(\Delta\Sigma/\Sigma)^3$), this correction is necessary to obtain good agreement between theory and simulations.

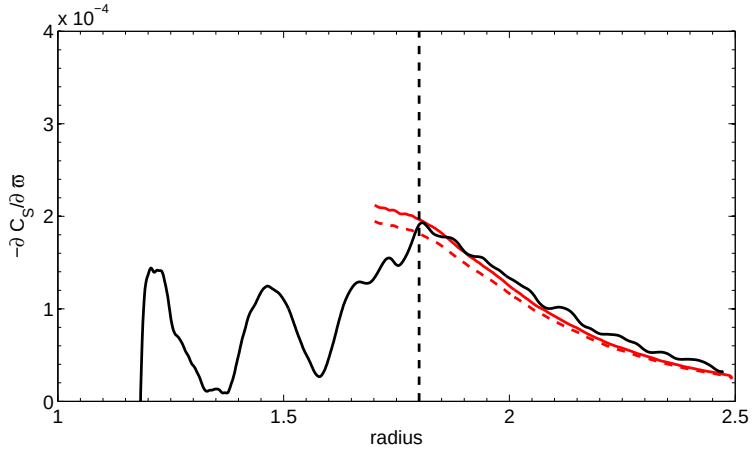


Figure 5.8: Plot of $-\partial C_S/\partial\varpi$ for simulation 3D9d at time $t = 75$. The dashed black line at $\varpi = 1.8$ denotes the radius at which the entire wave has shocked.

The agreement between the measured value of $\partial C_S/\partial\varpi$ and the theoretically-predicted one indicates that angular momentum radiated away from the evanescent region into the disk is redistributed by shock dissipation. This dissipation is most vigorous after the wave has

completely shocked around $\varpi \approx 1.8$, but the steepest parts of the wave shock earlier at $\varpi < 1.8$, so angular momentum starts to be redistributed even before the entire wave has shocked. Since $\Omega_P > \Omega$ for the upper branch outside the evanescent region in the disk, the wave carries positive angular momentum, and dissipation of the wave spins up the disk fluid, pushing matter outward.

Star

Radiation from the BL is emitted not only into the disk, but into the star as well. The amplitude of acoustic waves traveling into the star is proportional to $\rho^{-1/2}$, so they don't shock in our simulations and propagate out through the inner boundary of the simulation domain.

The inner radial "do nothing" boundary condition is not perfectly absorbing, so waves incident upon it are reflected with a reflection coefficient

$$\epsilon_R \equiv \frac{\delta\Sigma_R}{\delta\Sigma_{\rm out}}. \tag{5.50}$$

Here, $\delta\Sigma_{\rm in}$ is the amplitude of the outgoing wave (with respect to the BL), and $\delta\Sigma_R$ is the amplitude of the reflected wave. As long as ϵ_R is not close to 1, the reflected waves will not fundamentally affect the dynamics of the instabilities in the boundary layer, since the "overreflection" mechanism described in Belyaev & Rafikov (2012) only works if $\epsilon_R \approx 1$. However, the angular momentum current due to stresses measured by equation (5.41) will underestimate the true current, since the measured current contains components due to both the true outgoing waves (with respect to the BL) and the artificial reflected waves from the inner boundary. Nevertheless, the flux due to only the outgoing component, $C_{S,\rm out}$, can be estimated in terms of the measured flux, $C_{S,\rm meas}$, as

$$C_{S,\rm out} = \frac{C_{S,\rm meas}}{1-\epsilon_R^2}. \tag{5.51}$$

This equation can be derived by considering a linear superposition of an outgoing wave and the reflected wave. The reflected wave has the opposite sign of C_S as the outgoing wave and an amplitude that is second order in ϵ_R, since angular momentum flux is a second order quantity.

Fig. 5.9a shows the measured current (black line) calculated using equation (5.41), and the analytically-predicted current due to waves (red line) calculated using equation (5.45). The analytically-predicted current oscillates around the measured current, which is roughly constant for $\varpi \lesssim .96$. These oscillations can be explained by the presence of a reflected wave from the inner boundary with amplitude $\epsilon_R \approx .3$. This amplitude can be estimated from the straightforward-to-derive relation

$$\epsilon_R = \frac{C_{S,\max}^{1/2} - C_{S,\min}^{1/2}}{C_{S,\max}^{1/2} + C_{S,\min}^{1/2}}, \tag{5.52}$$

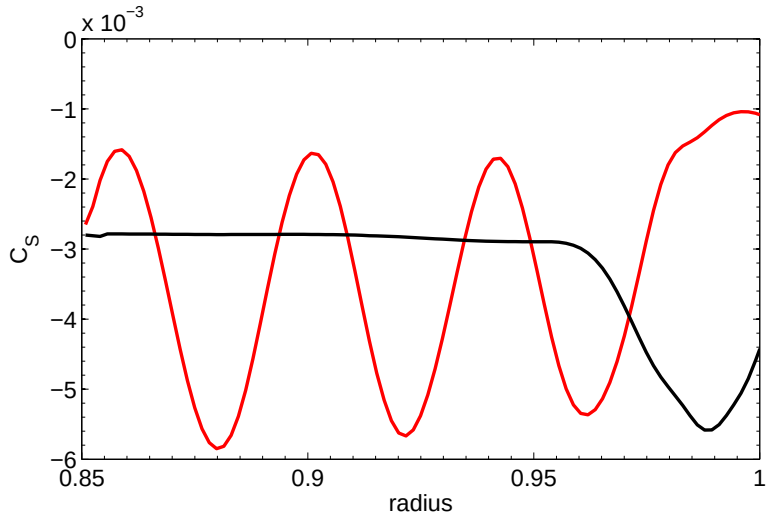
where $C_{S,\max}$ and $C_{S,\min}$ are the maximum and minimum values of the oscillations in the red, analytically predicted flux curve in Figure 5.9a.

The reason for the oscillations in the red curve of Fig. 5.9a is that equation (5.45) is an accurate estimator of the current due to waves if there are *only* outgoing waves present; it does not account for reflected waves. However, it is straightforward to modify equation (5.45) so that it estimates the current due to only the outgoing component. To do this, we assume that there is a single outgoing mode present with a constant value of k_ϖ that is reflected at the inner boundary into an incoming mode with the same value of k_ϖ and an amplitude which is a fraction ϵ_R of the amplitude of the outgoing mode. Under these assumptions, the current due to only the outgoing component, $C_{S,\text{out}}$, can be expressed in terms of the uncorrected current given by equation (5.45), $C_{S,\text{unc}}$, as

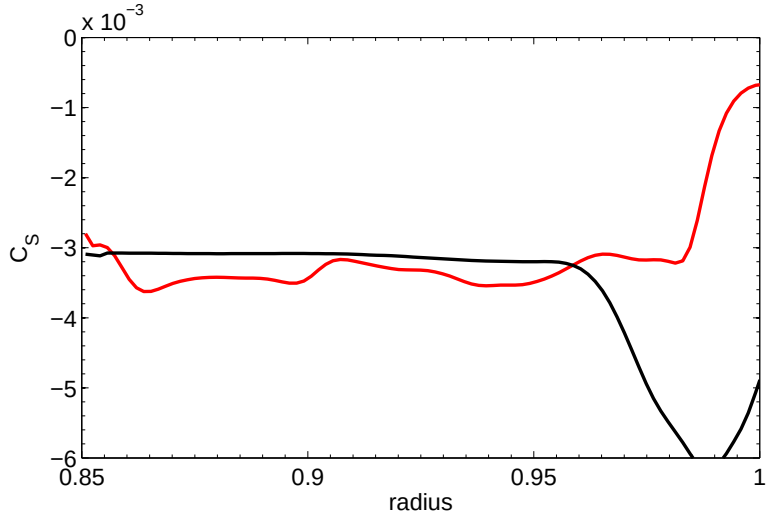
$$C_{S,\text{out}} = \frac{C_{S,\text{unc}}}{1 - 2\epsilon_R \cos(2k_\varpi \varpi + \psi) + \epsilon_R^2}, \tag{5.53}$$

where ψ is a free phase parameter.

The red curve in Fig. 5.9b shows $C_{S,\text{out}}$ as computed from equation (5.53), and the black curve shows $C_{S,\text{out}}$ according to equation (5.51). The oscillations in the red curve have all but disappeared after applying the correction to compute the flux from only outgoing waves. Moreover, the red and black curves are seen to be roughly constant for $\varpi \lesssim .96$ and to have very similar amplitudes. This proves that in the star, just as in the disk, angular momentum is carried



(a)



(b)

Figure 5.9: a) Uncorrected current due to stresses inside the star computed using equations (5.41) (black line) & (5.45) (red line). b) Corrected current due to outgoing waves computed using equations (5.51) (black line) & (5.53) (red line).

away from the BL by waves. However, unlike in the disk, the waves do not shock as they penetrate into the star, but rather diminish in amplitude to conserve energy and angular momentum.

Comparing the scales on Figs. 5.6 and 5.9b, we see that the angular momentum flux into the star is larger than the angular momentum flux into the disk by an order of magnitude. This

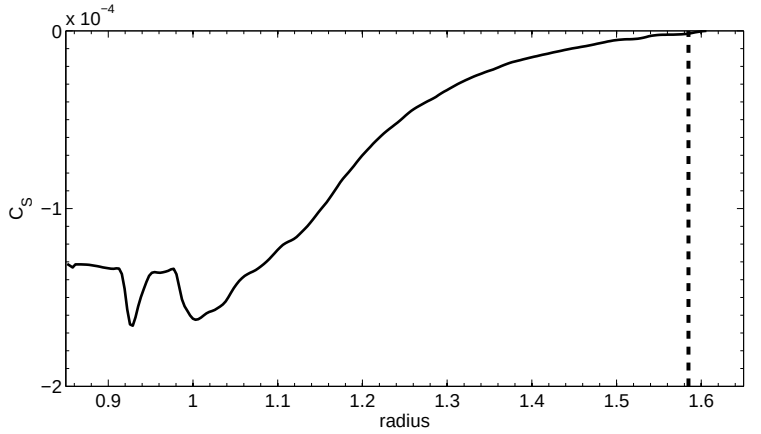
means that most of the angular momentum lost by the inner part of the disk goes into spinning up the star and only a small fraction is transported outward.

4.3 Lower Branch

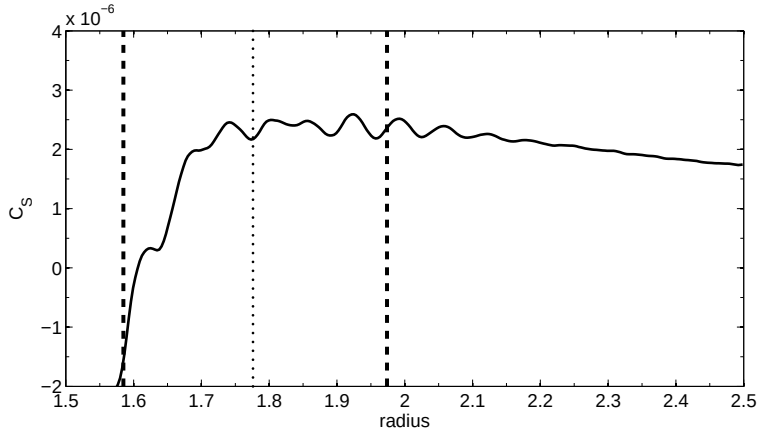
We turn now to angular momentum transport for the lower branch. Fig. 5.10 shows C_S calculated using equation (5.41) for simulation 3D9e at time $t = 320$; the same time as Fig. 5.3b, when the lower branch is clearly dominant. Panel a of Fig. 5.10 depicts C_S from the inner edge of the simulation domain up to the inner edge of the evanescent region in the disk at $\varpi = 1.58$. Panel b, which has a different scale than panel a, depicts C_S from just inside the inner edge of the evanescent region to the outer edge of the simulation domain. The dashed lines in panel b depict the edges of the evanescent region, and the dotted line is the corotation radius ($\Omega_P \approx .42$). We point out that although the magnitude of C_S for the lower mode in Fig. 5.10 is smaller than the magnitude of C_S for the upper mode in Fig. 5.9, the amplitude of either mode is not constant in time. In fact the magnitude of C_S inside the star is as high for the lower mode as for the upper mode at earlier times (see Fig. 5.11 in §4.4).

In contrast to the upper branch, it is more difficult to estimate the current due to waves using equations (5.46) and (5.45) in both the star and the disk for the lower branch. In the disk, the difficulty comes about due to the fact that there are both outgoing and reflected shocks between the surface of the star and the Lindblad resonance in the disk (Fig. 5.3b). Equation (5.46) only applies if there are exclusively outgoing waves, and it is not straightforward to modify it to account for interference effects from reflected waves. Without modification, the plot of the analytically predicted current, C_S, from equation (5.46) would show large spikes at shock crossings, and only in between shock crossings when the outgoing and reflected waves are well-separated is there reasonable agreement between the measured and analytically predicted values of C_S (see Fig. 5 of Belyaev et al. (2012)).

The complication with applying equation (5.45) to analytically predict C_S inside the star is that $k_\varpi \approx 0$ (to zeroth order in M^{-1}) for the lower mode (§3.2), which makes the current



(a)



(b)

Figure 5.10: a) C_S for simulation 3D9e at time $t = 320$ inside the inner edge of the evanescent region in the disk. The dashed line marks the inner edge of the evanescent region in the disk b) Same as a, but C_S is shown within the evanescent region and beyond it. The evanescent region itself is located within the dashed lines and the dotted line is the corotation radius.

estimated from equation (5.45) equal to zero. Thus, in order to use equation (5.45) we would need to know k_ϖ to first order in $1/M$. We choose not to pursue such a calculation here.

One thing to notice in Fig. 5.10 is that C_S vanishes close to the edge of the evanescent region in the disk. This is to be expected if we have near perfect reflection, since $C_S = 0$ at the point of reflection if the amplitudes of the outgoing and reflected shocks are the same. $C_S \neq 0$ throughout the entire region between the BL and the inner edge of the evanescent region due to shock dissipation, which causes the shock amplitude, and consequently $|C_S|$, to diminish with increasing path length traveled by the shock. This makes $C_S < 0$ between the BL and the point of reflection,

because the shock pattern has a negative angular momentum density inside corotation, and the outgoing shocks, which have a larger amplitude than the incoming ones, propagate in the $+\varpi$ direction.

We can estimate a lower bound on the reflection coefficient from the evanescent region by comparing the scales of Figs. 5.10a and 5.10b. The absolute value of C_S (for outgoing shocks only) is ~ 100 times lower outside the evanescent region than inside it. Since C_S is a second order quantity in $\delta\Sigma$, the reflection coefficient as defined in equation (5.50) is $\epsilon_R > .9$. This is only a lower bound on the reflection coefficient, since outside the evanescent region C_S could be dominated by an upper branch component.

We also point out that C_S changes sign within the evanescent region close to the corotation radius in the disk ($\varpi_{\rm CR} = 1.78$), as expected for angular momentum transport by waves. C_S does not change sign at the corotation radius located in the BL at $\varpi \approx 1$, since both the direction of wave propagation, and the sign of the angular momentum density change there. In other words, inside corotation at $\varpi \approx 1$ the angular momentum density is positive, but waves propagate in the $-\varpi$ direction so $C_S < 0$. Just outside it, the angular momentum density is negative, but waves propagate in the $+\varpi$ direction so $C_S < 0$ as well.

4.4 Relation of Angular Momentum Transport to Temporal Evolution

Angular momentum carried by the waves launched in the BL is eventually deposited into the disk fluid as a result of wave dissipation. We now discuss how angular momentum transport in our simulations controls the temporal evolution of the system. One can use a characteristic value of $|C_S| \sim 3 \times 10^{-3}$ taken from Fig. 5.9 to estimate a typical "evolution time", for the system when the upper branch is dominant. We define $t_{\rm evol}$ as the time it takes for the evanescent region (upper branch) in the disk to lose half its angular momentum. Taking the the evanescent region for upper branch to extend from $1 < \varpi < 1.25$, we estimate

$$t_{\rm evol} \sim 300. \tag{5.54}$$

Fig. 5.11 shows a radius-time plot of C_S for simulation 3D9a. From the figure, it is clear that $t_{\rm evol}$ is within a factor of several of the span of time during which the upper branch is dominant. Moreover, we see as well from Fig. 5.11 that $t_{\rm evol}$ is also a good estimator of the timespan during which there is a significant angular momentum current radiated away from the BL and the accretion rate is highest.

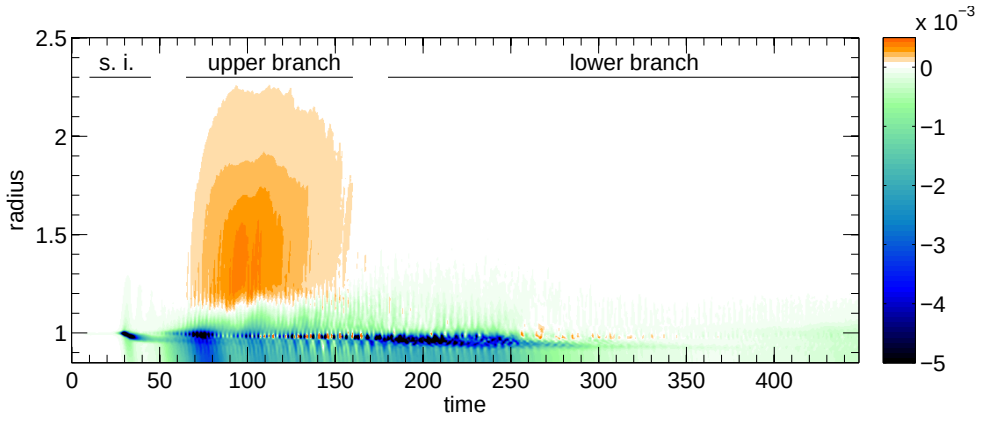


Figure 5.11: Radius-time image of C_S for simulation 3D9a. The horizontal bars show the periods of time when the sonic instabilities are active, the upper branch is dominant, and the lower branch is dominant.

The fact that the evolution time is comparable to both the timespan over which the upper branch is dominant and the timespan for significant mass accretion in the simulations suggests the following scenario for the temporal evolution of the system. The amplitude of the upper branch is initially high, but diminishes when it has depleted the evanescent region in the inner part of the disk of angular momentum. The system then switches to lower branch behavior with continuing mass accretion. However, without a mechanism of resupply for the inner disk, which does not exist in our simulations, the rate at which the inner disk is depleted of angular momentum must drop. Thus, the angular momentum current and the mass accretion rate both plummet for $t \gtrsim t_{\rm evol}$ as seen in Figs. 4.5b and 5.11. This occurs in step with a reduction in the amplitude of the acoustic modes, which are responsible for the angular momentum transport.

In contrast to our simulations, there does exist a mechanism of resupply for the inner disk in an astrophysical system, namely accretion due to turbulent stresses. These stresses are not present in our simulation, since we do not have magnetic fields, which lead to the MRI instability

in the disk. However, one may speculate that if the accretion time due to turbulent stresses were comparable to or shorter than $t_{\rm evol}$, then the acoustic modes would operate at a high amplitude indefinitely. Indeed, the amplitude of the modes themselves could potentially be controlled by the time for MRI to resupply the inner part of the disk.

4.5 Relation of Angular Momentum Transport to Mass Accretion Rate

In this section we relate the angular momentum transport rate to the mass accretion rate, $\dot{M}$, defined in equation (5.18). We can use equations (5.8) and (5.9) to write $\dot{M}$ in terms of C_S as

$$\dot{M} = \left[\frac{\partial}{\partial \varpi}\left(\Omega \varpi^2\right)\right]^{-1}\left[2\pi\varpi^3\Sigma_0\frac{\partial \Omega}{\partial t} + \frac{\partial C_S}{\partial \varpi}\right]. \tag{5.55}$$

Time evolution of Ω represented by the first term on the right hand side forces gas to move radially, since to conserve angular momentum fluid elements must readjust their radial distance, ϖ, when Ω varies. The $\partial\Omega/\partial t$ term in equation (5.55) vanishes for a steady state disk, but is potentially important for our simulations, since the rotation profile evolves in time (Fig. 4.6).

We plot the mass accretion rate in the BL as a function of radius for simulation 3D9a averaged between times $t = 70 - 100$ in Fig. (5.12). The solid red and blue curves show the contributions of the $\partial C_S/\partial\varpi$ and $\partial\Omega/\partial t$ terms, respectively, to the mass accretion rate (equation [5.55]), as measured from the simulation, and the black curve shows the total mass accretion rate measured directly from the simulation using equation (5.18). It is clear that both the $\partial\Omega/\partial t$ and $\partial C_S/\partial\varpi$ terms contribute significantly to the mass accretion rate, even far out in the disk. As a consistency check, the sum of the solid red and blue curves is shown in purple and is seen to equal the black curve up to small wiggles that are artifacts of the measurement procedure.

Fig. 5.12 clearly shows that the $\partial\Omega/\partial t$ term is important for the calculation of $\dot{M}$. In our case, it is significant because the inner disk is depleted of mass as a result of angular momentum transport by acoustic modes. This causes time-varying density and pressure gradients in the disk, which is significant even quite far from the BL, at separations $\sim \varpi_\star$ from it. Time evolution of

this pressure support ultimately causes explicit time dependence of Ω and drives accretion even in the region where the wave has not shocked yet (interior to $\varpi \approx 1.8$ in Fig. 5.12).

Prior to its dissipation the wave propagating through the disk cannot affect its state (Goldreich & Nicholson, 1989). Only after it shocks, transfer of its angular momentum to the disk drives additional mass accretion. The dashed red curve in Fig. 5.12 shows the theoretically predicted value for the component of mass accretion due to the $\partial C_S/\partial\varpi$ term in equation (5.55), assuming the $\partial C_S/\partial\varpi$ term is entirely due to shock dissipation (Appendix D). In other words, $\partial C_S/\partial\varpi$ is computed using equation (5.47), where we use equation (5.49) to calculate dE/dm, and measure $\Delta\Sigma/\Sigma$ in the same way described in §4.2.

The good agreement between the solid and dashed red curves for $\varpi \gtrsim 1.8$ in Fig. 5.12 shows that the $\partial C_S/\partial\varpi$ component of the mass accretion rate is well-described by dissipation in shocks. For smaller values of ϖ, the waves emitted from the BL have not yet fully shocked (§4.2), so the agreement is not as good.

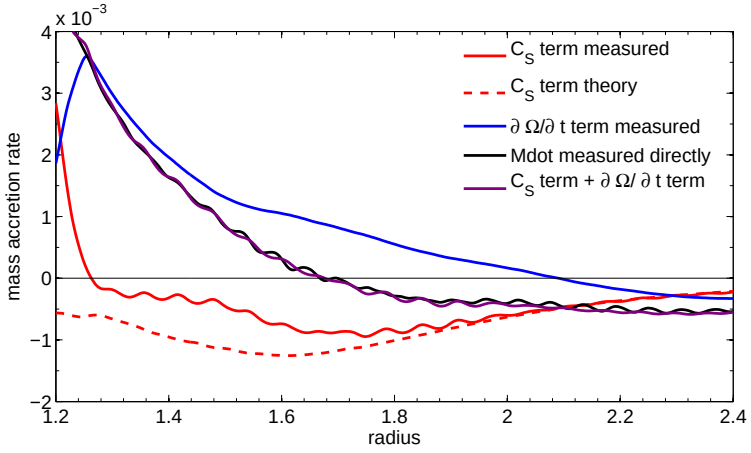


Figure 5.12: Plot of $\dot{M}$ measured from the simulations (black line) and the contributions to $\dot{M}$ from the $\partial C_S/\partial\varpi$ (solid red line) and $\partial\Omega/\partial t$ (blue line) terms in equation (5.55). The dashed red line shows the theoretical estimate for the $\partial C_S/\partial\varpi$ term assuming wave dissipation in shocks.

It is interesting to note that the mass accretion rate due to wave dissipation is negative in Fig. 5.12. This is due to the fact that Fig. 5.12 corresponds to a time when the upper branch is dominant. As discussed in §3.2, the upper branch has a fast pattern speed with a corotation radius in the disk at $\varpi_{\rm cr} \approx 1.12$ for this simulation. Outside of corotation ($\varpi > \varpi_{\rm cr}$), $\Omega_P > \Omega$ so

the wave has a positive angular momentum density. Thus, dissipation of the wave increases the angular momentum of the fluid elements in the disk, causing them to move outwards and resulting in a negative mass accretion rate.

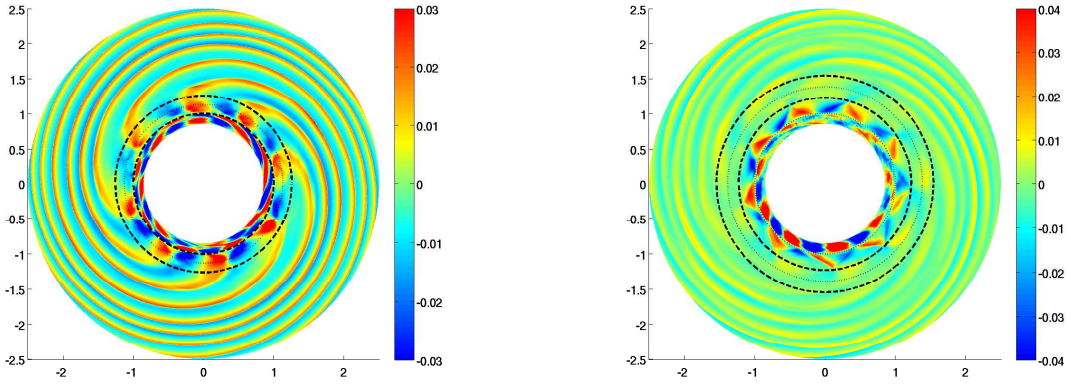
The situation is different for the lower and middle branches. Unlike the upper branch which has an evanescent region directly adjacent to the boundary layer, the middle and lower branches have their evanescent regions in the disk separated from the boundary layer. Waves can propagate between the BL and the evanescent region in the disk. Since $\Omega_P < \Omega$ in this region, this implies that the wave has negative angular momentum density and dissipation of the wave results in a positive mass accretion rate. Beyond the evanescent region in the disk, $\Omega_P > \Omega$ for both the lower and middle branches so the mass accretion rate due to wave dissipation is in principle negative in this region, just as for the upper branch. However, very little flux penetrates the evanescent region (§4.3), so the contribution to mass accretion from wave dissipation beyond the evanescent region in the disk is very small for the lower and middle branches.

5 Effect of Stratification on Acoustic Modes

Up to now we have discussed the results of unstratified simulations, and we find that stratification does not produce fundamentally different behavior. In particular, the upper, lower, and middle branches are all observed in stratified simulations, as well, and facilitate angular momentum transport.

Panels a and b of Fig. 5.13 show snapshots of the upper and lower branches for simulation 3D9c at times $t = 160$ and $t = 320$ in the color variable $\varpi\sqrt{\Sigma}\langle v_\varpi\rangle_z$. Comparing Fig. 5.13 with Fig. 5.3, we see that the spatial morphology of the wave branches is the same in the stratified and unstratified cases. In addition, we showed in §3 that the dispersion relations (5.24) (upper branch), (5.30) (lower branch), and (5.34) (middle branch) provided a good estimate of the pattern speed in simulations irrespective of stratification. Thus, we conclude that stratification has little effect on the dynamics and morphology of the modes for an isothermal equation of state.

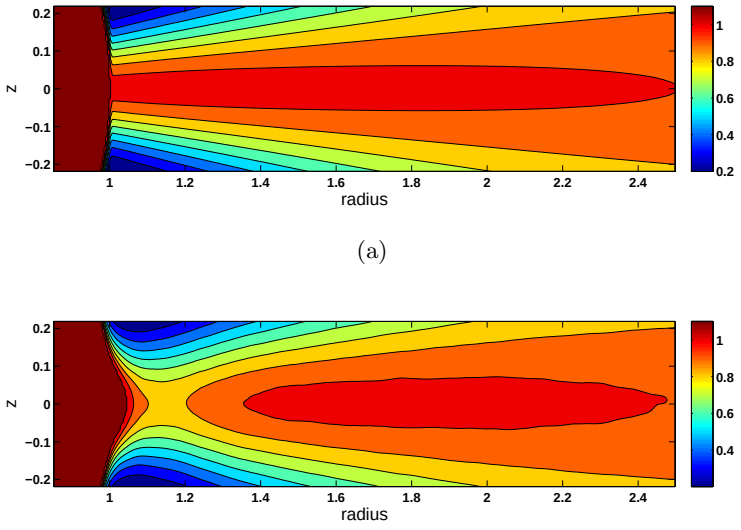
Although stratified and unstratified simulations exhibit similar behavior, there are some obvious differences. For instance, in stratified simulations we observe the formation of a neck in



(a) (b)

Figure 5.13: Panels a and b show snapshots of $\varpi\sqrt{\Sigma}\langle v_\varpi\rangle_z$ when the upper and lower waves are dominant, respectively, although there appears to be a superposition of both types of waves in the panels. The dashed and dotted circles depict the boundaries of evanescent regions and corotation radii, respectively. In panel a, the evanescent region in the disk extends all the way to the BL.

the density profile, which is shown in Fig. 5.14. The formation of this neck implies that sonic instabilities operate preferentially near the equator and spin up an equatorial belt on the star.



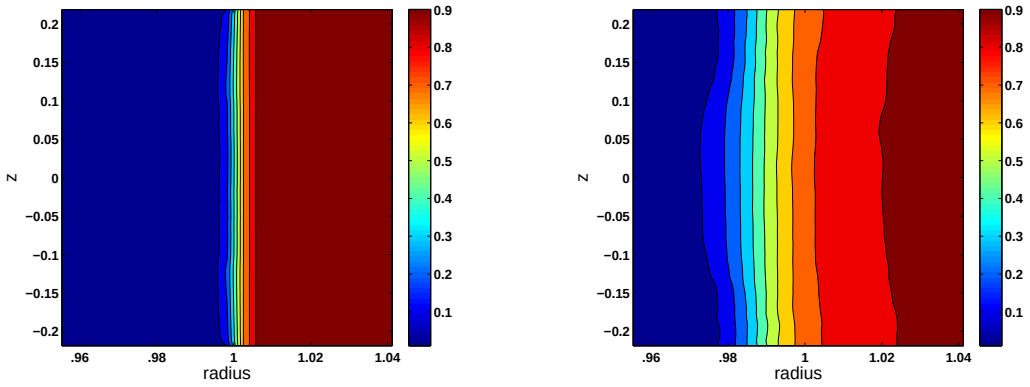
(a)

(b)

Figure 5.14: Panels a and b show contours of the azimuthally-averaged density profile at $t = 0$ and $t = 150$, respectively, for simulation 3D9c. Formation of a neck in the density distribution is clearly visible in panel b.

Further evidence in favor of a spun up equatorial belt can be seen in Fig. 5.15, which shows contours of the density-weighted azimuthal average of v_ϕ at $t = 0$ (panel a) and $t = 150$ (panel b). It is clear from panel b that the equatorial region of the star is spinning faster than higher latitudes. For an isothermal equation of state or more generally for any equation of state that is a function of the pressure alone, deviation from rotation on cylinders as see in Fig. 5.15b implies the existence of meridional circulation. Thus, although we do not see evidence of significant azimuthal spreading of disk material over the surface of the star, we do observe the sonic instabilities to induce meridional flows.

In principle, one may also interpret the vertical extent of the equatorial bulge of the spun-up fluid in our stratified simulations as evidence for the emergence of a spreading layer (Inogamov & Sunyaev, 1999; Piro & Bildsten, 2004b) on the stellar surface. However, given the simplified nature of our runs (e.g. isothermal EOS), it difficult to unambiguously claim observation of this phenomenon in the simulations.



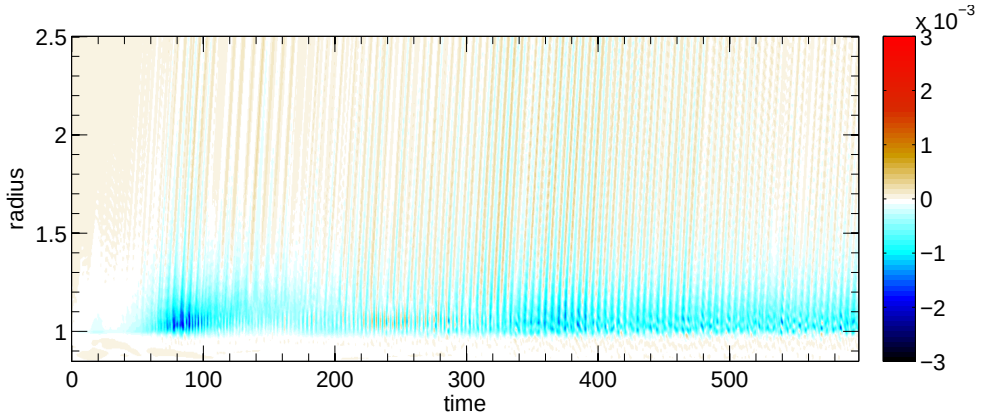
(a) (b)

Figure 5.15: Panels a and b show contours of the density-weighted azimuthal average of v_ϕ at $t = 0$ and $t = 150$, respectively, for simulation 3D9c. There is a slight deviation from rotation on cylinders in panel b with the equatorial plane rotating faster than higher latitudes.

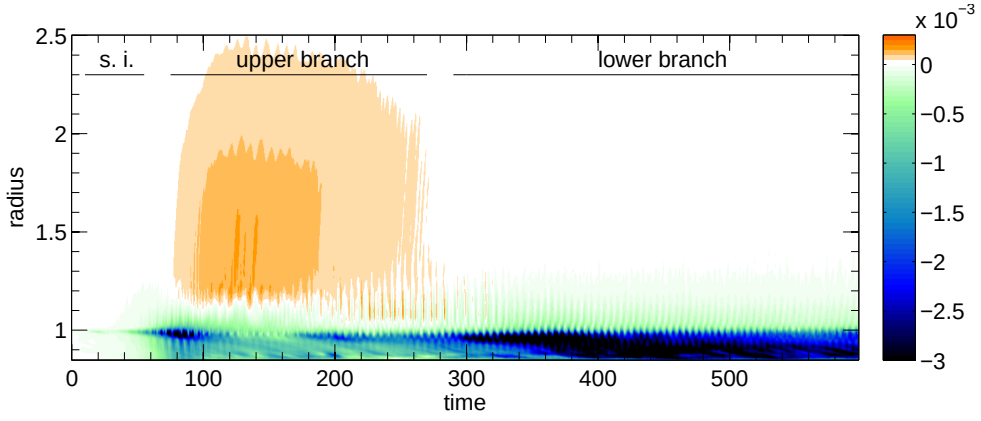
Another difference between stratified and unstratified simulations is that $t_{\rm evol}$ as defined in equation (5.54) is a factor of two or so higher in the stratified case. This implies that the acoustic modes have lower amplitudes and take a longer time to transport angular momentum away from the inner disk in the stratified case. Thus, mass accretion and angular momentum transport can

occur at an appreciable rate for a longer time before shutting off when the inner disk has been depleted of material (§4.4).

Panels a and b of Fig. 5.16 show radius-time plots of $\langle v_{\varpi} \rangle$ and C_S, respectively, for the stratified simulation 3D9c. These radius-time plots can be compared with those for the unstratified case shown in Figs. 4.5b and 5.11. Both the unstratified and stratified radius-time plots look fundamentally similar. However the features in the stratified simulation appear to be "stretched" in time as compared to the unstratified one, providing evidence that $t_{\rm evol}$ is longer in the stratified case.



(a)



(b)

Figure 5.16: Panels a and b show radius-time plots of $\langle v_{\varpi} \rangle$ and C_S for simulation 3D9c.

6 The Incompatibility of α Models and Angular Momentum Transport by Waves

As we have shown, angular momentum transport in our simulations is facilitated by quasi-2D acoustic waves, rather than turbulent stresses. This assertion follows from the fact that C_S is well-described by theoretical formulas applicable for waves §4.2, and that most of the power in the fluctuations is in $k_z = 0$ modes §3.4. Because α-models are based on the notion of a local effective viscosity due to turbulent stresses, whereas waves are inherently nonlocal, transporting angular momentum over long distances before they are absorbed or dissipate, it is clear that any conventional model of α viscosity is inapplicable to the BL.

We can make this point more concrete with three specific reasons why an α model is not applicable to transport by waves. First, in conventional α models the stress vanishes (and C_S changes sign) when $\partial\Omega/\partial\varpi = 0$, and this is not observed in our simulations. Instead, in a wave model, the stress vanishes (and C_S changes sign) when $\Omega = \Omega_P$, and we do see evidence of this (see §4.2 and 4.3). Although there is a corotation resonance in the BL, which could in principle be located close to the point where $d\Omega/d\varpi = 0$, this is a fundamentally different criterion. Moreover, for waves there is another corotation resonance in the disk, where C_S changes sign, which is an effect not captured by α models.

Second, equations (5.45) and (5.46), which describe transport by waves are fundamentally different in structure from equations (5.19)-(5.21) and depend on quantities such as $\delta\Sigma/\Sigma$ and Ω_P. The former is a function of time that depends in a complicated way on the details of the sonic instability, and the latter depends on the particular wave branch. Thus, although possible, it would be contrived to boil down an expression containing these quantities into an effective viscosity parameter; any such parameter would be a complicated function of the wave branch (upper, lower, or middle), azimuthal wavenumber, wave amplitude, Mach number, radius, etc.

Third, Navier Stokes viscosity with an enhanced value of the viscosity coefficient, ν, due to turbulence assumes *local* transport of angular momentum, which is the reason why the stress is proportional to $\partial\Omega/\partial\varpi$. When angular momentum is carried by waves over long distances, the transport is *nonlocal*. Thus any model, such as α viscosity, which is based on Navier Stokes

viscosity no longer applies. The possibility of non-local momentum transport has been hinted at by Inogamov & Sunyaev (2010), who postulated that angular momentum transport within the spreading layer (a BL with substantial extent in the θ direction) of a neutron star occurs by wave damping, in order to avoid excessive heating at the base of the layer.

For these reasons, we believe it is better to use equations (5.45) and (5.46) as they are for estimating angular momentum transport in the BL. We do not provide an effective α for our simulations, since it is incorrect to adopt an α viscosity model when angular momentum is transported by waves.

7 Discussion

The major result of this work is a new picture of the momentum, energy, and mass transfer in astrophysical BLs. We have found that the isothermal boundary layer naturally supports three $k_z = 0$ branches of acoustic modes when there is a supersonic velocity drop across it. These three types of acoustic modes are directly related to the three types of waves found for the isothermal vortex sheet in Belyaev & Rafikov (2012). Each of the three acoustic mode wave branches is associated with a different spatial morphology. However, two features common to all of the wave branches are emission of sound waves from the BL into both the star and the disk and the presence of two corotation radii – one within the disk and the other within the BL. The corotation radius within the disk lies inside a broad evanescent region (see Fig. 5.3).

The behavior of a particular mode is affected by the density stratification inside the star and the differential rotation inside the disk. The latter can potentially lead to the formation of a pattern of trapped shocks inside a resonant cavity in the disk near the BL. For this to occur, the inner edge of the evanescent region inside the disk must be well-separated from the BL.

An important point is that the dispersion relations for all three acoustic mode wave branches remain the same in 2D, 3D unstratified, and 3D stratified simulations. This can be seen from Tables 5.1 & 5.2 and Figure 5.2. Thus, the proposed picture of angular momentum transport in the BL is robust with respect to the dimensionality of the problem, strengthening the results previously obtained by Belyaev et al. (2012).

An acoustic mode with pattern speed Ω_P couples to fluid at the corotation radius within the BL ($\Omega(\varpi_c) = \Omega_P$), sapping it of angular momentum and driving accretion onto the central object. Thus, the fluid in the BL loses angular momentum to waves, which propagate away from the BL.

A fraction of the angular momentum radiated away from the BL is redeposited in the disk by wave dissipation in shocks, which drive the evolution of the disk surface density (§4.5). An additional factor in the time-evolution of the disk surface density is the time-dependence of Ω, which is connected with the temporal evolution of the radial pressure gradient in the disk. The time-dependence of Ω is an important effect in our naturally-evolving simulations. However, in a truly steady-state model of the BL, this contribution to the temporal evolution of the disk surface density would be absent.

The remainder of angular momentum lost by fluid in the BL is radiated into the star. Waves propagating away from the BL and into the star weaken in amplitude as a result of angular momentum conservation in a medium with a rising density. For this reason, waves inside the star do not shock — their nonlinear evolution is too weak and in our simulations they simply propagate out through the inner boundary of the simulation domain. In a real system, they would presumably be damped by some *linear* dissipation process such as conduction or radiation, ultimately transferring their angular momentum and energy to the star.

The radiation of angular momentum by waves away from the BL and its subsequent redistribution by damping of these waves are manifestly nonlocal processes, see §6. This casts serious doubt on the utility of semi-analytic models employing an (intrinsically local) α-prescription for viscosity in predicting BL structure and observational manifestations.

The general picture of acoustic wave-mediated BL dynamics advanced in this work may potentially have several important consequences that we discuss next. We warn, however, that until simulations with a more realistic equation of state are performed, some of the following predictions may be somewhat speculative.

7.1 Implications: Energy Transport in the BL

Waves propagating away from the BL carry not only angular momentum but also energy, which is released by accreting material as it is spun down. Wave damping in the disk or star results in the *nonlocal* release of this accretion energy — energy is deposited into the disk or star *at the location where the wave damps*. For example, the rate of thermal energy release in the disk per unit radial distance due to dissipation of waves with pattern speed Ω_P is

$$\frac{\partial \dot{E}_d}{\partial \varpi} = [\Omega_P - \Omega(\varpi)] \frac{\partial C_S}{\partial \varpi}, \tag{5.56}$$

where $\partial \dot{E}_d / \partial \varpi$ denotes the energy dissipation rate per unit radius (i.e. $(\partial \dot{E}_d / \partial \varpi) d\varpi$ is the energy dissipated in an annulus between ϖ and $\varpi + d\varpi$). By our definition, which is consistent with the definition in §6.4.2 of Binney & Tremaine (2008), $\dot{E}_d \leq 0$ and is non-zero only where $\partial C_S / \partial \varpi \neq 0$, (i.e. after the wave has shocked in the disk). This non-local energy transport may affect the structure and observational manifestations of the BL in the following way.

Conventional wisdom based on local α-models (e.g. Balsara et al. (2009)) states that the intense energy release has to take place in the BL itself, heating the gas there and considerably modifying the structure of the BL. This does not need to be true in our picture of wave-mediated transport: kinetic energy of material accreting through the BL can be transported away from the layer by waves and deposited in both the disk and the star. This can easily prevent the layer from overheating, meaning that its structure may be affected by accretional energy dissipation *weaker* than was thought before. This is a very important consequence of wave-driven transport.

Unfortunately, we cannot explore the effect of nonlocal energy transport on BL structure in our simulations directly, since they employ an isothermal equation of state and may not accurately capture the details of wave dissipation, especially inside the star. However, the removal of accretion energy from the BL in the form of waves that is a prediction of our model adds some support to the results of our purely isothermal simulations, which assume the fluid temperature does not change at all.

As we have seen in §4.2, at least during some periods of time $|C_s|$ going into star is much larger than that going into the disk. Since the energy density of a wave is directly proportional to its angular momentum density, $E_{\rm w} = \Omega_P L_{\rm w}$ (Binney & Tremaine, 2008), it is natural to expect that most of the accretional energy released in the BL is ultimately deposited in the star, rather than in the disk. As a result, heating of disk material by wave dissipation, which is distributed over a radial range $\Delta\varpi \sim \varpi_\star$ is unlikely to exceed the energy release in the inner disk due to conventional anomalous viscosity, such as MRI. The latter does not operate in our simulations since we have focused on the pure hydro case. Thus, if acoustic waves dominate transport in the BL one might expect the effective temperature of the inner disk and its overall spectrum *not to change much* compared to models not accounting for the presence of a BL, which seems to be precisely what is observed in some systems (Ferland et al., 1982; Polidan et al., 1990).

Depending on the nature of the accreting object, deep heating occurring inside the star as a result of wave dissipation may affect its internal structure. This effect is likely to be minimal for white dwarfs and neutron stars, which are supported by degeneracy pressure, but may be important for accreting pre-main sequence stars. Indeed, a typical T Tauri star accreting at the rate $\dot{M} = 10^{-6} M_\odot$ yr^{-1} (typical during the so-called FU Orioni outbursts) should have a rate of accretional energy release in the BL comparable to its own luminosity $\sim L_\odot$. Depending on the depth at which the waves excited in the BL dissipate, the nonlocal energy transport into the star may be able to affect its structure (Prialnik & Livio, 1985; Hartmann et al., 1997; Popham, 1997). In fact, Kenyon et al. (1988) and Popham et al. (1996) have previously shown that during FU Orioni outbursts, T Tauri stars may increase their radii by a factor ~ 2, which might be explained in our model by accretional energy release inside the star mediated by acoustic waves.

Observational signatures of the BL should also be affected by nonlocal transport of energy in the form of waves. Accretional energy carried away by waves is either buried in the star or transferred to the disk, both of which affect the spectrum of the BL. Given that wave dissipation is expected to only mildly heat the inner disk above its standard temperature set by the visco-turbulent heating rate (Shakura & Sunyaev, 1973), it may even be natural that the spectrum of the system will have a rather weak contribution from the BL as most of the liberated

energy is buried in the star. In the case of protostellar accretion, the sequestration of accretional energy released during FU Orioni outbursts inside the star may help explain the so-called "luminosity problem" — an apparent discrepancy between the expected accretion luminosities of protostars and their observed luminosities (Kenyon et al., 1990; Evans et al., 2009). BL formation is expected during FU Orioni outbursts with their high value of $\dot{M}$, which allows the disk to overcome magnetic truncation. A sizeable fraction of the energy released during these intense bursts of accretion can then be deposited deep inside the star by dissipation of acoustic modes. This energy would later leak out of the star, on a timescale which is of the order of the thermal timescale at the depth where the energy carried by waves is deposited.

The same process could potentially explain why BL emission is missing from some observations of accreting systems (Ferland et al., 1982; Polidan et al., 1990). In this framework, existing observations of high-energy spectral excesses from accreting systems, such as cataclysmic variables (Pandel et al., 2005), conventionally ascribed to BL emission, may in fact be due to some sort of coronal emission produced above the inner disk. Hard X-ray excesses found in accreting neutron star systems can be due to emission from a spreading layer (Gilfanov et al., 2003; Revnivtsev & Gilfanov, 2006), which has a different morphology from the BL.

7.2 Implications: stellar spinup

Deposition of angular momentum carried by waves deep into the star will cause stellar spinup to occur in a non-trivial fashion — angular momentum will be added to the star where waves dissipate, spinning up the inner parts of the star, which are hidden from direct view. As a result, the surface layers of the star may rotate *slower* than would be expected if the angular momentum of accreted material were deposited locally, near the BL. Unfortunately, we cannot directly explore this issue in detail in our simulations due to their simplified nature.

Previously Barker & Ogilvie (2010) have proposed a similar picture of inside-out stellar spinup by dissipation of tidally excited internal gravity waves near the stellar center. Clearly, this mode of stellar spinup is quite different from the predictions of standard BL models based on the notion of local α-viscosity (Kippenhahn & Thomas, 1978).

7.3 Implications: mixing in the BL

The standard paradigm of local viscosity in the BL generally assumes that angular momentum transport in the BL is facilitated by turbulence resulting from nonlinear saturation of some local instability such as Kelvin-Helmholtz (Kippenhahn & Thomas, 1978; Inogamov & Sunyaev, 2010), baroclinic (Piro & Bildsten, 2007), etc. Quite naturally, turbulence in the layer would also result in efficient mixing of fluid elements, leading to elemental homogeneity if different parts of the layer have different chemical compositions.

The situation is different if transport in the layer is facilitated by acoustic modes as we find in this work. Wave-driven transport in the supersonic case does not need an exchange of fluid elements to occur and thus does not necessarily result in efficient mixing inside the layer. This agrees with what we generally find in our simulations, which typically exhibit large-scale regular structures like the pattern of trapped shocks and show very little evidence for small-scale turbulence that would efficiently mix the layer. Thus, one may expect elemental mixing to be less prominent in our picture of the BL, compared to conventional models.

Having said that we point out that previously Belyaev et al. (2012) found using 2D simulations that the regular pattern of fluid motion in the vicinity of the layer can be occasionally interrupted by the short-term bursts of very irregular, rather turbulent behavior, which might result in efficient mixing of the layer. However, we do not observe such bursts in our 3D simulations, possibly because in 3D as opposed to 2D, our simulations do not develop an inflection point in the rotation profile within the BL. This important issue clearly needs further study.

7.4 Implications: variability of emission

Another implication of transport by waves is that they naturally produce temporal variability, since a pattern of acoustic modes rotating at a well-defined pattern speed invariably leads to periodic emission from the BL. Note that this mechanism of variability is completely different from previous suggestions such as a non-axisymmetric bulge in the disk near the BL (Popham,

1999) or shallow surface waves on a spreading layer (Piro & Bildsten, 2004a), which can provide additional sources of variability.

Our simulations do not implement radiative transfer and thus cannot directly link periodicity of fluid patterns to spectral variability of the BL. Nevertheless, temporal behavior of the BL has the potential to provide the most direct link between our work and observations, since from our dispersion relations for the upper, middle, and lower branches it is possible to work out the *frequency spectrum* of the BL. It is clear that it should feature a peak at frequency $\omega = m\Omega_P$, which corresponds to the apparent periodicity of the wave pattern to an external observer.

In our simulations, we typically find quite high values of $\omega = m\Omega_P \sim (4-6)\Omega(\varpi_\star)$ for the most commonly observed pattern of trapped lower branch modes. Moreover, from equation (5.31), we have the following lower bound for the frequency of the lower branch $m\Omega_P > M\Omega(\varpi_\star)/2$. This lower bound makes it unlikely that acoustic modes (or at the very least the lower mode, which is prevalent at late times in our simulations) can explain the origin of dwarf novae oscillations (DNOs) in cataclysmic variables (Warner, 2004), which typically have $M \sim 100$ and $m\Omega_P \lesssim \Omega(\varpi_\star)$ (Patterson, 1981). Moreover, if the wavelength of the dominant mode scales inversely with the width of the BL, then we expect $m \propto M^2$, implying very high frequency variability in real astrophysical systems.

On the other hand, the nature of our simulations may prevent us from seeing all possible sources of variability in the BL. In particular, a well known peculiarity of the isothermal equation of state used in this work is that the Brunt-Väisälä frequency

$$N^2 = (\gamma - 1)\frac{g^2}{s^2} \tag{5.57}$$

is zero if $\gamma = 1$. This means that gravity waves (g-modes) in the star are neutrally buoyant ($\omega = 0$) and thus do not show up in our simulations.

A more realistic equation of state having $\gamma > 1$ would be able to support both acoustic modes (p-modes) and gravity waves (g-modes) inside the star. The latter correspond to the lower ("$-$") sign in the dispersion relation (5.26) and have lower frequency than acoustic modes, potentially making them relevant for explaining DNOs. In principle, density waves in the disk could couple

to both g-modes and p-modes in the star, whereas only the latter coupling is possible for the isothermal equation of state. Thus, a real BL would likely support more than just the three acoustic wave branches described in this work and Belyaev & Rafikov (2012), and the dispersion relation for gravity modes in the star coupled to density waves in the disk remains to be worked out.

7.5 Future prospects

Our study employs two crucial simplifying assumptions: an isothermal EOS and lack of magnetic fields. Relaxing the first assumption requires using a more realistic EOS and properly characterizing radiation transfer in the system. In addition to previously mentioned consequences — e.g. appearance of new modes, see §7.1 & 7.4 — a better treatment of thermodynamics will have other implications.

For example, damping of modes excited in the BL depends on thermodynamics: it was previously shown by e.g. Lubow & Ogilvie (1998), Bate et al. (2002) that *thermal* stratification results in wave action channeling towards the low density regions, which also brings the shocking radius closer to the star. This would affect the dissipation pattern of waves, bringing disk regions where wave energy and momentum are deposited closer to the BL and making the BL more pronounced from an observational point of view. Additionally, compressional heating of accreted material in the BL can promote the formation of a spreading layer (Inogamov & Sunyaev, 1999; Piro & Bildsten, 2004b) on the surface of the accreting object.

Inclusion of magnetic field in our calculations should also have interesting consequences. First, it would result in the presence of MRI within the disk, which will provide a means of mass delivery from the outer disk to the BL region. At the moment, during the periods of lower mode dominance in our simulations, the fluid outside of the evanescent region in the disk remains unaffected by acoustic modes. As a result, mass depleted from the innermost disk does not get replenished by external accretion. Second, MRI would introduce turbulent motions in the disk, which may interact with the BL modes in a non-trivial fashion and enhance the importance of $k_z \neq 0$ modes for angular momentum transport within the disk. Third, the number of possible

wave branches the system could support would be even higher in the MHD case, since the disk would be able to support slow, fast, and Alfvén waves, which could couple to p and g-modes in the star. Finally, field amplification by intense shear in the BL would affect the internal dynamics of the layer. We leave the detailed exploration of these issues to future study.

Resources supporting this work were provided by the NASA High-End Computing (HEC) Program through the NASA Advanced Supercomputing (NAS) Division at Ames Research Center. We thank Jeremy Goodman and Anatoly Spitkovsky for useful discussions. The financial support for this work is provided by the Sloan Foundation and NASA grant NNX08AH87G.

Bibliography

Balbus, S. A. & Hawley, J. F. 1991, ApJ, 376, 214

Balbus, S. A. & Papaloizou, J. C. B. 1999, ApJ, 521, 650

Balsara, D. S., Fisker, J. L., Godon, P., & Sion, E. M. 2009, ApJ, 702, 1536

Barker, A. J. & Ogilvie, G. I. 2010, MNRAS, 404, 1849

Bate, M. R., Ogilvie, G. I., Lubow, S. H., & Pringle, J. E. 2002, MNRAS, 332, 575

Belyaev, M. A. & Rafikov, R. R. 2012, ApJ, 752, 115

Belyaev, M. A., Rafikov, R. R., & Stone, J. M. 2012, ApJ, 760, 22

Bergeron, P., Saffer, R. A., & Liebert, J. 1992, ApJ, 394, 228

Binney, J. & Tremaine, S. 2008, Galactic Dynamics: Second Edition (Princeton University Press)

Evans, II, N. J., Dunham, M. M., Jørgensen, J. K., Enoch, M. L., Merín, B., van Dishoeck, E. F., Alcalá, J. M., Myers, P. C., Stapelfeldt, K. R., Huard, T. L., Allen, L. E., Harvey, P. M., van Kempen, T., Blake, G. A., Koerner, D. W., Mundy, L. G., Padgett, D. L., & Sargent, A. I. 2009, ApJS, 181, 321

Ferland, G. J., Pepper, G. H., Langer, S. H., MacDonald, J., Truran, J. W., & Shaviv, G. 1982, ApJ, 262, L53

Gerwin, R. A. 1968, Reviews of Modern Physics, 40, 652

Ghosh, P. & Lamb, F. K. 1978, ApJ, 223, L83

Gilfanov, M., Revnivtsev, M., & Molkov, S. 2003, A&A, 410, 217

Glatzel, W. 1988, MNRAS, 231, 795

Goldreich, P. & Nicholson, P. D. 1989, ApJ, 342, 1075

Goldreich, P. & Tremaine, S. 1978, ApJ, 222, 850

Goodman, J. & Rafikov, R. R. 2001, ApJ, 552, 793

Hachisu, I. 1986, ApJS, 62, 461

Hartmann, L., Cassen, P., & Kenyon, S. J. 1997, ApJ, 475, 770

Hawley, J. F. & Balbus, S. A. 1991, ApJ, 376, 223

Inogamov, N. A. & Sunyaev, R. A. 1999, Astronomy Letters, 25, 269

Inogamov, N. A. & Sunyaev, R. A. 2010, Astronomy Letters, 36, 848

Kenyon, S. J., Hartmann, L., & Hewett, R. 1988, ApJ, 325, 231

Kenyon, S. J., Hartmann, L. W., Strom, K. M., & Strom, S. E. 1990, AJ, 99, 869

Kippenhahn, R. & Thomas, H.-C. 1978, A&A, 63, 265

Kluźniak, W. 1987, PhD thesis, Stanford Univ.

Landau, L. D. & Lifshitz, E. M. 1959, Fluid mechanics

Larson, R. B. 1990, MNRAS, 243, 588

Lesur, G. & Longaretti, P.-Y. 2005, A&A, 444, 25

Lubow, S. H. & Ogilvie, G. I. 1998, ApJ, 504, 983

Lynden-Bell, D. & Pringle, J. E. 1974, MNRAS, 168, 603

Miles, J. W. 1958, Journal of Fluid Mechanics, 4, 538

Narayan, R., Goldreich, P., & Goodman, J. 1987, MNRAS, 228, 1

Pandel, D., Córdova, F. A., Mason, K. O., & Priedhorsky, W. C. 2005, ApJ, 626, 396

Papaloizou, J. C. B. & Pringle, J. E. 1987, MNRAS, 225, 267

Patterson, J. 1981, ApJS, 45, 517

Patterson, J. 1984, ApJS, 54, 443

Pessah, M. E. & Chan, C.-k. 2012, ApJ, 751, 48

Piro, A. L. & Bildsten, L. 2004a, ApJ, 616, L155

Piro, A. L. & Bildsten, L. 2004b, ApJ, 610, 977

Piro, A. L. & Bildsten, L. 2007, ApJ, 663, 1252

Polidan, R. S., Mauche, C. W., & Wade, R. A. 1990, ApJ, 356, 211

Popham, R. 1997, ApJ, 478, 734

Popham, R. 1999, MNRAS, 308, 979

Popham, R., Kenyon, S., Hartmann, L., & Narayan, R. 1996, ApJ, 473, 422

Popham, R. & Narayan, R. 1995, ApJ, 442, 337

Prialnik, D. & Livio, M. 1985, MNRAS, 216, 37

Revnivtsev, M. G. & Gilfanov, M. R. 2006, A&A, 453, 253

Shakura, N. I. & Sunyaev, R. A. 1973, A&A, 24, 337

Vallis, G. K. 2006, Atmospheric and Oceanic Fluid Dynamics

Warner, B. 2004, PASP, 116, 115

A Dispersion Relation for Loosely Wound Modes Having $m \gg 1$ in the Disk

We derive here the dispersion relation for loosely wound modes having $m \gg 1$ in an isothermal disk (equation [5.24]). We assume a two dimensional setup in the ϖ-ϕ plane and ignore stratification. Thus, we replace the density ρ by the surface density Σ.

We start by explicitly writing the continuity and momentum equations in cylindrical coordinates (e.g. Binney & Tremaine (2008)), along with the isothermal equation of state. We denote the radial and azimuthal velocities by u and v respectively

$$\frac{\partial \Sigma}{\partial t} + \frac{1}{\varpi}\frac{\partial}{\partial \varpi}(\varpi \Sigma u) + \frac{1}{\varpi}\frac{\partial}{\partial \phi}(\Sigma v) = 0 \tag{5.58}$$

$$\frac{\partial u}{\partial t} + u\frac{\partial u}{\partial \varpi} + \frac{v}{\varpi}\frac{\partial u}{\partial \phi} - \frac{v^2}{\varpi} = -\frac{\partial \Phi}{\partial \varpi} - \frac{1}{\Sigma}\frac{\partial P}{\partial \varpi} \tag{5.59}$$

$$\frac{\partial v}{\partial t} + u\frac{\partial v}{\partial \varpi} + \frac{v}{\varpi}\frac{\partial v}{\partial \phi} + \frac{vu}{\varpi} = -\frac{1}{\varpi}\frac{\partial \Phi}{\partial \phi} - \frac{1}{\Sigma \varpi}\frac{\partial P}{\partial \phi} \tag{5.60}$$

$$P = \Sigma s^2 \tag{5.61}$$

Next, we assume a constant equilibrium disk density, which through the equation of state implies a constant equilibrium disk pressure. We also ignore self-gravity so there is no perturbation to the potential. Specifying first order quantities with a preceding δ, the linearized momentum and continuity equations then become

$$\frac{\partial \delta\Sigma}{\partial t} + \Omega\frac{\partial \delta\Sigma}{\partial \phi} + \frac{\Sigma}{\varpi}\frac{\partial \delta v}{\partial \phi} + \frac{\Sigma}{\varpi}\delta u + \Sigma\frac{\partial \delta u}{\partial \varpi} = 0 \tag{5.62}$$

$$\frac{\partial \delta u}{\partial t} + \Omega\frac{\partial \delta u}{\partial \phi} - 2\Omega\delta v + \frac{1}{\Sigma}\frac{\partial \delta P}{\partial \varpi} = 0 \tag{5.63}$$

$$\frac{\partial \delta v}{\partial t} + \Omega\frac{\partial \delta v}{\partial \phi} + \frac{\partial(\varpi\Omega)}{\partial \varpi}\delta u + \Omega\delta u + \frac{1}{\Sigma \varpi}\frac{\partial \delta P}{\partial \phi} = 0 \tag{5.64}$$

$$\delta P - s^2 \delta\Sigma = 0 \tag{5.65}$$

Taking perturbations in the form $\exp[i\int^{\varpi} d\varpi' k_{\varpi}(\varpi') + im(\phi - \Omega_P t)]$ and eliminating δP in favor of $\delta\Sigma$, the linearized set of equations becomes

$$im(\Omega - \Omega_P)\frac{\delta\Sigma}{\Sigma} + \frac{1}{\varpi}(1+in)\delta u + \frac{im}{\varpi}\delta v = 0 \tag{5.66}$$

$$im(\Omega - \Omega_P)\delta u - 2\Omega\delta v + \frac{is^2 n}{\varpi}\frac{\delta\Sigma}{\Sigma} = 0 \tag{5.67}$$

$$im(\Omega - \Omega_P)\delta v + \frac{\kappa^2}{2\Omega}\delta u + \frac{is^2 m}{\varpi}\frac{\delta\Sigma}{\Sigma} = 0, \tag{5.68}$$

where we have defined

$$n(\varpi) \equiv \varpi k_{\varpi}, \tag{5.69}$$

and used the epicyclic frequency

$$\kappa^2 = 2\Omega\left(2\Omega + \varpi\frac{d\Omega}{d\varpi}\right). \tag{5.70}$$

We can eliminate δv in equations (5.66) and (5.67) by using (5.68) to arrive at

$$i\left[m^2(\Omega - \Omega_P)^2 - \frac{s^2 m^2}{\varpi^2}\right]\frac{\delta\Sigma}{\Sigma} - \frac{m}{\varpi}\left[\frac{\kappa^2}{2\Omega} - (1+in)(\Omega - \Omega_P)\right]\delta u = 0 \tag{5.71}$$

$$\left[m^2(\Omega - \Omega_P)^2 - \kappa^2\right]\delta u - \frac{s^2 m}{\varpi}\left[2\Omega i - n(\Omega - \Omega_P)\right]\frac{\delta\Sigma}{\Sigma} = 0. \tag{5.72}$$

After some algebra, the above system of equations reduces to

$$\left[m^2(\Omega - \Omega_P)^2 - \frac{s^2 m^2}{\varpi^2}\left(1 + \frac{n^2}{m^2} - i\frac{n}{m^2}\right) - \kappa^2\right] + \frac{is^2}{\varpi^2(\Omega - \Omega_P)}\left[-2\Omega(i-n) - \frac{n\kappa^2}{2\Omega}\right] = 0. \tag{5.73}$$

We now make the approximations $m \gg 1$ and $n/m \ll 1$, and we shall refer to the latter as the "loose winding" approximation. In that case, equation (5.73) can immediately be simplified to

$$\left[m^2(\Omega - \Omega_P)^2 - \frac{s^2 m^2}{\varpi^2} - \kappa^2\right] + \frac{is^2}{\varpi^2(\Omega - \Omega_P)}\left(-2\Omega(i-n) - \frac{n\kappa^2}{2\Omega}\right) = 0. \tag{5.74}$$

We see that the term in the square brackets is the dispersion relation (5.24). Therefore, it is left to show that the other terms are negligible. To start, note that if we take in order of magnitude $\kappa \sim \Omega$, then the "other" terms are in order of magnitude

$$\frac{1}{m(\Omega - \Omega_P)} \left[\kappa \frac{s^2 m^2}{\varpi^2} \max\left(\frac{1}{m}, \frac{n}{m}\right) \right]. \tag{5.75}$$

It is straightforward to show that regardless of whether $\kappa \gg sm/\varpi$, $\kappa \ll sm/\varpi$, or $\kappa \sim sm/\varpi$ the term in equation (5.75) is smaller than $m^2(\Omega - \Omega_P)^2$ (and hence the dominant terms in the square brackets in equation (5.74)) by a factor of *at least*

$$\max\left(\frac{1}{m}, \frac{n}{m}\right) \ll 1. \tag{5.76}$$

Thus, as long as $m \gg 1$ and $n/m \ll 1$, the dispersion relation is accurately given by equation (5.24). In our simulations $10 < m < 40$, so the first of these conditions is typically well-satisfied. It is more difficult to get a handle on how well the "loose winding" condition is satisfied. However, the fact that Table 5.1 shows that there is agreement between theory and simulations at the several percent level is good justification for the use of equation (5.24).

B Dispersion Relation for an Isothermal Stratified Atmosphere in Cylindrical Geometry

We consider the dispersion relation for an unrotating stratified atmosphere in cylindrical geometry. Our aim is to justify our use of equation (5.30), which is valid for plane-parallel geometry. For simplicity, we assume two-dimensional perturbations in the $\varpi - \phi$ plane. However, we do not initially specify the form of the gravitational potential $\Phi(\varpi)$, only specifying it when necessary to make the calculations tractable.

As in Appendix A, we start with equations (5.58)-(5.61). We take small perturbations on top of the equilibrium state, and again denote small first order quantities with a preceding δ. The linearized forms of the continuity and momentum equations and the equation of state are then

given by

$$\frac{1}{\Sigma}\frac{\partial \delta\Sigma}{\partial t} - h_s^{-1}\delta u + \frac{1}{\varpi}\frac{\partial}{\partial \varpi}(\varpi \delta u) + \frac{1}{\varpi}\frac{\partial \delta v}{\partial \phi} = 0 \tag{5.77}$$

$$\frac{\partial \delta u}{\partial t} + \frac{1}{\Sigma}\frac{\partial \delta P}{\partial \varpi} + s^2 h_s^{-1}\frac{\delta\Sigma}{\Sigma} = 0 \tag{5.78}$$

$$\frac{\partial \delta v}{\partial t} + \frac{1}{\Sigma\varpi}\frac{\partial \delta P}{\delta \phi} = 0 \tag{5.79}$$

$$\delta P - s^2 \delta\Sigma = 0, \tag{5.80}$$

where we have defined

$$h_s(\varpi) \equiv -\left(\frac{1}{\Sigma}\frac{d\Sigma}{d\varpi}\right)^{-1} \tag{5.81}$$

to be the local scale height of the atmosphere.

We now assume perturbations in the form $f(\varpi)\exp[i(m\phi - \omega t)]$. Eliminating $\delta\Sigma$ and δv from equations (5.77)-(5.80) we have

$$-i\omega\frac{\delta P}{P} + \left[\frac{1}{\varpi}\left(1 - \frac{\varpi}{h_s}\right) + \frac{\partial}{\partial \varpi}\right]\delta u + i\left(\frac{m^2}{\varpi^2}\right)\frac{s^2}{\omega}\frac{\delta P}{P} = 0 \tag{5.82}$$

$$-i\omega\delta u + \frac{s^2}{P}\frac{\partial \delta P}{\partial \varpi} + \frac{s^2}{h_s}\frac{\delta P}{P} = 0. \tag{5.83}$$

Finally, eliminating δu in terms of δP we arrive at the second order differential equation in terms of $\delta P/P$

$$\left(\frac{\omega^2}{s^2} - \frac{m^2}{r^2}\right)\frac{\delta P}{P} + \left(1 - \frac{\varpi}{h_s}\right)\frac{1}{\varpi}\frac{\partial}{\partial \varpi}\left(\frac{\delta P}{P}\right) + \frac{\partial^2}{\partial \varpi^2}\left(\frac{\delta P}{P}\right) = 0. \tag{5.84}$$

We can gain insight by comparing the differential equation (5.84) to the second order equation for $\delta P/P$ in the plane-parallel case for constant gravity with stratification in the x-direction. The latter is given by Vallis (2006) as

$$\left(\frac{\omega^2}{s^2} - k_y^2\right)\frac{\delta P}{P} - \frac{1}{h_s}\frac{\partial}{\partial x}\left(\frac{\delta P}{P}\right) + \frac{\partial^2}{\partial x^2}\left(\frac{\delta P}{P}\right) = 0. \tag{5.85}$$

Equation (5.84) reduces *locally* to equation (5.85) at a given radius $\overline{\varpi}$ in the limit

$$\frac{h_s(\overline{\varpi})}{\overline{\varpi}} \ll 1, \tag{5.86}$$

if we make the association $k_y \rightarrow m/\overline{\varpi}$. In our simulations, $h_s/\varpi \sim .02$, so the condition (5.86) is well-satisfied. The local equivalence of equations (5.85) and (5.84) thus provides a justification for our use of an effective radius in the dispersion relation (5.30).

C Parseval's Theorem

In this Appendix, we go through the details of the derivation of equation (5.45) and the application of Parseval's theorem. Starting from equations (5.43) and (5.44), we can write

$$C_{S,m}(\varpi) = \sum_{m=-\infty,\ m\neq 0}^{\infty} \left(\frac{k_\varpi \varpi}{m}\right) \frac{\pi s^4 \Sigma_0}{\Omega_P^2} \left(\frac{\delta\Sigma_m}{\Sigma_0}\right)^2. \tag{5.87}$$

Here, modes with positive m are used to denote outgoing waves and modes with negative m to denote incoming waves; under this definition $k_\varpi(m) = k_\varpi(-m)$ and k_ϖ is always positive. Note, the $m = 0$ mode does not transport angular momentum and should be excluded from the sum.

Taking only outgoing modes in equation (5.87), we can write

$$C_{S,m}(\varpi) = \frac{\pi s^4 \Sigma_0}{\Omega_P^2 \Sigma_0^2} \sum_{m=1}^{\infty} \left(\frac{k_\varpi \varpi}{m}\right) \delta\Sigma_m^2. \tag{5.88}$$

Taking a characteristic value of m corresponding to the dominant mode, $\overline{m}$, we can take the $k_\varpi \varpi/m$ term out of the summation in equation (5.87) and write

$$C_{S,m}(\varpi) = \frac{\pi s^4 \Sigma_0}{\Omega_P^2 \Sigma_0^2} \left(\frac{k_\varpi(\overline{m})\varpi}{\overline{m}}\right) \sum_{m=1}^{\infty} \delta\Sigma_m^2. \tag{5.89}$$

Next we use Parseval's theorem to complete the dervation. Parseval's theorem can be stated as

$$\frac{1}{\pi}\int_0^{2\pi} d\phi \left(\delta\Sigma(\phi)\right)^2 = \frac{1}{\pi}\sum_{m=1}^{\infty}\delta\Sigma_m^2 \int_0^{2\pi} d\phi \left[\sin(m\phi - \phi_0(m))\right]^2 \tag{5.90}$$

$$= \sum_{m=1}^{\infty}\delta\Sigma_m^2, \tag{5.91}$$

where $\phi_0(m)$ is a phase offset for each mode. Using Parseval's theorem to replace the summation with an integral in equation (5.89), we arrive at equation (5.45).

D Mass Accretion Rate Due to Weak Shocks.

The mass accretion rate through the disk can be expressed through the divergence of the angular momentum current $C_{S,\mathrm{w}}$ due to waves (acoustic modes) as a result of their dissipation at shock fronts (Lynden-Bell & Pringle, 1974)

$$\dot{M}(r) = \left(\frac{dl}{d\varpi}\right)^{-1}\frac{\partial C_{S,\mathrm{w}}}{\partial\varpi}, \tag{5.92}$$

where $l = \Omega(\varpi)\varpi^2$ is the specific angular momentum for circular orbits. The subsequent derivation is based in part on the work by Larson (1990).

It is difficult to calculate $\partial C_{S,\mathrm{w}}/\partial\varpi$ from first principles. However, one can relate $\partial C_{S,\mathrm{w}}/\partial\varpi$ to the energy dissipation rate in shocks. The reason behind using this approach is that dissipation along a given fluid element's trajectory occurs only at the shocks (unlike azimuthal acceleration and deceleration due to pressure gradients that occurs also between the shocks) — between the shocks the flow is adiabatic (in the absence of numerical dissipation).

The relation between the rate of energy dissipation by the shock in an annulus of width $d\varpi$, $\dot{E}_{\mathrm{s}}$, and the wave energy dissipation rate in the same annulus, $\dot{E}_{\mathrm{w}}$, *in steady state* is given by (Goodman & Rafikov, 2001; Binney & Tremaine, 2008)

$$\dot{E}_{\mathrm{s}} = \frac{\Omega_P - \Omega(\varpi)}{\Omega_P}\dot{E}_{\mathrm{w}}. \tag{5.93}$$

The dissipated wave energy in the annulus and the angular momentum current through its edges are related by $\dot{E}_{\rm w} = \Omega_P(\partial C_{S,{\rm w}}/\partial\varpi)d\varpi$. Thus equation (5.93) can be rewritten as

$$\frac{\partial \dot{E}_{\rm s}}{\partial \varpi} = (\Omega_P - \Omega(\varpi))\frac{\partial C_{S,{\rm w}}}{\partial \varpi}. \tag{5.94}$$

Note that this formula is applicable for any dissipation process, not necessarily dissipation in shocks, although we shall assume the latter in what follows.

In an annulus of width $d\varpi$ the mass $dm = n\,|\Omega_P - \Omega(\varpi)|\,\varpi\Sigma_0 dt d\varpi$ crosses one of the n shocks per time dt. For the upper branch, $n = m$, since there are only outgoing shocks, whereas for the lower branch $n = 2m$, since each outgoing shock is reflected into an incoming shock. This leads to the formula

$$\frac{\partial \dot{E}_{\rm s}}{\partial \varpi} = -n|\Omega_P - \Omega(\varpi)|\varpi\Sigma_0\frac{dE}{dm} \tag{5.95}$$

Combining equations (5.94) and (5.95), we have

$$\frac{\partial C_{S,{\rm w}}}{\partial \varpi} = -{\rm sgn}[\Omega_P - \Omega(\varpi)]n\varpi\Sigma_0(dE/dm) \tag{5.96}$$

$$\dot{M}(r) = -{\rm sgn}[\Omega_P - \Omega(\varpi)]\left(\frac{dl}{d\varpi}\right)^{-1} n\varpi\Sigma_0(dE/dm) \tag{5.97}$$

Note, these formulas only apply *in steady state*, which was an assumption implicit in equation (5.93).

E Dissipation Rate in the Isothermal Limit

We derive here a formula for the energy dissipation per unit mass due to a shock in the isothermal limit, $\gamma \to 1$. This is important in the context of our simulations, since the entropy is not well-defined if $\gamma = 1$ This can be seen from the expression for the entropy per unit mass for

an ideal gas

$$\frac{dS}{dm} = \frac{s^2}{T\gamma(\gamma-1)} \ln\left(P\rho^{-\gamma}\right) \tag{5.98}$$

is ill-defined if $\gamma = 1$.

The energy dissipation rate of the wave used in equation (5.47) for an isothermal shock[1] is given by

$$\frac{dE}{dm} = T\Delta\frac{dS}{dm} \tag{5.99}$$

where the Δ denotes the difference in a quantity across the shock. It is important to show that $\Delta dS/dm$ and hence dE/dm converges to a well-defined value when $\gamma \to 1$. We perform this below, and derive an exact result for the dissipation rate dE/dm in the isothermal limit. Larson (1990) has given an approximate expression for dE/dm valid for arbitrary γ in the limit of weak shocks. We note that our exact expression (equation [5.49]) matches the expression of Larson (1990) when $\gamma = 1$ (equation [5.48]) to leading order (third) in $\Delta\Sigma/\Sigma$.

To start, we combine equations (5.98) and (5.99) to write

$$\frac{dE}{dm} = \frac{s^2}{\gamma(\gamma-1)} \ln\left[\frac{P_1}{P_0}\left(\frac{\rho_1}{\rho_0}\right)^{-\gamma}\right], \tag{5.100}$$

where the subscripts "0" and "1" denote pre and postshock quantities respectively. Using the Rankine-Hugoniot relations and defining $\gamma = 1 + \delta$ and $\epsilon \equiv \rho_1/\rho_0 - 1$, equation (5.100) becomes

$$\frac{dE}{dm} = \frac{s^2}{(1+\delta)\delta} \ln\left[\frac{2+\epsilon(2+\delta)}{2-\epsilon\delta}(1+\epsilon)^{-(1+\delta)}\right]. \tag{5.101}$$

[1] An isothermal shock means that the temperature is the same on either side of the shock but not necessarily that $\gamma = 1$.

Next, we take the isothermal limit $\delta \to 0$ and expand the expression inside the logarithm in powers of δ. Equation (5.101) then becomes

$$\frac{dE}{dm} = \frac{s^2}{(1+\delta)\delta} \ln \left[1 + \left(\frac{\epsilon(2+\epsilon) - (1+\epsilon)\ln(1+\epsilon)}{2(1+\epsilon)} \right) \delta + \mathcal{O}\left(\delta^2\right) \right]. \tag{5.102}$$

Expanding the logarithm in powers of δ and keeping the highest order term we arrive at equation (5.49)

$$\frac{dE}{dm} = s^2 \frac{\epsilon(2+\epsilon) - 2(1+\epsilon)\ln(1+\epsilon)}{2(1+\epsilon)}. \tag{5.103}$$

Note that this expression is valid for all values of ϵ.

Chapter 6

Angular Momentum Transport: MHD Simulations.

Abstract

We perform global unstratified 3D magnetohydrodynamic simulations of an astrophysical boundary layer (BL) – an interface region between an accretion disk and a weakly magnetized accreting object such as a white dwarf – with the goal of understanding the effects of magnetic field on the BL. We use cylindrical coordinates with an isothermal equation of state and investigate a number of initial field geometries including toroidal, vertical, and vertical with zero net flux. Our initial setup consists of a Keplerian disk attached to a non-rotating star. In a previous work, we found that in hydrodynamical simulations, sound waves excited by shear in the BL were able to efficiently transport angular momentum and drive mass accretion onto the star. Here we confirm that in MHD simulations, waves serve as an efficient means of angular momentum transport in the vicinity of the BL, despite the magnetorotational instability (MRI) operating in the disk. In particular, the angular momentum current due to waves is at times larger than the angular momentum current due to MRI. Our results suggest that angular momentum transport in the BL and its vicinity is a global phenomenon occurring through dissipation of waves and shocks. This point of view is quite different from the standard picture of transport by a local anomalous turbulent viscosity. In addition to angular momentum transport, we also study magnetic field amplification within the BL. We find that the field is indeed amplified in the BL, but only by a factor of a few and remains subthermal.

1 Introduction

The mechanism of angular momentum transport in the boundary layers (BLs) of accreting compact objects and stars is an open problem that is both interesting from a physical point of view and important for modeling BL spectra from these sources (Narayan, 1992; Popham & Narayan, 1992, 1995; Inogamov & Sunyaev, 1999; Piro & Bildsten, 2004). In this work, we shall focus on the case of an accretion disk that does not undergo disruption by the magnetic field of an accreting opbject (for the case of magnetically disrupted disk see Ghosh & Lamb (1978), Koldoba et al. (2002)) and extends all the way to the surface of the compact object or star. Such a situation is expected to be naturally realized in weakly magnetized neutron stars producing Type-I X-ray bursts as well as during FU Orioni outbursts in pre-main sequence stars and dwarf nova outbursts in cataclysmic variables when the mass accretion rate is high.

Accretion of matter through the BL must be accompanied by the angular momentum transport in the layer, but the nature of this transport has remained elusive. The BL is linearly stable to the magnetorotational instability (MRI; Velikhov (1959); Chandrasekhar (1960); Balbus & Hawley (1991)) that is thought to give rise to anomalous viscosity in the bulk of well-ionized accretion disks, because the angular velocity, Ω, necessarily *increases* with radius in this region. Of course linear stability does not imply a nonturbulent flow. Turbulence, once generated by some nonlinear mechanism, can persist without decaying in certain classes of rotating, linearly stable hydrodynamical flows (Lesur & Longaretti, 2005). However transport mechanisms, both magnetic and hydrodynamic involving an anomalous viscosity have never been definitively demonstrated to operate inside the BL.

Recently Belyaev & Rafikov (2012) and Belyaev et al. (2012a,b) showed both theoretically and computationally that non-axisymmetric acoustic modes are excited in the BL when it is thin in comparison with the stellar radius. These acoustic modes manifest themselves as sound waves that propagate away from the boundary layer, efficiently transporting angular momentum into both the star and the disk and driving accretion. However, the studies of Belyaev & Rafikov (2012), Belyaev et al. (2012a,b) were purely hydrodynamical, and it is the purpose of the present

study to check their results on angular momentum transport by waves generated in the BL in the presence of a magnetic field.

There are several reasons why the MHD case could be fundamentally different from the hydrodynamical case. First, the presence of a seed magnetic field in the disk leads to turbulence generated by the MRI. Potentially, the turbulence could interact with the acoustic modes in the disk, modifying their properties or washing them out completely. Second, magnetic field advected into the BL by accreting gas will be amplified by the shear present there (Pringle, 1989; Armitage, 2002). A strongly magnetized BL could have different properties than an unmagnetized one, again influencing the properties of acoustic modes. Third, magnetic field in the BL can give rise to other MHD effects such as the Tayler-Spruit dynamo (Tayler, 1973; Spruit, 1999, 2002), which may produce additional momentum transport in the BL (Piro & Bildsten, 2007).

One of our aims in this work is to determine the extent to which a magnetic field affects the properties of and angular momentum transport by waves generated in the BL. We find that in the presence of a magnetic field, the acoustic modes studied by Belyaev et al. (2012a,b) become magnetosonic modes. However, when the ratio of gas pressure to magnetic pressure $\beta \gg 1$, the magnetic field has only a weak, $\mathcal{O}\left(\beta^{-1}\right)$ effect on the dynamics of acoustic modes. In our simulations, β is indeed large, and we find that magnetosonic modes play an important role in angular momentum transport in the BL and its vicinity.

Previously, Armitage (2002) and Steinacker & Papaloizou (2002) each performed MHD simulations of the BL. However, these studies did not reveal the importance of the transport by waves, and we discuss our work in relation to theirs in §7. Also, Heinemann & Papaloizou (2009a), Heinemann & Papaloizou (2009b), Heinemann & Papaloizou (2012) studied angular momentum transport by spiral density waves in MRI turbulent disks, which were sourced by vorticity generated in non-linear MRI turbulence. However, the mechanism for driving these waves is entirely different from the mechanism for generating the magnetosonic modes discussed here. The latter are sourced by shear in the BL and launched away from it into both the star and the disk.

There have also been a number of other analytical and numerical studies of disk wave phenomena in the vicinity of the innermost stable circular orbit of a black hole and near the BL

(Li et al., 2003; Li & Narayan, 2004; Lai & Tsang, 2009; Tsang & Lai, 2009a,c,b; Fu & Lai, 2012). However, these studies were primarily addressing the possible connection between the non-axisymmetric modes and quasi-periodic oscillations observed in accreting objects, whereas our main focus is on the fundamental nature of the angular momentum transport within the BL. Moreover, with the exception of Tsang & Lai (2009c) and Li & Narayan (2004), these studies did not include a magnetic field.

The chapter is organized as follows. In §2 we introduce notation and define quantities used throughout the chapter when discussing angular momentum transport. Then, in §3 we talk about angular momentum transport by MRI in the disk and show that our results agree with previous studies of the MRI. §5 discusses how acoustic modes studied by Belyaev et al. (2012a,b) are modified by the presence of a magnetic field, becoming magnetosonic modes. Finally, §6 discusses angular momentum transport by these magnetosonic modes in the star, BL, and inner disk.

2 Angular Momentum Transport: Equations

In this section, we introduce the notation used throughout this chapter when discussing angular momentum transport. When analyzing simulation results, we perform both density weighted and volume weighted averages of quantities over the z and ϕ directions. A volume weighted average is denoted by an overline:

$$\overline{f} \equiv \frac{1}{\Delta z \Delta \phi} \int dz d\phi f, \tag{6.1}$$

where Δz and $\Delta \phi$ are the extents of the simulation domain in the z and ϕ dimensions respectively. A density weighted average is denoted by angle brackets:

$$\langle f \rangle \equiv \frac{1}{\Delta z \Delta \phi \Sigma_0} \int dz d\phi \rho f, \tag{6.2}$$

where $\Sigma_0 = \overline{\rho}$ is the volume weighted average density.

For ideal MHD, the one dimensional equation of angular momentum transport can be formulated in terms of density weighted and volume weighted averages as (Balbus & Papaloizou, 1999)

$$\frac{\partial}{\partial t}\left(\varpi^2\Sigma_0\Omega\right) + \frac{1}{\varpi}\frac{\partial}{\partial \varpi}\left(\varpi^3\Omega\Sigma_0\langle v_\varpi\rangle + \varpi^2\overline{T_{\varpi\phi}}\right) \;=\; 0, \tag{6.3}$$

where $\Omega \equiv \langle v_\phi\rangle/\varpi$ is the density-weighted angular velocity, and $T_{\varpi\phi}$ is the ϖ, ϕ component of the stress tensor

$$T_{\varpi\phi} \equiv \rho v_\varpi\left(v_\phi - \varpi\Omega\right) - \frac{B_\varpi B_\phi}{\mu}. \tag{6.4}$$

The first term in the space derivative in equation (6.3) equals the advected angular momentum current, C_A, divided by 2π, and the second term equals the stress angular momentum current, C_S, divided by 2π. For a steady state disk, $C_A + C_S = 0$, although the disks in our simulations are not in steady state, and undergo temporal evolution.

The stress current, C_S, can be further decomposed into hydrodynamical and magnetic terms

$$C_{S,H}(\varpi,t) \;\equiv\; 2\pi\varpi^2\Sigma_0\langle v_\varpi\left(v_\phi - \varpi\Omega\right)\rangle \tag{6.5}$$

$$C_{S,B}(\varpi,t) \;\equiv\; -2\pi\varpi^2\frac{\overline{B_\varpi B_\phi}}{\mu} \tag{6.6}$$

$$C_S \;=\; C_{S,H} + C_{S,B}. \tag{6.7}$$

Note that C_S includes contributions to the stress from both waves and the action of turbulence.

Finally, we define an α parameter to parametrize the angular momentum transport rate by turbulent viscosity. There are many possible definitions for α, especially in the context of the BL (Narayan, 1992; Popham & Narayan, 1995), but the ones used in this work are

$$\alpha(\varpi,t) \;\equiv\; \frac{\overline{T_{\varpi\phi}}}{\overline{P}} = \frac{\overline{T_{\varpi\phi}}}{\Sigma_0 s^2} \tag{6.8}$$

$$\alpha_\nu(\varpi,t) \;\equiv\; \frac{\overline{T_{\varpi\phi}}}{\Sigma_0 s H d\Omega/d\ln\varpi}. \tag{6.9}$$

The first form of α is just the ratio of the stress to the pressure. The second is the α for a turbulent anomalous viscosity (Shakura & Sunyaev, 1973; Lynden-Bell & Pringle, 1974), where H is the vertical scale of the problem. In an astrophysical disk, $H = s/\Omega$ and increases radially for constant s. Our simulations, however, are in cylindrical geometry and $H = \Delta z$, where Δz, the extent of the simulation domain in the vertical direction, is a constant.

Analogous to the splitting of C_S into hydrodynamical and magnetic terms (equation [6.7]), it is useful to split α into hydrodynamical and magnetic components:

$$\alpha_H(\varpi, t) \equiv \frac{\langle v_\varpi \left(v_\phi - \varpi\Omega\right)\rangle}{s^2} \tag{6.10}$$

$$\alpha_B(\varpi, t) \equiv -\frac{\overline{B_\varpi B_\phi}}{\mu\Sigma_0 s^2} \tag{6.11}$$

$$\alpha = \alpha_H + \alpha_B. \tag{6.12}$$

Although α is a useful parametrization of angular momentum transport by MRI turbulence in the disk, it is not applicable to transport by waves. In the latter case, the relevant quantity is C_S (Belyaev et al., 2012b), and since angular momentum is transported by both waves and MRI turbulence in our simulations, we need to consider both C_S and α when analyzing results.

Another useful parameter we refer to often when analyzing simulations is β (equation [3.11]), and from now on we take

$$\beta(\varpi, t) \equiv \frac{\Sigma_0 s^2}{\overline{B^2}/2\mu}. \tag{6.13}$$

3 Angular Momentum Transport by MRI in the Disk

In this section, we focus on angular momentum transport in the disk and show that we obtain resolved MRI turbulence in our simulations. Thus, this section serves as a check of our simulations against previous work, and the reader who is primarily interested in new results about wave transport of angular momentum may choose to skip ahead to the next section.

3.1 Magnetic Pitch Angle

The primary diagnostic we use to check that the disk reaches a resolved quasi-steady state of MRI turbulence is the magnetic pitch angle

$$\theta_B \equiv \frac{\sin^{-1}(\alpha_B \beta)}{2}. \tag{6.14}$$

Equation (6.14) gives an approximation for the angle of the magnetic field with respect to the ϕ direction if $B_\phi \gg B_\varpi$ and $B_\varpi \gg B_z$ (Guan et al., 2009). Sorathia et al. (2012) found that θ_B was a particularly good indicator of convergence, since it varies monotonically with resolution and converges to a value of $\theta_B \approx 13^\circ$ in resolved simulations. A similar indicator of convergence is the relation $\alpha\beta \approx 1/2$ (Guan et al., 2009; Hawley et al., 2011; Sorathia et al., 2012). However, α includes both hydrodynamical and magnetic stresses, whereas α_B is calculated using only magnetic stresses. We find in our simulations that the hydrodynamical stress due to waves is non-negligible in the disk, but waves do not contribute to the magnetic stress. Thus, a diagnostic based on α_B is strongly preferred to one based on α, when assessing the convergence of MRI turbulence in a simulation that includes a BL.

Fig. 6.1 shows radius time plots of θ_B for simulations M9d,e,f in the annulus $1 \leq \varpi \leq 3$. Ignoring the region near $\varpi = \varpi_\star = 1$ where the rotation profile is strongly non-Keplerian, we see that $\theta_B \approx 12 - 14^\circ$ in the disk proper for the NAF and ZNF simulations (panels b and c) once MRI turbulence is fully developed. In the NVF simulations, $\theta_B \approx 12 - 14^\circ$ in the inner disk, but rises with radius. Nevertheless, the values of θ_B observed in our simulations are in good agreement with Sorathia et al. (2012). This gives us confidence that we have properly resolved the MRI in the disk.

3.2 Convergence Across Different Resolutions

The second diagnostic of convergence we perform is a measurement of the r.m.s. volume weighted average of B_ϖ, B_ϕ, and B_z for simulations with the same initial magnetic field geometry, but having a different resolution. Panels a,b,c of Fig. 6.2 show r.m.s. averages of B_ϖ, B_ϕ, and B_z at

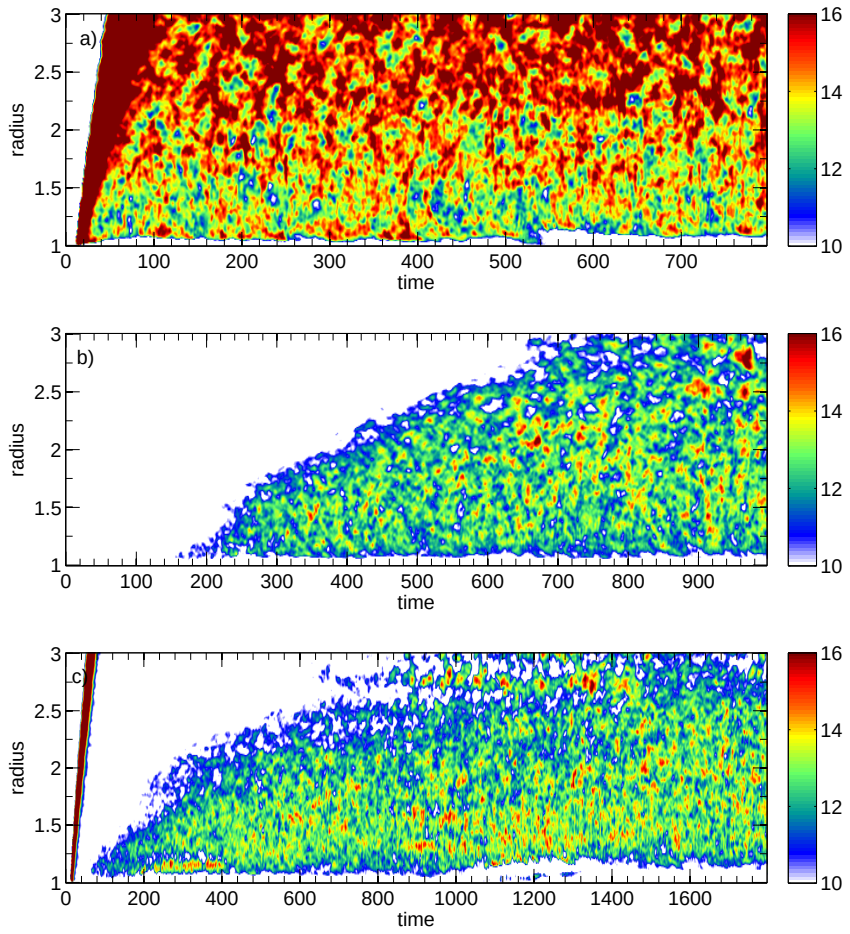


Figure 6.1: Panels a,b,c show θ_B for simulations M9d (NVF), M9e (NAF), and M9f (ZNF). The band on the left hand side of panel c is due to a transient burst of activity that occurs when the MRI first goes nonlinear. Note the different scale on the time axis in the figures.

$t = 400$ for NVF simulations (M9a,d), NAF simulations (M9b,e), and ZNF simulations (M9c,f), respectively. We see that the NVF and NAF simulations are converged, although the magnetic field in the outer disk of the NAF simulation is still approaching a steady state. The reason why we did not perform the convergence study at a later time is that it was too expensive to run the high resolution simulations beyond a time of $t = 450$.

In the ZNF case, magnetic field components for the low resolution simulation have a higher amplitude than for the high resolution simulation, and we have checked that this is true at all times, not just at $t = 400$. However, in (§3.1) we showed that MRI turbulence is resolved in ZNF simulations based on the pitch angle indicator.

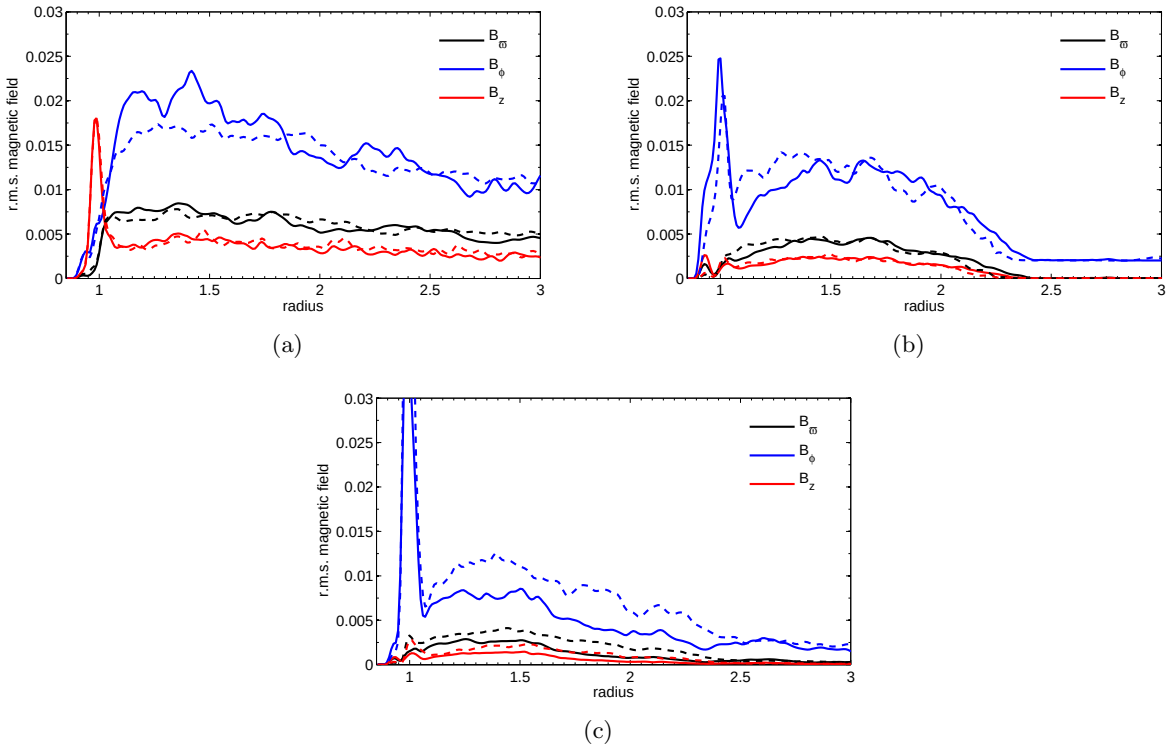


Figure 6.2: The volume weighted r.m.s magnetic field components at $t = 400$ for NVF simulations (panel a), NAF simulations (panel b), and ZNF simulations (panel c). In each case, the solid line is the simulation with the higher z-resolution.

Taken together, these two pieces of information suggest that MRI turbulence in our ZNF simulations is resolved, but that for a given simulation, the r.m.s field strength in the saturated state of MRI turbulence is influenced by the effective numerical viscosity and resistivity, which depend on the grid resolution (Fromang & Papaloizou, 2007). In order to make the results of ZNF simulations independent of resolution, we could add explicit viscosity and resistivity (Fromang et al., 2007).

However, given the exploratory nature of this chapter, the exact value of the viscous and resistive coefficients is of secondary importance. What is more important is that for a given value of these coefficients, MRI turbulence is properly resolved, which is indeed the case according to the pitch angle indicator of §3.1.

3.3 The Value of α due to MRI Turbulence in the Disk

The most important parameter that characterizes transport by MRI turbulence in the disk is α. However, α in our simulations is not a constant and is a function of both time and radius. One reason for this is that the timescale for instability is longer in the outer parts of the disk than in the inner parts, so the inner parts reach a quasi-steady state faster. However, even in the quasi-steady state, we find $\alpha \propto \varpi^{-3/2}$, which is not a surprising scaling, and implies a constant value of α_ν (equation [6.9]). The reason α and α_ν have a different radial dependence in simulations is that the height of the simulation domain, Δz is fixed, whereas the scale height in a Keplerian disk goes as $H = s/\Omega \propto \varpi^{3/2}$ for constant s. Thus, we define

$$\alpha_{\rm eff} \equiv \alpha \varpi^{3/2}. \tag{6.15}$$

Since, $s/\Omega = \Delta z$ at $\varpi = \varpi_\star = 1$, $\alpha_{\rm eff}$ can be thought of as the "effective" value of α for a Keplerian disk, based on our simulation results. The assumption here is that the angular momentum transport rate is proportional to the vertical scale of the problem, which is fixed for our simulations but goes as $H \propto \varpi^{3/2}$ for a Keplerian disk with a constant value of s.

Another complication to measuring the α due to MRI turbulence is the presence of waves emitted from the BL, which contribute to the value of α in the disk. Therefore, rather than showing $\alpha_{\rm eff}$ directly, we show $\alpha_{\rm B,eff}$, which is simply the component of $\alpha_{\rm eff}$ that is due to magnetic stresses (i.e. $\alpha_{\rm B,eff} = \alpha_B \varpi^{3/2}$). As mentioned in §3.1, $\alpha_{\rm B}$ is insensitive to waves, which contribute primarily to the hydrodynamical stress. Studies of the MRI typically find that $\alpha \approx 5/4 \alpha_B$ (Sorathia et al., 2012), which also roughly holds for our simulations.

Fig. 6.3 shows radius time plots of $\alpha_{\rm B,eff}$ for simulations M9d,e,f. Once a quasi-steady state has been reached, the value of $\alpha_{\rm B,eff}$ for the NVF simulation (M9d) is $\alpha_{\rm B,eff} \approx .02 - .03$, for the NAF simulation (M9e) is $\alpha_{\rm B,eff} \approx .0075 - .0125$, and for the ZNF simulation (M9f) is $\alpha_{\rm B,eff} \approx .004 - .01$. These values of α are consistent with those obtained by Steinacker & Papaloizou (2002) in their BL simulations. However, the value of α in ZNF simulations does depend on the resolution, for the same reasons as the r.m.s. magnetic field value depends on the resolution (§3.2).

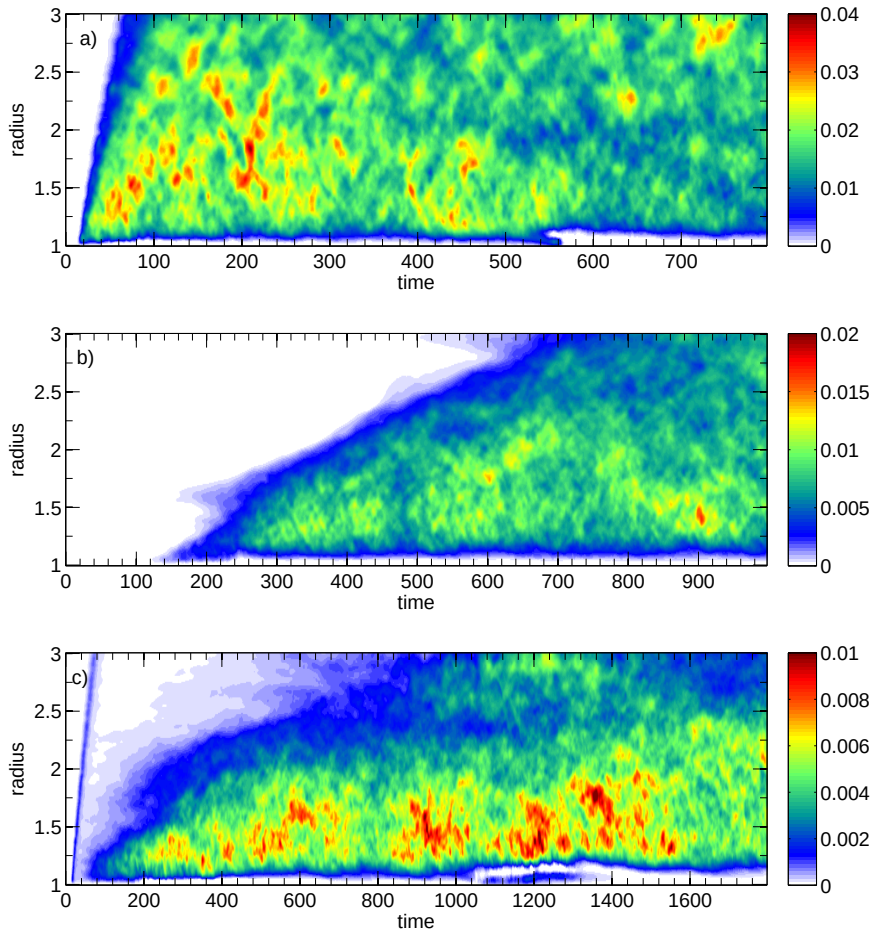


Figure 6.3: Panels a,b,c show $\alpha_{\rm B,eff}$ for simulations M9d,e,f respectively. Note the different scale on the time axis in the figures.

4 Magnetic Field Amplification in the BL

It has been speculated that the strong shear present in the BL can amplify the magnetic field to the point that $\beta < 1$ (Pringle, 1989). Armitage (2002) observed amplification of the field in the BL in MHD simulations with an isothermal equation of state, but found $\beta^{-1} \lesssim .1 - .2$, everywhere throughout the simulation domain, including the BL. His setup assumed initial net vertical field and is most similar to our NVF model.

We also observe amplification of the B_ϕ field component in the BL in our simulations, although the amplification is highly time-variable. Referring back to Fig. 6.2, we see a bump in B_ϕ within the BL for the ZNF case (panel c), which clearly indicates shear amplification of the

B_ϕ component. There are also bumps in B_z and B_ϕ in panels a and b of Fig. 6.2, respectively. However, since panels a and b correspond to simulations having net vertical and azimuthal flux, respectively, the bump in B_z and B_ϕ within the BL is due, at least in part, to a combination of flux freezing and compression of accreted material from the disk on the surface of the star (§6.1).

To disentangle amplification of magnetic field due to flux freezing and compression from shear amplification, we plot the maximum (in ϖ) of the r.m.s averaged field (in z and ϕ) as a function of time in Fig. 6.4 for simulations M9d,e,f. We see that the NVF and ZNF simulations (black and red curves) exhibit peaks, and the NVF simulation (black curve), in particular, has one large peak at $t \approx 560$. The NAF simulation (blue curve), on the other hand, exhibits a steady increase and contains small local peaks. The steady increase can be understood as compression of advected azimuthal field within the BL.

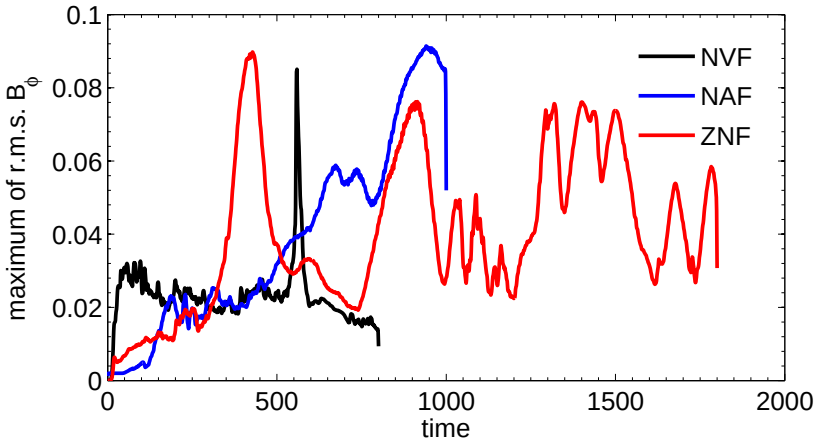


Figure 6.4: Plot of the maximum (in ϖ) of the r.m.s average (in z and ϕ) of B_ϕ as a function of time for simulations M9d,e,f (NVF, black curve; NAF, blue curve; ZNF, red curve). The spikes correspond to transient shear amplification of the B_ϕ component of the field within the BL.

The peaks in Fig. 6.4 are due to transient shear amplification of the field in the BL, and the baseline level in the NVF simulations (black curve) is simply set by the value of B_ϕ in the saturated state of MRI turbulence in the disk. Fig. 6.5 shows the r.m.s value of B_ϕ as a function of radius from simulation M9d at times $t = 400$ when there is little or no amplification and $t = 560$, which corresponds to the peak in the black curve in Fig. 6.4. From Fig. 6.5 it is clear that amplification of the field does indeed take place in the BL and that it is time-dependent.

The cause for the time-dependency has not been explored, but it is possible that it is related to the re-excitation of acoustic modes within the BL (§6).

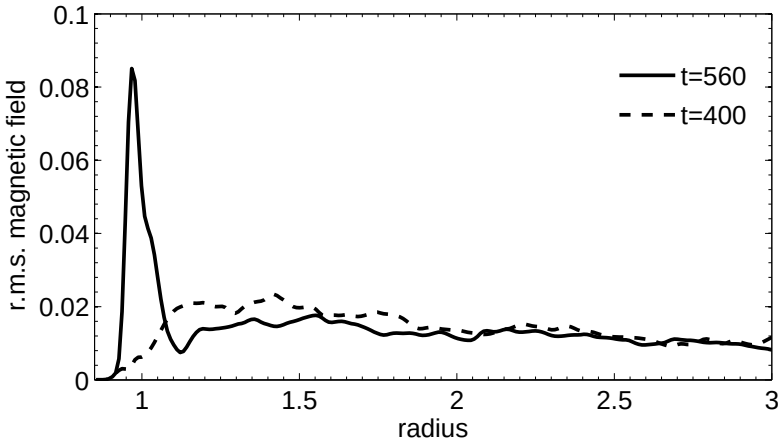


Figure 6.5: Plot of the r.m.s average (in z and ϕ) of B_ϕ for simulation M9d (NVF) at two different points in time. The dashed line corresponds to $t = 400$ when there is little shear amplification of the magnetic field in the BL and the solid line to $t = 560$ when shear amplification reaches a maximum in time.

Although there is field amplification in the BL in our simulations, the field always remains strongly subthermal, consistent with the findings of Armitage (2002). Fig. 6.6 shows radius-time plots of β^{-1} (equation [3.11]) for simulations M9d,e,f, respectively. If magnetic pressure and thermal pressure are comparable, then $\beta \sim 1$ and if thermal pressure dominates magnetic pressure, $\beta \gg 1$. In the figures, $\beta^{-1} \lesssim .06$ for all time and throughout the entire simulation domain, which implies a significantly subthermal field.

5 Acoustic Modes in the MHD context

Before beginning a discussion of angular momentum transport by waves in the BL and the star, we first show that waves are indeed present in our simulations. The waves being referred to are the MHD analogs of the acoustic modes discussed by Belyaev et al. (2012a,b) in the hydrodynamical case. We start by discussing how the hydrodynamical dispersion relation is modified in the presence of a magnetic field and then discuss simulation results.

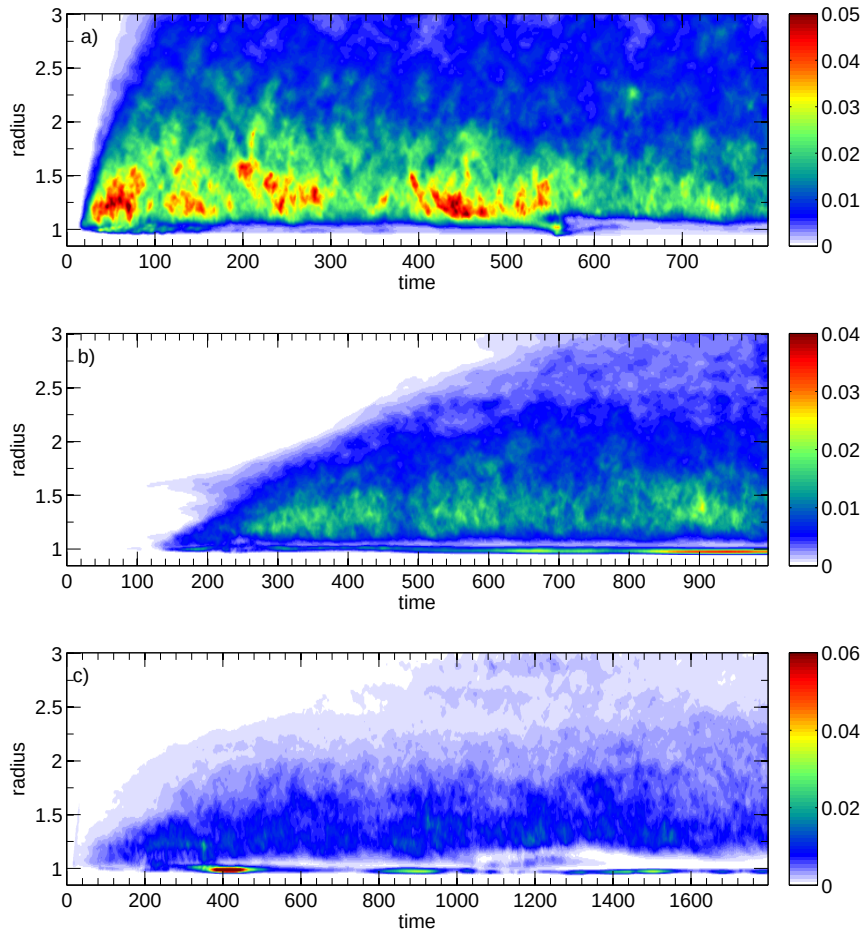


Figure 6.6: Panels a,b,c show radius time plots of β^{-1} from simulations M9d,e,f respectively. There is evidence for amplification of the magnetic field in the BL, but the field remains strongly subthermal.

5.1 Modification to the Hydrodynamical Dispersion Relation

Belyaev et al. (2012b) found that for the isothermal BL, there were three branches of acoustic modes, and they found dispersion relations that matched simulation results for each of these three branches. However, their results were for the pure hydro case, and we comment on how they should be modified to account for the presence of a magnetic field in the disk.

It is natural to expect that the major modification to the dispersion relation of the acoustic modes in the limit of $\beta \gg 1$ is the replacement of the sound speed with the magnetosonic speed.

$$v_{\rm ms} = \sqrt{s^2 + v_A^2} \tag{6.16}$$

$$= s\sqrt{1 + \frac{2}{\gamma}\beta^{-1}} \tag{6.17}$$

where v_A is the Alfvén speed, and $\gamma = 1$ for an isothermal equation of state.

In reality, the situation is slightly more complicated, and the dispersion relation depends on the jump in magnetic field across the BL. We show this explicitly in Appendix A, where we derive an analytic dispersion relation for the 2D modes of a compressible vortex sheet (Miles, 1958; Gerwin, 1968; Belyaev & Rafikov, 2012) in the presence of a magnetic field that is perpendicular to the plane of the modes. This is not a realistic setup, but it highlights how the hydrodynamical dispersion is modified when a magnetic field is introduced.

The main result of the analysis, in the context of astrophysical BLs, is that in the limit of $\beta \gg 1$, the dispersion relation for the model system is only modified by terms of $\mathcal{O}\left(\beta^{-1}\right)$. This result, which may be expected to hold for more general field configurations, shows that when gas pressure dominates magnetic pressure, acoustic modes should still be present, and their properties should only be slightly modified as compared to the hydro case. In a typical astrophysical context, such as in MRI turbulence, the magnetic field is subthermal, meaning $\beta > 1$. As we have shown in §4, the same is also true inside the BL, meaning that the modes present in the layer and its vicinity are essentially acoustic modes, weakly modified by a magnetic field.

In addition to magnetosonic waves, an ideal fluid in the presence of a magnetic field also supports Alfvén and slow waves. One may wonder whether there are also modes of the system that correspond to a coupling of these waves in the disk across the BL to either gravity or sound waves in the star. This subject is beyond the scope of the present work. However, we mention that in our simulations, the modes that show up most clearly are the analogs of the acoustic modes discussed by Belyaev et al. (2012a,b). Thus, it is natural to expect that these magnetosonic modes are the most important ones for transporting angular momentum in the presence of a magnetic field, when $\beta \gg 1$.

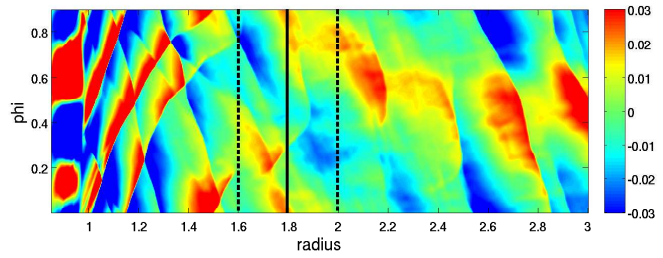
5.2 Simulation Results

We observe excitation of magnetosonic modes in our simulations, which persist, typically, for the duration of the simulation. Fig. 6.7 shows both the simple vertical average and the cross-section through the $z = 0$ plane of both $\varpi\sqrt{\rho}v_\varpi$ and the magnetic field magnitude for simulation M9f at time $t = 1000$. The dominant mode in Fig. 6.7 is the $m = 14$ lower branch mode[1]. It appears prominently in $\varpi\sqrt{\rho}v_\varpi$ (panels a and b), but only weakly in the magnetic field magnitude (panels c and d). The measured pattern speed of the $m = 14$ mode from simulations is $\Omega_P \approx .4$, which is in good agreement with the theoretically predicted pattern speed for the $m = 14$ lower branch mode, $\Omega_P = .415$ (Belyaev et al., 2012b).

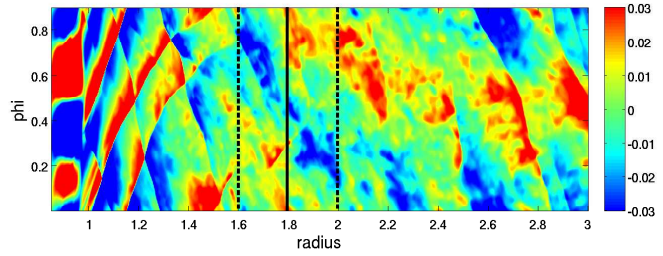
We also point out that the mode depicted in Fig. 6.7 is effectively two-dimensional, since there is not much difference between the vertically averaged image of $\varpi\sqrt{\rho}v_\varpi$ (panel a) and the cross-sectional slice (panel b). The magnetic field, on the other hand, exhibits much more vertical structure (panels c and d), which is indicative of turbulence.

The lower branch has an evanescent region in the disk around the corotation radius and waves incident on the evanescent region are reflected back towards the BL. The edges of this evanescent region are located approximately at the Lindblad radii, which are implicitly defined by the condition $\Omega(\varpi_{\rm LR}) = \Omega_P \pm \kappa(\varpi_{\rm LR})/m$, where κ is the epicyclic frequency. The dashed lines in Fig. 6.7 show the edges of the evanescent region, as predicted by hydrodynamical theory assuming a Keplerian rotation profile, and the solid line shows the corotation radius of the mode in the disk. Even though we now have MRI turbulence in the disk, shocks still reflect off inner edge of the evanescent region. This fact, together with the agreement between the measured pattern speed and that from hydrodynamical theory, means hydrodynamical theory provides a good description of the properties of magnetosonic modes even in the presence of MRI turbulence in the disk. As argued earlier, this can be attributed to the fact that $\beta^{-1} \ll 1$ in the simulations, so the magnetic field does not significantly affect the properties of acoustic modes.

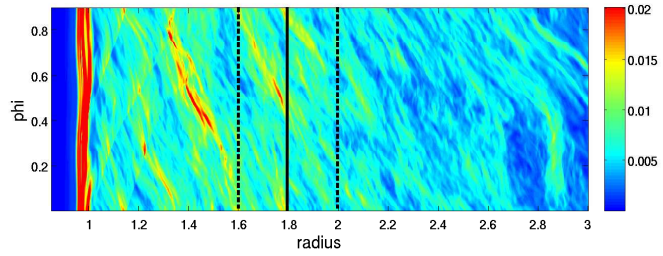
[1]For a discussion of wave branches, including the lower branch, see Belyaev et al. (2012b).



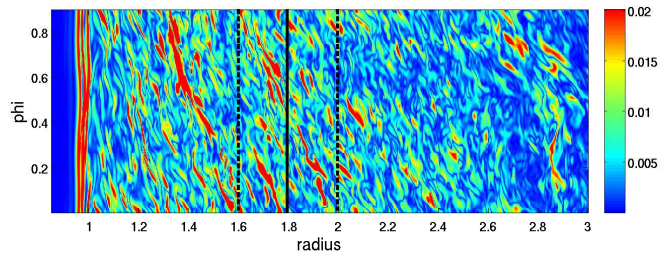
(a)



(b)



(c)



(d)

Figure 6.7: Snapshots at $t = 1000$ from simulation M9f. Panel a) shows the simple vertical average of $\varpi\sqrt{\rho}v_\varpi$, and b) shows a slice through the $z = 0$ plane of $\varpi\sqrt{\rho}v_\varpi$. Panel c) shows the simple vertical average of the magnetic field magnitude and d) shows a slice through the $z = 0$ plane of the magnetic field magnitude. The dashed lines mark the edges of the evanescent region for the $m = 14$ lower branch mode, and the solid line marks the location of the corotation radius in the disk for that mode.

Although the hydrodynamical and MHD cases exhibit many similarities, some differences are apparent. The first difference is that MHD simulations are typically "noisier" than hydro runs (Belyaev et al., 2012a,b) with a superposition of modes present. The second difference is that unlike the hydrodynamical case, there can be significant wave action tunneling through the evanescent region in MHD runs.

The presence of a superposition of acoustic modes in the disk is a generic feature, independent of initial magnetic field geometry. In addition to the lower branch, which is persistent in all of our simulations for $t \gtrsim 60$, we also observe the upper branch at the beginning of some simulations, but only in transience. Fig. 6.8 shows the upper branch at $t = 40$ in simulation M9c. The mode depicted in the figure has $m = 14$ and a measured pattern speed of $\Omega_P = .84$. This agrees well with the theoretically predicted pattern speed for this mode, which is $\Omega_P = .87$.

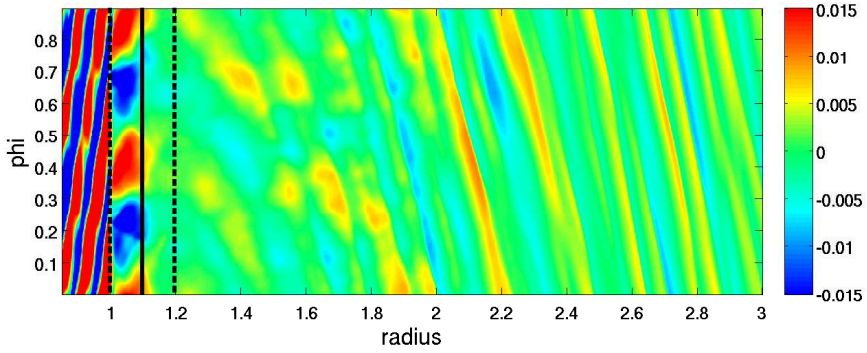


Figure 6.8: Image of the simple vertical average of $\varpi\sqrt{\rho}v_\varpi$ at $t = 40$ for simulation M9c. The $m = 14$ upper branch mode is clearly present in the image. The magnetic field is not shown, since at this time, the MRI instability has not yet fully developed. The dashed lines mark the edges of the evanescent region for the $m = 14$ upper mode, and the solid line shows the corotation radius for that mode.

6 Angular Momentum Transport by Waves in the BL, Star, and Inner Disk

Having shown that magnetosonic modes are present in our simulations and have similar properties to the acoustic modes discussed in Belyaev et al. (2012b), we now show that they are able to transport angular momentum in the star and inner disk just as in hydrodynamical simulations.

6.1 Density Gap in the Inner Disk and Accretion onto the Star

We begin our discussion of wave transport of angular momentum by showing the evolution of the density profile. Fig. 6.9 shows radius time plots of $\Sigma_0(\varpi, t)$ in simulations M9d,e,f. In each case, a gap in the density develops in the inner disk in the vicinity of the BL ($\varpi \gtrsim 1$). The gap is opened up relatively rapidly, over a time of $\lesssim 10$ orbits, and in panels a and c, gap formation is followed at a later time by gap deepening. Concentrating on panel c, after the initial gap opening event at $t \approx 200$, the density profile of the gap stays approximately constant, until $t \approx 1100$ when it undergoes substantial gap deepening. For $t > 1100$, the gap is gradually filled in by the action of turbulent viscosity in the disk.

Belyaev et al. (2012b) also observed gap formation in their hydrodynamical simulations, which was driven by angular momentum transport by acoustic modes. Consistent with their results, we find that magnetosonic modes are responsible for opening up the gap in our MHD simulations, and we discuss the link between acoustic modes and the gap in the inner disk in more detail in §6.2.

Material gets removed from the inner part of the disk between the BL and the wave reflection point at the inner Lindblad resonance by the action of magnetosonic modes. In this region gas orbits the star faster than the pattern of acoustic modes, and every time a fluid element encounters a weak shock (into which modes evolve) it loses angular momentum and moves towards the star, giving rise to continuing accretion. Fig. 6.10 shows plots of the instantaneous mass accretion rate through radius ϖ, $\dot{M}(\varpi)$, for simulations M9d,e,f (panels a,b,c) and for a $M = 9$ hydro simulation from Belyaev et al. (2012b) (panel d). The solid curves correspond to

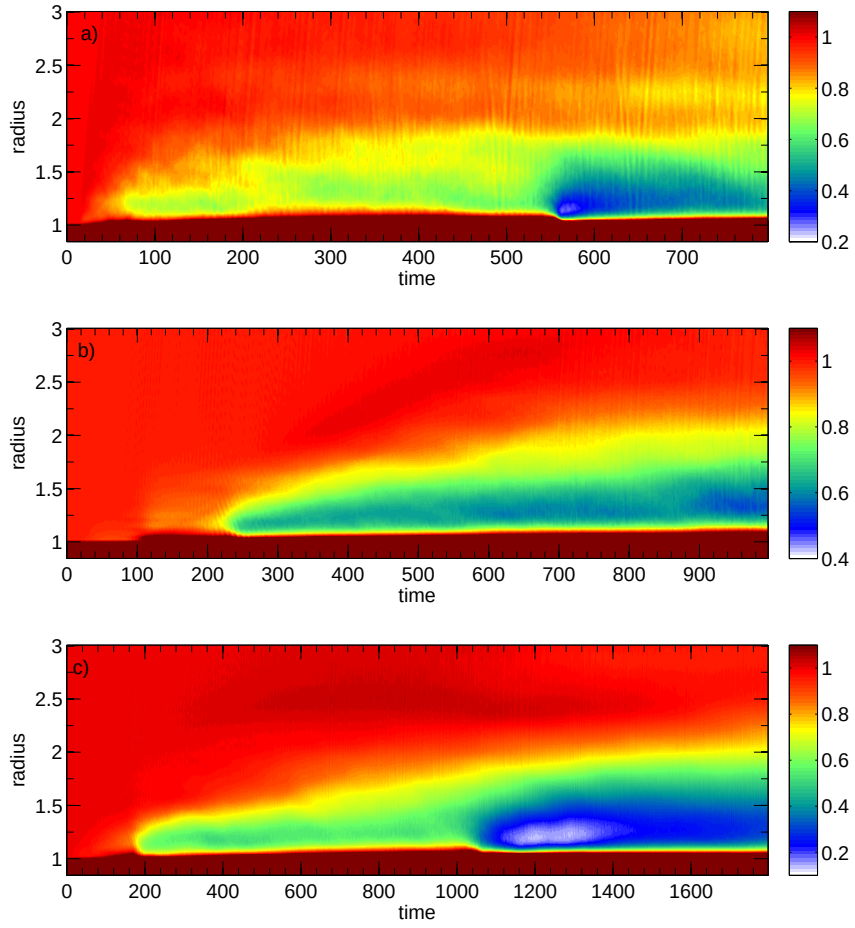


Figure 6.9: Panels a,b,c show radius time plots of Σ_0 from simulations M9d,e,f (NVF, NAF, ZNF) respectively. A density gap in the disk near $\varpi = 1$ develops in all of the simulations and in panels a and c gap deepening is observed at a later time.

periods when magnetosonic/acoustic modes are excited to a high amplitude (high shock accretion rate) and the dashed curves to periods when their amplitude is not as high (low shock accretion rate). Each of the solid curves in panels a-c corresponds to one of the gap formation or opening events in Fig. 6.9.

In panels a-c, the dashed and solid curves converge to approximately the same value of $\dot{M}$ in the outer disk in Fig. 6.10, but the solid curves have a significantly higher amplitude than the dashed ones in the inner disk ($\varpi \gtrsim 1$). The extra contribution to $\dot{M}$ for the solid curves in the inner disk in panels a-c is provided by magnetosonic modes, and the base level of $\dot{M}$ in the outer disk is due to MRI turbulence.

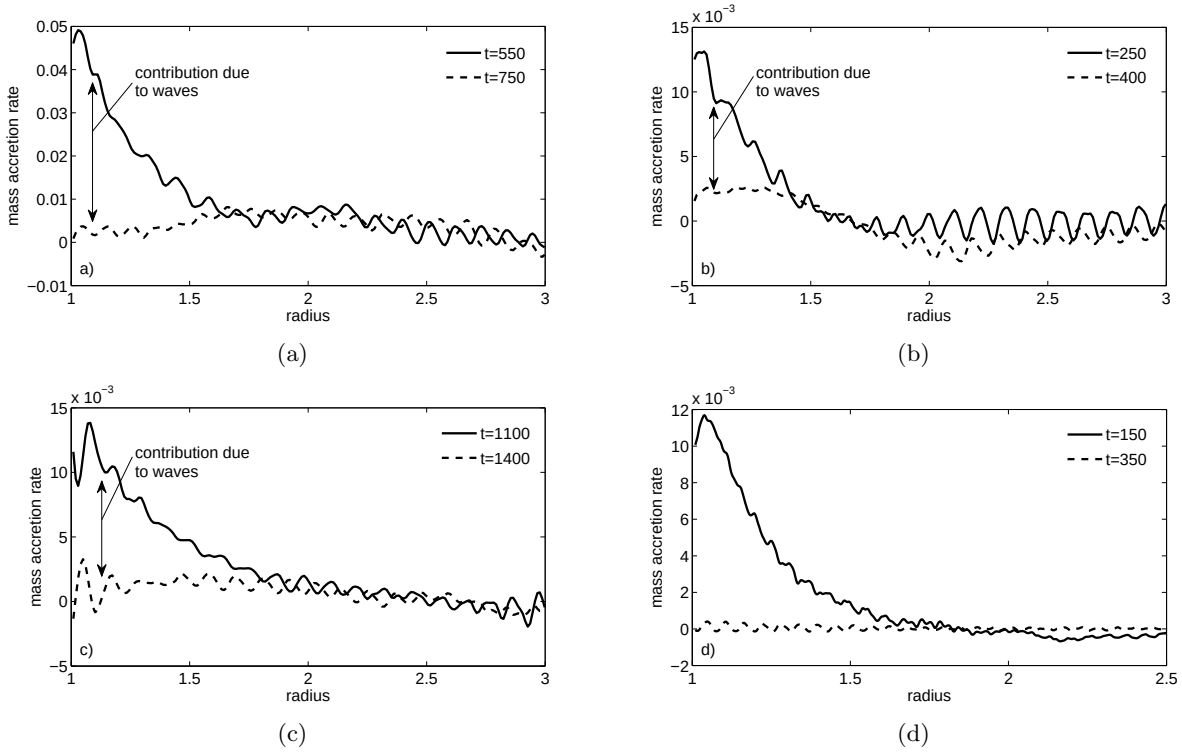


Figure 6.10: Panels a, b, c show plots of the instantaneous mass accretion rate, $\dot{M}$, from simulations M9d,e,f (NVF, NAF, ZNF) at the times indicated in the legends. Panel d shows the mass accretion rate for an $M = 9$ hydro simulation considered in Belyaev et al. (2012b) (their 3D9a simulation). The solid and dashed lines show $\dot{M}$ during periods when acoustic modes have relatively high and low amplitudes, respectively. The large spike in accretion rate in the inner disk for the solid curves as compared to the dashed ones is caused by shock accretion in the inner disk due excitation of modes to a high amplitude.

Evidence for this assertion is provided by considering panel d of Fig. 6.10. Since the simulation corresponding to panel d is hydrodynamical, there is no MRI in the disk. This explains why the dashed line is everywhere approximately zero, since in the absence of waves excited to a high amplitude or MRI, there is no efficient mechanism for angular momentum transport in the disk. On the other hand, the shape and amplitude of the solid curve in the inner disk in panel d are similar to those of the solid curves in panels a-c. This shows that in the MHD case, the mass accretion rate in the inner disk due to shocks can dominate that due to MRI, during periods when modes are excited to a high amplitude.

Indeed, we can write the following expression for the combined mass accretion rate close to the star (interior to the evanescent region in the disk) driven by both the MRI and shocks:

$$\dot{M} = \frac{\Sigma s^2}{\Omega}\left[4\pi\alpha q \frac{\partial \ln\left(\alpha q s^2 \Sigma \varpi^2\right)}{\partial \ln \varpi} + \frac{m}{3(2-q)}\left(1+\frac{\Delta\Sigma}{\Sigma}\right)^{-2}\left(\frac{\Delta\Sigma}{\Sigma}\right)^3\right], \tag{6.18}$$

where $q(\varpi) \equiv -d\ln\Omega/d\ln\varpi$ is the local shear rate ($q = 3/2$ for a Keplerian disk but is a function of ϖ for a general rotation profile), m is the azimuthal wavenumber of the mode, and $\Delta\Sigma/\Sigma$ is the density contrast across the shock (mode) fronts. The first term in brackets is the contribution from MRI (α here is solely due to MRI) and can derived using the results of Lynden-Bell & Pringle (1974) and Rafikov (2012). The second term is the contribution from magnetosonic waves following from Belyaev et al. (2012a), namely from their equation (B7). For a characteristic azimuthal wavenumber of $m \sim 15-30$ and MRI viscosity $\alpha \lesssim 10^{-2}$ (see Fig. 6.3) measured in our simulations, one finds that both transport mechanisms provide comparable contribution to $\dot{M}$ if $\Delta\Sigma/\Sigma \sim 0.2$.

However, during periods of strong wave excitation $\Delta\Sigma/\Sigma$ increases and the wave term strongly dominates $\dot{M}$ because of the steep (cubic) dependence of $\dot{M}$ upon $\Delta\Sigma/\Sigma$. For instance, the amplitude of the $m = 14$ magnetosonic mode changes by a factor of ≈ 5 in simulation M9f between $t = 900$ and $t = 1100$. This results in a predicted mass accretion rate due to shocks in the inner disk that is higher by approximately two orders of magnitude at $t = 1100$ as compared to $t = 900$.

This effect of enhanced mass accretion rate by shocks during periods when magnetosonic modes are excited to a high amplitude is demonstrated by the solid curves in Fig. 6.10. Equation (6.18) also explains the characteristic spatial dependence of $\dot{M}$ on ϖ: approximate conservation of the wave angular momentum flux (neglecting for the moment dissipation at the shock fronts) results in (see equation (25) of Belyaev et al. (2012a))

$$\frac{\Delta\Sigma}{\Sigma} \propto \left[\frac{|\Omega(\varpi)-\Omega_P|}{\Sigma s^3 \varpi}\right]^{1/2}. \tag{6.19}$$

This expression shows that $\Delta\Sigma/\Sigma$ is highest near the BL, where $|\Omega(\varpi)-\Omega_P|$ is large and goes to zero in the evanescent region where $\Omega = \Omega_P$. This explains why during the high wave amplitude

episodes, when mass accretion is clearly dominated by dissipation of acoustic modes, $\dot{M}$ is largest near the BL, but rapidly decays to small value as ϖ approaches the evanescent region in the disk.

Note that inside the BL MRI does not operate, $\alpha = 0$, and the first term in equation (6.18) vanishes, leaving wave dissipation as the only means of mass transport. On the other hand, in the disk outside the corotation radius, waves do not contribute to transport and second term in equation (6.18) disappears. Thus, MRI remains the only mass transport mechanism outside the resonant cavity in which the pattern of standing acoustic modes exists, in agreement with the picture outlined in Belyaev et al. (2012a) and Belyaev et al. (2012b).

6.2 Angular Momentum Transport due to Waves and MRI

In this section, we connect the density gap in the inner disk to magnetosonic modes and discuss angular momentum transport in the star, BL, and inner disk more generally.

Fig. 6.11 shows radius time plots of the angular momentum current, C_S, from simulations M9d,e,f. In the disk, far away from the BL, angular momentum transport is due primarily to MRI turbulence (§3), and C_S is approximately constant at a given radius once the MRI has saturated. We note that the striations appearing in C_S are caused by waves. The striations in the panels of Fig. 6.11 are predominantly downward sloping in the inner disk, indicating inward propagating waves. These waves are excited at the "front" of MRI turbulence which propagates radially outward through the disk over the course of the simulation. Although potentially a nuisance, these waves do not play a major role in angular momentum transport in our simulations.

In contrast to the outer disk, where the value of C_S at a given radius is approximately constant in time once MRI turbulence has saturated, C_S varies by more than an order of magnitude in the star and inner disk over the course of a simulation. This implies a mechanism of angular momentum transport that is decoupled from MRI turbulence. As we shall shortly demonstrate, this mechanism is transport of angular momentum by magnetosonic modes. Given this fact, we can directly link magnetosonic modes to the gap formation and deepening events in Fig. 6.9, since these are simultaneous with the periods when C_S is large in the BL and star in Fig. 6.11.

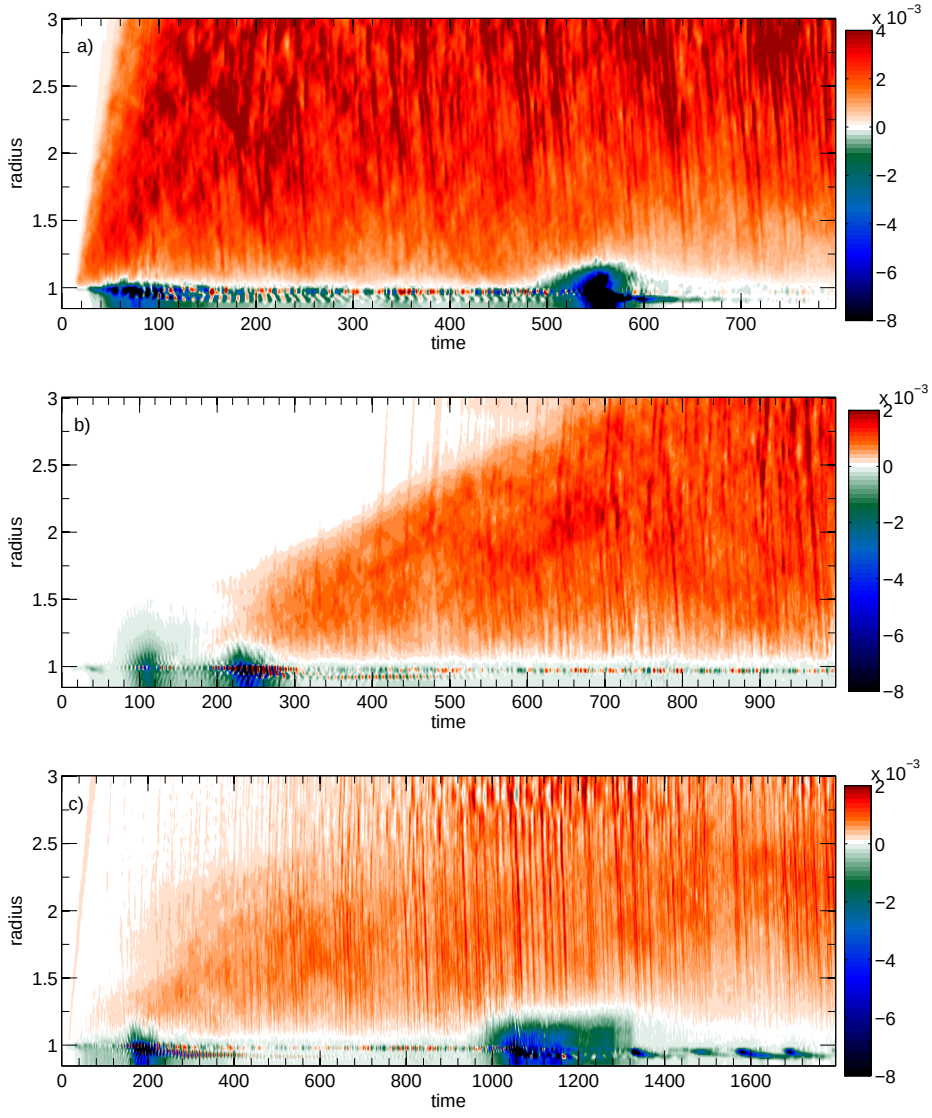


Figure 6.11: Panels a,b,c show radius time plots of the angular momentum current C_S from simulations M9d,e,f (NVF, NAF, ZNF) respectively. Notice that C_S changes sign in the vicinity of the BL with $C_S < 0$ for $\varpi \lesssim 1$ and $C_S > 0$ for $\varpi \gtrsim 1$.

In addition to waves dominating angular momentum transport in the star and BL, we find that they also contribute significantly to angular momentum transport in the inner disk. Fig. 6.12 shows C_S and Ω superimposed on the same plot for simulations M9d,e,f at times $t = 550$, 250, and 1100, when the angular momentum current due to waves is high in each simulation. The dashed vertical line denotes the radius at which $C_S = 0$, and for an anomalous viscosity model, $C_S = 0$ and $d\Omega/d\varpi = 0$ occur at the same radius (equation [6.9]). However, we see in Fig. 6.12

that the radius at which $C_S = 0$ is significantly displaced into the disk compared to the radius at which $d\Omega/d\varpi = 0$. This implies that C_S contains a contribution due to waves in the disk, since $C_S < 0$ for outgoing waves up to the corotation radius in the disk, which is located at $\varpi_{\rm cr} \approx 1.8$ ($m = 14$ mode) in each of the panels in Fig. 6.12.

We conclude that when waves are excited to a high amplitude, they significantly modify the profile of C_S in the inner disk compared to what is expected for a turbulent viscosity model. In particular, if both magnetosonic modes and anomalous viscosity contribute appreciably to C_S, then the radius at which $C_S = 0$ in the disk is neither at the corotation radius of the mode, nor at the radius where $d\Omega/d\varpi = 0$, but somewhere in between.

We also mention that the variation of C_S with radius in the star and BL in each of the panels in Fig. 6.12 is consistent with $C_S(\varpi)$ for the lower branch (Fig. 12 of Belyaev et al. (2012b)). Since the lower branch is directly observed in our simulations (§5), this provides further confirmation that angular momentum is transported by waves in the BL and star.

6.3 Hydrodynamical Nature of Angular Momentum Transport in the Star and BL

Having established that magnetosonic modes transport angular momentum in the BL and star, and also influence transport in the inner disk, we now demonstrate that the mechanism of angular transport by acoustic modes is essentially hydrodynamical in nature. This provides evidence for the argument presented in §5.1 that when $\beta \gg 1$, the properties of acoustic modes are not significantly affected by the magnetic field, and the results of Belyaev et al. (2012b) are valid.

To show that stresses in the BL are hydrodynamical, we split C_S into magnetic and nonmagnetic components (equation [6.7]). Fig. 6.13 shows $C_{S,B}$ and $C_{S,H}$ for each of simulations M9d,e,f, and several things are immediately apparent. The first is that $C_{S,B}$ is several times larger than $C_{S,H}$ in the disk, which is consistent with the fact that the magnetic stress is several times the hydrodynamical stress for MRI turbulence (Sorathia et al., 2012). The second is that $C_{S,B}$ vanishes going into the star and there is no bump in $C_{S,B}$ within the BL. This means that magnetic stresses are *not* important for transport in the BL. This is consistent with the results of Pessah & Chan (2012), who found that in the shearing sheet approximation, the magnetic stress

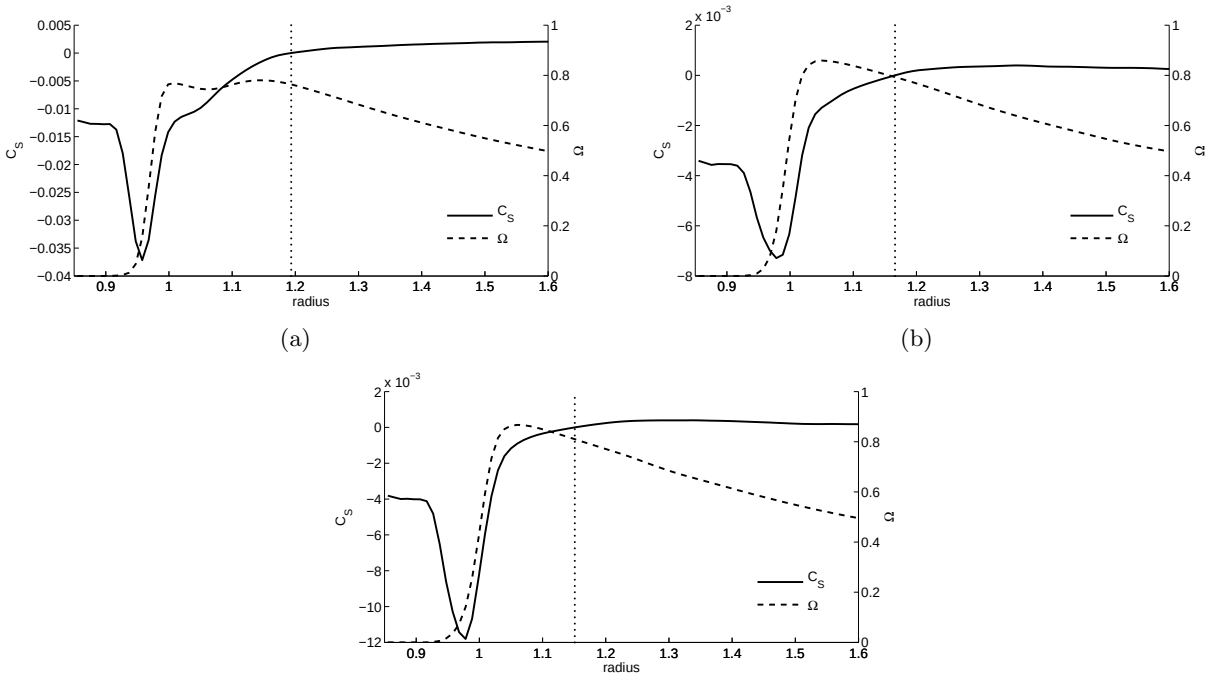


Figure 6.12: Panels a,b,c show plots of C_S and Ω for simulations M9d,e,f at times $t = 550$, 250, and 1100. The dashed vertical line denotes the radius at which $C_S = 0$ and is significantly displaced into the disk relative to the radius at which $d\Omega/d\varpi = 0$. In general, when angular momentum in the disk is transported by both a magnetosonic mode and turbulent viscosity, the location at which $C_S = 0$ occurs between the radius at which $d\Omega/d\varpi = 0$ and the corotation radius of the mode, $\varpi_{\rm cr} \approx 1.8$ in this example.

oscillates about zero for a rising rotation profile ($d\Omega/d\varpi > 0$), as in the BL. The third is that $|C_{S,H}| \gg |C_{S,B}|$ in the star and BL, which is definitive proof that a hydrodynamical mechanism of angular momentum transport operates there – namely acoustic modes weakly modified by a magnetic field.

6.4 Boundary Layer Width

Belyaev et al. (2012a) and Belyaev et al. (2012b) found that in hydro simulations the BL settled to a radial width of $6 - 7$ radial scale heights ($h_s \equiv s^2/g(\varpi_\star)$). Using their definition for the BL

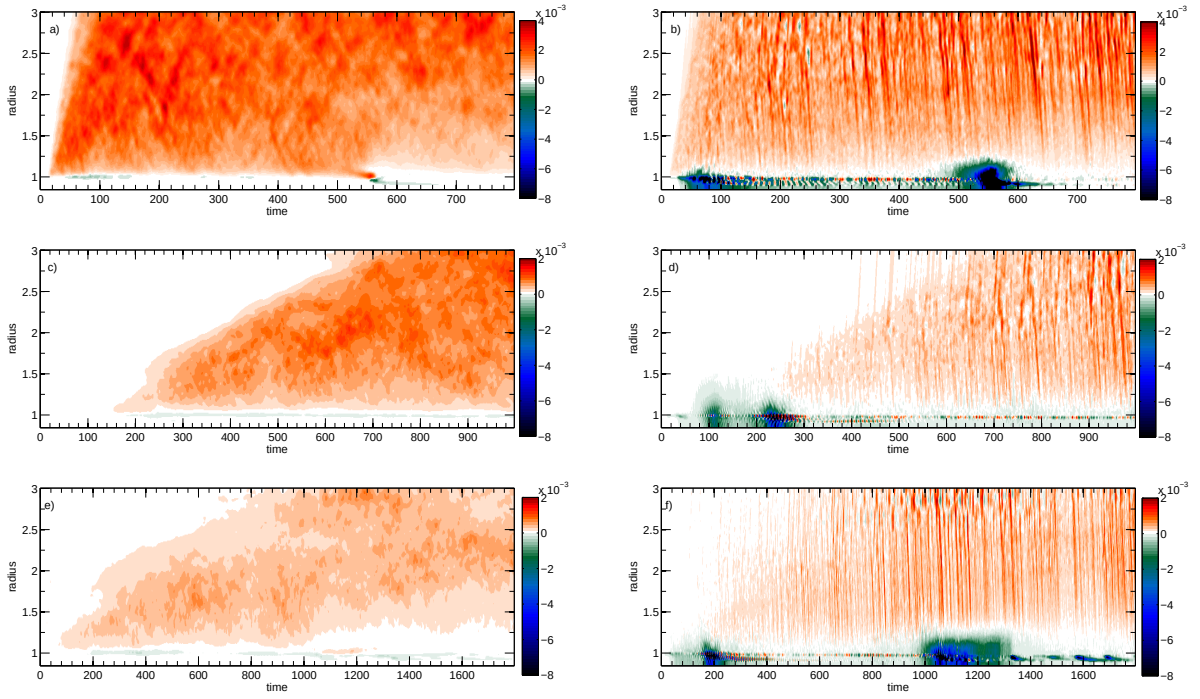


Figure 6.13: Panels a,c,e show radius time plots of $C_{S,B}$ from simulations M9d,e,f (NVF, NAF, ZNF) respectively, and panels b,d,f show radius time plots of $C_{S,H}$ from simulations M9d,e,f. The scale, colormap, and axes labels for each simulation (M9d,e,f) are the same as in Fig. 6.11. Notice that $C_{S,B}$ vanishes inside the star, and there is no bump in $C_{S,B}$ within the BL. On the other hand, $C_{S,H}$, is large inside the BL and is both large and approximately constant (spatially) within the star, which suggests transport by waves.

as the region in which

$$0.1 < \langle v_\phi(\varpi)\rangle / v_K(\varpi) < 0.9, \tag{6.20}$$

we confirm that after the initial gap opening event, the BL in our MHD simulations also settles down to a radial width of 6-7 radial scale heights (Fig. [6.14]). However, the BL undergoes widening events that are coincident with gap deepening events (§6.1) and the periods when C_S is large in the star and BL (§6.2). Stochastic widening events were also observed by Belyaev & Rafikov (2012) in 2D hydro simulations, and it appears that in both hydro and MHD cases these events are mediated by the action of shocks on the fluid in the inner disk.

The fact that the BL widening events occur simultaneously with gap deepening events, suggests a common origin, implying that magnetosonic modes play a critical role in regulating the width of the BL. However, given the occurrence of stochastic widening events in the simulations, the width of the BL is time-variable and it is not possible to assign a single number to it. Nevertheless, what the simulations suggest is that the BL initially settles down to a steady state width of 6-7 radial scale heights and is subsequently widened, during periods when magnetosonic modes are excited to a high amplitude.

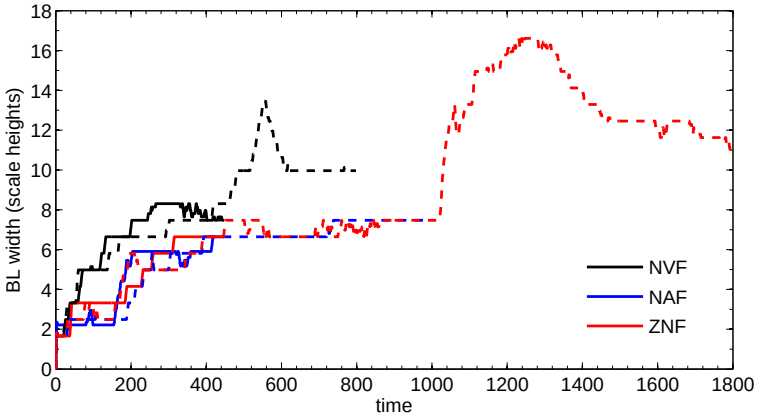


Figure 6.14: Boundary layer width in units of scale height s^{-2} (defined implicitly in equation [6.20]) as a function of time, for each of our simulations. The black, blue, and red curves correspond to NVF, NAF, and ZNF simulations respectively. The solid lines correspond to simulations with the higher resolution for a given magnetic field geometry.

7 Discussion

We have shown that even in the presence of MRI turbulence in the disk, waves dominate angular momentum transport in the BL, and influence transport in the inner disk. The importance of waves for angular momentum transport in the BL was previously shown by Belyaev et al. (2012b) for the purely hydrodynamical case.

We find that when a magnetic field is introduced, the acoustic modes discussed by Belyaev et al. (2012b) become magnetosonic modes. These magnetosonic modes have a dispersion relation that differs from the dispersion relation for acoustic modes by factors that are $\mathcal{O}(\beta^{-1})$. Since the

field in our simulations is highly subthermal ($\beta^{-1} \lesssim .06$) everywhere, including the BL, the hydrodynamical theory of Belyaev et al. (2012b) remains a good approximation to the dynamics of magnetosonic modes in our simulations.

Unlike MRI turbulence, which can be parametrized by an anomalous viscosity, the transport of energy and angular momentum in the BL is a *non-local* process, as has been emphasized in Belyaev et al. (2012b). Energy and momentum are carried away from the BL by acoustic waves weakly modified by magnetic field into both the star and the disk and can be deposited far away from the BL. This has important implications for stellar spinup, heating of the star, disk and the BL itself, and for observational manifestations of the BL phenomenon (Belyaev et al., 2012b). In the MHD case, additional dissipation is produced in the disk due to the operation of MRI but, as one can infer from Fig. 6.3 where α_B is seen to vanish in the BL, the MRI-generated heat is unlikely to penetrate into the BL and affect its structure.

Amplification of the magnetic field in the BL that we see in our simulations (§4) is consistent with earlier theoretical expectations (Pringle, 1989) but does not result in efficient magnetically-mediated transport of angular momentum in this region. Our study is in agreement with the analytical work of Pessah & Chan (2012), who analyzed the evolution of MHD modes in presence of shear with $\partial\Omega/\partial\varpi > 0$ and demonstrated that although the energy density of these modes can be amplified significantly, their associated stresses oscillate around zero, rendering them inefficient at transporting angular momentum. As a consequence, angular momentum transport in the BL is mediated by quasi-acoustic modes, and in particular shock dissipation of these modes in the inner disk.

Previously, Steinacker & Papaloizou (2002), Armitage (2002) performed isothermal MHD simulations of the BL, and the setup of Armitage (2002) in particular was nearly identical to ours. Therefore, a natural question that arises is why did these authors not observe acoustic modes and recognize their importance for angular momentum transport in the BL? Interestingly, the answer to this question may be that the modes were in fact observed in these early simulations, but their presence and significance were not fully appreciated.

For instance, Fig. 3 of Armitage (2002) shows an image of relative density perturbation averaged over the z-dimension. The density fluctuations in the image exhibit a leading/trailing mode pattern that looks strikingly similar to the lower mode trapped between the BL and the evanescent region in the disk, see Fig. 6.7. Note that $\Delta\Sigma/\Sigma \propto \Sigma^{-1/2}$ for an acoustic mode propagating into the star by angular momentum conservation, see equation (6.19), which explains why the amplitude of density fluctuations rapidly decreases going into the star in Fig. 3 of Armitage (2002).

It is harder to comment on whether Steinacker & Papaloizou (2002) observed acoustic modes, since they used a different initial setup than ours and *prescribed* a rotation profile for the BL region in their simulations. In contrast, the profile of Ω in the BL is naturally established in our simulations due to action of the sonic instability early on in the simulations (Belyaev et al., 2012a,b), which widens the initial interfacial region into a self-consistent BL. Nevertheless, it is quite possible that Steinacker & Papaloizou (2002) also observed acoustic modes excited in the BL, as they briefly mentioned the presence of "stochastic spiral patterns" in their simulations, which could well have been the manifestation of acoustic modes (e.g. see Fig. 7 of Steinacker & Papaloizou (2002)).

Another important question that arises is given that we have used an isothermal equation of state, what might be expected for a more realistic equation of state? As discussed in Belyaev et al. (2012b) one pathology of the isothermal equation of state is that the Brunt-Väisälä frequency, $N^2 = (\gamma - 1)g^2/s^2$, is equal to zero. This means that our computational model does not support gravity waves and in a real star with nonzero Brunt-Väisälä frequency, magnetosonic waves in the disk could couple to gravity waves in the star increasing the number of possible modes in the star-BL-disk system.

Another difference is that the sound speed is not constant in a real star and is an inverse function of the radius. This means that the cutoff frequency below which sound waves do not propagate is also an inverse function of the radius and without a damping process, such as radiative damping, waves propagating into the star would reflect back towards the BL. A simple way to model this effect in simulations would be to introduce a reflecting wall at the inner

boundary of the simulation domain. Glatzel (1988), Belyaev & Rafikov (2012) found analytically that for the case of a supersonic shear layer with a linear velocity profile, instability was present for both reflecting wall and radiation boundary conditions. Therefore, although reflection at an inner boundary would likely modify the details of angular momentum transport by waves, in particular the spinup rate of the star and possibly the wavelength of the dominant mode, magnetosonic modes would still be excited in such a system.

Resources supporting this work were provided by the NASA High-End Computing (HEC) Program through the NASA Advanced Supercomputing (NAS) Division at Ames Research Center. We thank Jeremy Goodman and Anatoly Spitkovsky for useful discussions. The financial support for this work is provided by NASA grant NNX08AH87G.

Bibliography

Alexakis, A., Young, Y., & Rosner, R. 2002, Phys. Rev. E, 65, 026313

Armitage, P. J. 2002, MNRAS, 330, 895

Balbus, S. A. & Hawley, J. F. 1991, ApJ, 376, 214

Balbus, S. A. & Papaloizou, J. C. B. 1999, ApJ, 521, 650

Belyaev, M. A. & Rafikov, R. R. 2012, ApJ, 752, 115

Belyaev, M. A., Rafikov, R. R., & Stone, J. M. 2012a, ApJ, 760, 22

Belyaev, M. A., Rafikov, R. R., & Stone, J. M. 2012b, ArXiv e-prints

Chandrasekhar, S. 1960, Proceedings of the National Academy of Science, 46, 253

Fromang, S. & Papaloizou, J. 2007, A&A, 476, 1113

Fromang, S., Papaloizou, J., Lesur, G., & Heinemann, T. 2007, A&A, 476, 1123

Fu, W. & Lai, D. 2012, ArXiv e-prints

Gerwin, R. A. 1968, Reviews of Modern Physics, 40, 652

Ghosh, P. & Lamb, F. K. 1978, ApJ, 223, L83

Glatzel, W. 1988, MNRAS, 231, 795

Guan, X., Gammie, C. F., Simon, J. B., & Johnson, B. M. 2009, ApJ, 694, 1010

Hawley, J. F., Guan, X., & Krolik, J. H. 2011, ApJ, 738, 84

Heinemann, T. & Papaloizou, J. C. B. 2009a, MNRAS, 397, 52

Heinemann, T. & Papaloizou, J. C. B. 2009b, MNRAS, 397, 64

Heinemann, T. & Papaloizou, J. C. B. 2012, MNRAS, 419, 1085

Inogamov, N. A. & Sunyaev, R. A. 1999, Astronomy Letters, 25, 269

Koldoba, A. V., Romanova, M. M., Ustyugova, G. V., & Lovelace, R. V. E. 2002, ApJ, 576, L53

Lai, D. & Tsang, D. 2009, MNRAS, 393, 979

Lesur, G. & Longaretti, P.-Y. 2005, A&A, 444, 25

Li, L.-X., Goodman, J., & Narayan, R. 2003, ApJ, 593, 980

Li, L.-X. & Narayan, R. 2004, ApJ, 601, 414

Lynden-Bell, D. & Pringle, J. E. 1974, MNRAS, 168, 603

Miles, J. W. 1958, Journal of Fluid Mechanics, 4, 538

Narayan, R. 1992, ApJ, 394, 261

Pessah, M. E. & Chan, C.-k. 2012, ApJ, 751, 48

Piro, A. L. & Bildsten, L. 2004, ApJ, 610, 977

Piro, A. L. & Bildsten, L. 2007, ApJ, 663, 1252

Popham, R. & Narayan, R. 1992, ApJ, 394, 255

Popham, R. & Narayan, R. 1995, ApJ, 442, 337

Pringle, J. E. 1989, MNRAS, 236, 107

Rafikov, R. R. 2012, ArXiv e-prints

Shakura, N. I. & Sunyaev, R. A. 1973, A&A, 24, 337

Sorathia, K. A., Reynolds, C. S., Stone, J. M., & Beckwith, K. 2012, ApJ, 749, 189

Spruit, H. C. 1999, A&A, 349, 189

Spruit, H. C. 2002, A&A, 381, 923

Steinacker, A. & Papaloizou, J. C. B. 2002, ApJ, 571, 413

Tayler, R. J. 1973, MNRAS, 161, 365

Tsang, D. & Lai, D. 2009a, MNRAS, 393, 992

Tsang, D. & Lai, D. 2009b, MNRAS, 400, 470

Tsang, D. & Lai, D. 2009c, MNRAS, 396, 589

Velikhov, E. P. 1959, J. Exptl. Theoret. Phys., 36, 1398

A Dispersion Relation for the Compressible Vortex Sheet in the Presence of a Constant Magnetic Field that is Oriented Perpendicular to the Motion

Here we present the dispersion relation for modes of the compressible vortex sheet with wavevectors lying in the x-y plane, when a z-directed magnetic field is present. Under this set of assumptions, the $\boldsymbol{B} \cdot \boldsymbol{\nabla} \boldsymbol{B}$ term in the MHD equations is zero, which means Alfvén waves are not permitted, the slow wave is null, and only the fast magnetosonic wave survives. In fact, in such a setup the magnetic field simply provides pressure support and behaves as though it were a fluid with an effective adiabatic index of $\gamma_B = 2$. Although this is not a realistic description for

astrophysical boundary layers, it gives us a flavor for how the dispersion relation of acoustic modes is modified when a weak magnetic field is introduced. In particular, it shows that for a weak magnetic field, the corrections to the dispersion relation are small and are of order $\mathcal{O}\left(\beta^{-1}\right)$.

Since all fluid quantities in our setup are independent of z we are essentially studying a 2D problem. In that case, the ideal MHD equations with an adiabatic equation of state can be formulated as

$$\frac{\partial \rho}{\partial t} + \boldsymbol{\nabla} \cdot (\rho \boldsymbol{v}) = 0, \tag{6.21}$$

$$\frac{\partial (\rho \boldsymbol{v})}{\partial t} + \boldsymbol{\nabla} \cdot (\rho \boldsymbol{v}\boldsymbol{v}) = -\boldsymbol{\nabla}\left(P + \frac{B_z^2}{2\mu}\right), \tag{6.22}$$

$$P = K\rho^{\gamma}, \tag{6.23}$$

$$B_z = \sigma\rho, \tag{6.24}$$

where, we have replaced the induction equation (3.4) with the frozen-in law (6.24) and introduced the "magnetization" of the fluid per unit mass, σ. Equations (6.21-6.24) can be simplified to

$$\frac{\partial \rho}{\partial t} + \boldsymbol{\nabla} \cdot (\rho \boldsymbol{v}) = 0, \tag{6.25}$$

$$\frac{\partial (\rho \boldsymbol{v})}{\partial t} + \boldsymbol{\nabla} \cdot (\rho \boldsymbol{v}\boldsymbol{v}) = -\boldsymbol{\nabla}\left(K\rho^{\gamma} + \frac{\sigma^2}{2\mu}\rho^2\right). \tag{6.26}$$

Written in this form, it is clear that for our setup the magnetic field behaves in the same manner as a fluid with $\gamma_B = 2$.

We now describe the compressible vortex sheet setup, following the notation of Belyaev & Rafikov (2012). The velocity profile of the model setup is given by

$$V_y(x) = \begin{cases} \bar{V}_y, & x > 0 \\ -\bar{V}_y, & x < 0, \end{cases} \tag{6.27}$$

where $\bar{V}_y$ is a constant, and a velocity discontinuity is present at $x = 0$. For $x > 0$, the density, magnetization, and sound speed are constant and are given by ρ_+, σ_+, and s_+, respectively.

Similarly, for $x < 0$ these parameters are constant as well and are given by ρ_-, σ_-, and s_-, respectively.

Using the techniques laid down in (Gerwin, 1968; Alexakis et al., 2002; Belyaev & Rafikov, 2012), it is a straightforward if lengthy exercise to derive the dispersion relation for linearized perturbations of this system. Thus, we omit the derivation and simply state the dispersion relation, which is

$$\epsilon^2 \left[(M_{\rm ms}+\varphi)^2\epsilon^{-1}(1+\delta)^{-1}-1\right](M_{\rm ms}-\varphi)^4 = \left[(M_{\rm ms}-\varphi)^2-1\right](M_{\rm ms}+\varphi)^4 . \tag{6.28}$$

Here, $\epsilon \equiv \rho_+/\rho_-$ is the density contrast across the vortex sheet, $\varphi \equiv \omega/k_y s_+$ is the dimensionless phase speed, $M_{\rm ms} \equiv \bar{V}_y/\sqrt{s_+^2+v_{A,+}^2}$ is the magnetosonic Mach number, and δ is defined through the relation

$$\epsilon(1+\delta) \;=\; \frac{s_-^2+v_{A,-}^2}{s_+^2+v_{A,+}^2}. \tag{6.29}$$

As in the text, v_A denotes the Alfvén velocity.

Equation (6.28) is identical to equation (39) of Belyaev & Rafikov (2012) for the unmagnetized case, except that the Mach number has been replaced by the magnetosonic Mach number, and there is an additional factor of $(1+\delta)^{-1}$. The first of these modifications, the replacement of the Mach number with the magnetosonic Mach number, is to be expected and was argued for in the text. The second is harder to anticipate and a nonzero δ can be thought of as coming from a difference in the effective γ of the fluid across the vortex sheet. The effective γ of the fluid is a suitably weighted combination of γ and γ_B.

The major point of equation (6.28) as regards astrophysical BLs is to show that for a weak magnetic field, the dispersion relation for the compressible vortex sheet is only modified up to terms of $\mathcal{O}\left(v_A^2/s^2\right)$ (i.e. $\mathcal{O}\left(\beta^{-1}\right)$). Since the dispersion relation for the three wave branches of acoustic modes discussed in §5 is simply related to the dispersion relation for the compressible vortex sheet (Belyaev et al., 2012a), we reason that properties of acoustic modes are also only modified by terms of $\mathcal{O}\left(\beta^{-1}\right)$ in the presence of a magnetic field. Since β tends to be large in our

simulations, even in the BL, we reason that the magnetic field due to MRI perturbs the acoustic modes, but does not modify them in a fundamental way.